ACCRETION FLOWS IN POLARS

MARGARET K. HARROP-ALLIN

A thesis submitted to the University of London

for the degree of Doctor of Philosophy

Department of Space and Climate Physics

Mullard Space Science Laboratory

University College London

January 1999

ProQuest Number: 10797704

ProQuest 10797704

"Thus he who has raised himself above the alms-basket, and, not content to live lazily on scraps of begged opinions, sets his own thoughts on work, to find and follow truth, will (whatever he lights on) not miss the hunter's satisfaction; every moment of his pursuit will reward his pains with some delight; and he will have reason to think his time not ill spent, even when he cannot much boast of any great acquisition."

Human Understanding, John Locke.

"··· and I dream every night, not to speak of my automatic writing, which puts my absurd love for Nature in its place — for in reading what I have written, as it were in a trance, I can see how foolish it is to give a thought to natural phenomena, which are, after all, nothing but an accretion of accidents."

Gormenghast, Mervyn Peake.

"My joy in learning is partly that it enables me to teach."

Letters to Lucilius, Seneca.

ABSTRACT

This thesis investigates the accretion flows in polars: close binaries in which a red dwarf transfers matter to a strongly magnetic, synchronously rotating white dwarf.

After an introductory chapter to establish the scientific context, I present a detailed review of our current perceptions of the accretion flow in polars, ending with a list of unanswered questions regarding the nature of the flow.

This is followed by an infrared spectroscopic study of V1309 Orionis. The K-band continuum is dominated by cyclotron radiation from the accretion region on the white dwarf. I use models of the cyclotron continuum to deduce the bolometric luminosity of the system and hence the mass transfer rate through the stream.

I then develop a method to construct images of the accretion stream in eclipsing polars using photometric eclipse profiles. The optimization technique incorporates a genetic algorithm to maximize the chances of finding the global optimum in the multi-dimensional parameter space. The method is tested using synthetic data.

The indirect imaging technique is then applied to high accretion state $UBVR$ data of HU Aquarii. The modelling procedure provides estimates of the radius at which the accretion stream threads onto the magnetic field and hence the mass transfer rate in the stream. I also investigate the wavelength dependence of emission from different sections of the stream and its implications for the temperature structure along the stream.

To explore changes in the accretion flow as a function of the overall accretion rate, I examine simultaneous intensity and polarization data of HU Aquarii obtained in a low state. The eclipses are modelled using the stream imaging technique, while the polarization light curves are modelled using Stokes Imaging, another genetic algorithm-based technique that uses cyclotron models to reconstruct the accretion region on the white dwarf.

The thesis concludes with a discussion of the main results. The results are compared to the questions raised in the review chapter in order to identify the issues that require further investigation.

Contents

List of Figures

List of Tables

Chapter 1

Scientific context

1.1 Close binary systems

Most stars in our Galaxy are not single stars like the Sun, but occur in binary or multiple star systems. Of the seven nearest star systems (including the Sun), five are at least double (Allen 1976). The fraction of stars in the Galaxy that are binaries is significantly larger than 50 per cent. About half of these binaries are systems where the stellar components are very far apart, taking perhaps hundreds or thousands of years to complete a revolution about their common centre of mass. These stars interact only in the sense that they are gravitationally bound, and the evolutionary path of each component star is not affected by the other member of the system. Other binaries, however, are sufficiently close that the evolutionary path of each of the components departs appreciably from the evolution of single stars. The two stars in a close binary can interact in a variety of ways, for instance via radiation (where a hot star can irradiate the face of the other component) or via tidal forces, where gravitational and centrifugal effects distort the shapes of one or both components. As a result of these interactions, close binary systems present intriguing problems of their own. The variety of fascinating phenomena observed in close binaries, which have no counterparts among the single stars, are of major

interest in modern astronomical research.

This thesis examines the accretion flows in a group of close binaries, the *polars* or AM Herculis stars. These are a subclass of the *cataclysmic variables* (CVs), in which a tidally-distorted red dwarf star transfers matter to a white dwarf. I begin by outlining the classification of close binaries according to Roche geometry, and describe how mass transfer occurs by Roche lobe overflow from the mass donating star to the accreting star. This is followed by an outline of the main characteristics of the various CV subtypes, and a brief overview of our current understanding of CV evolution. I then describe the characteristics of the magnetic CVs, in particular the strongly magnetic polars, in order to provide a context for the main theme of the thesis: the accretion flow in polars.

1.2   The Roche geometry and mass transfer

In a binary system, the gravitational and centrifugal potential of the system can be described using equipotential surfaces. If both component stars can be approximated by point masses [1], the Roche approximation (Kopal 1959) can be used. The shapes of the Roche equipotentials are functions only of the mass ratio q of the binary, defined as $q = M_2/M_1$, where M_1 is the mass of the primary star, and M_2 is the mass of the secondary[2]. The more massive star has the more extensive Roche surface. The scale of the system is determined by a, the separation between the centres of mass of the two stars. This is given by Newton's generalization of Kepler's third law, which in a convenient form is

$$a = 3.53 \times 10^{10} M_1^{1/3} (1 + q)^{1/3} P_{\mathrm{orb}}^{2/3} \mathrm{~cm} \tag{1.1}$$

where P_{orb} is the orbital period of the system in hours. Within a certain distance of

---

[1] This approximation holds for CVs, because the white dwarf is small in comparison to its Roche lobe, and the red dwarf star is similar to a main sequence star and is therefore centrally condensed.

[2] Throughout this thesis, M_1 and M_2 denote the stellar masses in solar units.

the centre of each star, the Roche surfaces are closed around that star. Beyond this distance, each equipotential surface encloses both components of the binary. The critical Roche surface is the unique double-lobed surface which just encloses both stars. The two lobes are in contact at the inner Lagrangian point (L_1): this is one of the five Lagrangian points (see Fig. 1.1) where a test particle (one of negligible mass) will remain stationary in the binary frame unless perturbed by an external force. The points L_1, L_2 and L_3 are points of unstable equilibrium.

Close binaries are classified according to the Roche model in the following way. *Detached binaries* are systems where the envelopes of both stars lie well within their respective Roche lobes. *Contact binaries* are systems where the envelopes of both stars fill or exceed their Roche lobes (e.g. the W UMa stars). When one star's envelope coincides with its Roche lobe, and the other star lies within its Roche lobe, the system is a *semi-detached binary*. CVs are members of this last category: the white dwarf is the (detached) primary, and the red dwarf the (Roche lobe-filling) secondary.

The concept of a critical Roche surface fixed in the binary frame is applicable only when the binary orbit is circular, since an elliptical orbit introduces a time-dependent potential and thus a time-dependent critical surface. However, in CVs, the effects of tidal interaction on the secondary cause its rotation to synchronize with that of the orbital revolution, and any initial eccentricity of the binary orbit is removed on a time scale much shorter than the lifetime of the CV. Most CVs (and certainly those with $P_{\mathrm{orb}} \ll 1\,\mathrm{d}$) can be assumed to have circular orbits and synchronously rotating secondaries.

Kuiper (1941) was the first to suggest that semi-detached binaries must undergo mass transfer, and that the Lagrangian points of the Roche model must play a central role. Since part of the secondary envelope lies close to L_1, any perturbation of the gas in this region will push it over the L_1 point into the Roche lobe of the primary, where it will inevitably be captured by the primary star. Such a perturbation can be provided by pressure forces within the secondary envelope.
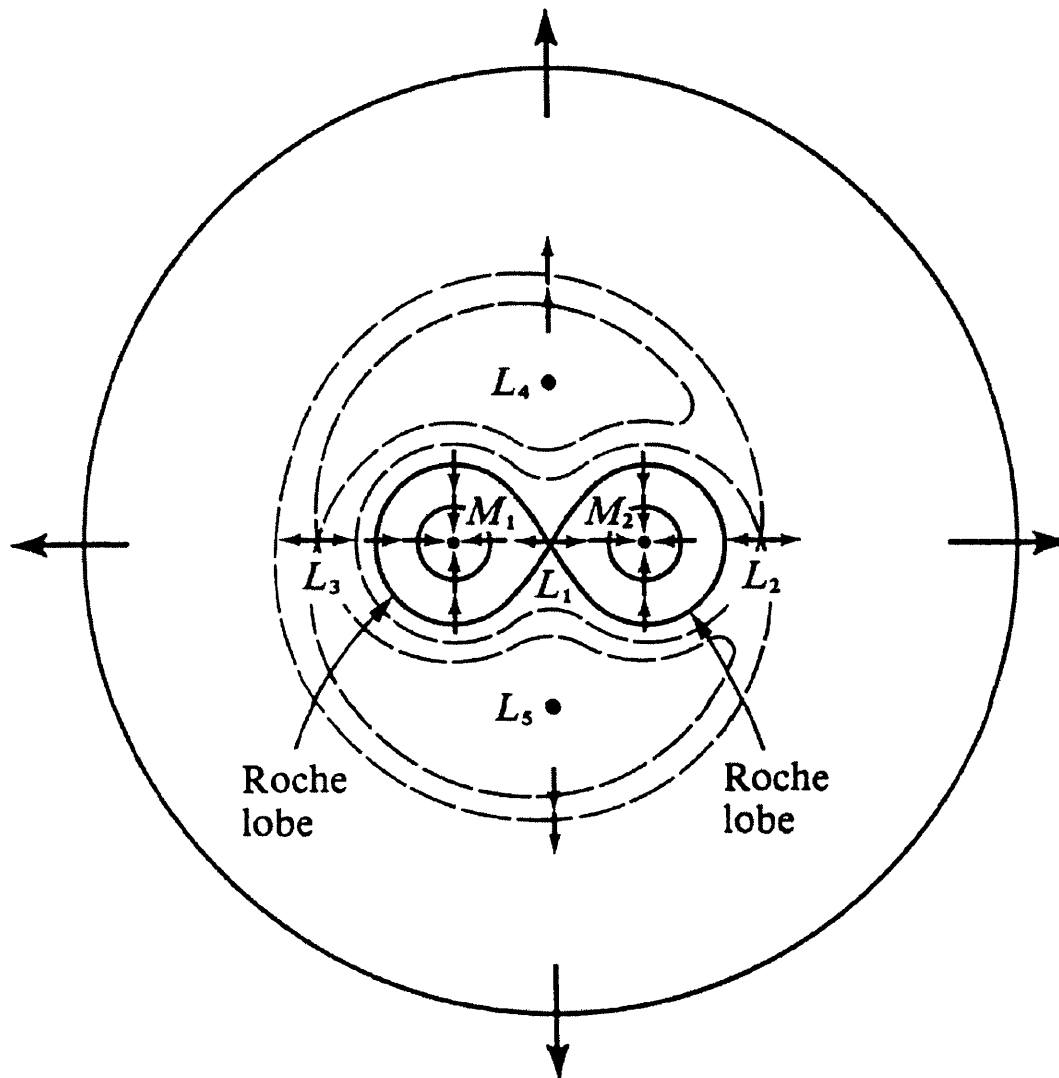
Figure 1.1: Roche equipotentials for a binary with a mass ratio of 2/3. The arrows show the local direction of the effective gravitational field as experienced by a test particle in the rotating frame of the binary. The effective gravity vanishes at the five Lagrangian points $L_1, \cdots, L_5$. The double-lobed 'figure 8' passing through the L_1 point is the critical Roche surface which contains the two Roche lobes of the component stars. From Shu (1982).

The transfer of mass from the secondary to the primary will change the mass ratio q of the system, leading to changes in a and P_{orb} because of the redistribution of angular momentum in the system. Since a and q determine the Roche geometry, changes in these quantities tend to shrink or enlarge the critical Roche lobe. For conservative mass transfer (i.e. where all the the mass lost by the secondary is accreted by the primary), it can be shown that if $q > \frac{5}{6}$, the Roche lobe of the mass-losing star shrinks in response to mass loss (Frank, King & Raine 1992) — the precise figure depends on the mass-radius relation of the secondary. Unless the secondary is able to contract rapidly to keep pace with the shrinking Roche lobe, the overflow will become a runaway process and will proceed on a dynamical or thermal time scale (depending whether the star's envelope is convective or radiative).

If $q < \frac{5}{6}$, however, the Roche lobe expands in response to mass transfer, and stable mass transfer is possible. However, mass transfer will soon cease unless the stellar envelope can be kept in contact with the Roche lobe, either by the expansion of the secondary, or by the loss of angular momentum from the system as a whole. The former case can occur where the secondary is evolving off the main sequence, expanding on a nuclear time scale determined by hydrogen shell burning. However, in CVs, where the secondary is a low-mass star, its main sequence lifetime is longer than the Hubble time, and this mechanism cannot be operating. Stable mass transfer in CVs is therefore possible only if the system can lose orbital angular momentum. In short period systems ($P_{orb} \lesssim 2\,h$), orbital angular momentum loss is thought to proceed by gravitational radiation (Faulkner 1971). In this case the mass transfer rate $\dot{M}$ of the system will be given by

$$\dot{M} \approx 2.0 \times 10^{17} \left[\frac{M_1^2 M_2^2}{(M_1 - M_2)(M_1 + M_2)^{1/3}} \right] \left(\frac{P_{orb}}{100\,\mathrm{min}} \right)^{-8/3} \mathrm{g\,s^{-1}} \qquad (1.2)$$

(Faulkner 1971; Wickramasinghe & Wu 1994). In longer period systems (with $P_{orb} \gtrsim 3\,h$), the mechanism for orbital angular momentum loss is magnetic braking (Verbunt & Zwaan 1981): the ionized stellar wind emanating from the late-type secondary

star co-rotates on magnetic field lines out to the Alfvén radius ($\sim 100\,R_\odot$; see section 1.7.2). This brakes the rotation of the secondary, and since the secondary's rotation is coupled tidally to the primary, this brakes the system as a whole (see also section 1.6).

Having established the mechanisms whereby stable mass transfer could occur in CVs, we now consider the results of the mass transfer process. Because the matter from the secondary possesses angular momentum due to the binary rotation, it cannot accrete directly onto the surface of the primary. If the primary does not have an appreciable magnetic field that disrupts the flow[3], the stream is able to flow past the primary and collide with itself at a point well inside the primary's Roche lobe. The relative kinetic energy of the impact is radiated away, and the mass transfer stream forms a ring around the primary. In the presence of viscous effects, the ring subsequently spreads into a disc.

In the absence of a strong white dwarf field, the distance of closest approach of the initial mass transfer stream to the white dwarf, R_{min}, can be calculated from single particle trajectories (Lubow & Shu 1975) and is approximated to an accuracy of 1 per cent by

$$\frac{R_{\mathrm{min}}}{a} = 0.0488\,q^{-0.464}, \qquad 0.05 < q < 1.0 \tag{1.3}$$

(Warner 1995). The radius of the initial ring of gas, R_{r}, is the smallest outer radius any disc can theoretically possess. An approximate expression for R_{r} is

$$\frac{R_{\mathrm{r}}}{a} = 0.0859\,q^{-0.426} \tag{1.4}$$

for $0.05 \leq q < 1$, accurate to 1 per cent (Hessman & Hopp 1990). The properties of accretion in systems with a white dwarf primary that *does* have an appreciable magnetic field are introduced in section 1.7.2 and are reviewed in detail in chapter 2.

---

[3]In CVs, an "appreciable" magnetic field strength is $B \approx 5 - 10\,\mathrm{MG}$ for a system where the primary's rotation is synchronized with the orbital period.

Useful expressions for the radius of the white dwarf as a function of its mass are

$$R_9 = 0.73 M_1^{-1/3}, \qquad\qquad 0.4 < M_1 < 0.7 \qquad\qquad (1.5)$$

$$R_9 = 1.12 \left[1 - \frac{M_1}{M_{ch}}\right]^{3/5}, \qquad 0.7 < M_1 < 1.3 \qquad\qquad (1.6)$$

(Warner 1995), where R_9 is the radius of the white dwarf in units of 10^9 cm and M_{ch} is the Chandrasekhar mass ($M_{ch} = 1.44\,M_\odot$).

1.3   The identification of CVs as detached binaries

The cataclysmic variables (CVs) include dwarf novae, recurrent and classical novae, and the nova-like variables. Their name refers to the outbursts that characterize the class — outbursts which are violent, but not fatal to the star. The realization that CVs are close binary systems was a result of the introduction (in the mid-1940s) of the 1P21 photomultiplier, enabling light curves with a time resolution shorter than a minute to be recorded. A.P. Linnell's 1949 study of UX UMa (which was, at the time, the eclipsing binary with the shortest known orbital period) revealed low-amplitude flickering in the light curve, and a complex and variable eclipse profile (Linnell 1949; Linnell 1950). A photometric survey of CVs carried out in the early 1950s by M.F. Walker revealed rapid brightness variations in a number of nova remnants, dwarf novae and nova-like variables (Walker 1954a,b). During this survey, Walker discovered eclipses in the classical nova DQ Her (Nova Her 1934), and speculated that *all* novae might be close binaries (Walker 1954b). A number of CVs were subsequently shown to be binary systems following an intensive programme of spectroscopic observations (e.g. Joy 1954a; Joy 1954b; Crawford & Kraft 1956; Kraft 1962; Kraft 1964; Krzeminski & Kraft 1964). This lead to the suggestion by Kraft (1963) that all cataclysmic variables are close binaries.

CVs are now known generally to comprise a white dwarf and a late-type dwarf star on or near the main sequence in a close binary configuration. Apart from a

few exceptions like GK Per (with an orbital period $P_{\rm orb} \sim 2\,{\rm d}$), the T CrB systems (with giant secondaries and $P_{\rm orb} \sim 200\,{\rm d}$), and the helium-rich double-degenerate AM CVn stars (with $P_{\rm orb} \lesssim 0.5\,{\rm h}$), CVs have orbital periods between 1.3 and 10 hours, and the separation of the stellar components is $\lesssim 2 {\rm R}_\odot$. Approximately 320 CVs are now known. The most recent catalogue of CVs is Downes, Webbink & Shara (1997). A recent catalogue of CVs and related objects such as low mass X-ray binaries (with neutron star or black hole primaries) is Ritter & Kolb (1998).

1.4 CV evolution

Before providing a more detailed description of the subclasses of CVs (sections 1.5 and 1.7), I outline the current understanding of the origin of CVs and their evolutionary path. In particular, we need to identify possible evolutionary paths for CVs which have strongly magnetic primaries.

Ever since their identification as close binaries, there has been considerable discussion as to how CVs form. The main problem is how a close binary could contain a white dwarf, since white dwarfs are formed only at the cores of red giant stars which are considerably larger (50–$500\,R_\odot$) than the orbital separation of the CV system ($\sim$few $R_\odot$). CVs can develop only from wide binaries in which the primary is able to develop into a white dwarf undisturbed. The system must then somehow lose angular momentum and energy in order to draw the component stars together. The two braking mechanisms mentioned earlier (gravitational radiation and magnetic braking) are inadequate to provide the reduction in angular momentum required to produce a CV within the age of the Galaxy: a much more efficient mechanism is required.

The generally accepted solution to this problem is that the binary reduces its period by common-envelope evolution (Ostriker 1976; Paczyński 1976). The scenario is as follows. The more massive star in the binary will begin to evolve off the main sequence before its companion does, and it will expand to fill its Roche lobe. Mass

transfer will thus begin from the red giant to the companion. This mass transfer will be dynamically unstable (as discussed in section 1.2) since the mass donor is more massive than the accreting star (i.e. $q > 1$), and because a giant with a convective envelope tends to expand in response to mass loss. The dynamically unstable mass transfer rates are so high that the secondary is unable to adjust its structure at the rate at which mass is arriving. The transferred matter fills the companion's Roche lobe until further mass transfer is prevented, and the system becomes a common-envelope binary. Both components experience a strong drag force as they revolve around their common centre of gravity within the giant envelope, and the two cores spiral together towards the centre of the envelope. The heat deposited in the envelope eventually exceeds the envelope's binding energy, and the whole envelope is ejected as a planetary nebula. The binary now consists of a main sequence secondary orbiting a hot subdwarf primary. The lifetime of the common envelope phase is $\sim 10^3$ y (Iben & Livio 1993).

The details of the frictional process whereby the orbital energy of the components is converted to envelope kinetic energy are not well established. Some authors use purely hydrodynamical solutions (e.g. Livio & Soker 1988). Regős & Tout (1995) point out that the spiralling components will inevitably produce differential rotation in the envelope. This, together with the fact that the giant envelope is largely convective, sets up a powerful magnetic dynamo. The resulting magnetic fields can drive both the spiralling-in process and the envelope ejection. This magnetic formulation also provides a mechanism whereby the white dwarf in a CV can be formed with a range of field strengths: the white dwarf field is created by the common envelope dynamo. The common envelope field is strongest for systems that coalesce, and is ~ 1 MG for CVs that just avoid coalescence. As the subdwarf core contracts to become fully degenerate, the field is concentrated by a factor of about 25, leading to a range of field strengths (0–50 MG) that is not dissimilar to that observed for CV primaries (Regős & Tout 1995). The CVs with the most strongly magnetic primaries would be those that emerge from the common envelope with the

shortest orbital periods. This mechanism may explain why there are more magnetic white dwarfs in CVs than in field white dwarfs (about 20 per cent of CVs have magnetic primaries while only 3–5 per cent of field white dwarfs are magnetic). The mechanism may, however, have trouble in accounting for systems such as V1309 Ori (with its exceptionally long 8 h orbital period and relatively high 60 MG primary field strength), and AR UMa (with a primary field strength of 230 MG).

The progenitors of CVs are relatively rare: approximately 1–2 per cent of main sequence binaries with primary masses greater than $0.95\,M_\odot$ will evolve into cataclysmic variables (Kolb 1995). The space density of CVs in the Galaxy is about 10^{-5}–$10^{-4}\,pc^{-3}$ (de Kool 1992).

1.5   The classification of non-magnetic CVs

The various subclasses of non-magnetic CV are defined as follows. Classical novae are novae which have shown only one outburst, with an amplitude of up to 20 mag. Recurrent novae have more than one nova outburst. The outbursts in novae are probably thermonuclear runaways in the hydrogen-rich material accreted onto the surface of the white dwarf primary. Nova-like variables are an inhomogeneous group of non-eruptive CVs which include pre- and post-novae, stars whose observational baseline is too short for their outbursts to have been observed. The nova-like variables show slow variations in brightness but no outburst behaviour. They are thought to possess steady-state discs with a high rate of mass transfer through the disc.

Dwarf novae (DN) have outbursts of 2 – 5 mag, although a few objects have very large outburst amplitudes of more than 6 mag (see e.g. Howell, Szkody & Cannizzo 1995). The mechanism of the DN outburst was a source of debate for many years, but is now thought to be the result of a thermal instability in the disc which results in an enhancement of the rate of mass transfer through the disc (see, for instance, the review by Cannizzo 1993). A number of DN, the SU UMa stars, show (in addition

to the normal outbursts) unusually bright and long superoutbursts in which the maximum brightness exceeds the usual outburst maximum by ~ 0.7 mag. A large fraction (0.3 – 0.4 mag) of the extra superoutburst light is modulated as prominent periodic humps — superhumps — with periods a few percent in excess of the orbital period.

In addition to the hydrogen-rich systems described above, there is also a small subclass of helium-rich CVs, the AM CVn stars. The AM CVn stars comprise a degenerate helium-rich secondary transferring matter to a DB white dwarf. They have orbital periods between 17 and 46 minutes, and are therefore even more compact than their hydrogen-rich counterparts, resulting in a variety of phenomena which are probably caused by the strong tidal interactions between the outer accretion disc and the secondary (as seen in the SU UMa dwarf novae) and by irradiation-driven mass transfer (as observed in the VY Scl stars). A review of the AM CVn stars is given by Warner (1995b). The first candidate for a strongly magnetic AM CVn star has now been identified (Cropper et al. 1998, see section 1.7.4).

1.6 The CV period gap

The orbital period distribution of non-magnetic CVs is characterized by a dearth of systems with $2.3\,\mathrm{h} \lesssim P_{\mathrm{orb}} \lesssim 2.8\,\mathrm{h}$. The accepted explanation for this "period gap" was proposed by Robinson et al. (1981) to account for a cessation of mass transfer in MV Lyr (which is at the long-period edge of the gap). They note that the range of masses of secondaries in the gap coincides with the range of masses of low-mass main sequence stars where the star is fully convective. Rappaport, Joss & Verbunt (1983) and Spruit & Ritter (1983) suggest that when the secondary becomes fully convective, the stellar wind is lowered because of the rearrangement of the field structure within the secondary, and the efficiency of the magnetic braking mechanism is severely reduced. The main mechanism whereby the system loses orbital angular momentum is thus removed (see section 1.2), and this leads to a

cessation of mass transfer. The system remains as a low luminosity, detached binary until sufficient orbital angular momentum has been lost (by gravitational radiation and any residual magnetic braking) to bring the secondary into contact with its Roche lobe once again; this occurs at $P_{orb} \approx 2.3\,h$.

There is evidence that systems with strongly magnetic primaries do not have as significant a period gap as those with weakly or non-magnetic primaries (see section 1.7.1).

1.7 The magnetic CVs

In almost a quarter of CVs, the primary has a sufficiently large magnetic field to disrupt, completely or partially, the formation of an accretion disc. These are the magnetic CVs (mCVs), of which there are two subclasses: the polars (or AM Herculis stars) and the intermediate polars (IPs). Comprehensive reviews of polars may be found in Cropper (1990) and Warner (1995 chapter 6); reviews of IPs include Warner (1995 chapter 7) and Patterson (1994).

There is no strict division between the non-magnetic CV and the mCV classifications — many systems have characteristics of both classes. For example, V1500 Cyg is a classical nova (Nova Cygni 1975) but has a primary with $B \sim 25\,MG$, and is classified as a polar (Stockman, Schmidt & Lamb 1988). The IP GK Per was Nova Per 1901. GK Per, together with the IPs TV Col, XY Ari and EX Hya, show dwarf nova outbursts (Kim, Wheeler & Mineshige 1992; Hellier 1993; Hellier, Mukai & Beardmore 1997). TV Col, in addition, shows superhumps (Hellier 1993). RX J1914.4+2456 (Cropper et al. 1998) is probably a double-degenerate polar, a magnetic analogue of the AM CVn stars.

Broadly speaking, the differences between IPs and polars are due to the magnetic moment of the primary. The available evidence suggests that polar primaries have stronger magnetic fields than IP primaries. It is difficult to confirm this directly, however, because magnetic fields in IPs are extremely difficult to measure (see

section 1.7.3). The distinguishing characteristics of polars and IPs are described in section 1.7.1 and the physical causes of these differences are outlined in section 1.7.2.

1.7.1 Observational characteristics of polars and IPs

Polars

Polars are characterized by powerful X-ray emission and strong, variable linear and circular polarization at optical and infrared wavelengths. Polars also have high excitation UV, optical and infrared spectra with strong, variable multi-component emission lines (the strengths of He II $\lambda 4686\,\text{Å}$ and Hβ are usually comparable). No observational signatures of accretion discs have been found in polars.

In most systems, polarimetric and photometric modulations occur only at the orbital frequency (and occasionally harmonics thereof). In particular, the principal period derived from radial velocity variations or eclipse studies (the orbital period) and that from polarimetry (the white dwarf spin period), are identical to within a very small tolerance. Biermann et al. (1985) find that in DP Leo, the fractional error between the two is less than 2×10^{-6}. In V1309 Ori, Buckley & Shafter (1995) find a difference between the orbital period (obtained from eclipse observations) and the spin period (deduced from circular polarimetry) of less than 10^{-3}. Since very few intensive long-term monitoring campaigns on polars have been carried out, it is not certain whether polars are synchronized over long periods of time ($\sim$ years). Most systems, however, are synchronized within the observational uncertainties. There are exceptions to this rule, which are discussed in section 1.7.4.

Polars have high ratios of soft-to-hard X-ray luminosity, and their X-ray spectra usually comprise both a soft and a hard X-ray component. The soft component can be characterized by a blackbody spectrum with a temperature of $\sim$ few $\times$ 10 eV, while the hard component is bremsstrahlung with temperatures of $\sim$ few $\times$ 10 keV. The total X-ray to optical flux ratio in polars is large, in the range 3–300 (Warner 1995).

Polars show large-amplitude brightness variations on a time scale of months to years. The variations are probably due to a reduction in the mass transfer rate from the secondary star, and are thus usually referred to as 'high accretion' and 'low accretion' states (e.g. Liebert & Stockman 1985). In polars, a reduction in $\dot{M}$ from the secondary has an immediate effect on the overall luminosity of the system because polars lack accretion discs which would act as temporary reservoirs of gas[4].

Most polars have orbital periods below the period gap. Prior to the launch of *ROSAT*, a significant fraction of known polars had periods clustering in a "spike" near 114 min. The significance of the spike has subsequently diminished due to the discovery of over 30 new polars by *ROSAT* and other X-ray satellites, and the period distribution of polars is now more uniform. Interestingly, there are several systems *in* the period gap: these include RX J0531.5–4624 (Reinsch et al. 1994), QS Tel (Wickramasinghe et al. 1993) and RX J0803.4–4748 (Schwarz & Greiner 1999).

Mass transfer rates in polars below the orbital period gap are low, $\dot{M} \sim 2.5 \times 10^{15}\,\mathrm{g\,s^{-1}}$ (Warner 1995), in agreement with the rate expected for gravitational radiation alone (equation 1.2). The mass transfer rates for systems above the period gap, however, are much higher — V1309 Ori has a mass transfer rate greater than $\sim 10^{17}\,\mathrm{g\,s^{-1}}$ (see chapter 3). Beuermann & Burwitz (1995) have estimated the mass transfer rates for several polars, and find a clear correlation of $\dot{M}$ with P_{orb} (see Fig. 1.2): the long period systems have accretion rates which exceed those of the short-period systems by typically an order of magnitude. The highest mass transfer rates for polars are less than the highest values of $\dot{M}$ obtained for non-magnetic systems.

---

[4]It is probable that the rate of mass transfer from the secondary undergoes fluctuations in most CVs, but in most cases these changes are not obvious because of the disc reservoir. A possible model to explain these fluctuations is described in section 7.2.2.
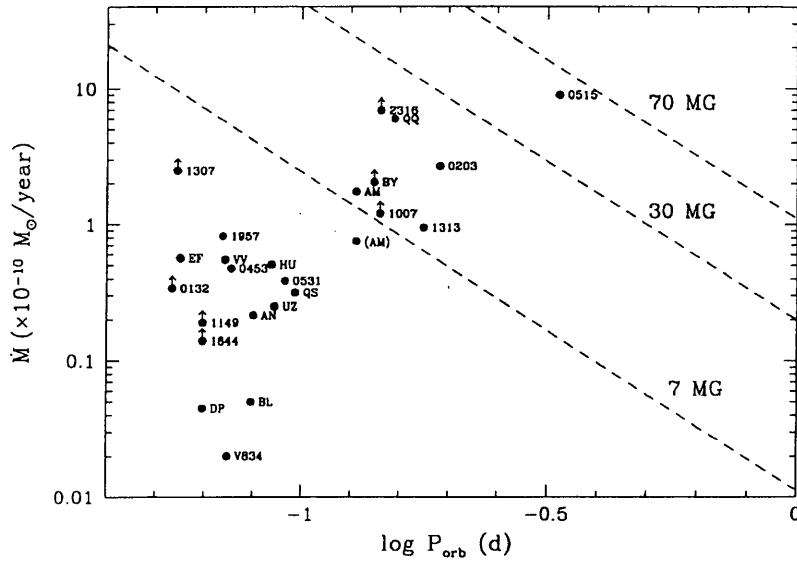
Figure 1.2: The mass transfer rate of polars versus orbital period. The long-period systems have accretion rates which exceed those of the short-period systems by typically an order of magnitude. From Beuermann & Burwitz (1995).

Intermediate polars

Most IPs have hard X-ray spectra with no soft X-ray blackbody component, most have orbital periods above the period gap, and most do not show detectable polarization. There are, however, exceptions to all of these: see section 1.7.4. The optical spectra of IPs resemble those of polars, but the He II $\lambda4686\,\text{Å}$ emission is usually weaker relative to Hβ.

IPs show multiple periodicities in their light curves. Most systems have three periods: two distinct periods and the beat period between the two. Some systems have periods that appear in the X-ray and optical light curves (e.g. AE Aqr: de Jager 1991; Patterson 1979, FO Aqr: Osborne & Mukai 1989; Norton et al. 1992, EX Hya: Jablonski & Busko 1985), and in others the X-ray and optical periodicities are distinct (e.g. V1223 Sgr: Osborne et al. 1985). TV Col has shown as many as four periods in its X-ray and optical light curves (Hellier 1993).

In some IPs there is strong evidence for the presence of an (at least partial)

accretion disc. Emission line profiles of EX Hya are double-peaked; in addition, there is a strong S-wave component which is attributed to a bright spot at the edge of a disc (Hellier et al. 1987). Other systems showing S-wave components include FO Aqr (Hellier, Mason & Cropper 1990), AO Psc (Penning 1985) and TX Col (Buckley & Tuohy 1989). Doppler tomograms of the Hβ emission line of DQ Her show a clear ring structure caused by emission in an accretion disc (Kaitchuck et al. 1994).

The fact that several systems show dwarf nova outbursts is clear evidence that accretion discs are present in IPs. The increase in amplitude of the X-ray pulsations in XY Ari in outburst is explained in terms of a truncated disc whose inner radius decreases in response to the enhanced $\dot{M}$ of the outburst (Hellier et al. 1997). During the outbursts of EX Hya, its eclipses become broad and shallow, consistent with an expanded disc (Reinsch & Beuermann 1990). Other IPs, however, show evidence of discless accretion: RX J1712.6–2414 (Buckley et al. 1995, Buckley et al. 1997) is a good candidate for a discless accretor. The observational evidence suggests, therefore, that there is a much wider variety of accretion modes in IPs than in polars.

Most IPs have orbital periods above the period gap, and no known IP has an orbital period in the gap. The accretion rates deduced for IPs are in general much larger than for polars, requiring magnetic braking as a driving mechanism. This suggests that the orbital evolution of IPs is similar to that of the non-magnetic systems, and dissimilar to that of the polars.

1.7.2 Origin of the observational characteristics

In polars, the primary's magnetic field is sufficiently strong ($B \sim 10$–$230\,\text{MG}$) to synchronize the rotation of the white dwarf with that of the binary[5]. This is the reason why only one modulation period is usually found in polars. In the IPs, the

---

[5]Some polars are *slightly* asynchronous: see section 1.7.4

white dwarf is not in synchronous rotation with the binary. The three frequencies seen in many IPs correspond to the spin frequency of the white dwarf, the orbital frequency, and the beat frequency between the two.

The strength of the magnetic field on the white dwarf determines to a large extent the accretion modes and the energy distribution of a given system. It also determines whether the white dwarf's rotation is synchronized with that of the binary.

Accretion modes

The stream of material transferred from the secondary falls initially on a ballistic trajectory towards the white dwarf[6]. At some point between the two stars, the white dwarf field will begin to oppose the motion of the stream plasma, since the stream is (at least partially) ionized. The boundary between the region in which the stream follows a ballistic trajectory, and the region in which the magnetic field strongly affects the flow of mass, energy and angular momentum (the *magnetosphere*), is thought to occur where the magnetic pressure of the field becomes comparable to the ram and gas pressure of the accreting material. This equilibrium radius is known as the Alfvén radius.

It is generally assumed that the field is a dipole; even if it is not, the dipole term of the field will dominate at large distances from the white dwarf surface. The magnetic field strength of a dipole field varies as

$$B(r) = \frac{\mu}{r^3} \tag{1.7}$$

where $B(r)$ is the magnetic field strength at a radial distance r and μ is the magnetic moment of the white dwarf (given by BR_1^3, where R_1 is the white dwarf radius and

---

[6]There is evidence to suggest that the initial trajectory of the stream in polars may not be purely ballistic (Heerlein, Horne & Schwope 1999). This is because the initial mass transfer stream may be subject to a magnetic drag force that acts transversely on the stream before the material is fully coupled to the field.

B is the polar field strength of the dipole field). The magnetic pressure of this field is $B^2(r)/8\pi$. The ram pressure of the stream is ρv^2, where v is the velocity of the infalling material and ρ is its density. The infall velocity is assumed to be the free-fall velocity: $v = v_{\mathrm{ff}} = (2GM_1/r)^{1/2}$.

For spherically symmetric infall, the balance between magnetic pressure and ram pressure is

$$\frac{B^2}{8\pi} = \rho\, v^2 = \frac{\dot{M}\, v_{\mathrm{ff}}}{4\pi r^2} \tag{1.8}$$

where $\dot{M}$ is the (isotropic) mass transfer rate. This implies an equilibrium radius $R_{\mu,\mathrm{sph}}$ given by

$$R_{\mu,\mathrm{sph}} = 9.9 \times 10^{10} \mu_{34}^{4/7} M_1^{-1/7} \dot{M}_{16}^{-2/7}\ \mathrm{cm} \tag{1.9}$$

where μ_{34} is the magnetic moment of the white dwarf in units of $10^{34}\,\mathrm{G\,cm^3}$ and $\dot{M}_{16}$ is the mass transfer rate in units of $10^{16}\,\mathrm{g\,s^{-1}}$. For accretion by a stream (as opposed to spherically symmetrical infall), the right-hand side of equation 1.8 becomes $\dot{M}v_{\mathrm{ff}}/\pi\sigma^2$, where σ is the radius of the stream. This implies an Alfvén radius R_μ given by

$$R_\mu = 1.45 \times 10^{10} \mu_{34}^{4/11} \sigma_9^{\,4/11} M_1^{-1/11} \dot{M}_{16}^{-2/11}\ \mathrm{cm} \tag{1.10}$$

(Mukai 1988) where σ_9 is the radius of the stream in units of $10^9\,\mathrm{cm}$ (the cross section of the stream is assumed to be circular). Values of σ can be obtained from Lubow & Shu (1975) or from measurements of the width of the pre-eclipse dip in systems that show this feature (as in Watson et al. 1995 and chapter 5).

For a fixed $\dot{M}$, the Alfvén radius for spherical accretion is much larger than for stream accretion, i.e. for stream accretion, the accretion flow will be able to travel much closer to the white dwarf before being disrupted by the field.

The radius R_μ is not necessarily the radius at which the bulk of the stream becomes *threaded* to the field, i.e. where the stream plasma is diverted out of the

orbital plane to follow the field lines down onto the white dwarf. The details of the threading of the stream depend on a large number of factors (plasma instabilities, field distortion and reconnection, whether the magnetosphere is rotating with respect to the incoming stream, and so on). These are discussed in chapter 2. Threaded material in the magnetosphere is often referred to as the 'accretion funnel' in the case of polars and the 'accretion curtain' in IPs; this terminology reflects the fact that threading is thought to occur over a wide range of azimuths (often from a truncated disc) in IPs but from a (relatively) smaller threading region in polars.

The radius R_μ can be used as a first approximation to determine whether or not an accretion disc can form in a given system. This is done by comparing the radius R_μ to the radii R_r and R_{min} (see equations 1.4 and 1.3). If $R_\mu < R_{min}$, a disc can certainly form, the inner edge of which is truncated by the field. If $R_\mu > R_{min}$ there are two possibilities, depending on the size of R_r. If $R_\mu > R_r$, the initial mass transfer stream cannot orbit the white dwarf without being disrupted, and a disc cannot form. If $R_{min} < R_\mu < R_r$ there is a possibility that a disc may form, provided that some of the stream can penetrate closer to the white dwarf to survive past R_{min} and initiate a disc.

There is an added complication in cases where the system is asynchronous, particularly if the white dwarf is spinning rapidly. King (1993), Wynn & King (1995) and Wynn, King & Horne (1997) point out that the criteria for disc formation in these systems must include a consideration of the spin rate of the accreting star. When the flow is modelled as inhomogeneous and diamagnetic, theory indicates that a substantial fraction of the matter transferred from the secondary can be ejected from the system. This could explain why the long-period IP AE Aqr (which should have a disc, given the large orbital separation of the components and a relatively low magnetic moment, hence $R_r > R_{min} \gg R_\mu$), shows no evidence of one (Wynn, King & Horne 1997).

The accretion mode in a given system can change on a time scale of months. Wheatley (1999) reports significant changes in the power spectra of XTE monitoring

observations of the IP TX Col, in which the relative power of the spin and beat modulations changes dramatically from month to month. The presence of a strong beat modulation in an IP is thought to be an indicator of discless accretion, since accreting material from the inner edge of a truncated disc should have no 'memory' of the orbital phase. The changes in the relative power of the spin and beat modulations thus indicate that the accretion mode can change on a time scale of less than a month.

Orbital evolution of polars

The existence of several polars with orbital periods in the period gap suggests that the period gap may not be as significant for polars as for more weakly magnetic systems. Since the period gap is thought to be caused by the cessation of magnetic braking, it would appear likely that the magnetic field of the primary disrupts the magnetic braking mechanism in some way. It has been a matter of debate whether a strong primary magnetic field inhibits or enhances magnetic braking, thereby speeding up or slowing down the evolution of a given system from longer to shorter orbital periods. Liebert & Stockman (1985), King (1985) and Hameury et al. (1987) suggest that the magnetospheres of both stars could contribute to the magnetic braking, leading to accelerated orbital evolution.

More detailed models by Li, Wu & Wickramasinghe (1994a,b) and Li & Wickramasinghe (1998) show, however, that the field lines of the secondary are either closed or connect to the field lines of the primary, thus creating a 'dead zone' which prevents an outflow of wind from the system as a whole. This inhibits magnetic braking and slows down the secular evolution of the system. The reduction in magnetic braking depends on the inclination of the primary and secondary's dipole fields with respect to the orbital plane — as the inclination of the dipoles increases, the reduction in magnetic braking decreases. However, a reduction in magnetic braking occurs for all configurations except in the extreme case where the dipoles of both the primary and the secondary are aligned in the orbital plane (Li & Wickramasinghe

1998).

Magnetic braking must still be operating in the long-period polars, since their mass transfer rates are several orders of magnitude higher than those predicted by gravitational radiation-driven orbital evolution (Fig. 1.2). Since the mass transfer rates for the polars with the longest values of P_{orb} are still an order of magnitude lower than non-magnetic systems with similar orbital periods, this suggests that magnetic braking is suppressed (but not eliminated) in highly magnetic systems.

Conditions for synchronism

The angular momentum of accreting material tends to increase the angular velocity of the white dwarf. The fact that stable equilibria between the orbital and the spin period exist in IPs, and that most polars are observed to have $P_{spin} = P_{orb}$, indicates that there are synchronizing torques that counteract this accretion torque.

The synchronizing torque is due to the primary's magnetic field, and is magnetohydrodynamical in nature. Lamb et al. (1983) describe a model in which the field lines of an asynchronously rotating primary are wound up and thread the secondary (if the secondary does not have an appreciable field) or connect with the secondary field lines (if it does). This causes large currents along the field lines and generates magnetic stresses which are able to synchronize an initially asynchronous system. This mechanism cannot *maintain* synchronism, since at least a slight asynchronicity is required to generate the torque. The additional force that is required to maintain synchronism arises in the interaction between the intrinsic fields of the primary and secondary (Campbell 1989; Wu & Wickramasinghe 1993; Campbell 1997; Warner 1997). The secondaries in CVs are likely to have field strengths of the order of hundreds to thousands of Gauss (e.g. Saar 1990).

It has been suggested that synchronism can be maintained if the Alfvén radius of the white dwarf exceeds the separation of the white dwarf and the secondary star (Patterson 1984). However, Lamb & Melia (1988) claim that this condition is not relevant for maintaining synchronism. The relevant synchronism criterion for a

disc less system is that the accretion torque should be less than the synchronizing torque, which leads to

$$\mu_{33} \gtrsim 0.14\,\dot{M}_{16} \tag{1.11}$$

(Warner 1997), where μ_{33} is the magnetic moment of the primary in units of $10^{33}\,\mathrm{G\,cm^3}$. This equation takes into consideration the dipole-dipole interaction between the magnetic moments of the primary and the secondary star.

The energy distribution

The plasma in the magnetosphere will fall along the field lines towards the white dwarf surface at highly supersonic velocities. Since the material is threaded onto the field, the flow is channeled onto a small fraction of the white dwarf surface near the magnetic poles. In the accretion region, the material is decelerated strongly and forms a shock as it reaches the white dwarf surface, where the specific kinetic energy of infall $\frac{1}{2}v_{\mathrm{ff}}^2 = GM_1/R_1$ is randomized and turned into thermal energy. Since, in general, the gas below the shock cannot cool as fast as it is heated by the shock, the post-shock flow expands, and the shock is raised above the white dwarf surface until such a volume is reached that the post-shock material can cool (the stand-off shock and the post-shock flow are often referred to as the 'accretion column'). The density of the flow increases by a factor of ~ 4 from before the shock to the post-shock flow; the velocity of the flow decreases by the same factor by continuity. The temperature of the post-shock flow emission depends on the amount of energy deposited there: this is determined primarily by the mass of the white dwarf (the deeper the potential well, the more kinetic energy will be deposited on the white dwarf surface by the accretion flow). The temperature and density structure of the post-shock flow has been modelled by Cropper, Ramsay & Wu (1998) to determine white dwarf masses in polars.

In a steady state, the accretion energy released in the post-shock flow must be

removed at the same rate as it arrives, implying the existence of efficient cooling mechanisms in the post-shock flow. Since the temperature of the plasma immediately after the shock is $\sim$ few $\times 10^8$ K, a significant fraction of the emerging radiation will be bremsstrahlung (from decelerated free electrons) at $\sim$ few $\times$ 10 keV. The shock also cools via cyclotron radiation from threaded electrons spiralling around the magnetic field lines, and Compton cooling through scattering of lower energy photons by the shocked electrons.

The height of the shock above the white dwarf surface depends on the time taken for the post-shock material to cool radiatively (via bremsstrahlung and cyclotron radiation) and by Compton cooling. The relative efficiency of these mechanisms depends primarily on the white dwarf field strength and the specific accretion rate (the accretion rate per unit area in the accretion region) which is proportional to L/f, where L is the total accretion luminosity and f is the fraction of the white dwarf surface onto which the accretion occurs. Three regimes in the $\log B$–$\log L/f$ plane have been identified by Lamb & Masters (1979) (see Fig. 1.3). Above a critical line bremsstrahlung dominates the radiative cooling. In this region (labelled I in Fig. 1.3), the temperature of the ions and electrons in the plasma are comparable, and the the plasma can be treated as a single fluid. Two-fluid effects become important in region II, where cyclotron cooling dominates bremsstrahlung (cyclotron radiation cools the electrons but not the ions). In region III, cyclotron cooling is so effective that the velocity distribution of the ions becomes non-Maxwellian. In the extreme case (where the field strength is high and the mass transfer rate low), the cyclotron cooling will dominate and a stand-off shock structure does not form, since all the accretion energy is radiated away in the shock itself. Solutions of the flow in this regime are called 'bombardment' solutions (e.g. Kuijpers & Pringle 1982; Thompson & Cawthorne 1987; Woelk & Beuermann 1992, 1993, 1996) because the flow consists of a low density stream of ions which impinge directly onto the white dwarf (without first passing through a post-shock flow).

The flux distribution from the accretion region thus comprises hard X-ray brems-
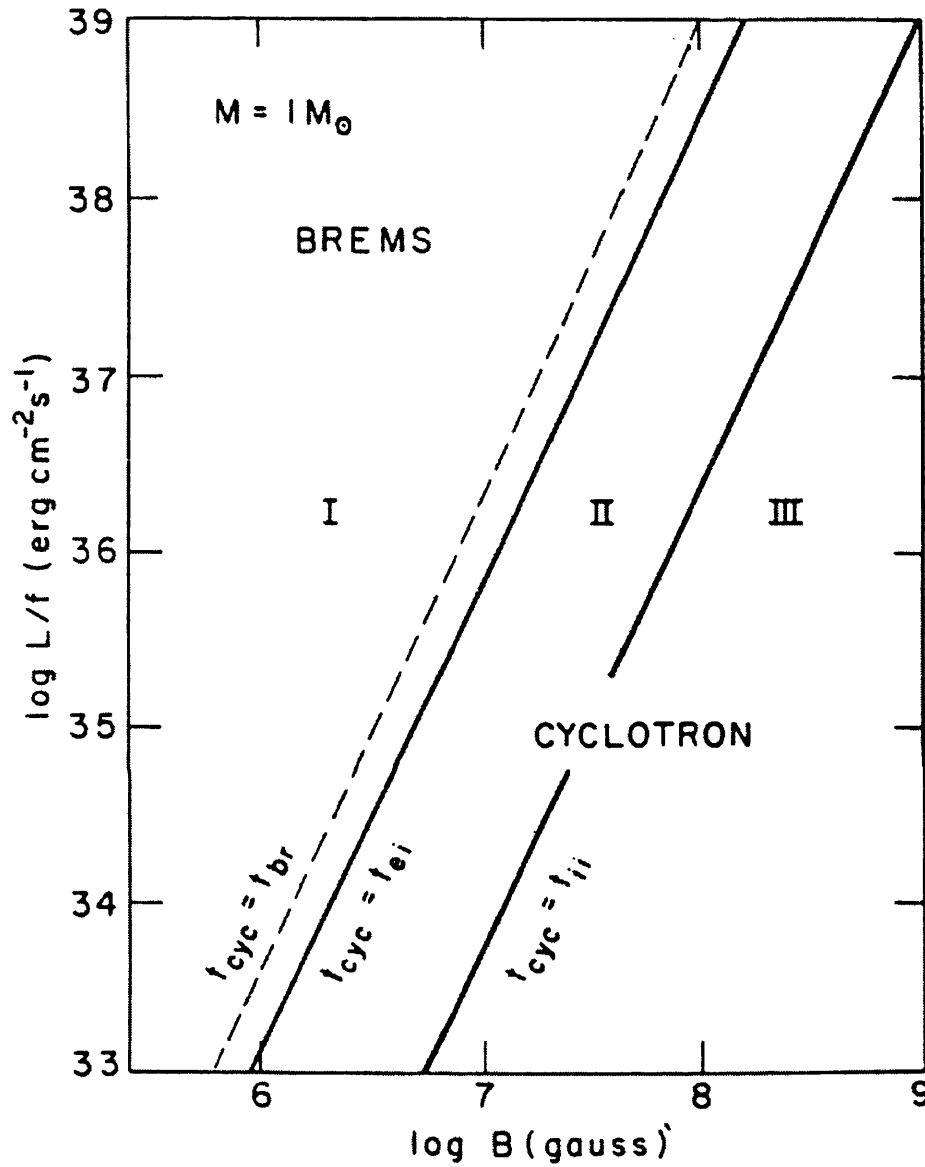
Figure 1.3: Cooling mechanisms for the post-shock flow in the $\log B$–$\log L/f$ plane. Bremsstrahlung cooling dominates above the dashed line, and cyclotron cooling dominates below. In region I, above the line marked $t_{\rm cyc} = t_{\rm ei}$, the ions and electrons are in equilibrium and the plasma can be treated as a single-temperature fluid. In region II, cyclotron cooling becomes more efficient, and the electrons are cooled to temperatures below the ion temperature; a two fluid treatment is required. In region III the cyclotron cooling is so efficient that a hydrodynamic treatment breaks down. From Lamb & Masters (1979).

strahlung and cyclotron radiation at UV, optical and infrared wavelengths. There is a third major contributor to the accretion region emission. The hot post-shock flow is situated on the surface of the primary, and nearly half its emission is intercepted by the primary. Some bremsstrahlung photons with $kT \gtrsim 20\,\text{keV}$ are reflected from the white dwarf photosphere, but the lower energy bremsstrahlung photons are absorbed, thermalized and re-emitted by the white dwarf photosphere. This produces an approximately blackbody spectrum in the EUV and/or soft X-ray region with $kT \sim \text{few} \times 10\,\text{eV}$. The temperature of the EUV emission is related to the accretion rate and the size of the accretion region on the white dwarf.

This theoretical framework accounts for the energy distribution of polars, but it remains to be explained why IPs (typically) have hard X-ray spectra and very little or no soft X-ray component (e.g. Osborne 1988 — but see section 1.7.4 for exceptions). The lack of soft X-rays in IPs is thought to be due to local absorption in the system. Because the threading of the material typically occurs over a wide range of azimuths in the orbital plane (e.g. from the inner edge of a truncated disc), this leads to a significant amount of material in the magnetosphere that can locally absorb the soft X-ray component. Since material couples onto a larger number of adjacent field lines in IPs than in polars, the accretion region(s) on the white dwarf are generally much larger (by factors of ~ 100–1000) than in polars (Warner 1995). The absence of detectable soft X-ray/EUV components in IPs may be due to the fact that the more extended accretion regions would emit radiation at a temperature too low to be detected. Such low temperature emission is particularly susceptible to interstellar absorption.

The above scenario implies that that the luminosity of the soft X-ray component L_{bb} should be approximately half that of the hard X-ray component L_{br} (taking into account the hard X-ray albedo). In polars, however, this prediction is violated by large factors. In many observed cases (see e.g. Ramsay et al. 1994; Beuermann & Burwitz 1995), the ratio $L_{\text{bb}}/L_{\text{br}}$ is large, often exceeding 50. Two extensions to the standard model have been proposed in order to account for this discrepancy. The

first is the 'bombardment solution' of Kuijpers & Pringle (1982), mentioned above. In these solutions, the cooling of the flow is so effective that no post-shock flow is formed, and the incoming gas will thermalize in a thin layer at the white dwarf surface. This yields a spectrum appreciably softer than in the conventional shock solution (Kuijpers & Pringle 1982, Thompson & Cawthorne 1987).

The second model proposed to account for the observed soft X-ray excesses in polars (also by Kuijpers & Pringle 1982) is that the accretion flow is non-homogeneous and incorporates dense blobs or clumps of material. This scenario is discussed more fully in chapter 2 because it is directly related to the nature of the accretion flow.

1.7.3   Measuring the field strength in mCVs

Magnetic field strengths in polars can be deduced using observations of Zeeman splitting of the white dwarf photospheric and accretion flow 'halo' absorption features, cyclotron harmonics in optical and infrared spectra, and by modelling polarization light curves. In systems where B has been determined using more than one method, the results are in good agreement (e.g. V834 Cen: Wickramasinghe, Tuohy & Visvanathan 1987; Schwope & Beuermann 1990, MR Ser: Wickramasinghe et al. 1991, EF Eri: Achilleos, Wickramasinghe & Wu 1992; Ferrario, Bailey & Wickramasinghe 1996, DP Leo: Cropper et al. 1990).

During low accretion states, the photospheres of the two component stars are major contributors to the total system luminosity, and it is possible to discern the Zeeman split Balmer absorption features from the primary's photosphere. The field of AR UMa, currently the highest field polar known, was deduced from the Zeeman split Lyman α features in the UV continuum (Schmidt et al. 1996). In some systems, Zeeman split features are visible during the faint part of the orbital cycle when the main accretion region is behind the limb of the white dwarf — in this case, the derived result will reflect the field strength of the non-accreting pole (e.g. ST LMi: Schmidt, Stockman & Grandi 1983). In principle, the variation of the Zeeman

features around the orbit provides a means of measuring the geometry of the field, but it is not straightforward to deduce the field strength in the *accretion region* itself. Observations of Zeeman split photospheric features are complicated by the fact that low states in polars cannot be predicted in advance. In addition, since polars in low accretion states can become very faint, large telescopes are required to obtain spectra of the signal-to-noise required for the Zeeman split features to be visible.

Zeeman split absorption features have also been observed during bright, cyclotron-dominated phases. These features disappear when the accretion region rotates out of view, indicating an origin in the accretion region, and not the photosphere of the white dwarf. They are thought to arise from a cool 'halo' of of unshocked gas surrounding the cyclotron emission region, which absorbs the cyclotron continuum from the post-shock flow (Wickramasinghe, Tuohy & Visvanathan 1987; Achilleos, Wickramasinghe & Wu 1992).

A widely applicable method is based on observations of the broad cyclotron harmonic features ('humps') in optical and infrared spectra. Almost all polars show cyclotron humps, provided the wavelength coverage and signal-to-noise ratios are sufficient (Cropper et al. 1989). The method has the added advantage of measuring directly the field in the cyclotron-emitting region, which occurs predominantly in the post-shock flow where the thermal velocities of the gyrating electrons are highest. The method is thus a direct probe of the field in the accretion region.

Field strengths in polars can also be deduced by modelling intensity and polarization light curves (e.g. Cropper & Warner 1986; Ferrario & Wickramasinghe 1990; Potter et al. 1997; see also chapter 3 and chapter 7). These models are based on detailed cyclotron emission calculations such as the constant temperature models of Meggitt & Wickramasinghe (1982) and Wickramasinghe & Meggitt (1985). The field strengths obtained in this way are less secure than those obtained using cyclotron humps, since the fits are model-dependent.

Primary field strengths in IPs are extremely difficult to obtain, and in most cases

field estimates are not possible. This is because only three IPs show polarization, and no detections of cyclotron humps have been made. Also, it has not yet been possible to obtain a spectrum of the photosphere of an IP primary during a low accretion state to search for Zeeman features.

Since IPs are thought to have low field strengths ($\lesssim 10\,\mathrm{MG}$), searches for cyclotron humps have been made in infrared spectra where the cyclotron harmonics are closer to their fundamental frequency and would therefore be more easily resolvable. A tentative detection of a cyclotron hump in a K-band spectrum of BG CMi was reported by Dhillon & Marsh (1993); this has subsequently turned out to be a mis-identification (Dhillon et al. 1997). Further K-band observations by Dhillon et al. (1997) of PQ Gem, BG CMi and EX Hya fail to reveal any secure cyclotron features — if any cyclotron emission is present in these IPs, it contributes less than ~ 3 per cent of the infrared continuum flux.

Deducing B from polarization measurements of IPs is more complicated than in the polar case due to possible sources of diluting flux. In polars, the emission from other parts of the system (such as the accretion stream) are generally assumed to be negligible (but see chapter 7). In IPs, however, a truncated disc and accretion curtain(s) could contribute substantially to the intensity variations and would dilute any polarization present. In addition to the complications of interpreting the polarization modelling, there are only three IPs which show detectable polarization. These are PQ Gem (e.g. Mason et al. 1992), BG CMi (e.g. Penning, Schmidt & Liebert 1986; West, Berriman & Schmidt 1987) and RX J1712.6–2414 (Buckley et al. 1995). Field estimates using polarization light curve modelling are in the ranges 9–21 MG for PQ Gem (Piirola, Hakala & Coyne 1993; Väth, Chanmugam & Frank 1996; Potter et al. 1997), 2–5 MG for BG CMi (Wickramasinghe, Wu & Ferrario 1991) and 8–27 MG for RX J1712.6–2414 (Buckley et al. 1995; Väth 1997).

Despite the paucity of direct field measurements, the presence of a partial accretion disc in many IPs, and the null detection of polarization in most, is strong evidence that the magnetic fields in IPs have systematically lower field strengths

than polars.

1.7.4   Systems with both polar and IP characteristics

There are several systems that straddle the IP/polar classification in that they show characteristics of both classes. These include IPs with polar-like soft X-ray or EUV components, low field polars, and asynchronous polars.

Recently, several IPs have been discovered with a soft X-ray/EUV emission component that is distinct from the hard X-ray component, as is typically observed in polars. These include PQ Gem (Mason et al. 1992), RX J0558.0+5353 (Haberl et al. 1994) and RX J0512.2–3241 (Burwitz et al. 1996). All three systems were discovered by *ROSAT*: PQ Gem was identified during the All Sky Survey and the other two during the *ROSAT* galactic plane survey. The soft component in these systems could arise if the accretion flow were highly collimated (resulting in small accretion regions on the white dwarf, as in polars) or if the absorbing column were unusually low. For example, PQ Gem is observed in a direction that was identified by Paresce (1984) as having a very low interstellar absorbing column (Mason et al. 1992). Another soft X-ray source identified during the *ROSAT* galactic plane survey, RX J1914.4+2456, was tentatively classified as a soft IP by Haberl & Motch (1995). This has been called into question by Cropper et al. (1998) and Ramsay et al. (1999b). The system shows only one period in its X-ray and infrared light curves, and lacks a hard bremsstrahlung component (making an IP interpretation less likely). RX J1914.4+2456 is probably a helium-transferring phase-locked polar with an extremely short orbital period, the first of its kind to be identified.

The field estimates for the three polarized IPs are similar to the field strengths of some of the low-field polars, such as V2301 Oph (1H 1752+081). This system has a primary with a field strength of only $\sim 7\,\mathrm{MG}$, measured from Zeeman split absorption lines (Ferrario et al. 1995). Other polars with field strengths that overlap the range of field strengths deduced for IPs include RX J1957.1–5738 ($B \sim 16\,\mathrm{MG}$:

Thomas et al. 1996) and EF Eri, which has two separate cyclotron emission regions of field strengths 16.5 MG and 21 MG (Ferrario, Bailey & Wickramasinghe 1996).

There are four polars that are slightly asynchronous: BY Cam (e.g. Mason, Liebert & Schmidt 1989), V1500 Cyg (e.g. Schmidt & Stockman 1991), V1432 Aql (RX J1940.2-1025, e.g. Watson et al. 1995) and RX J2115–5840 (e.g. Schwope et al. 1997b; Ramsay et al. 1999)[7]. These systems have been called 'near-synchronous' (e.g. Ramsay et al. 1999), since their spin and orbital periods differ by only a few per cent (unlike the IPs, where the orbital period is typically $\sim$ 10 times the spin period). Changes in the overall behaviour are observed on the beat period between the spin and the orbital period. For example, the Ginga light curves of BY Cam alternate between flaring and pulsing behaviour over its 14.5 day beat cycle (Ishida et al. 1991). The circular polarization variations in RX J2115–5840 over its 7 day beat cycle change from negative excursions, through zero net polarization, to positive excursions (Ramsay et al. 1999). The model that has been proposed to explain these observations is that of 'pole-switching' (e.g. Mason et al. 1998): during the spin–orbital period beat phase, the orientation of the magnetic field changes slowly with respect to the incoming accretion stream, and the stream is directed onto the geometrically preferred pole at each phase. Accretion thus alternates from one pole to the other once per beat period. This pole-switching model is very similar to that proposed for the discless IP RX J1712–2414 (Buckley et al. 1997), except that RX J1712–2414 has a beat period of 1003 s, as opposed to several days.

The near-synchronous systems must be in a state where the accretion torque is larger than the synchronization torque, or where this has been the case in the recent past. Clues regarding the origin of the increased accretion torque are provided by V1500 Cyg, which experienced a nova outburst in 1975: it is possible that the spin-

---

[7]Recently, the membership of V1432 Aql in the class of near-synchronous systems has been questioned by Mukai (1998), who proposes that the system could be an IP with a discless or hybrid accretion geometry. He argues that the data are insufficient to distinguish between the two models.

up of the white dwarf is a direct result of the nova explosion (the details of the process are described by Stockman et al. 1988). The spin period of the white dwarf in V1500 Cyg has been decreasing since 1975; Schmidt, Liebert & Stockman (1995) estimate that it will regain synchronism on a time scale of 170 ± 8 y. It is not clear whether this mechanism can be invoked to explain the asynchronicity of all four systems. It is interesting to note, however, that the C IV and N V abundances in ultraviolet spectra of BY Cam are similar to those expected as the result of a nova explosion (Bonnet-Bidaud & Mouchet 1987).

Chapter 2

The accretion flows in polars

2.1 Why study the accretion flows in polars?

Polars are an astronomical laboratory in which to investigate the interactions be-
tween dense, supersonic plasmas and strong magnetic fields. This is because the
magnetic field of the white dwarf prevents the formation of an accretion disc and
controls the accretion flow over large distances. In polars, therefore, it is possible to
observe aspects of magnetically-controlled accretion that are obscured or absent in
other binaries. For example, in low-mass X-ray binaries with neutron star primaries,
although the magnetic fields of neutron stars can reach values exceeding 10^{13} G, their
radii are much smaller than those of white dwarfs ($\sim 2 \times 10^6$ cm for neutron stars as
opposed to $\sim 5 \times 10^8$ cm for white dwarfs). This means that neutron star magnetic
moments are much smaller than those attained by magnetic white dwarfs. Using
typical values for stellar masses, radii and field strengths, and using equations 1.1
and 1.10, it can be seen that $R_\mu \sim a$ for polars, while $R_\mu \sim 0.008\, a$ for an accreting
neutron star with a mass transfer rate of $10^{16}\,\mathrm{g\,s^{-1}}$ (e.g. Frank, King & Raine 1992).
In general, R_μ for neutron stars is much less than the circularization radius R_r (see
equation 1.4) and a disc is almost certain to form. For R_μ to be comparable to the
orbital separation in a neutron star binary, the mass transfer rate would have to be

very low, and the system would be too faint ($\lesssim 10^{30}$ erg s^{-1}: Frank, King & Raine 1985) to be observable. Polars thus provide us with the best opportunity to observe magnetically-controlled accretion.

The accretion flow in polars is, in principle, accessible to both observation and modelling. The stream is fairly collimated both during the free-fall and the magnetically-channeled parts of the flow, and as a first approximation can be assumed to be quasi-one-dimensional. Also, the time scales of variability in polars are convenient in that several orbital cycles can usually be covered during one observing night. Since the system is phase-locked, the magnetic field is at a fixed orientation with respect to the incoming stream, or (in the case of the near-synchronous systems, section 1.7.4) the orientation changes on a time scale much longer than the orbital period.

Investigations of the accretion flow in polars are not straightforward, however, either from a theoretical or an observational point of view. The main obstacles to a self-consistent theoretical treatment of the accretion flow are the difficulty in establishing boundary conditions on the scale of interest, and the sheer number of complex and competing physical mechanisms that are thought to operate in the region where the stream interacts with the white dwarf field. An observational approach is also difficult because emission from the accretion flow is difficult to isolate. Even though accretion streams can be intrinsically bright (especially in the optical and UV), they emit chiefly in regions of the spectrum that are dominated by other, equally bright components of the system, such as the accretion region on the white dwarf.

In this chapter, I present a review of our current knowledge of the properties of the accretion flow based on observation and theory, beginning with a description of the discovery in 1977 of magnetically-controlled accretion in AM Her. This is followed by a description of some of the issues that need to be addressed to further our understanding of the accretion flow.

2.2 The discovery of magnetically-controlled accretion in polars

Intrinsic circular polarization of the emission from an astronomical object generally implies the presence of strong magnetic fields. Prior to 1977, several searches had been made for intrinsic polarization in X-ray binaries, with no detections exceeding the measuring uncertainty (e.g. Sco X-1: Nikulin, Kuvshinov & Severny 1971; Cyg X-1: Michalsky, Swedlund & Stokes 1975). The proposal of a magnetic accretor model for DQ Her (Bath, Evans & Pringle 1974) prompted searches for polarization in that system, but again the results were not significantly larger than the uncertainties (Swedlund, Kemp & Wolstencroft 1974).

AM Herculis (the prototype for the polar class) had been identified in 1924 and was classified as a nova-like variable. The true nature of AM Her remained unclear until 1976, when Berg & Duthie (1976) identified AM Her as the optical counterpart of the *Uhuru* X-ray source 3U 1809+50. AM Her was also observed to lie in the error box of a variable soft X-ray source detected by the *SAS-3* satellite (Hearn, Richardson & Clark 1976). This discovery prompted several optical spectroscopic and photometric follow-up studies (e.g. Szkody & Brownlee 1977; Priedhorsky 1977; Cowley & Crampton 1977 — all three of which appeared in the 1977 March volume of the Astrophysical Journal Letters). Polarization measurements by Tapia (1977a) (published in the same volume) revealed unprecedented levels of variable circular and linear polarization: the linear polarization varied from zero up to 7 per cent and the circular polarization from −9 to +3 per cent. Importantly, both the linear and the circular polarization were observed to vary smoothly on the orbital period of the system. Tapia concluded that the polarization in AM Her is produced by cyclotron radiation from hot electrons in the magnetic field of a white dwarf. Assuming that the cyclotron radiation is emitted at the fundamental cyclotron frequency ($\omega_c = eB/(mc)$), and observing that there was no significant polarization for wavelengths smaller than $\sim 5000\,\text{Å}$, Tapia estimated a field strength of $\sim 2 \times 10^8\,\text{G}$ for the white

dwarf.

The intensive campaign on AM Her culminated in the work of Chanmugam & Wagner (1977) and Stockman et al. (1977), who proposed a model for AM Her that remains, for the most part, true today. They proposed that the observations were consistent with a strongly magnetic white dwarf that rotates synchronously with the binary and that undergoes accretion from a low-mass secondary star. Both groups deduced the synchronous rotation of the primary from the identical radial velocity and polarization variations — this was later confirmed directly by Young & Schneider (1979) from observations of the Na I absorption doublet from the secondary. To estimate the extent to which the magnetic field of the primary affects the accretion flow, Stockman et al. (1977) calculated the Alfvén radius for isotropic accretion (equation 1.9), and concluded that an accretion disc could not form in AM Her. Both groups identified the accretion region on the white dwarf as the source of the X-ray emission. In addition, Stockman et al. (1977) mentioned the importance of plasma instabilities in the threading process, appealing to results from the work on accreting magnetic neutron stars by Elsner & Lamb (1976) and Arons & Lea (1976).

A search for circular polarization in known nova-like variables was launched, and two more AM Herculis-type stars were soon identified: VV Pup (Tapia 1977b) and AN UMa (Krzeminski & Serkowski 1977). The name for the class, 'polars', was coined by Krzeminski & Serkowski and refers to their distinctive high degree of polarization.

The high field strength estimates for polars were revised when cyclotron humps were detected in optical spectra of VV Pup (Visvanathan & Wickramasinghe 1979; Stockman, Liebert & Bond 1979). This led to the realization that the cyclotron emission was not radiated primarily at the fundamental frequency, and that previous estimates of field strengths were too large by a factor of ~ 5.

2.3 Where does the stream thread onto the field?

The estimate of Stockman et al. (1977) for the Alfvén radius was derived using the very large field strength from Tapia (1977a) and assuming spherically symmetric accretion; this led to $R_{\mu,\text{sph}} > a$. They therefore deduced that the accretion flow would be dominated by the white dwarf field to well beyond the orbit of the secondary, and that the ionized gas from the secondary would be threaded onto the field lines from the L_1 point. This remained the accepted view in subsequent studies, e.g. Schneider & Young (1980a,b) (although Schneider & Young 1980a acknowledge the possibility that 'the threading may occur elsewhere').

After the realization that the field strengths of polar primaries were much smaller than initially thought, many systems (particularly those with longer orbital periods) were seen to have $R_\mu < a$. Liebert & Stockman (1985) observe that in this configuration, the behaviour of the flow near the L_1 point would be similar to that in non-magnetic systems (as described by Lubow & Shu 1975).

Ferrario, Wickramasinghe & Tuohy (1989) point out that the location of the threading region depends also on the inclination of the dipole axis of the magnetic field to the white dwarf spin axis (the magnetic colatitude, usually denoted β). If the dipole axis is parallel to the spin axis of the white dwarf ($\beta = 0°$), none of the magnetic field lines that pass through the L_1 point are contained within the Roche lobe of the white dwarf (see Figure 2.1). Since the stream plasma leaves the L_1 point with a velocity of zero (in the binary frame), a threaded particle will reach the white dwarf only if, in moving along its field line, it does not pass outside the primary's Roche lobe. Thus for $\beta \sim 0°$, any material threading at the L_1 point cannot reach the primary, and (irrespective of R_μ) the stream has to penetrate into the magnetosphere some distance before reaching field lines that can feed either of the two magnetic poles. In their study of several systems, Ferrario et al. (1989) find values for R_μ in the range 10–30 R_1, implying that accretion streams travel on ballistic trajectories for more than half the distance between the secondary and the
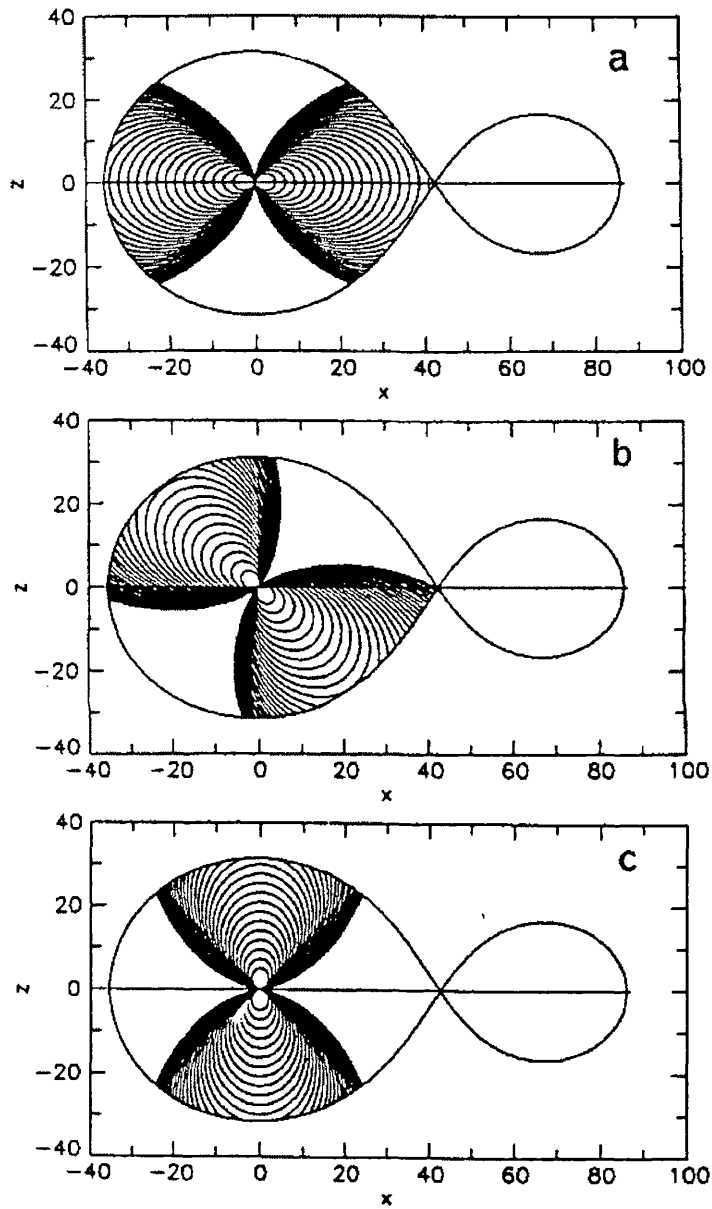
Figure 2.1: Field lines of the primary magnetic field that are contained within the primary Roche lobe for $q = 0.25$ and three values of the magnetic colatitude β: (a) $\beta = 0°$, (b) $\beta = 45°$, (c) $\beta = 90°$. The axes are in units of radii of the primary. From Ferrario, Wickramasinghe & Tuohy (1989).
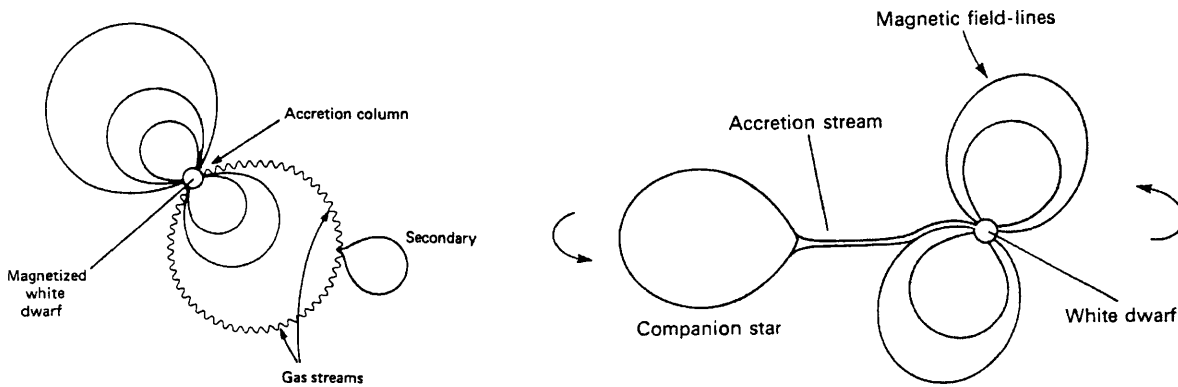
Figure 2.2: The changing perception of the location of the threading region. The schematic on the left is taken from Frank, King & Raine (1985) and shows an accretion flow that is threaded by the field from the L1 point. The schematic on the right is from Frank, King & Raine (1992): the stream travels on a ballistic trajectory for more than half the distance between the two stars before becoming threaded.

white dwarf before being threaded.

To illustrate the changing perceptions of where the stream threads onto the field lines of the magnetic field, Fig. 2.2 shows schematic diagrams of a polar. The diagram on the left is taken from the first edition of 'Accretion power in astrophysics' (Frank, King & Raine 1985) and the diagram on the right is taken from the second edition (Frank, King & Raine 1992). In the earlier view, there is no ballistic stream, and the stream is threaded onto the field from the L_1 point. In the schematic of 1992, by contrast, the stream travels over half the distance between the L_1 point and the primary before becoming threaded.

AR UMa, which has the most strongly magnetic white dwarf of the known polars ($B \sim 230 \, \mathrm{MG}$), is a system where one would expect the stream to thread near the L_1 point. Schmidt et al. (1996) calculate that the ratio of magnetic to thermal energy density is approximately 10:1 at the L_1 point, suggesting that even the atmosphere of the secondary should be threaded. However, Doppler tomograms of the He I λ 4471 Å, He II λ 4686 Å and Hβ lines show features consistent with emission

from a ballistic trajectory for the first ∼30–40 per cent of the distance between L_1 and the white dwarf (Hoard 1999). The fact that a ballistic stream occurs at all in such a strongly magnetic system suggests that the assumption of threading occurring where the magnetic and ram pressures are equal may be too simplistic.

What are the additional factors that have to be considered to establish where and how the accretion flow threads onto the field? These issues can be explored by considering ways in which the simple prescription of equation 1.10 is likely to be inadequate. One of the main assumptions is that the white dwarf field is dipolar. Although the dipole term of the field will certainly dominate far from the white dwarf, it is possible that higher-order terms will become significant nearer the white dwarf. The accretion stream is observed to penetrate deeply into the magnetosphere in many systems before being threaded. Wu & Wickramasinghe (1993) argue that this is difficult to explain if the primary field is a centred dipole, and propose that the field is dominated by a quadrupole term near the white dwarf. Accretion would occur mainly onto the equatorial pole of the quadrupole, resulting in an extended accretion region near the equator of the white dwarf.

Even if the dipole approximation holds, there are two additional assumptions that are unlikely to be true in practice. First, the stream material is assumed to thread instantaneously onto the field when the magnetic and ram pressures are equal. Secondly, the field is assumed to be rigid, i.e. the impact of the ballistic stream on the magnetosphere is assumed not to distort the field.

The first of the two assumptions is an oversimplification. The radius of the stream is large, ∼ 10^9 cm; this is comparable to the scale length over which the magnetic field changes significantly. Since the the magnetic field strength is not uniform across the stream, parts of the stream will thread before others. An extended threading region will also be formed if the stream has a density profile. If, for example, the core of the stream is more dense than the envelope, the outer parts of the stream will be threaded before the core, and the threading region will be extended along the ballistic trajectory.

There are situations when plasma will not thread even though the material pressure equals the local magnetic pressure. This would occur if the stream consists of dense diamagnetic 'blobs' embedded in a more rarefied medium. Since diamagnetic blobs are only slowly penetrated by the field, they can cross field lines to some extent, even though material stresses exceed magnetic ones (Hameury, King & Lasota 1986). This would be the case if the dynamical time scale of the blob is shorter than the time scale on which the field diffuses into the blob. A blob of this kind could cross field lines only by a series of magnetic reconnections (e.g. Li 1999). Such a process cannot occur in a rigid field, i.e. the second assumption of equation 1.10 has to be violated if blobs of material are to be threaded by the field. These considerations are important only if there is strong evidence that the accretion flow is highly inhomogeneous. What, then, is the evidence for inhomogeneities in the flow?

2.4 The evidence for an inhomogeneous accretion flow

The early models of the accretion column by Lamb & Masters (1979) and King & Lasota (1979) include a relatively self-consistent treatment of the hard X-ray, soft X-ray and cyclotron components of the accretion column spectrum. The models assumed homogeneous and radial accretion, and a uniform temperature and density in the radiating region (for a detailed review of the standard accretion column models, see Cropper 1990). As the quality of observational data improved, it became clear that two predictions of the standard models were contradicted by observation. Both of these are directly relevant to the nature of the accretion flow.

One problematic feature of the standard models is the discrepancy between the predicted and the observed optical energy distribution. The homogeneous shock models predict a peak in the optical energy distribution at $0.2\,\mu$m, while the observed distribution peaks in the infrared, at $1-2\,\mu$m (e.g. Bailey et al. 1985; Bailey 1988).

Liebert & Stockman (1985) realised that this discrepancy can be resolved if the optical and X-ray emission originate in separate regions. They proposed that this would occur if the stream were not homogeneous but had a denser core and a gradually tapering density towards the envelope of the stream. The accretion region would therefore have a compact bremsstrahlung dominated core surrounded by a more extended cyclotron emitting region. These ideas are developed by Schmidt, Stockman & Grandi (1983), Stockman & Lubenow (1987) and Stockman (1988), who construct models in which the stream density profile is an ideal function such as Gaussian, exponential or power law.

The observational evidence suggests that the high-energy radiation is emitted from a much smaller fractional area of the white dwarf than the optical and infrared radiation, which is emitted from more extended regions. This implies that the accretion region is *at least* as structured as a high-density core (emitting hard X-rays) with a less dense and more extended region (emitting polarized optical and infrared radiation). The observational evidence for structured emission regions is reviewed by Stockman (1995).

The cross-sectional density profile of the *stream itself* (as opposed to the resulting structure when the stream impacts on the white dwarf) can be deduced from observations of the absorption dips seen in the X-ray, optical and/or infrared light curves of many high-inclination polars (e.g. Watson et al. 1989; see also the review by Watson 1995). Absorption dips occur where emission from the accretion region is absorbed by the accretion stream at distances $\sim 10^{10}$ cm from the white dwarf. Dips should occur only in systems where the colatitude of the accretion region on the white dwarf does not exceed the binary inclination, so that the stream (usually the magnetically-channeled part of the stream, which is lifted out of the orbital plane) crosses the line of sight to the accretion region just prior to superior conjunction of the primary. One possible configuration where dips are expected to occur is shown in Fig. 2.3, which is a time-series of model drawings of HU Aqr from Glenn et al. (1994). Between orbital phases $\phi \approx 0.86$ and $\phi \approx 0.92$ the magnetically-channeled part of

the stream passes between the accretion region and the observer; the absorption of the accretion region emission by the stream produces the absorption dip at $\phi \approx 0.88$ (see also chapter 5).

The energy-dependence of X-ray absorption dips suggests photoelectric absorption in the stream, while the optical and infrared dips are probably caused by free-free absorption. Since the photoelectric and free-free optical depths for a given path length through a stream of number density n vary as n and n^2 respectively, the density profile of the stream can be deduced by comparing X-ray and optical/infrared dip profiles. In their study of the absorption dips in EF Eri, Watson et al. (1989) deduce that the stream consists of a core with a diameter $\sim 10^9$ cm and a much larger outer envelope (by a factor ~ 2.5). The electron density of the core exceeds 5×10^{12} cm^{-3}[1].

A further complication regarding the nature of the accretion flow is suggested by another prediction of the standard accretion column models that is contradicted by observation. As mentioned in chapter 1, the standard models predict that the luminosity of the soft X-ray component in the high-energy spectrum of polars should be approximately half that of the hard X-ray component. This prediction is violated in most observed systems by large factors. The problem was noticed as early as 1979 by King & Lasota (1979), who discuss the discrepancy when comparing the predictions of their model to observations of AM Her.

Kuijpers & Pringle (1982) were the first to suggest a solution to the problem in terms of a highly inhomogeneous stream: not merely a stream with a density profile, but one consisting of dense filaments ('blobs') embedded in a more rarefied medium. This idea was developed by Frank, King & Lasota (1988) and by Frank et al. (1992). A dense blob of accreting material could have sufficient ram pressure to penetrate into the photosphere of the white dwarf. As the energy of the blob is radiated, the

---

[1] Absorption dips can also be used to constrain the accretion geometry. The phase at which an absorption dip occurs in the light curve provides constraints on the trajectory of the stream by indicating the azimuth of absorbing material in the stream (see chapters 5 and 7).
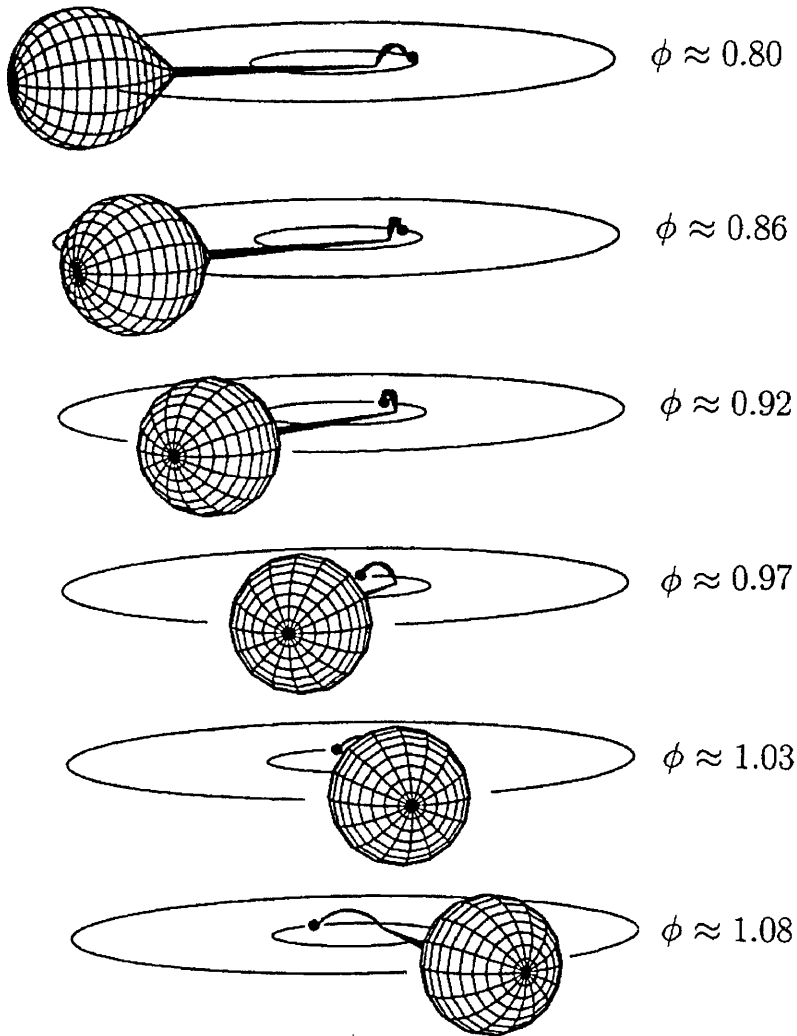
Figure 2.3: A time series of model drawings of HU Aqr to illustrate the origin of absorption dips in high-inclination polars. The orbital phase at each stage is indicated. Between phases $\phi \approx 0.86$ and $\phi \approx 0.92$ the magnetically-channeled part of the stream passes between the accretion region and the observer. If the stream is significantly optically thick to the accretion region emission, an absorption dip will be produced at $\phi \approx 0.88$. Adapted from Glenn et al. (1994).
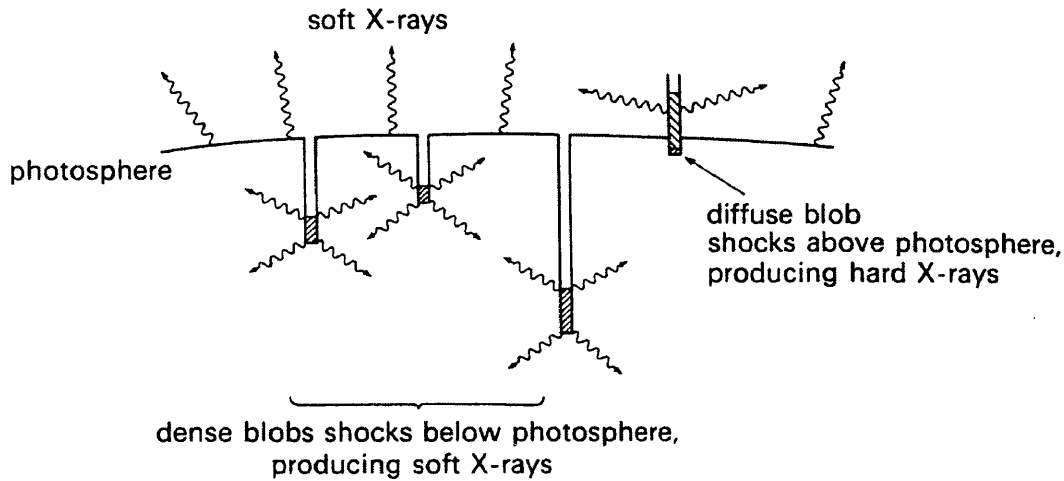
Figure 2.4: Highly inhomogeneous accretion onto a magnetic white dwarf. Sufficiently dense blobs in the flow can penetrate the photosphere and radiate most of their accretion luminosity as soft X-rays. More finely-divided material shocks at the white dwarf surface, producing hard X-rays. From Frank et al. (1992).

emission has to make its way through a substantial optical depth, and the radiation is degraded to soft X-rays before reaching the white dwarf surface. As a result, a significant fraction of the accretion luminosity is radiated in the form of soft X-rays. Hameury & King (1988) envisage a heirarchy of accretion zones: the instantaneous area A_{acc} onto which dense blobs accrete, the effective area A_{eff} radiating the blobs' accretion luminosity as soft X-rays, and the total area A_{zone} over which the blobs are scattered.

'Blobby' accretion is now widely accepted as the cause of the large soft X-ray excesses in polars. Ramsay et al. (1994) and Beuermann & Burwitz (1995) find that the magnitude of the soft X-ray excess is correlated with the primary magnetic field strength, in the sense that the systems that show the lowest excess have the lowest fields. This suggests that accretion flows in the systems with the strongest fields consist of a greater fraction of dense filaments than those with lower field strengths. Ramsay et al. (1994) also compare the soft X-ray excess to the (spherical) Alfvén

radius in each system: the systems with the smaller values for $R_{\mu,\text{sph}}$ appear to have the lower soft X-ray excesses, which suggests that if the flow threads far from the white dwarf, the fractional number of blobs is larger. If the correlation is true, this observation places constraints on the mechanisms whereby the stream initially becomes fragmented into blobs.

Recently, Greeley et al. (1999) have challenged the capability of blobby accretion to produce the UV luminosity of the accretion region of AM Her (based on observations with the Hopkins Ultraviolet Telesope). They claim that the the filling factor in the accretion flow must be less than 0.002 for the blobs to be sufficiently dense to bury themselves in the white dwarf photosphere. If only 0.2 per cent of the accretion region were emitting at any instant, this would be insufficient to produce the observed UV luminosity. Since both their emitting area and the estimate of the flare energy (and hence mass transfer rate) are model-dependent, this result is probably not sufficiently secure to throw serious doubt on the validity of blobby accretion as a method for producing the soft X-ray flux in polars.

In addition to the soft X-ray excesses in polars, considerable observational evidence has accumulated to support the idea that the accretion flow in polars is highly inhomogeneous. Some of the instances where blobby accretion has been invoked to explain observed phenomena are described below.

Hameury & King (1988) find that the soft X-ray light curves of AM Her in its 'anomalous' state (where the X-ray light curves have a square wave, as opposed to a quasi-sinusoidal shape) can be modelled by assuming that the accretion flow is concentrated almost entirely into dense blobs, with very little finely-divided material. Simulated soft X-ray curves constructed by assuming ~ 15 blobs of length $\sim 6.6 \times 10^{10}$ cm accreting at any instant, are very similar to the soft X-ray light curves of AM Her in its 'anomalous' state. In the normal state $A_{\text{eff}} \sim A_{\text{zone}}$ while in the 'anomalous' state $A_{\text{eff}} \ll A_{\text{zone}}$.

The sizes of the blobs in the accretion flow can be estimated from observations of flaring activity in polar light curves. Cropper & Warner (1986) observed strong

flaring behaviour in the optical light curves of VV Pup; the duration of the flares is typically 25 s. Since the velocity of infalling material at the shock front is $\sim$ 4000 km s^{-1} (i.e. the escape velocity of the white dwarf), a flare lasting 25 s implies a blob of length $\sim 10^{10}$ cm. Kuijpers & Pringle (1982) show that, in free fall, a threaded blob would be lengthened by a factor $(R_b/R_1)^{1/2}$, and (for a dipole field) squeezed by the field lines by a factor $(R_b/R_1)^{3/2}$ in the other two dimensions, where R_b is the radius from the white dwarf at which the blobs form. Using $R_b \sim$ 4×10^{10} cm (for blob formation in the threading region, see later) and $R_1 \sim 9 \times 10^8$ cm, Cropper & Warner (1986) estimate that the blobs causing the flares in VV Pup have typical lengths of $\sim 1.5 \times 10^9$ cm at R_b.

Constraints on blob sizes and numbers can also be deduced from observations of absorption dips. The wavelength dependence of the absorption dip in V1432 Aql (RX J1940.2-1025) is not consistent with free-free absorption in a homogeneous medium, but is in agreement with absorption in a stream consisting of blobs of dense material embedded in a less dense, optically thin medium. Watson et al. (1995) deduce that the blobs have radii $\lesssim 10^6$ cm and that there are more than ~ 4000 blobs in the stream at any given time.

The absorption dips in several systems (e.g. EF Eri: Watson et al. 1989; EK UMa: Clayton & Osborne 1994; UZ For: Watson 1995) show significant cycle to cycle variations, which can also be used to constrain the properties of inhomogeneities in the stream. In *ROSAT* PSPC observations of absorption dips in UZ For (Watson 1995), the edges of the dips show strong variability on time scales of 10–100 s during which the flux ranges from close to zero to values comparable to the average out-of-dip flux (see Fig. 2.5). These observations imply an inhomogeneous stream composed of dense, discrete filaments with widths $\sim 1 - 10$ per cent of the stream diameter and densities $n \sim 10^{12}$–10^{13} cm^{-3} if the filaments have a cylindrical cross-section.

Glenn et al. (1994) in their study of HU Aqr find that the Hα emission line splinters into multiple components around $\phi \sim 0.5$ (when the secondary is furthest from the observer). This is consistent with an inhomogeneous flow within the mag-
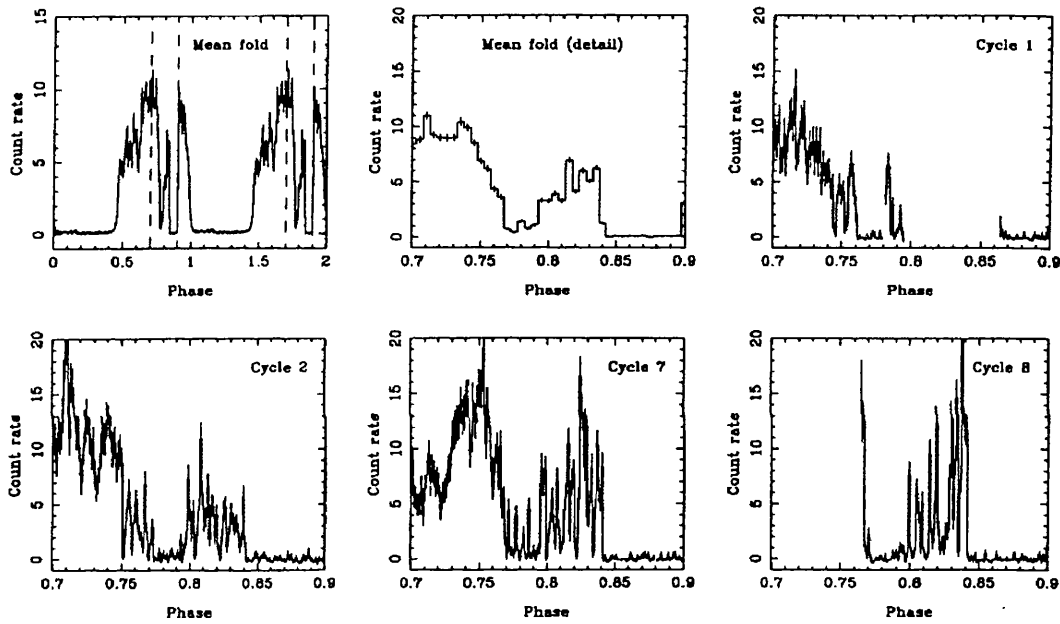
Figure 2.5: *ROSAT* PSPC light curves of UZ For, showing the structure in the absorption dip which indicates a variable, highly inhomogeneous flow. The first panel shows the folded data for the whole orbital cycle. The phase range indicated by the dashed lines in the first panel is shown on an expanded scale in the second panel. Subsequent panels show the individual dips in detail. From Watson (1995).

netosphere, perhaps consisting of elongated filaments following individual field lines.

Having outlined the importance of inhomogeneity in the threading process and the evidence supporting a highly inhomogeneous flow in polars, the next issue to address is the origin of the inhomogeneities. What mechanisms could produce blobs in the accretion flow, and where do they form?

2.5 The causes of inhomogeneities in the accretion flow

There are two mechanisms that have been proposed to produce inhomogeneities in the accretion flow. In one, the stream is fragmented during the process of Roche lobe overflow at the L_1 point; in the other, the stream is fragmented as a result of the interactions between the stream and the magnetic field in the threading region. Since neither mechanism precludes the other, it is possible that both may be operating simultaneously, with varying degress of importance, in a given system.

Cropper & Warner (1986) suggest that inhomogeneities in the stream may be the result of non-uniform mass transfer from the secondary, perhaps due to magnetic activity on the secondary. They estimate that the blob sizes deduced from the flaring activity of VV Pup (see above) are similar to the diameter of the L_1 nozzle. King (1989) and King (1995) show that a modulation of the overflow rate at the L_1 point can be caused by ionizing radiation from the primary. The ionizing flux disturbs the hydrostatic balance near L_1 on the dynamical time scale; this is about 5 percent of the binary period. If the oscillations are incoherent, i.e. have different phases in different parts of the L_1 nozzle, they will fragment the accretion flow. King (1995) notes that inhomogeneities produced in this way could occur in all CVs, but would go unnoticed in disc-fed systems where the inhomogeneities would be destroyed as the ballistic stream impacts on the outer edge of the disc. In addition, if the disc has a non-negligible vertical height, the L_1 point would be shielded from some or

all of the ionizing flux by the disc itself. The inhomogeneities produced by this mechanism would thus be more noticeable in discless systems.

Fragmentation of the accretion flow is also likely to occur as a result of the interactions of the stream with the magnetic field in the threading region. The processes that form the blobs in the flow are thus closely associated to the mechanisms whereby the stream is threaded onto the field. Due to the extraordinary complexity of the competing physical processes that operate in the threading region, no quantitative model of the threading region and funnel flow has yet been constructed. The following section outlines some of the steps that have been made towards this goal.

2.6 The properties of the threading region and the flow within R_μ

Stockman et al. (1977) noted that plasma instabilities will play a significant role in the threading of the accretion stream and the subsequent behaviour of the flow once it is threaded. Liebert & Stockman (1985) provide a qualitative description of the process; additional details are provided by Lamb (1985), Hameury et al. (1986), Lamb (1988), Warner (1995) and Li (1998).

It is believed that the magnetic field will begin to affect the shape and density of the flow when $r \lesssim R_{\text{th}}$, where R_{th} is the radius at which the magnetic pressure balances the thermal pressure of the plasma. The threading of the stream begins (but isn't neccessarily completed) in the region $R_\mu < r < R_{\text{th}}$, where the magnetic pressure increases faster than the stream material can adjust thermally. Since the stream is denser at its core than in its envelope, the effect of the magnetic field will be significant initially in the outer parts of the stream. As the flow approaches the threading region, stream motion perpendicular to the field begins to be resisted. This is because the stream material, being partially ionized, is a conducting fluid, and wherever a conducting fluid moves across field lines, currents are induced that

generate Lorentz forces opposing the cross-field motion.

By the time the flow reaches the threading region, the kinetic energy of the stream is significant, about 1–5 keV per nucleon. Unless the threading process is very gentle, a substantial fraction of this energy will be released in the threading region. The stream may produce a cavity in the magnetosphere (the 'stagnation region') in which plasma accumulates. If all the stream's kinetic energy were released in one or two hydromagnetic shocks in the stagnation region, the energy would be radiated as bremsstrahlung with a temperature ∼few keV. Since this radiation is not observed, it is likely that the stream adjusts to the field by a series of much weaker shocks (Liebert & Stockman 1985; Hameury et al. 1986).

A mechanism for the production of TeV gamma rays in the threading region via the diffusive shock acceleration process (Blandford & Eichler 1987) has been proposed by Kaul, Kaul & Bhat (1993). The shocked material in the threading region may accelerate protons to very high energies (this is possible because of the large spatial extent of the threading region). TeV gamma rays are produced when the particle beam impacts on the shock near the white dwarf surface.

The plasma in the threading region, supported by the magnetic field, is subject to a wide variety of plasma instabilities. Several of these result in the fragmentation of the stream into a mixture of diamagnetic blobs and finely-divided droplets. Rayleigh-Taylor instabilities arise where a heavy fluid (in this case the accretion stream) is supported against gravity by a lighter fluid (here the magnetic field and trapped low-density plasma), and result in the fragmentation of the stream into large diamagnetic blobs. A second instability, the Kelvin-Helmholtz instability, is caused by strong shear in a fluid with a density gradient; this results in the shredding of the stream plasma into finely-divided droplets. The Kelvin-Helmholtz instability probably strips material from the stream along its entire trajectory, not just within R_μ.

A third instability that can result in the formation of blobs in the threading region is that due to radiation cooling in the post-shock flow near R_μ. The cooling

of the gas in the stagnation region will tend to form condensations whose initial size depends on the cooling time and the sound speed of the hot gas.

To describe the subsequent behaviour of the blobs and the finely-divided material, one can compare the time scales on which the main physical processes are occurring. These include the time scale on which the blobs are moving (the dynamical time scale $\tau_{\mathrm{dyn}} = \sqrt{r^3/(GM_1)}$), the time scale on which the blobs are eroded by the Kelvin-Helmholtz instability (τ_{KH}), the time scale on which the motion of the blobs perpendicular to the field is resisted by the field (τ_{drag}), and the time scale on which the blobs can be penetrated by the field (τ_{pen}) (Hameury et al. 1986; King 1993).

The time scale τ_{KH} on which the blobs are eroded by Kelvin-Helmholtz instabilities is

$$\tau_{\mathrm{KH}} = \frac{c_{\mathrm{A}}\, l_{\mathrm{b}}}{\eta\, c_{\mathrm{s}} v_{\mathrm{b}}} \qquad (2.1)$$

(Arons & Lea 1980), where $\eta \lesssim 0.1$ is the Kelvin-Helmholtz efficiency, l_{b} is the blob length, $v_b \lesssim v_{\mathrm{ff}}$ is the infall velocity of the blob, c_{s} is the sound speed in the blobs, and $c_{\mathrm{A}} = B/(4\pi\rho_{\mathrm{i}})^{1/2}$ is the Alfvén speed in the inter-blob plasma. The density ρ_{i} of the inter-blob plasma can be estimated by assuming that the inter-blob material is the plasma whose density is too low near the shocks at R_μ to have condensed by the time it reaches the white dwarf surface. This gives $\rho_{\mathrm{i}} \gtrsim 2 \times 10^{-11}\,\mathrm{g\,s^{-1}}$ (Hameury et al. 1986).

The time scale τ_{pen} on which the magnetic field can penetrate the blobs (via ohmic diffusion) is

$$\tau_{\mathrm{pen}} = 10^{-7} l_{\mathrm{b}}^2 T_4^{3/2}\,\mathrm{s} \qquad (2.2)$$

(Hameury et al. 1986), where T_4 is the blob temperature in units of 10^4 K. The blobs are optically thick, so T_4 is at least as high as the local radiation temperature. The blob temperature is probably higher that this, since compression by converging field lines will heat the entrained material.

The blobs will be subject to a drag force exerted by the field. As they move

perpendicular to the field, currents are induced on the blob surfaces. The surface currents will generate a Lorentz force which acts as a drag force, opposing the blobs' cross-field motion. The blobs lose energy by exciting Alfvén waves in the surrounding field, since the field is distorted by the motion of the blobs perpendicular to the field. The time scale for energy loss is

$$\tau_{\mathrm{drag}} = \frac{c_A m_{\mathrm{b}}}{B^2 l_{\mathrm{b}}^2} \qquad (2.3)$$

(Drell, Foley & Ruderman 1965), where m_{b} is the mass of a blob. King (1993) and Wynn & King (1995) have quantified this effect by modelling the drag as a velocity-dependent force that is proportional to the square of the local field strength.

The subsequent behaviour of the dense blobs and the finely-divided material depends on the relative magnitudes of τ_{pen}, τ_{drag}, τ_{KH}, and τ_{dyn}. Since the finely-divided material has $\tau_{\mathrm{pen}} \ll \tau_{\mathrm{dyn}}$, it will be threaded almost immediately and forced to co-rotate with the field (i.e. at the angular velocity of the binary). The blobs, however, have $\tau_{\mathrm{pen}} \gg \tau_{\mathrm{dyn}}$, and proceed to plough their way through the field via a series of magnetic reconnections (Li 1999). At each reconnection event, Kelvin-Helmholtz instabilities erode the surface of the blob. The efficiency of the instability and the drag time scale will determine whether a blob is eroded completely before it reaches the white dwarf or whether the blob can reach a region in which $\tau_{\mathrm{pen}} < \tau_{\mathrm{dyn}}$, where the blob as a whole can be threaded. The fine rain produced at each reconnection event is penetrated by the field and threaded (this process is illustrated in Fig. 2.6). The threaded droplets constitute a cross-wind that can assist the Kelvin-Helmholtz instability in eroding the unthreaded blobs.

The precise manner in which threaded material is lifted out of the orbital plane is a difficult problem which has only recently been addressed (Li 1998). The acceleration of the particles at each reconnection event may be significant in lifting the material out of the orbital plane and onto the field lines.

Within the magnetosphere, the flow consists of threaded droplets, threaded blobs that have survived the shredding process, and perhaps some denser blobs that are
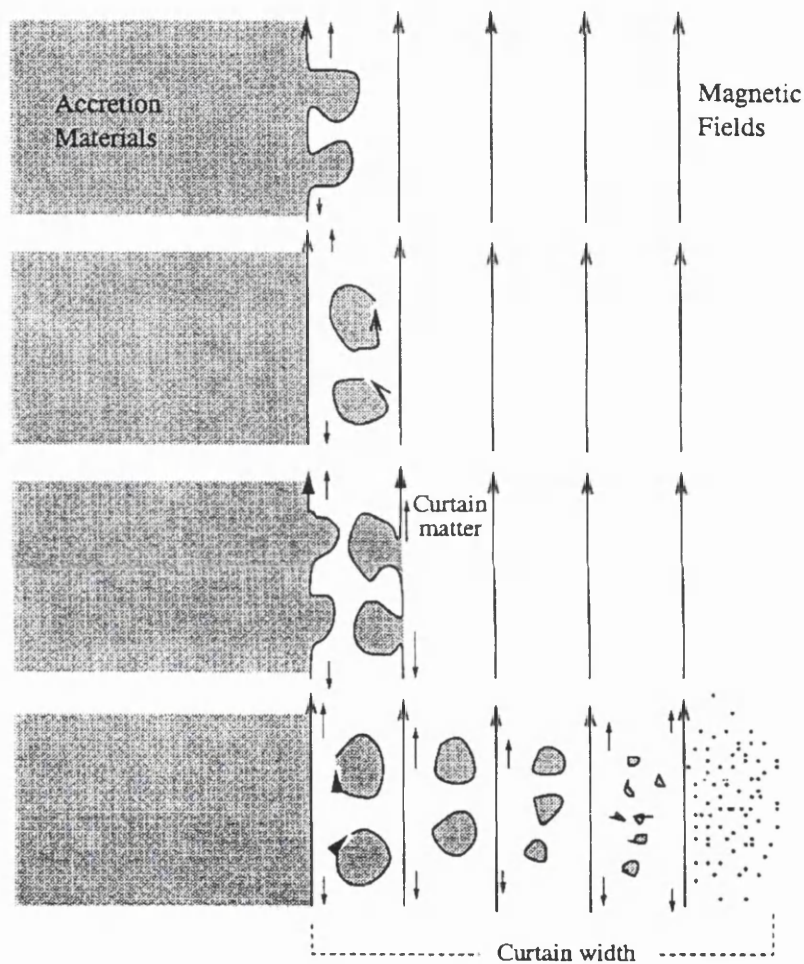
Figure 2.6: The threading process as envisaged by Li (1999). Blobs created by plasma instabilities penetrate into the magnetosphere via a series of magnetic reconnections. At each stage, the blob surface is eroded by the Kelvin-Helmholtz instability, releasing finely-divided material that is threaded rapidly by the field.

still moving perpendicular to the field. The impact of the surviving blobs on the white dwarf will lead to the flares and the soft X-ray excess described in section 2.4. The flow within the magnetosphere (in particular the threaded blobs that are compressed and elongated by the field) probably shows structure similar to that observed in (for example) coronal loops on the Sun. This is despite the fact that the plasma densities and magnetic field strengths in polars are orders of magnitude larger than those in solar phenomena: the field strength in a sunspot is about $\sim 1000\,\mathrm{G}$ and the density of solar material in a coronal loop is about $10^9 - 10^{10}\,\mathrm{cm}^{-3}$.

The location, shape and emission properties of the accretion region(s) on the white dwarf are a direct result of the way in which material is threaded onto the field. If the field is not distorted by the threading process, and if each particle in the stream is threaded at a point along its ballistic trajectory, the resulting shape of the accretion region will be a narrow arc. For this reason, models of polarization light curves based on the Wickramasinghe & Meggitt (1985) cyclotron emission models often assume thin arc-shaped accretion regions (e.g. Ferrario & Wickramasinghe 1990; Piirola, Hakala & Coyne 1993; Bailey et al. 1995; Potter et al. 1997). In these models, the shapes of the emission regions are adjusted using a trial and error approach until the fit to the intensity and polarimetry light curves is acceptable. Recently, Potter et al. (1998) have developed a method for modelling polarization light curves that does not assume *a priori* the shape of the emission region (see chapter 7 for an application). The accretion regions deduced from the method are in general not long and thin, but broader and more extended (see Fig. 2.7). A possible implication of this result is that threading does not occur along the ballistic trajectory and/or that the field is distorted significantly by the incoming field. This is consistent with the theoretical framework described above.
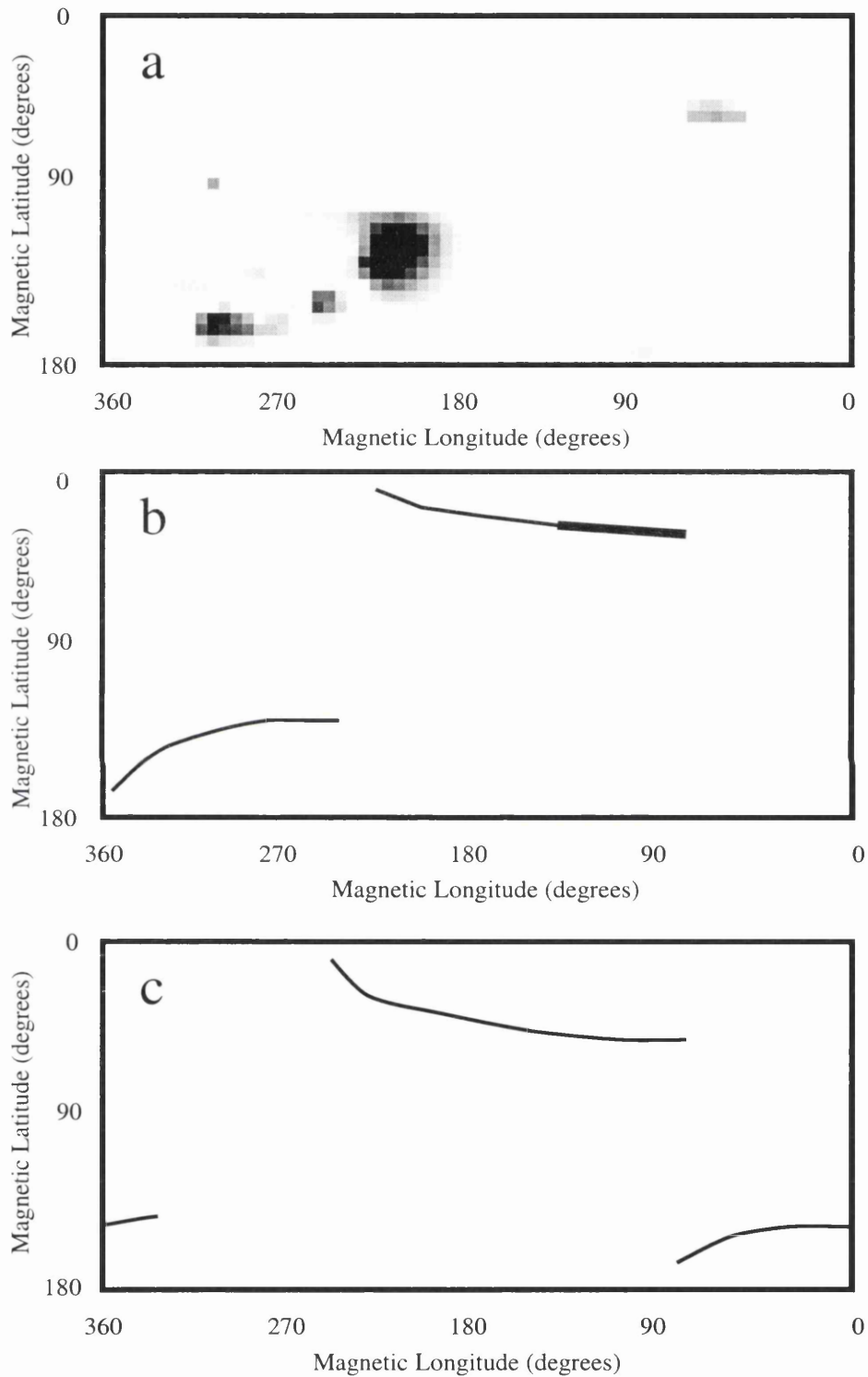
Figure 2.7: A comparison from Potter (1998) of models of the accretion region of V347 Pav deduced from fits to intensity and polarization light curves. The top panel shows the accretion region derived using the method of Potter et al. (1998). The middle panel is taken from Ramsay et al. (1996) and the bottom panel is from Bailey et al. (1995).

2.7   The variability of the accretion flow

In addition to the long-term variations in overall luminosity caused by modulations of the mass transfer rate from the secondary (see section 1.7.1), polars frequently show variations in behaviour that can be attributed to changes in the accretion geometry. These changes sometimes appear to be related to the luminosity state of a system, but on occasion rapid changes are observed without a change in the overall brightness.

For example, the shape of the soft X-ray light curve of QQ Vul changed from a complex waveform in June 1985 to a nearly sinusoidal shape in September 1985. Interestingly, the mean count rate is approximately the same in the two light curves. Osborne (1988) attributes this to a change from one to two-pole accretion. The normal and 'anomalous' accretion modes of AM Her are also thought to be due to changes from a one-pole to a two-pole geometry (e.g. Heise et al. 1985).

A change from a one to a two-pole geometry has also been observed in QS Tel. When discovered by the *ROSAT* WFC, QS Tel displayed a simple light curve consisting of one bright and one faint phase per orbital cycle (Buckley et al. 1993). The EUV light curve observed by Rosen et al. (1995), however, has two peaks per orbital cycle, indicating two-pole accretion. Rosen et al (1995) suggest that such a change would be possible if the accretion rate were higher during the EUV observations — the stream would penetrate further into the magnetosphere and be capable of feeding material to both poles.

Schwope et al. (1995b) report some interesting behaviour in BL Hyi during *ROSAT* observations. The system switches (within several tens of orbital cycles) from steady accretion onto one pole to a supersoft, flaring state during which strong ($75\,\mathrm{c\,s^{-1}}$ in the *ROSAT* PSPC) flaring episodes, lasting up to $0.2\,P_{\mathrm{orb}}$, alternate with phases of zero X-ray flux. Since the flaring episodes occur at random orbital phases, it would appear that the flares originate from either pole.

The structure of the absorption dip in UZ For (see Fig. 2.5) changes noticeably
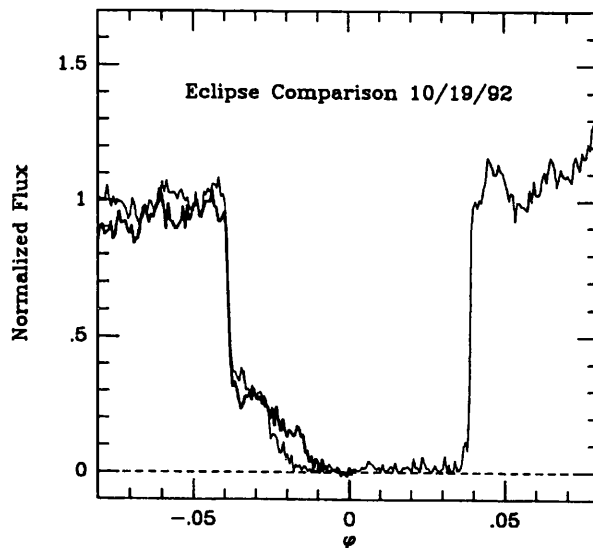
Figure 2.8: Two successive eclipses of HU Aqr observed in a low accretion state. The bold line indicates the second consecutive eclipse. The duration of the stream ingress component changes by more than a minute from one cycle to the next. From Glenn et al. (1994).

from cycle to cycle. This suggests variability in the number and alignment of discrete filaments in the stream on an orbital time scale.

Glenn et al. (1994) observe a dramatic change in two successive eclipses of HU Aqr (observed in a low accretion state). The duration of the accretion stream ingress component changes by more than a minute between two successive eclipses (see Fig. 2.8). This implies a displacement of the stream by a distance greater than the radius of the white dwarf in less than two hours, during which time the mean system brightness remains constant.

The examples described above of changes in accretion geometry demonstrate that the interaction between the magnetic field and the incoming flow can alter on an orbital time scale. Changes in the accretion geometry are often observed without overall changes in the system luminosity (i.e. changes in the mass transfer rate through the stream).

2.8   Emission from the accretion stream

Given the complex picture of the accretion flow that is described in the previous
sections, an important issue to discuss is this: how does the stream radiate? What
kinds of emission can be expected from each section of the stream? To address this
question, the mechanisms whereby the stream is heated and subsequently cools must
be identified for each part of the flow. In section 2.6, several possible heating and
cooling mechanisms were mentioned for the threading region. These are summarized
here; in addition, I list some of the radiation processes that could operate in other
parts of the stream.

2.8.1   Heating mechanisms

The excitation mechanisms that operate along the length of the stream are photoion-
ization by high-energy photons from the white dwarf and collisional heating within
the stream. Photoionization is probably the most important excitation mechanism
in the magnetically-controlled flow, since the magnetized flow presents a large area
to the accretion region on the white dwarf. The stream is evidently a very good
absorber of soft X-rays and EUV radiation (and is not itself a source of X-rays).
This is seen in *ROSAT* HRI light curves of HU Aqr where, during the pre-eclipse
absorption dip, the count rate drops to zero, and only partially recovers before the
eclipse by the secondary (Schwope et al. 1998).

Other possible heating mechanisms in the magnetized flow are the compression
of threaded blobs by the converging field lines, and shock heating of any surviving
unthreaded blobs by the threaded material (since the relative velocities are likely to
be supersonic: Warner 1995).

It is clear that one or more efficient ionizing mechanisms operate in the ballistic
stream, otherwise its behaviour would not be affected by the field at $\sim R_\mu$. If the
secondary is strongly irradiated by the primary (as is often the case, e.g. Schwope
et al. 1997), this emission could heat the stream in the vicinity of L_1.

Possible excitation mechanisms for the flow in the region $R_\mu \lesssim r \lesssim R_{\text{th}}$ include heating from hydromagnetic shocks in the threading region, reconnection and ohmic heating, collisional ionization, and perhaps proton acceleration by the diffusive shock mechanism (see section 2.6).

2.9   Cooling mechanisms

The line emission in polars has received considerable attention (e.g. Cowley & Crampton 1977; Schneider & Young 1980a,b; Rosen, Mason & Cordova 1987; Ferrario, Wickramasinghe & Tuohy 1989; Shafter et al. 1995; Schwope, Mantel & Horne 1997; Hoard 1999). The lines are composite structures of emission from several different regions in the binary and therefore consist of several components, each of which has a distinctive width and radial velocity behaviour. Most systems show at least two components in their lines: a broad base component (with a velocity width of $\sim 1000\,\text{km}\,\text{s}^{-1}$) which contains most of the emission line flux, and a narrower, peak component ($\sim 100\,\text{km}\,\text{s}^{-1}$ in width). Some systems show additional narrow high velocity components (e.g. VV Pup: Cowley, Crampton & Hutchings 1982; EF Eri: Mukai & Charles 1985; HU Aqr: Schwope et al. 1997; MN Hya: Ramsay & Wheatley 1998). The location of the emitting gas for each line component can be identified using Doppler tomography, which has been applied successfully to spectra of HU Aqr (Schwope et al. 1997), QQ Vul (Schwope et al. 1998), V2301 Oph (Šimić et al. 1998), V1309 Ori, V884 Her and AR UMa (Hoard 1999).

It should be remembered that the stream is also a strong source of unpolarized continuum radiation, which in most cases exceeds the line flux by a significant amount (Liebert & Stockman 1985; see also section 5.4.4 and section 8.3). Strong continuum emission along the entire length of the stream is evident in eclipsing polars, where broad-band eclipse profiles often show bright components due to the accretion stream. The shape of this stream component reflects the variations in brightness along the stream. Systems that show bright stream components

in their eclipses include HU Aqr (e.g. Hakala et al. 1993; Schwope et al. 1997), V895 Cen (D. Buckley, private communication), V2301 Oph (e.g. Barwig, Ritter & Bärnbantner 1994) and UZ For (Bailey 1995).

In the threading region, if the stream adjusts to the field via a series of small shocks, the gas will be cooled rapidly by continuum (free-free) radiation and will be almost isothermal (Liebert & Stockman 1985). Stockman et al. (1977) suggest that threaded material also cools by free-free emission. Cyclotron cooling will become increasingly important as the flow approaches the white dwarf.

2.10 Models of the accretion flow

I now summarize the approaches that have been used in the literature to model the accretion flow.

Mukai (1988) constructs a stream with a smooth Gaussian density profile (with no blob structure). The magnetic field is dipolar and is assumed not to be distorted by the incoming field. The stream falls initially on a ballistic trajectory. An element in the stream is assumed to thread onto the field when its ram pressure exceeds the local magnetic pressure and if the potential path is not blocked by a denser stream element. When an element is threaded, the component of the element's velocity parallel to the field line is conserved, while the component perpendicular to the field is thermalized. Ballistic considerations are used to determine onto which footpoint of a field line a threaded element will fall; in most cases this results in one-pole accretion at the geometrically-preferred pole. The resulting accretion region on the white dwarf is elongated and shows a concentration at one end, corresponding to the point where the centre of the stream is threaded, and beyond which no stream element can penetrate. Mukai (1988) uses this model to calculate the shape and location of the the accretion region, and the temperature of the soft X-ray black body component, in QQ Vul and ST LMi. The model produces results that are roughly in agreement with observation. In particular, the models predict that the

accretion region of ST LMi is comprised of two distinct spots; this is consistent with polarimetric observations by Cropper (1986).

King (1993) and Wynn & King (1995) construct an accretion flow that consists of diamagnetic blobs. Rather than making an abrupt transition from the ballistic flow to a magnetically-channeled flow, the blobs are treated as test particles moving under the influence of gravity and a magnetic drag force (described in section 2.6), so that the cross-field motion of a blob is reduced on a time scale given by equation 2.3. The blobs are assumed to be confined to the orbital plane. Although this will clearly not be the case near the white dwarf, the model can describe most of the flow between the two stars. King (1993) finds that blobs can be accreted by the primary or ejected from the system depending on the relative values of the initial specific energy and momentum of the blobs, and the spin frequency of the accreting star. The diamagnetic accretion model has been applied successfully to the mCV AE Aqr, where the model shows that most of the mass transferred from the secondary is ejected from the system in a magnetic 'propeller'. The ejected blobs carry away kinetic energy and angular momentum from the system: this explains the discrepancy between the large spin-down power of the white dwarf (inferred from the rapid rate at which the primary's spin period is decreasing) and the observed luminosity of the system (Wynn, King & Horne 1997). The magnetic propeller mechanism may also be able to explain some of the enigmatic features of the SW Sex stars (Horne 1999).

A similar approach to that of Mukai (1988) is taken by Heerlein, Horne & Schwope (1999) in their 'magnetic stripping' model for the stream. The model is essentially a modified version of the gas dynamical models of Lubow & Shu (1975, 1976) but includes the effect of the magnetic field. The field is assumed to be rigid and dipolar, and the stream is assumed to have a Gaussian density profile. The influence of the field is accounted for by comparing at each stage the relative values of the ram pressure and the magnetic pressure: when the sum of the thermal and ram pressures exceeds the local magnetic pressure, the material can couple to a field line.

The model assumes that the stripping of the stream is driven primarily by Kelvin-Helmholtz instabilities. The droplets stripped from the stream follow the magnetic field lines immediately after they are formed. As in the Mukai (1988) model, motion parallel to the field lines is conserved, while the motion perpendicular to the field is thermalized. Threading of the finely-divided material is found to occur along almost the whole length of the ballistic stream, but the bulk of the stream is threaded near the primary (see Fig. 2.9). The model calculates the velocity and density of the material at each point along the flow, and can thus be used to construct phase-resolved spectra and Doppler tomograms, which are compared to observations. Heerlien et al. (1999) find that trailed spectra and tomograms of HU Aqr in the high accretion state are reproduced well by the model.

A full theoretical treatment of the accretion flow would have to be much more complicated than the models described above. For example, all of the above models assume that the field is rigid and is not affected by the infalling stream; this will not be the case, given the large infall velocities and the very high density of the flow. The fact that the accretion flow comprises a plasma moving through an external field is complicated enough. The movement of a conducting fluid with respect to a magnetic field generates an electric field $\mathbf{E}$, which produces currents in the plasma. The curl of $\mathbf{E}$ in turn generates the time evolution of $\mathbf{B}$ according to Faraday's law. The changes in $\mathbf{B}$ then affect the movement of the fluid through the field, inducing slightly different currents in the plasma, which further modify the field, and so on. A full description of the stream flow must thus include a self-consistent treatment of the manner in which the fluid motion affects the external $\mathbf{B}$, and how the time evolution of $\mathbf{B}$ in turn affects the motion of the fluid. In addition, plasma instabilities and stream inhomogeneities have to be accounted for.
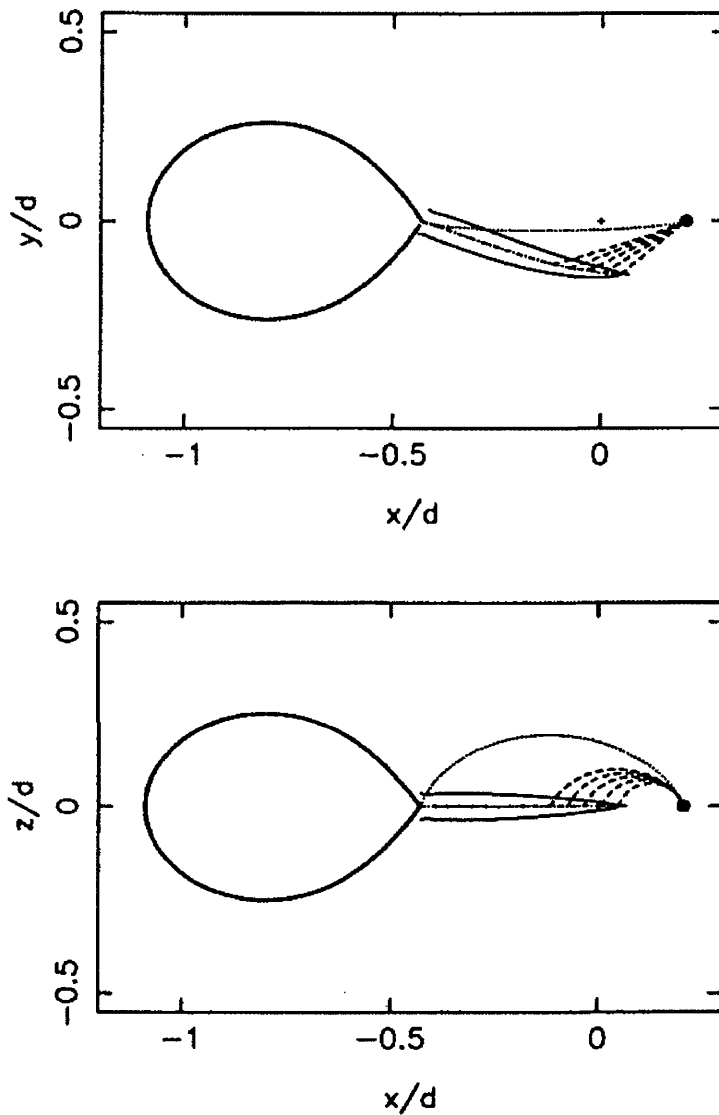
Figure 2.9: The geometry of the accretion flow of HU Aqr in the high accretion state, according to the 'magnetic stripping' model of Heerlein et al. (1999). The top panel is a projection onto the orbital plane and the bottom panel is a projection onto the plane perpendicular to the orbital plane and passing through the centre of both stars. 'd' is the orbital separation of the system. The magnetically-threaded material is indicated by the dashed lines; the dotted line is the trajectory of matter that is threaded from the L_1 point.

2.11 Unanswered questions

In this section I describe some of the remaining questions concerning the nature of the accretion flow in polars. Most of the unanswered questions originate in our incomplete understanding of the manner in which inhomogeneities in the stream form and how they affect the threading process.

1. Are inhomogeneities in the stream formed at the L_1 point (cf. Cropper & Warner 1986; King 1989) or by plasma instabilities in the threading region, or both? Would blobs formed at the secondary be obliterated in the threading region or would they be enhanced?

2. What factors control the composition of the stream, in terms of the fraction composed of blobs, and the fraction that is in the form of finely-divided droplets? The fraction of dense blobs in the stream appears to be correlated to the magnetic field strength (this is suggested by the correlation between soft X-ray excess and magnetic field strength observed by Ramsay et al. 1994 and Beuermann & Burwitz 1995). What other factors are operating? Is the composition dependent on, for instance, the mass transfer rate through the stream? The light curves of many systems show a greater degree of flickering in high states than in low (e.g. HU Aqr: Hakala et al. 1993; Schwope et al. 1997, V895 Cen: D. Buckley, private communication); does this imply that the higher the mass transfer rate through the stream, the larger the blob fraction?

3. By which processes does the accretion stream radiate? In particular, which processes give rise to the bright *continuum* radiation from the stream?

4. Is the threading region very bright? One might expect this to be the case, given the large number of heating mechanisms that are thought to operate in this region.

5. In eclipsing polars, why do some systems show bright stream components in their eclipse profiles (e.g. HU Aqr: Hakala et al. 1993), and some not (e.g. V1309 Ori: Shafter et al. 1995)? The fractional contribution of the stream to the overall emission appears to be a function of the mass transfer rate: for example, in HU Aqr, the stream is noticeable in U-band eclipses but is very faint in the other bands in the low state, while in the high state, the stream is bright in all wavebands (e.g. Schwope et al. 1997; chapter 5). Is the stream brightness correlated with $\dot{M}$ in all systems?

6. The eclipse profiles of HU Aqr (in its high state) and V2301 Oph (Barwig et al. 1994) are very similar, showing two separate components that correspond to accretion region and the accretion stream. Their comparable shapes suggest that the accretion geometry in both systems is similar. Why, then, does HU Aqr have a pre-eclipse absorption dip, and V2301 Oph has none?

7. What causes the variability in the trajectory of the accretion flow? Are changes in accretion geometry caused by changes in the mass transfer rate or can changes occur without a change in $\dot{M}$? Given a steady $\dot{M}$, is the stability of the accretion geometry related to the degree of inhomogeneity in the stream? For example, does a larger blob fraction cause a more variable geometry since more of the flow will penetrate into the magnetosphere and disrupt the field?

2.12 Tackling these issues using an observational approach

There are three ways in which accretion streams are observable directly. The accretion flow can be studied using observations of absorption dips, the emission lines, or the eclipse profiles of systems where a bright stream component is visible. A more indirect way of exploring the structure of the stream and the threading region is to examine the accretion region on the white dwarf, since the location and shape of the

accretion region are a direct result of the way in which the stream is threaded. In this thesis, I make use of three of the four approaches (I do not make use of velocity information in the emission lines), focusing on the information present in the eclipse profiles of systems with bright stream components.

In chapter 3 I present infrared spectroscopy of the longest period polar, V1309 Ori. Because of the large orbital separation, it is possible that $R_r \approx R_\mu$, which might allow an accretion disc to form. To investigate this, I deduce the mass transfer rate of the system by calculating the bolometric flux of the system using cyclotron models of the optical and infrared continuum. The strong emission lines are examined to see whether constraints can be placed on the physical conditions and the location of the line-emitting gas.

In chapter 4 I develop a technique that uses the information in eclipse profiles to derive the brightness distribution along the stream. I approximate the trajectory of the stream using a simple quasi-one-dimensional model. The stream is assumed to make an instantaneous transition from the ballistic trajectory to follow a field line above and/or below the orbital plane. Threading is assumed to occur instantaneously at R_μ: the steep dependence of the magnetic pressure on the distance from the primary makes this a good order-of-magnitude estimate (Frank et al. 1992; Li 1999) despite the uncertainties. The dipolar field of the primary is assumed to be rigid. In the light of the descriptions of accretion flow models in section 2.10 this may seem a rather unsophisticated scenario to adopt, but given our incomplete understanding of the accretion flow, it is not yet clear which prescription is a better approximation to reality. I therefore view this model as one with the smallest number of geometrical parameters which can be used to obtain the first estimates of the brightness distribution along the stream.

The stream imaging technique is based on a genetic optimization method which maximizes the chances of finding the global optimum in the multi-dimensional parameter space. I test the method using synthetic data and show that the method is able to retrieve details of the stream brightness distribution from an eclipse profile

in the presence of moderate noise and reduced phase resolution.

In chapters 5 and 6 I apply the method to high accretion state *UBVR* eclipses of HU Aqr. The system shows a prominent absorption dip prior to eclipse: this is used to deduce the radius of the stream and to constrain the accretion geometry. Stream images of five eclipses in all four bands are constructed; these are used to examine the brightness distribution of the stream and the wavelength dependence of the stream emission.

In chapter 7 I present simultaneous polarimetry and photometry of HU Aqr in a low accretion state. The eclipse profiles are modelled using the stream imaging method to deduce the geometry and brightness distribution along the stream. The polarimetry is modelled using Stokes Imaging (Potter et al. 1998) to deduce the shape and location of the emission region on the white dwarf. The results of the two methods are compared to see whether the two methods provide a consistent picture of the accretion flow.

In chapter 8 I summarize the progress that has been made by by relating the results of chapters 3– 7 to the questions in section 2.11. In this way, I identify areas where progress has been made and highlight issues that require further investigation.

Chapter 3

Infrared spectroscopy of V1309 Orionis

In this chapter I present an infrared spectroscopic investigation of the polar V1309 Orionis (RX J0515.6+0105). The aim of the investigation is to test the perceptions of the accretion flow described in chapters 1 and 2 in an extreme case, namely, the polar with the longest orbital period.

The large orbital separation of the stellar components suggests that the system may have R_μ less than R_{min}, and this would allow the formation of an accretion disc. To investigate this possibility, I estimate the mass transfer rate of the system using the bolometric flux of the system and a distance estimate obtained from the infrared spectra. The emission lines are examined to see whether constraints can be placed on the location and the physical conditions of the line-emitting gas.

A shortened version of this chapter has been published in *Monthly Notices of the Royal Astronomical Society* (Harrop-Allin et al. 1997).

3.1 The polar with the longest orbital period

V1309 Orionis (RX J0515.6+0105) was discovered as a soft X-ray source in the *ROSAT* All-Sky Survey. The source was identified as a magnetic cataclysmic vari-

able by Beuermann & Thomas (1993), who reported a tentative optical and X-ray periodicity near 8 hours. The star was discovered independently by Walter, Wolk & Adams (1995) as a serendipitous *ROSAT* source during a programme to study the spatial distribution of low-mass, pre-main-sequence stars in the Ori OB1 association. Follow-up observations by Garnavich et al. (1994) led to the discovery of deep (~ 1 mag in V) total eclipses in the optical light curve. On the basis of its variable X-ray emission (Walter et al. 1995), the detection of circular polarization (Shafter et al. 1995) and the phase-dependent behaviour of emission lines in its optical spectra (Garnavich et al. 1994; Shafter et al. 1995), the star was identified as an eclipsing magnetic cataclysmic variable with an orbital period of 7.98 hours. Phase-resolved polarimetry by Buckley & Shafter (1995) showed that the circular polarization varies at the orbital period (to within 0.01 %), and this confirmed V1309 Ori as a polar. V1309 Ori has the longest orbital period of any polar yet identified.

Infrared spectroscopy is a valuable tool for determining the magnetic field strength of the white dwarf in polars with $B \lesssim 40$ MG. This is because the cyclotron fundamental occurs at wavelengths longer than ~ 2.5 microns and cyclotron humps are thus discernible in infrared spectra. Magnetic field strength estimates for ST LMi, AM Her, EF Eri and BL Hyi have been made from the identification of cyclotron humps in the range 1.0–2.5 microns (Bailey, Ferrario & Wickramasinghe 1991; Ferrario, Bailey & Wickramasinghe 1993; Ferrario, Bailey & Wickramasinghe 1996). In V1309 Ori, however, cyclotron humps are visible in the optical, and this indicates a much higher white dwarf field strength than in other polars, with $B \sim 60$ MG (Shafter et al. 1995; Garnavich et al. 1994). V1309 Ori has one of the highest field strengths of the known polars (the polar with the strongest known primary field is AR UMa (Schmidt et al. 1996), with $B \sim 230$ MG).

Infrared spectra of V1309 Ori were obtained in order to confirm the absence of cyclotron features in the K-band (this would indicate a strong magnetic field) and to search for spectral features of the secondary star. The wide separation implied by the large orbital period suggests that the secondary should be visible in the infrared,

Table 3.1: Log of observations

Star	Class or Spectral type	UT start	UT end	Total exposure time (s)
BS 1687	F5V	04h39	04h46	72
GL 229	M1V	05h00	05h07	72
V1309 Ori	polar	05h21	06h24	3120
BS 2500	F6V	07h00	07h07	72

thus providing constraints on the system distance. The wide orbital separation also suggests the possibility that R_μ (equation 1.10) in V1309 Ori could be less than the minimum radius for an accretion disc, R_{min} (equation 1.3); this might allow the formation of an accretion disc in the system.

3.2 UKIRT observations and data reduction

3.2.1 Details of observing procedure

K-band spectra (first order, 1.81–2.44 μm) of V1309 Ori were obtained in photometric conditions on 6 February 1996, using the Cooled Grating Spectrograph 4 (CGS4, Mountain et al. 1990) on the United Kingdon Infrared Telescope (UKIRT) on Mauna Kea, Hawaii. A log of observations is presented in Table 3.1.

CGS4 is a 1–5 μm spectrometer housing a 256 × 256 InSb detector array. The 75 line per mm grating and the 150 mm camera were used. The slit width was one pixel, corresponding to approximately 1.22 arcsec on the sky. To improve the resolution, the spectra were optimally sampled by mechanically shifting the detector array in the dispersion direction over two pixels in steps of half a pixel. The reduced spectrum has a resolution of $\sim 350\,\mathrm{km\,s^{-1}}$ over the wavelength range covered. The sampling is performed over two pixels so that each data point in the final spectrum

is observed by two adjacent pixels; when the data from each sampling position are interleaved, the data from any bad pixel is replaced by that of its good neighbour. Except at the edges of the array, or where there is a bad pixel, each data point in the final array is the average of two measurements. Sky subtraction was performed by nodding the telescope between two positions on the detector, and the readout noise was reduced using the non-destructive readout mode of the detector.

3.2.2 Data reduction

The two-dimensional frames were acquired and reduced in real-time at the telescope using CGS4DR (Daly & Beard 1994). The software applies a bad pixel mask to each image, subtracts a bias frame and a dark frame and divides the image by a flat-field frame. Integrations taken at different detector positions are interleaved according to the oversampling, and nodded frames are subtracted to correct for sky variations.

Subsequent data reduction was performed using FIGARO (Shortridge et al. 1996). Residual sky is present in the subtracted sky-object pairs where the atmospheric conditions vary between nods. The residual sky lines were removed by fitting a polynomial in the spatial direction after masking out the stellar spectra. The positive and negative spectra were then optimally extracted and combined. The next step was to remove the ripple in the spectra: ripple is caused by slit losses and transparency variations that occur while stepping the detector. The target spectra were de-rippled by dividing throughout by a calculated ripple profile. Wavelength calibration was obtained from an argon arc spectrum. A second-order fit of wavelength versus resolution element number was a good match to the dispersion curve, yielding an error of $0.54\,\text{Å}$ (rms).

The target spectra were divided by the spectrum of a standard FV star. As well as providing a flux calibration of the target spectra, the division by the standard star removes telluric atmospheric absorption features from the target spectra. The F6V star BS 2500 was used to calibrate the M1V star GL 229 (the secondary of

V1309 has a secondary star of approximately this spectral type), and the F5V star BS 1687 was used to calibrate the polar. They were assumed to have blackbody spectra with temperatures of 6380 K and 6530 K, and K-magnitudes of 4.71 and 4.80, respectively. Prominent absorption lines in the spectrum of the standard stars (e.g. Brackett-γ) were removed prior to taking ratios.

The standard and target star spectra were obtained using the same slit width. In the absence of seeing and transparency variations, and provided tracking and guiding errors are negligible, slit losses for both the standard and the target stars will be the same. The flux calibration procedure should, in the ideal case, correct for slit losses in the target spectra. However, if there are relative slit losses between the target and the standard star spectra, the flux calibration provides only an approximation to the absolute flux.

3.3 Results

Figure 3.1 shows the K-band spectra of V1309 Ori and the M1V star GL 229. Also shown is the F6V star BS 2500 that was used for calibration (this spectrum indicates the location of atmospheric absorption features). The M1V star spectrum shows residual atmospheric features between 1.8 and 2.0 μm — this is the boundary between the H and K bands which is dominated by telluric absorption. Spectral features in this region are thus very uncertain.

According to the ephemeris of Buckley & Shafter (1995), our spectra of V1309 Ori were obtained between orbital phases 0.43 and 0.56 with a cumulative uncertainty in phase of $\sim$ 0.02 (where orbital phase zero is defined to be the mid-point of the eclipse). Any emission from the secondary observed at these phases will originate from the *irradiated* hemisphere which may have an earlier spectral type than the cooler M0–M1 hemisphere observed at mid-eclipse in the optical by Shafter et al. (1995). It transpires that the system was observed at the phases least favourable for the detection of M0–M1 features from the secondary; conversely, our observa-
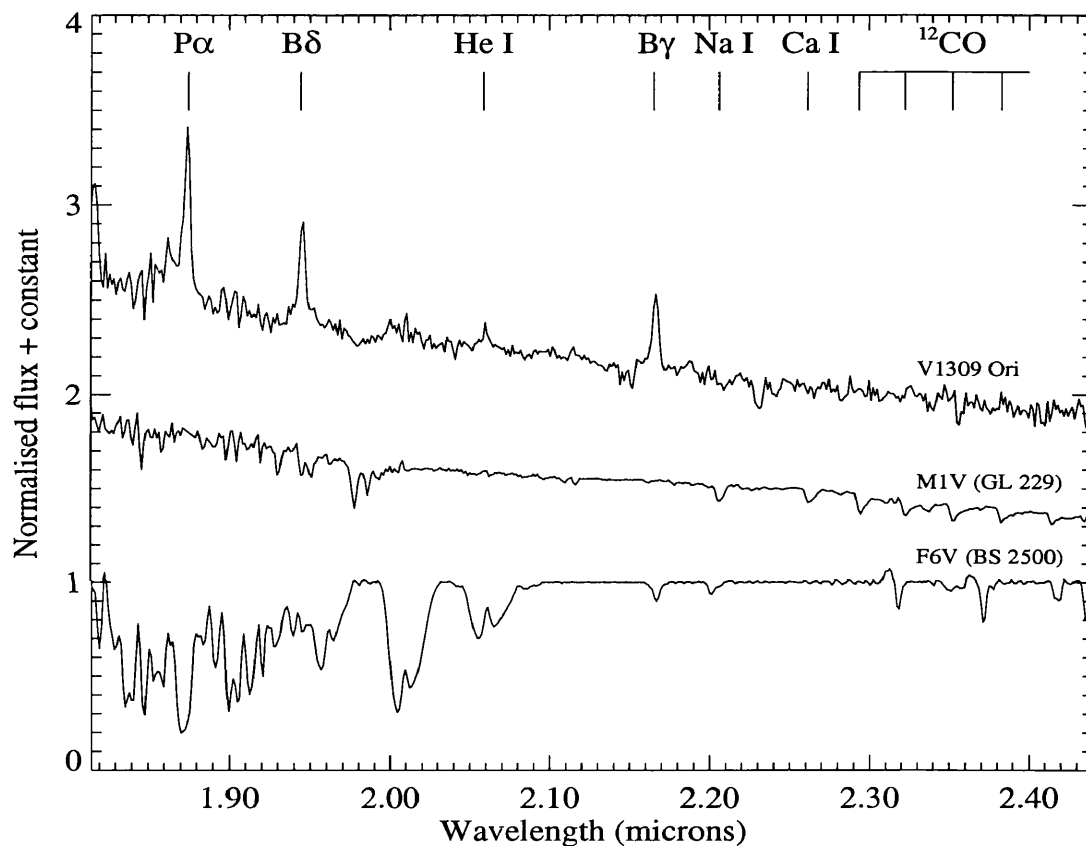
Figure 3.1: K-band spectra of V1309 Ori, the M1V star (GL 229) and the F6V star BS 2500. The M star and the polar spectra have been normalized by dividing throughout by the flux at 2.20 μm and have been offset by adding 0.5 and 1.0 to each spectrum respectively. The BS 2500 spectrum has been normalized by dividing by a spline fit to the continuum regions (the apparent P Cyg profiles at 2.32 μm and 2.37 μm are artefacts of the division by the spline curve). This spectrum shows the location of the atmospheric absorption features in the K-band.

tions were obtained at phases that favour the detection of infrared emission from the accretion stream, the accretion column and the irradiated inner hemisphere of the secondary star.

3.3.1 The emission lines

A comparison of the K-band spectrum of V1309 Ori with that of the M1V star GL 229 (Figure 3.1) shows that there are no obvious ^{12}CO bandheads or NaI absorption from a M1V secondary star in the polar spectrum. Higher signal-to-noise spectra will be required to determine the absence or presence of secondary absorption features in the K-band spectrum. The wavelengths and equivalent widths of the principal infrared spectral lines (labelled in Figure 3.1) are shown in table 3.2.

The most prominent features in the K-band spectrum of V1309 Ori are emission lines of neutral hydrogen (Brackett and Paschen series) and helium. This is consistent with the optical spectra of V1309 Ori (Walter et al. 1995; Shafter et al. 1995) and with infrared spectra of other polars. For example, ST LMi (Ferrario et al. 1993) shows the same line species as V1309 Ori and in addition shows strong He I emission at 1.909 μm (features in this region of our spectrum are, however, uncertain due to atmospheric absorption). Due to the limited resolution of the spectrum, a multi-component structure in the emission lines of V1309 Ori cannot be discerned. As a result, it is not possible to identify emission from the irradiated hemisphere of the secondary, which is expected to produce a narrow component in the emission lines (as is observed in high-resolution optical spectra of HU Aqr: Schwope et al. 1997). Strong He II λ4686 Å emission is seen in optical spectra of this and other polars: however, no higher-excitation lines are apparent in the K-band spectrum of V1309 Ori, nor are they apparent in infrared spectra of other polars (Ferrario et al. 1993; Ferrario et al. 1996). High-excitation lines are also absent from K-band spectra of the intermediate polars EX Hya, PQ Gem and BG CMi (Dhillon et al. 1997).

There are unidentified absorption features in the spectrum of V1309 Ori at $\sim$

Table 3.2: Wavelengths and equivalent widths of the principal lines in the K-band spectra of V1309 Ori and GL 229 (M1V). The rest wavelengths have been taken from Dhillon et al. (1997) and Lang (1974); the rest wavelengths of the ^{12}CO lines refer to the band-heads.

Star	Line	Rest wavelength (Å)	Equivalent width (Å)
V1309 Ori	Paα	18751	24 $\pm$ 5
	Brδ	19446	21.5 $\pm$ 0.4
	He I	20587	4 $\pm$ 2
	Brγ	21655	15.6 $\pm$ 0.5
GL 229	Na I	22062, 22090	-4.0 $\pm$ 0.2
	Ca I	22614, 22631	-5.2 $\pm$ 0.1
	^{12}CO	22935	-5.5 $\pm$ 0.8
	^{12}CO	23227	-3.2 $\pm$ 0.3
	^{12}CO	23525	-4.3 $\pm$ 0.4
	^{12}CO	23830	-4.3 $\pm$ 0.3

2.24 μm and $\sim$ 2.36 μm. These features may be significant but do not correspond to anticipated line species in the M star or atmospheric features in the F star.

3.3.2 The continuum

If the white dwarf in V1309 Ori has a magnetic field strength of 55–61 MG (Garnavich et al. 1994; Shafter et al. 1995), the fundamental cyclotron harmonic will occur between 1.78 and 1.94 μm. It is plausible, therefore, that the main contribution to the infrared continuum is cyclotron emission, and that the observed continuum is the long-wavelength tail of the cyclotron fundamental. Cyclotron humps are not present in the infrared spectrum of V1309 Ori because the wavelength range covered

is at or beyond the fundamental cyclotron harmonic.

To isolate the cyclotron flux from the infrared spectrum, the contribution of the secondary star in the K-band must be estimated and subtracted. To model the cyclotron continuum emission, estimates are required of the shape of the accretion region, the inclination of the system, the offset between the magnetic field and the white dwarf spin axis and the temperature of the material in the post-shock region from which the majority of the cyclotron radiation is emitted.

The contribution of the secondary

The contribution to the K-band spectrum from the secondary is estimated using the assumption that the secondary is an M1V star (Shafter et al. 1995). I followed the approach used by Dhillon et al. (1997) whereby scaled secondary star contributions are subtracted from the polar spectrum and the residuals are inspected for any trace of (reversed) M star spectral features. In this way, it is estimated that the secondary contribution to the K-band flux of V1309 Ori is $\lesssim 20\%$. This result is similar to estimates of the secondary contribution in K-band spectra of intermediate polars: Dhillon et al. (1997) find upper limits of $\sim 50\%$ and $\sim 30\%$ to the K-band contribution of the secondary stars in BG CMi and PQ Gem, respectively.

This estimate of the upper limit to the fraction of the K-band flux produced by the secondary depends on the adoption of the M1V spectral type. This could be problematic on two counts: first, the secondary may not be in thermal equilibrium (see section 3.4.3 below) so that its optical and infrared spectrum may not be characterized appropriately by a single main sequence spectral type. Secondly, the irradiation of the observed hemisphere may result in an earlier spectral type than the M1V seen at mid-eclipse.

To investigate the sensitivity of the result to the choice of the spectral type of the secondary star, the calculations were repeated using K-band spectra of an M4.5V star (GL 83.1) and a K5V star (61 Cyg A). These stars have spectral types which are (approximately) the extremes of the range of spectral types expected for the

secondary of V1309 Ori. A Roche lobe-filling secondary in a CV with an orbital period of 7.98 h has a spectral type between K1 and K6 (Allen 1973; Warner 1995), while the secondary star spectral type can be as late as M4.5V in the shorter-period polars (Warner 1995). Using the method described above, it is estimated that a K5V star can contribute no more than 30 % of the infrared flux, while a M4.5V star would contribute less than 20 %.

The cyclotron flux

To investigate whether the continuum in our spectrum is consistent with cyclotron emission due to a primary magnetic field in the range predicted by optical studies, the continuum of the K-band spectrum is compared to the constant temperature cyclotron models of Wickramasinghe & Meggitt (1985). For a given size parameter Λ (approximately the optical depth at the cyclotron fundamental) and an electron shock temperature T_e, the models predict the intensity of the cyclotron radiation and the percentage linear and circular polarization of emission from a point source for various viewing angles and for each cyclotron harmonic. Wickramasinghe & Meggitt (1985) point out that the available observational evidence for polars supports small ($\Lambda \lesssim 10^6$) high temperature ($T_e > 5\,\mathrm{keV}$) cyclotron emission regions.

Observational estimates for T_e of V1309 Ori are not available. Walter et al. (1995) observed no significant hard X-ray component in their *ROSAT* PSPC spectra, and find that the bremsstrahlung temperature and normalization are unconstrained. To characterize the shock temperature of the region in the accretion column where the majority of the accretion energy is radiated, the stratified temperature models from Cropper, Ramsay & Wu (1998) are used. For a range of white dwarf masses from 0.4 to 1.0 $M_\odot$, and assuming a mass transfer rate of $1\,\mathrm{g\,s^{-1}cm^{-2}}$ and an accretion region with a height of 10^8 cm, the models predict that the bulk of the radiation is emitted from a region in the post-shock flow with a temperature of $7 - 10\,\mathrm{keV}$. The 10 keV model of Wickramasinghe & Meggitt (1985) was therefore used to characterize the shock in V1309 Ori.
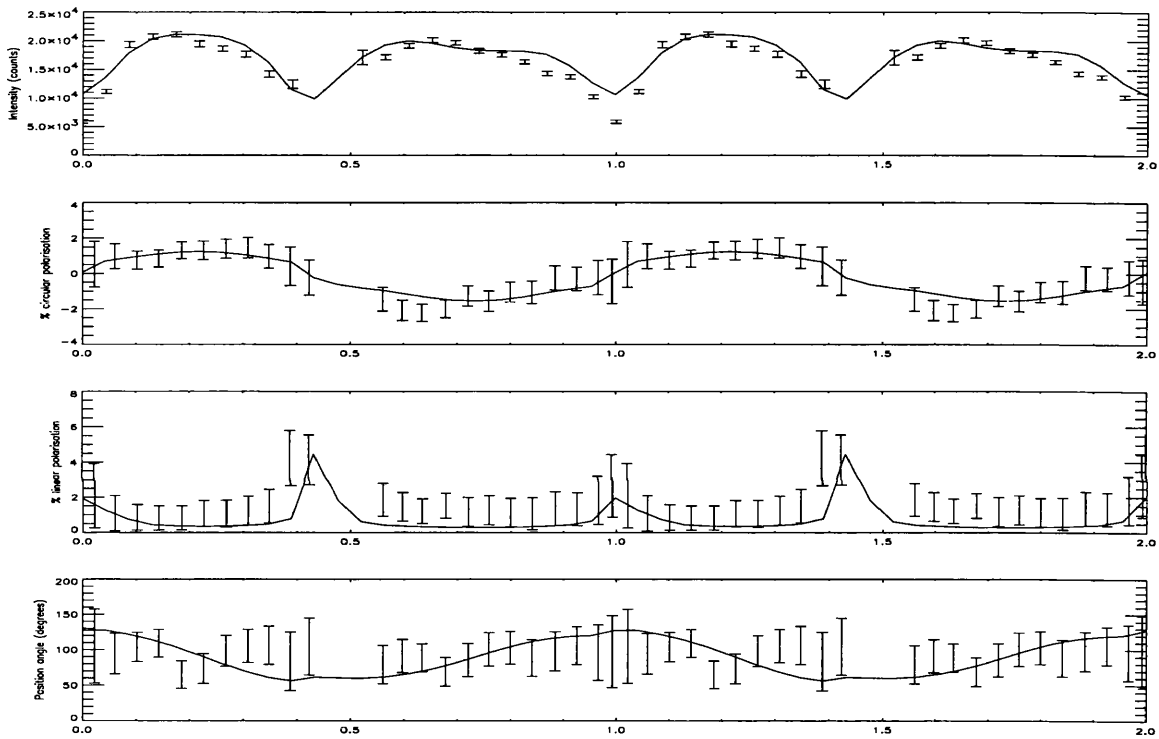
Figure 3.2: Orbital phase-binned white light polarization and light curves from Euckley & Shafter (1995) overlaid by a model of cyclotron emission from two diametrically opposed cyclotron emission points. A good fit was obtained for a polar magnetic field strength of 60 MG, size parameter $\Lambda = 10^5$ and a shock temperature of 10 keV. The orbital inclination for the model is 80° and the dipole offset is 30°.

To obtain a simple model of the accretion geometry on the surface of the white dwarf I used the white light polarimetry from Buckley & Shafter (1995), kindly supplied in electronic form by D.A.H. Buckley. In order not to over-interpret the data, the simplest accretion geometry that would provide an acceptable fit was chosen. The intensity and polarization light curves are modelled using cyclotron emission from two diametrically opposed emission points on the white dwarf (for more details of the modelling procedure see Potter et al. 1997). A model fit was also attempted for two emission points at the footpoints of the same magnetic field line, but this did not produce acceptable fits. The results of the model fits for the diametrically opposed emission points with $T_e = 10\,\mathrm{keV}$, $\Lambda = 10^5$ and $B = 60\,\mathrm{MG}$ are shown in Figure 3.2. A good fit was obtained for an offset of 30° between the magnetic and the spin axis and an orbital inclination of 80°. The latter value is equal to the upper limit for the orbital inclinaton deduced by Garnavich et al. (1994) from measurements of the eclipse width. The emission region in the hemisphere closest to the observer is at a magnetic latitude of 10° and a longitude of 270°, while the diametrically opposed emission point is at a magnetic latitude and longitude of 170° and 90°, respectively. Here the magnetic longitude is measured in an anticlockwise direction from the line joining the magnetic and spin poles, while magnetic latitude is measured from the north magnetic pole. Equally good fits to the polarization and intensity light curves were obtained using values of the size parameter Λ from 10^5 to 10^7 — the models cannot therefore be used to provide constraints on Λ. In addition, Λ is not constrained by the optical spectrum of Shafter et al. (1995) (see section 3.4.3).

With the optical estimates of the magnetic field, the temperature of the post-shock flow and a simple model of the accretion geometry, the predicted cyclotron continuum can now be calculated and compared to the optical and infrared continua. The cyclotron intensity predicted for the model in Figure 3.2 is shown in Figure 3.3 together with the infrared spectrum and the secondary-subtracted optical spectrum from Shafter et al. (1995).
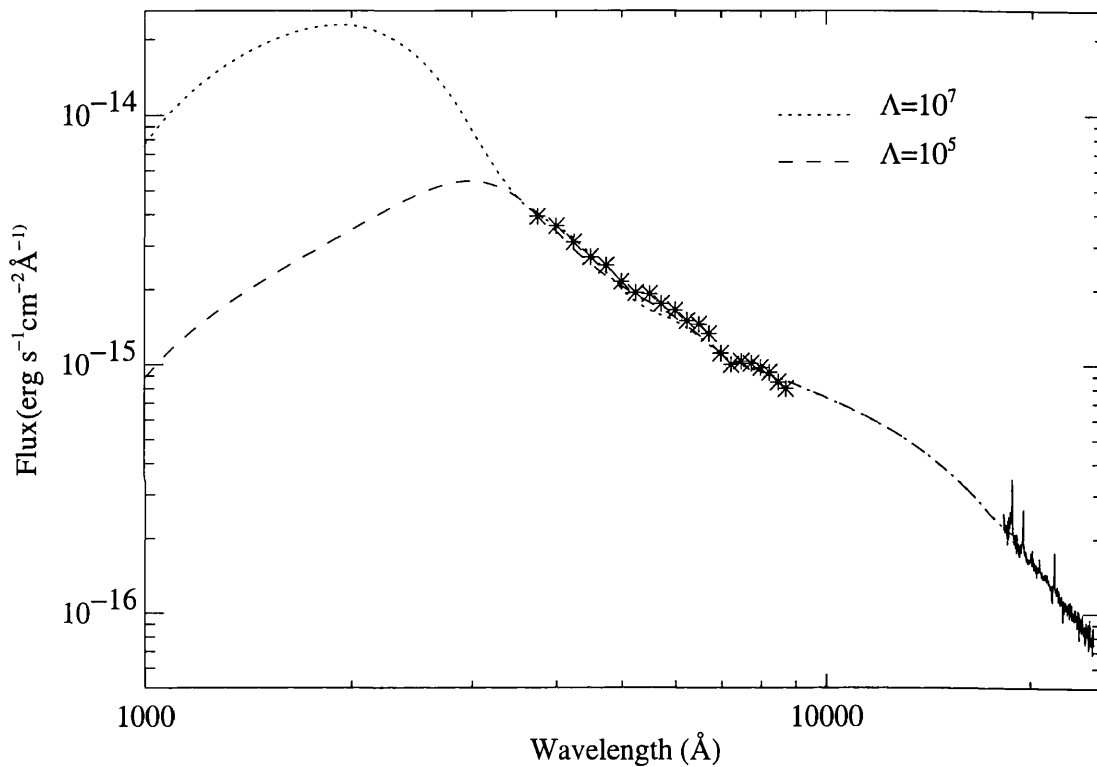
Figure 3.3: Observed and model cyclotron spectra of V1309 Ori. The optical spectrum was estimated from figure 10(a) of Shafter et al. (1995). Superimposed is a spline fit to the cyclotron emission from the model in Figure 3.2 for $\Lambda = 10^5$ (dashed line) and 10^7 (dotted line). The fit has been extended to the infrared spectrum for the purposes of calculating the cyclotron flux.

To the extent that the optical and infrared observations are not simultaneous, and given that both the optical and the infrared fluxes are subject to errors from slit losses, the optical and infrared continuum flux is consistent with a cyclotron continuum produced by a magnetic field of $\sim 60\,$MG. The modelling of the polarization and intensity light curves of Buckley & Shafter (1995) is also consistent with this magnetic field strength.

3.4 Discussion

3.4.1 The emission lines

It is notoriously difficult to obtain information on the physical conditions in the emission line regions in polars: a calculation of the line emission must take into account collisional and shock heating, irradiation by high energy photons from the accretion region and the velocity flows and inhomogeneities in the stream (see section 2.8). The investigation was thus restricted to the predictions for Case B in the sense of Baker & Menzel (1938) (Case B refers to a medium in which the Lyman lines are taken to be optically thick, while all other lines are optically thin). It is then possible to place limits on the temperature and density of the line-emitting region by considering the theoretical predictions for hydrogen recombination line intensities from Storey & Hummer (1995).

The hydrogen recombination equivalent widths in Figure 3.1 are in the ratio $Pa\alpha : Br\delta : Br\gamma = 1 : 0.6 : 0.4$. Under the assumptions of Case B, the ratios predict $T_e \lesssim 500\,$K and $10^{10} < N_e < 10^{12}\,$cm^{-3}. This density is somewhat lower than found typically in the optical, where densities $N_e \sim 10^{14}\,$cm^{-3} (Stockman et al. 1977). The temperature is much lower than the $10^4\,$K found in the optical (Liebert & Stockman 1985).

It may be tempting to speculate that the very low temperature obtained above indicates that the hydrogen recombination lines originate in a particularly cool part

of the flow, perhaps in the ballistic stream near the secondary. However, such an interpretation is precluded by the widths of the lines, which are $\gtrsim 800\,\mathrm{km\,s^{-1}}$. This indicates that the lines are formed closer to the white dwarf, where the flow velocities are becoming comparable to the free-fall velocity ($\sim$ several thousand $\mathrm{km\,s^{-1}}$).

It is probable, therefore, that the line emitting region does not conform to the criteria of Case B — this is not particularly surprising, given the complexity of the physical processes that occur in the line emission regions of the accretion flow.

3.4.2 The distance

Assuming that the secondary is an M1V star, and the secondary contribution is $\lesssim 20\,\%$ of the K-band flux (section 3.3.2), an approximate lower limit to the K magnitude of the secondary can be obtained by multiplying the scaled spectrum of GL 229 by the K-band filter response and integrating over the K-band wavelength range. The secondary flux at $2.20\,\mu\mathrm{m}$ is less than $1.5 \times 10^{-13}\,\mathrm{erg\,cm^{-2}\,s^{-1}\,\mathring{A}^{-1}}$, corresponding to a K-magnitude of $\gtrsim 15.5$. If the seeing conditions during the acquisition of the standard star and the V1309 Ori spectra were not identical, these estimates of the secondary star K-band flux and K-magnitude are subject to a further uncertainty that will depend on the relative slit losses between the standard spectrum and the V1309 Ori spectrum.

To check how this result depends on the spectral type adopted for the secondary star, the calculation was repeated using the template M4.5V and K5V star spectra. The estimated upper limits to the contributions of these stars to the K-band flux of V1309 Ori are 20 % and 30 %, (see section 3.3.2), corresponding to K-magnitudes greater than 15.4 and 15.0, respectively.

The system distance is estimated using Bailey's (1981) relation:

$$S_\mathrm{k} = K + 5 - 5\log D + 5\log R_2 \tag{3.1}$$

where S_k is the K surface brightness of the secondary, D is the distance in parsecs,

and R_2 is the radius of the secondary in solar units. A Roche lobe-filling secondary in a CV with an orbital period of 7.98 h is $R_2 = 0.89\,R_\odot$ (Warner 1995). This is used to take into account the difference in luminosity between a main sequence star and a Roche lobe-filling star of the same spectral type. Assuming that the spectral type of the secondary is M1, and with $S_k = 4.4$ (Ramseyer 1994), the distance to V1309 Ori is found to be greater than 1500 pc. Although S_k is unlikely to be the same for a Roche lobe-filling M1 star and a main sequence M1V star, the error introduced is small, since S_k is not strongly dependent on values of $V - K$ between 2.5 and 5.0 (Ramseyer 1994).

Another estimate of the lower limit to the system distance can be obtained using the equation

$$\log D = \frac{K}{5} - 1.06 + \log R_2 + 1.56 \log P_{\text{orb}} \tag{3.2}$$

(Warner 1995) where P_{orb} is the orbital period of the system in hours. In the case of an M1 star, the lower limit to the distance implied by equation 3.2 is 2000 pc. Here, too, the Roche lobe radius of the secondary is used instead of the main sequence radius to account for the differences in luminosity between an M1V star with a radius of $0.56\,R_\odot$, and the Roche lobe-filling secondary, which will have a radius of $0.89\,R_\odot$.

These estimates of the lower limit to the system distance are not sensitive to the choice of the spectral type of the secondary star. For a M4.5V secondary the lower limit is 1300 pc (using Bailey's method and $S_k = 4.6$). For a secondary of type K5V the distance is also at least 1300 pc (using $S_k = 4.2$).

These results are consistent with Shafter et al. 's (1995) lower limit of 500 pc, but imply distances that are rather larger than generally found for polars. However, this conclusion is inescapable: even if *all* the K-band flux is ascribed to the secondary star, the derived distance is greater than 500 pc. This has implications for the mass transfer rate and the synchronism of the system.

3.4.3 $\dot{M}$ and thermal equilibrium of the secondary

The finding by Shafter et al. (1995) that the secondary in V1309 Ori has a spectral type of M0–M1, while a Roche lobe-filling secondary in a cataclysmic variable with $P_{\rm orb} = 7.98\,{\rm h}$ would have a spectral type between K1 and K6 if it were on the main sequence, was accounted for by Frank, Lasota & Chanmugam (1995) by requiring the secondary to be out of thermal equilibrium. For a range of white dwarf masses, the mass transfer rate must satisfy

$$\dot{M}_{16} \gtrsim 13 - 25 \qquad\qquad (3.3)$$

for the secondary to be out of thermal equilibrium. Here $\dot{M}_{16}$ is the mass transfer rate of the system in units of $10^{16}\,{\rm g\,s^{-1}}$. With the estimates of the cyclotron flux (section 3.3.2) and the lower limit to the system distance (section 3.4.2), I now consider whether this explanation remains viable by placing a limit on the mass transfer rate using estimates of the *bolometric* flux of the system.

The K-band spectrum of V1309 Ori shows that the infrared flux is primarily of accretion origin. In addition, from the modelling of the cyclotron radiation in section 3.3.2, the optical continuum is consistent with cyclotron emission (which also originates in the accretion region). The *total* cyclotron emission can now be estimated by interpolating between the K-band and optical continua, extrapolating into the UV using the cyclotron model and integrating the flux between 1000 and 25000 Å. The total cyclotron flux is found to be $f_{\rm cyc} \sim 2.5 \times 10^{-11}\,{\rm erg\,cm^{-2}\,s^{-1}}$.

The unabsorbed blackbody X-ray flux can be estimated from the mean PSPC count rate (0.21 counts/s in 0.1–2 keV) and the column density (5.4×10^{20} cm^{-2}) in Walter et al. (1995) to be $f_{\rm x} = 1.8 \times 10^{-11}\,{\rm erg\,cm^{-2}\,s^{-1}}$, comparable to the cyclotron flux. However, the soft X-ray flux depends strongly on the temperature adopted for the blackbody, the absorption and the mean count rate. If the higher count rate (0.5 counts/s) and lower temperature (25 eV) from Beuermann & Burwitz (1995) are used (these are the values from the *ROSAT* All-Sky Survey observations), then

the soft X-ray flux increases to $2 \times 10^{-10}\,\mathrm{erg\,cm^{-2}\,s^{-1}}$ (assuming the same column density). In addition, at some level there will be flux from an undetected hard X-ray component. To provide a conservative estimate for the mass transfer rate, the Walter et al. (1995) soft X-ray flux is added to the integrated cyclotron flux, giving a flux of $f_{\mathrm{bol}} = 4.3 \times 10^{-11}\,\mathrm{erg\,cm^{-2}\,s^{-1}}$ from $2\,\mathrm{keV} - 2.4\,\mu\mathrm{m}$.

A lower limit to the mass transfer rate can now be deduced using the lower limit to the distance obtained in section 3.3.2. Following Walter et al. (1995) and substituting the bolometric luminosity for the accretion luminosity,

$$\dot{M}_{16} = 2.6 \times 10^9 f_{\mathrm{bol}}\, M_1^{-4/3} D_{200}^2. \tag{3.4}$$

Here f_{bol} is the bolometric flux in $\mathrm{erg\,cm^{-2}\,s^{-1}\,\mathring{A}^{-1}}$, M_1 is the mass of the primary in solar units and D_{200} is the system distance in units of $200\,\mathrm{pc}$. The derivation of equation 3.4 assumes a mass-radius relation for the primary, given by equation 1.5. The primary mass is assumed to be $M_1 = 0.7$ (this is the average primary mass for magnetic CVs from Warner 1995). With this assumption, and using a lower limit to the distance of $1500\,\mathrm{pc}$, equation 3.4 implies a mass transfer rate greater than $1.0 \times 10^{17}\,\mathrm{g\,s^{-1}}$. This lower limit approaches the values required by equation 3.3 for the secondary to be out of thermal equilibrium.

Equation 3.3 is satisfied more comfortably if the higher values of the soft X-ray flux are adopted. Using a higher value of Λ than 10^5 for the cyclotron model (section 3.3.2) adds additional UV / blue flux to the cyclotron spectrum, increasing the predicted mass transfer rate still further: for example if $\Lambda = 10^7$, the cyclotron flux increases to $5.3 \times 10^{-11}\,\mathrm{erg\,cm^{-2}\,s^{-1}}$, and the predicted mass transfer rate is greater than $6.0 \times 10^{17}\,\mathrm{g\,s^{-1}}$.

3.4.4 Synchronism

The estimates of $\dot{M}$ for V1309 Ori obtained in section 3.4.3 are considerably larger than the mass transfer rates deduced for polars below the orbital period gap. For

eight polars with $1.35\,\mathrm{h} \leq P_{orb} \leq 3.71\,\mathrm{h}$, Warner (1995) finds a mass transfer rate of $\dot{M} \sim 2.5 \times 10^{15}\,\mathrm{g\,s^{-1}}$, independent of P_{orb} and mass ratio, in agreement with the mass transfer rate expected for gravitational radiation alone. Given the large accretion torque implied by such a high $\dot{M}$, I now consider whether it is plausible that V1309 Ori is synchronized.

For a white dwarf mass of $0.7\,M_{\odot}$ and an M0–M1 secondary, the condition that the Alfvén radius should exceed the orbital separation of the two stars (Patterson 1984; see chapter 1) predicts that a mass transfer rate of more than $\sim 3 \times 10^{16}\,\mathrm{g\,s^{-1}}$ will break synchronism. Since this criterion may not be relevant to the maintenance of synchronism (Lamb & Meila 1988), I use instead the criterion derived by Warner (1997, equation 1.11), which is based on the dipole-dipole interaction between the primary and the secondary star.

For V1309 Ori, $\mu_{33} = 33$ for $M_1 = 0.7$. The most severe test of equation 1.11 is for the higher mass transfer rates deduced in section 3.4.3 above, corresponding to the higher values of the soft X-ray fluxes and the larger values of Λ. For a distance of 1500 pc, an X-ray flux of $2 \times 10^{-10}\,\mathrm{erg\,cm^{-2}\,s^{-1}}$ and a cyclotron flux of $5.3 \times 10^{-11}\,\mathrm{erg\,cm^{-2}\,s^{-1}}$ (corresponding to $\Lambda = 10^7$), the mass transfer rate from equation 3.4 is $\sim 6 \times 10^{17}\,\mathrm{g\,s^{-1}}$. This value for $\dot{M}$ satisfies the synchronism criterion. If the synchronism criterion is correct, and if $M_1 \sim 0.7$, the mass transfer rate in V1309 Ori would have to be larger than $2.4 \times 10^{18}\,\mathrm{g\,s^{-1}}$ to break synchronism. This would require (from equation 3.4) a distance greater than 3 kpc, which seems unlikely.

The high mass transfer rate deduced for V1309 Ori should be compared to the estimate by Beuermann & Burwitz (1995), who obtain $\dot{M} \sim 6 \times 10^{16}\,\mathrm{g\,s^{-1}}$ for V1309 Ori. Their value is derived by fitting the soft X-ray flux with a blackbody spectrum — the strong cyclotron component of the accretion flux is neglected. In a system with $B \approx 60\,\mathrm{MG}$, the cooling of the post-shock flow is likely to be dominated by cyclotron emission (see Fig. 1.3), and thus the cyclotron emission must be included when estimating the bolometric flux of the system.

The mass transfer rate of V1309 Ori is several orders of magnitude larger than is predicted for gravitational radiation-driven orbital evolution ($\sim 8 \times 10^{14}\,\mathrm{g\,s^{-1}}$, using equation 1.2). The large mass transfer rates in V1309 Ori and other systems with $P_{\mathrm{orb}} \gtrsim 3\,\mathrm{h}$ (Fig. 1.2) imply that the orbital evolution of polars cannot be driven by gravitational radiation alone. Magnetic braking still plays a significant role, even though its effectiveness is reduced due to the suppression of the wind from the secondary (Li & Wickramasinghe 1998).

3.4.5 Is there an accretion disc in V1309 Ori?

Given the estimate of the mass transfer rate, it is now possible to compare the quantities R_{μ} and R_{min} to see whether an accretion disc could form in V1309 Ori. Using equations 1.3 and 1.10, and assuming $M_1 = 0.7$, $\sigma_9 \sim 1$ and $\dot{M}_{16} \approx 60$, the values for R_{min} and R_{μ} are very similar: $8.3 \times 10^9\,\mathrm{cm}$ and $1.0 \times 10^{10}\,\mathrm{cm}$ respectively.

Due to the uncertainties in the parameters used to calculate R_{μ} and R_{min}, it is not clear whether the two radii are sufficiently similar to warrant any further speculation, although it can be seen that if $\dot{M}$ is higher than $20 \times 10^{17}\,\mathrm{g\,s^{-1}}$, R_{μ} will be less than R_{min}. It should be noted, however, that there is no evidence for an accretion disc in Hβ and He II $\lambda4686\,\mathrm{\AA}$ Doppler tomograms of this system (Hoard 1999).

Chapter 4

Indirect imaging of the accretion stream

In this chapter I develop a method that can be used to provide observational constraints on the properties of the accretion flow. The method is an indirect imaging technique which uses broad-band optical eclipse profiles of polars to determine the distribution of brightness along the accretion stream. Tests with synthetic data are presented; these show that, provided the phase resolution of the light curve is good, the method is able to retrieve unambiguously the stream brightness distribution from an eclipse profile, even in the presence of moderate noise. The technique can also be used to obtain estimates of the radius R_μ where the ram pressure of the accretion stream equals the magnetic pressure, and hence estimates of the mass transfer rate through the stream via equation 1.10.

Another technique that has been used recently to image the accretion stream in polars is Doppler tomography (Marsh & Horne 1988, used by e.g. Diaz & Steiner 1994, Schwope et al. 1997 and Šimić et al. 1998). Doppler tomography provides an image of the line emission from the accretion flow in velocity space, whereas the stream imaging method provides an image of the *total* emission of the accretion flow in *spatial* coordinates. The two methods are thus complementary, but the stream

imaging method can give a more complete idea of the brightness distribution between the two stars.

A shortened version of this chapter has been published in *Monthly Notices of the Royal Astronomical Society* (Harrop-Allin, Hakala & Cropper 1999a).

4.1   Description of the method

4.1.1   Previous work

Hakala (1995) (hereafter H95) presents a method to deduce the accretion stream brightness in the eclipsing polar HU Aquarii from photometric eclipse profiles. The method has close parallels with eclipse mapping of accretion discs in non-magnetic systems (e.g. Horne 1983; Horne 1985) in that both reconstruct the brightness of the region between the stellar components and both make use of Maximum Entropy regularization to constrain the problem (in general, there are more model parameters than there are data points). A brief summary of the method is presented here; further details are available in H95. The new improvements to the method are presented in section 4.1.2.

A model accretion stream is created by placing evenly-spaced emission points along a pre-set stream trajectory. The accretion regions on the white dwarf are modelled as single bright points, the brightnesses of which are fixed for each model calculation. This stream is then observed through an eclipse by the Roche lobe-filling secondary. A model light curve is generated by summing the brightnesses of the points that are visible at each orbital phase. The brightnesses of the emission points are optimized using a genetic algorithm (GA). Genetic algorithms mimic biological natural selection: the optimization proceeds by 'breeding' the 'fittest' solutions from an initial population of random solutions (for an introduction to GAs and their applications in astronomy see Charbonneau 1995). The brightnesses are adjusted in order to minimize the quantity

$$F = \sum_{i=1}^{N} \left(\frac{\text{model}_i - \text{data}_i}{\sigma_i} \right)^2 - \lambda S. \tag{4.1}$$

where N is the number of data points in the original light curve, model_i is the brightness of the ith model light curve point, data_i is the brightness of the ith point in the original light curve and σ_i is its uncertainty. In the second term of equation 4.1, $\lambda > 0$ is a Lagrange multiplier, and the quantity S is the entropy of the solution, defined as

$$S \equiv \sum_{j=1}^{M} p_j - m_j - p_j \ln(p_j/m_j), \tag{4.2}$$

where M is the number of brightness points along the model accretion stream, p_j is the normalized brightness of model stream point j and m_j is the local geometric mean of the brightness of the emission points neighbouring point j on the model stream — this is $m_j = \sqrt{p_{j-1}p_{j+1}}$ for an emission point flanked by two neighbouring points. At the endpoints of the 1-dimensional distribution m_j is given by $\sqrt{p_j p_{j+1}}$ for a point j at the beginning of a section of the stream and $\sqrt{p_j p_{j-1}}$ for a point j at the end of a section of the stream. The local geometric mean is used as the default brightness so that the stream brightness distribution obtained is locally smooth. To minimize F, the entropy must be maximized: this occurs as $p_i \longrightarrow m_i$.

The first summation on the right hand side of equation 4.1 is the χ^2 for the fitted model light curve, while the second summation is the Maximum Entropy (ME) regularization term (H95 uses a slightly different form of the regularization term). The χ^2 term ensures that the optimization finds a solution that is consistent with the original data, while the ME term ensures that the problem is not under-constrained. The degree of smoothness required is adjusted by changing the value of λ (see section 4.1.4 for more details).

4.1.2 Improvements to the method of H95

The method of Hakala (1995) is developed and extended by including projection effects of the emission point brightnesses and by using a more realistic accretion stream trajectory. The GA optimizing procedure is improved, and the solution found by the GA is refined by using a line minimization technique.

Projection effects in the stream can be important in the high accretion state of polars (e.g. HU Aquarii: Schwope et al. 1997). The accretion stream path leads the line of centres between the two stars (Lubow & Shu 1975), and thus presents a larger projected area to the observer after the eclipse than before. The result is that the observed pre-eclipse light level is lower than the post-eclipse level. To account for this effect in the stream model, the brightness of each point along the model accretion stream is weighted by a projection factor equal to the sine of the angle between the line of sight and the tangent to the stream at that point.

The main difference between the model in H95 and that presented here is the assumed trajectory for the accretion stream. H95 approximates the accretion stream trajectory as an arc connecting the L1 point to the white dwarf; the stream is assumed to be confined to the orbital plane, and the white dwarf is treated as a dimensionless point. The trajectory used here is a combination of a ballistic trajectory from the L1 point (Lubow & Shu 1975), followed by a magnetically-channeled trajectory that follows a dipole field line out of the orbital plane. The white dwarf's magnetic field is assumed to be a centred dipole that can be inclined to the spin axis of the white dwarf by an angle β and rotated by an angle ζ with respect to the line of centres (this calculation follows the formalism of Cropper 1989). The point where the ballistic trajectory meets the magnetically-channeled trajectory occurs at R_μ, and from this point the stream follows the field line above and/or below the orbital plane. The stream trajectory ends at the surface of the white dwarf at the footpoint(s) of the dipole field line. The white dwarf is not assumed to be a point source: allowance is made for self-occultation of the accretion

regions by the white dwarf as well as by the Roche lobe-filling secondary. The radius of the white dwarf is calculated using equation 1.5 or equation 1.6 depending on its mass. Approximately 200 emission points are used for a stream accreting onto both poles, and ~ 125 points are used for a stream accreting at one pole.

The brightnesses of the emission points along the stream are optimized in the first instance using a GA. Some improvements have been made to the GA algorithm described by H95. These include increasing the selection pressure on the better solutions as the population of solutions evolves, and by the use of additional mutation operations that diversify the solutions and explore the parameter space more effectively.

Parent solutions in the GA are ranked according to their fitness F (evaluated using equation 4.1). The rank number of a selected parent solution determines the probability that the solution will be used to produce 'child' solutions by, in this case, uniform crossover (the brightness of each emission point on the stream in the child solution is taken either from one parent or the other). The selection scheme used for this technique becomes increasingly biased towards better solutions as the GA proceeds, as follows. The rank numbers of selected parents are obtained using

$$R = \text{INT}\left(-\frac{N_{\text{pop}}}{10}s^{i-1}\log(10^{-20} + RND)\right) + 1 \qquad (4.3)$$

where R is the rank number of the selected parent solution, i is the generation number, $N_{\text{pop}} = 500$ is the population size, $0 < s < 1$ is a scale factor and RND is a random number uniformly distributed between 0 and 1 (the term 10^{-20} is added to the random number before the logarithm is applied to avoid floating overflows). At the first generation $(i = 1)$, 90 per cent of the chosen parent solutions are in the first 50 ranked solutions. The scale factor is chosen such that 90 per cent of the chosen solutions are in the first ~ 5 ranked solutions by the end of the GA run. The higher-ranked solutions are thus chosen as parents with increasing frequency as the GA proceeds.

Mutation is applied individually to each child solution. The mutation procedure

alters each parameter p_j in the solution with a small probability (a probability of 0.005 was used here). The manner in which a mutated value of the brightness of an emission point is calculated has a significant effect on the final solution produced by the GA. The scheme used here is as follows: for each individual mutation, there is an equal probability that the mutated parameter is assigned a random number from a uniform distribution, *or* a random number chosen from a Gaussian distribution centred on the old value of the parameter, *or* the mean brightness of the two neighbouring points on the stream. The mutation procedure thus has a multiple effect on the solution: depending on the selected mutation method, the solution is either diversified (so as to explore new regions of the parameter space) or smoothed.

The chief motivation for using a GA instead of a more conventional optimization routine is to maximize the chances of finding the global optimum in the multi-dimensional space. GAs cannot guarantee that the global optimum will be reached but, unlike conventional steepest descent algorithms, they are capable of climbing away from local optima. It remains possible that the GA will fail to find the global minimum before it is terminated (see section 4.1.3), and the algorithm will converge on a local minimum in the parameter space. Although it cannot be proven that the solutions do reach the global minimum, the stability of the solutions obtained can be demonstrated empirically by using different random initial populations and evolving them in the same way. This is illustrated in section 4.2.3.

The best solution at the end of the GA stage is thus likely to be in the neighbourhood of the global optimum, but may not be a precise estimate of this optimum. To refine the solution for the stream brightness distribution, the best solution from the GA is used as the starting point for a more conventional line minimization routine (Powell's method, e.g. Press et al. 1992). In this way, the complementary strengths of the two optimization methods are exploited. The genetic algorithm performs an efficient search of the multi-dimensional optimization space because of its implicit parallelism, but the amount of computer time required to obtain a precise estimate of the global optimum is prohibitive. The line minimization routine, given a starting

point, will converge rapidly and with high precision to the optimum nearest that starting point. Therefore, the GA is used to place the solution in the neighbourhood of the global minimum and Powell's method is then used to refine the solution within this neighbourhood. Another example of the improvement of a GA solution using a line minimization routine can be seen in Potter, Hakala & Cropper (1998).

4.1.3 Stopping criteria

It is not possible to define a formal convergence criterion for the GA in terms of gradient information (e.g. in conventional ME optimization, one can ensure that the entropy has been maximized for a given value of λ by requiring the angle between the gradient of χ^2 and the gradient of the entropy sum to approach zero). This is because the GA does not make use of gradient information to improve its solutions from one generation to the next, but rather makes quasi-random jumps throughout the multi-dimensional space. The algorithm then breeds the solutions that give the smallest values of the fitness function to form the next generation of solutions. Certain stochastic convergence criteria have been proposed for GAs (e.g. Beasley, Bull & Martin 1993) but these are dependent on the specific algorithm used. The best one can do is to monitor the progress of the algorithm and to terminate it when the rate of improvement of the solutions from one generation to the next has decreased to a very low value. The stopping criterion used for the GA is the following: if the value of F does not improve by more than than 1 per cent over 20 successive generations, the algorithm is terminated. During the subsequent stage of the algorithm where the solution is refined using Powell's method, convergence is reached (in theory) when the local gradient of the parameter space is zero. In practice, the stopping criterion in Press et al. (1992) is used: the algorithm is terminated if the fractional decrease in F between successive iterations is less than a certain tolerance (a value of 10^{-5} was used).

The usual criterion for a good fit is $\chi^2 = N$, the number of data points in

the original light curve (this condition is used in other applications of ME image reconstruction, e.g. Cropper & Horne 1994). For synthetic data the criterion is usually satisfied after application of Powell's method. For real data, the solutions seldom reach $\chi^2 = N$. This is because the very steep changes in the eclipse profile (due to the ingress and egress of the accretion region) are not instantaneous, whereas the model assumes that the accretion regions are point sources. In the model, the ingress and egress of the accretion region are thus unresolved, irrespective of the phase resolution. A very slight misalignment between the model curve and a data point on the steep component of a real eclipse profile results in a significant contribution to χ^2. For real data, therefore, a 'good' fit is where $\chi^2/N \approx 3.0$. The alternative is to allocate artificially large errors to the light curve during the ingress and egress of the accretion region, in which case fits with $\chi^2 \lesssim N$ are possible.

4.1.4 Parameters

The fixed parameters used to model the brightness distribution of the accretion stream fall into two groups: parameters that determine the properties of the numerical algorithm, and the physical and geometric parameters that define the characteristics of the binary system and the accretion stream trajectory. The remaining set of parameters are those that are adjusted to minimize the fitness function F (equation 4.1) and thus produce the optimal solution: these are the brightnesses p_j of the emission points along the stream trajectory.

Parameters that determine the properties of the algorithm include the population size used in the GA, the mutation rate (described above), the number of generations (iterations) performed by the GA, and the value of the Lagrange multiplier λ used in the GA and in the line minimization routine.

The smoothness of the final solution is determined by the Lagrange multiplier λ in equation 4.1. If the value of λ is too small, the model light curve will fit noise features in the original data; if λ is too large, the model cannot fit the small-scale

features of the original data and the resulting stream brightness distribution will lack resolution. To find the balance between these two extremes, a value of λ is chosen such that the ME sum (the magnitude of the second sum in equation 4.1) is larger than χ^2 for the initial generations, and towards the end of the GA, χ^2 is larger than the ME sum. It is possible to find such a λ because the magnitudes of the two sums in equation 4.1 decrease at different rates during the GA. The same value of λ is then used for Powell's method. The range of values of λ allowed by the above criterion is large, and the precise value chosen is arbitrary within this range. Although there are no formal methods for choosing λ, it is fairly easy to find a suitable value by trial and error; this is demonstrated in section 4.2.5. We have tried other schemes for λ, such as using a value that evolves during the course of the GA (as used by Potter et al. 1998), but the results are not noticeably different to those obtained using a constant λ. We have thus opted for the simpler scheme.

The stream trajectory and the properties of the binary system are pre-set in each model calculation using various geometric and physical parameters. These include the mass ratio q of the two stars, the mass M_1 of the white dwarf (required to determine the radius of the white dwarf via equation 1.5 or 1.6) and the binary inclination i. The parameters that determine the accretion stream trajectory are the magnetic colatitude of the dipole (β), the magnetic longitude of the dipole field (ζ), and the radius R_μ at which the stream changes from a ballistic trajectory to follow a dipole field line. The number of emission points along the stream trajectory and the brightnesses of the points on the white dwarf that represent the accretion regions are also held constant during the optimization.

4.2 Tests with simulated data

The method was tested using synthesized data to confirm that the imaging technique can reproduce the stream brightness distribution using an eclipse profile in an unambiguous way. In model streams that accrete onto both poles, in particular, one has to

ensure that there is sufficient information in the eclipse profile to determine uniquely the distribution of brightness along both halves of the magnetically-channeled parts of the accretion stream.

A synthetic stream brightness distribution is constructed by manually assigning brightnesses to points along a pre-existing stream trajectory. A synthetic light curve is obtained by 'observing' the synthetic stream through an eclipse by the secondary star (given values for q and i). The synthetic light curve is used as an input for the optimizing algorithm. The stream brightness distribution produced by the algorithm is then compared to that of the original stream to assess the reliability of the method. Both two-pole and one-pole stream geometries are discussed, and the effects of increased noise and decreased phase resolution on the stream images are described.

4.2.1   Ideal test cases

I first establish that the method is able to retrieve information from an eclipse profile in the ideal case, i.e. when applied to a light curve with no added noise, very small uncertainties σ_i and a high phase resolution.

One-pole geometry

The input stream has a brightness enhancement at the junction between the ballistic trajectory and the magnetic trajectory. The motivation for choosing this brightness distribution is to check whether the optimizing algorithm is able to reproduce any brightening that might be associated with the threading region. The model parameters used are $R_\mu = 0.18a$, $i = 85.0°$, $q = 0.25$, $M_1 = 0.9$, $\beta = 30°$, $\zeta = 10°$ and a normalized brightness of 0.23 for the accretion region. The stream has a total of 127 emission points along its length. The size of the phase bins is $d\phi = 0.0001$: this corresponds to an integration time of $\sim 0.72\,$s in a binary with a $2\,$h orbital period (the effect of using larger phase bins is described in section 4.2.2).
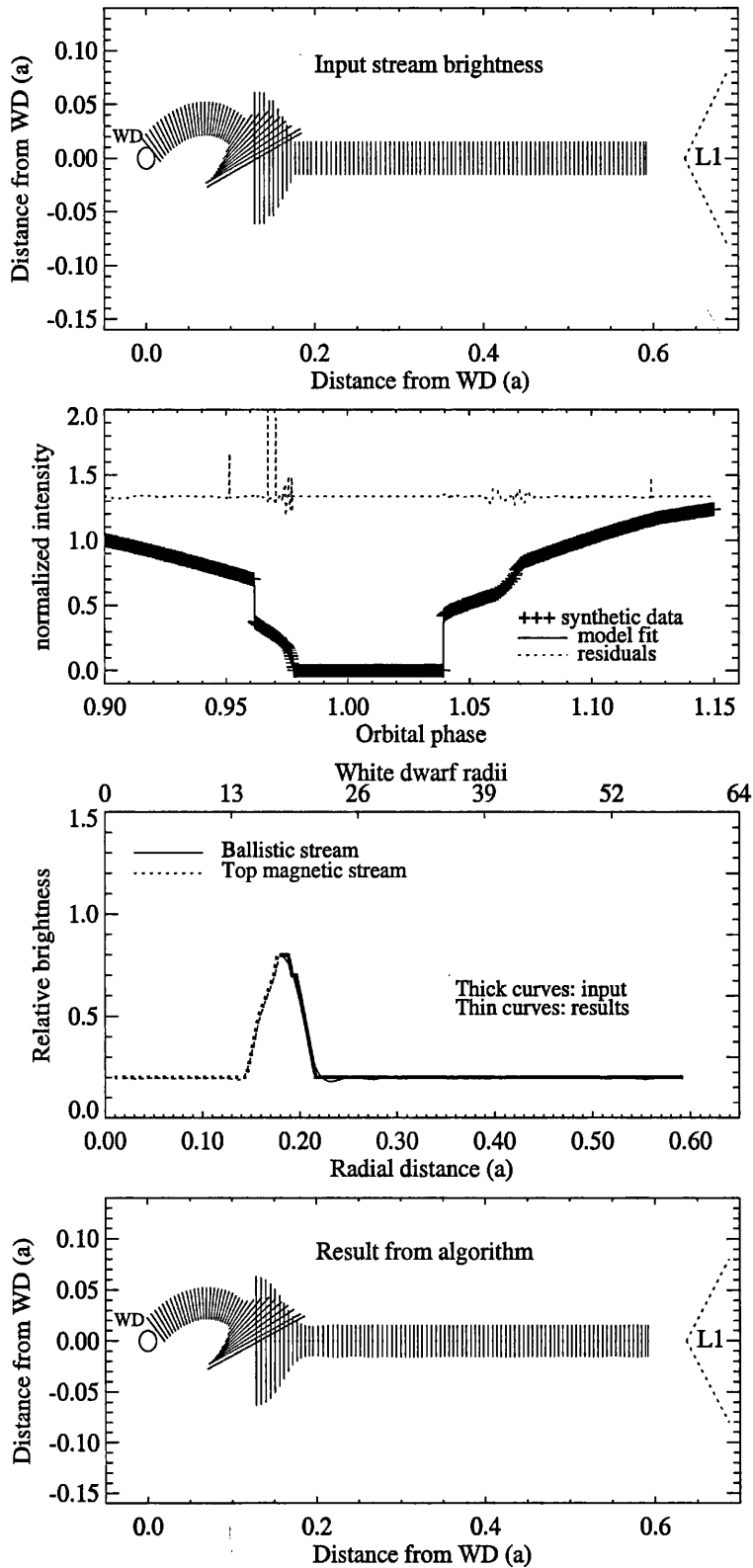
Figure 4.1: Simulation for a stream accreting onto one footpoint of a (dipole) magnetic field line. The details of the figure are described in the text in section 4.2.1.

The input stream is shown in the top panel of Fig. 4.1 projected onto the plane perpendicular to the orbital plane and passing through the centre of both stars. The brightness of each emission point is shown as a line through the point, perpendicular to the stream; the length of each line indicates the brightness of the point. The emission points along the magnetically-confined part of the stream appear more closely spaced than those on the ballistic stream due to the projection of the curved stream onto a flat plane; in reality the points are evenly spaced along the trajectory. The white dwarf is shown to scale as a circle (labelled 'WD'), and the secondary is shown (not to scale) to mark the position of the L1 point (labelled 'L1' on the figure). The second panel shows the synthetic light curve ('+' signs) and the model fit superimposed as a solid line. The uncertainties σ_i required in equation 4.1 are calculated using $\sigma_i = \text{model}_i/SNR$, where SNR is an assigned signal-to-noise ratio ($SNR = 1000$ was used for this ideal test case). No artificial noise is added to the synthetic light curve. The fit has $\chi^2/N = 0.13$. The dotted line shows the residuals $(\text{model}_i - \text{data}_i)/\sigma_i$ on a scale of -15 to 15, shifted vertically by $+7$ for clarity. The third panel of Fig. 4.1 shows the relative brightness of the stream as a function of radial distance from the white dwarf centre. The input values are shown as thick lines and the results are the superimposed thin lines. The model stream is shown in the bottom panel of Fig. 4.1 in the same projection as in the top panel. The main features of the input model are reproduced well by the algorithm. In particular, the position, width and amplitude of the feature at R_μ are reproduced. The third panel of Fig. 4.1 shows that the artefacts introduced by the algorithm (e.g. around $0.23a$) are at a very low level ($\lesssim 3$ per cent); it is difficult to distinguish between the input and the model stream brightness distributions.

Two-pole geometry

The simulated light curve is constructed using a synthetic stream with a brightening towards the L1 point and a brightness enhancement on the magnetic field line below the orbital plane (see Fig. 4.2). This test case was chosen to check whether the

method is capable of reconstructing a brightening near the L1 point which might arise as a result of irradiation of the secondary (as is observed in e.g. HU Aqr in its high state: Schwope et al. 1997). This test example also checks whether the method can reproduce bright regions on one of the two halves of the magnetically-channeled stream, and thus locate bright regions within the magnetosphere. The parameters used in the model are $R_\mu = 0.20$, $i = 85.0°$, $q = 0.25$, $M_1 = 0.9$, $\beta = 25°$, $\zeta = 10°$, a normalized brightness of 0.23 for the upper accretion region and 0.15 for the lower. The stream has a total of 197 emission points along its length. As in the previous simulation, the data have $d\phi = 0.0001$, and a signal-to-noise ratio of 1000. No noise is added to the synthetic light curve.

The model fit to the synthetic data is shown in the second panel of Fig. 4.2 and has $\chi^2/N = 0.51$. The model stream brightness distribution is shown in the bottom panel of Fig. 4.2: the position, amplitude and width of the main features of the input stream are reproduced well by the model. The artefacts introduced by the optimizing procedure are at a slightly higher level ($\lesssim 6$ per cent) than in the one-pole geometry simulation: the reason for this is explained in section 4.2.2.

4.2.2   The effect of noise and decreased phase resolution

For a given stream trajectory and a fixed number of emission points along the stream, there are two factors that affect the artefact level in the stream brightness distributions. These are the noise level in the light curve, and the phase resolution of the light curve.

First, the effect of reducing the phase resolution in the noiseless case is discussed, and then the effect of noise in light curve with a high phase resolution is described. Finally, I present the results from a noisy synthetic light curve at a reduced phase resolution.
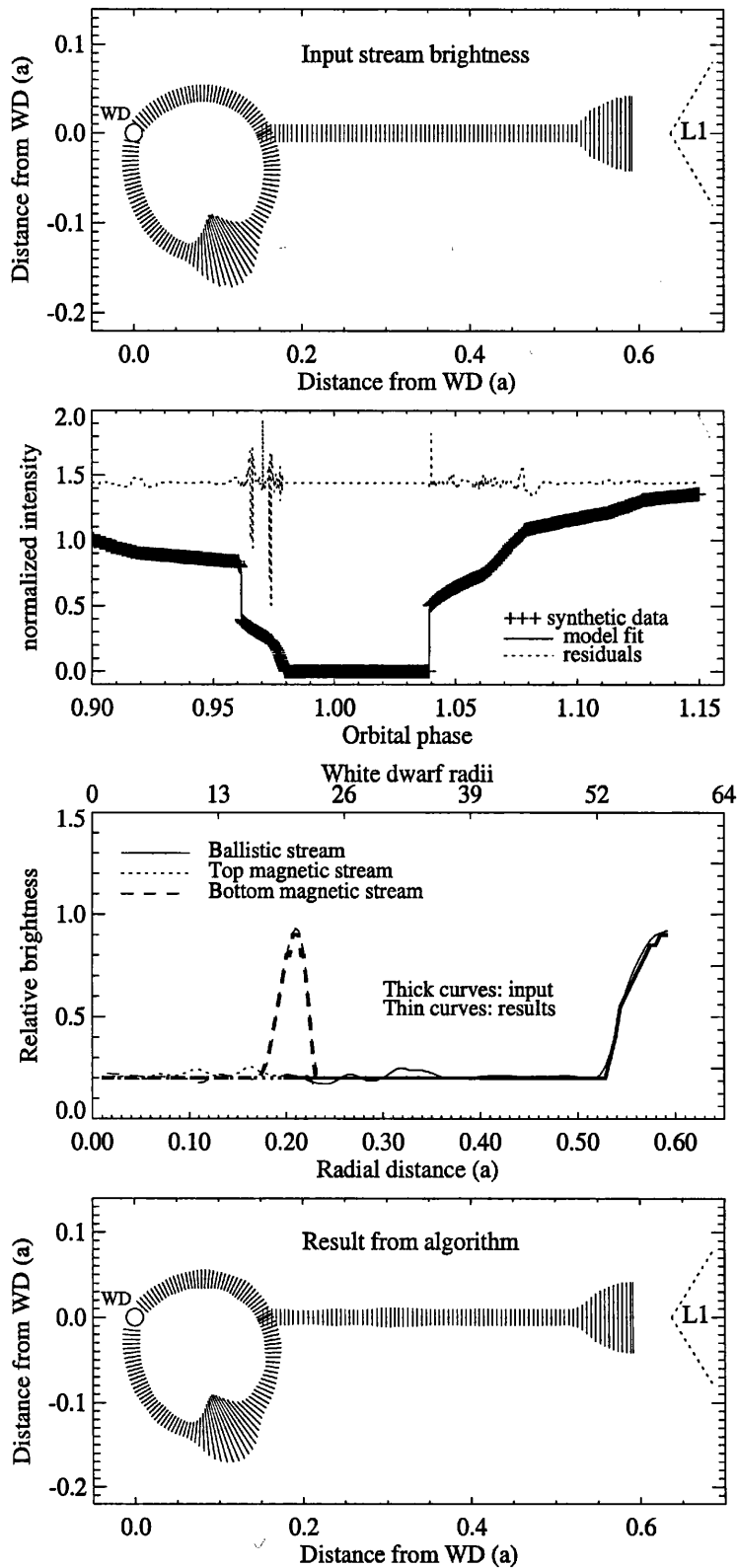
Figure 4.2: As for Fig. 4.1 but for a stream accreting onto both footpoints of a dipole magnetic field line. The residuals in the second panel are plotted on a scale of -15 to 15 and are shifted vertically for clarity.
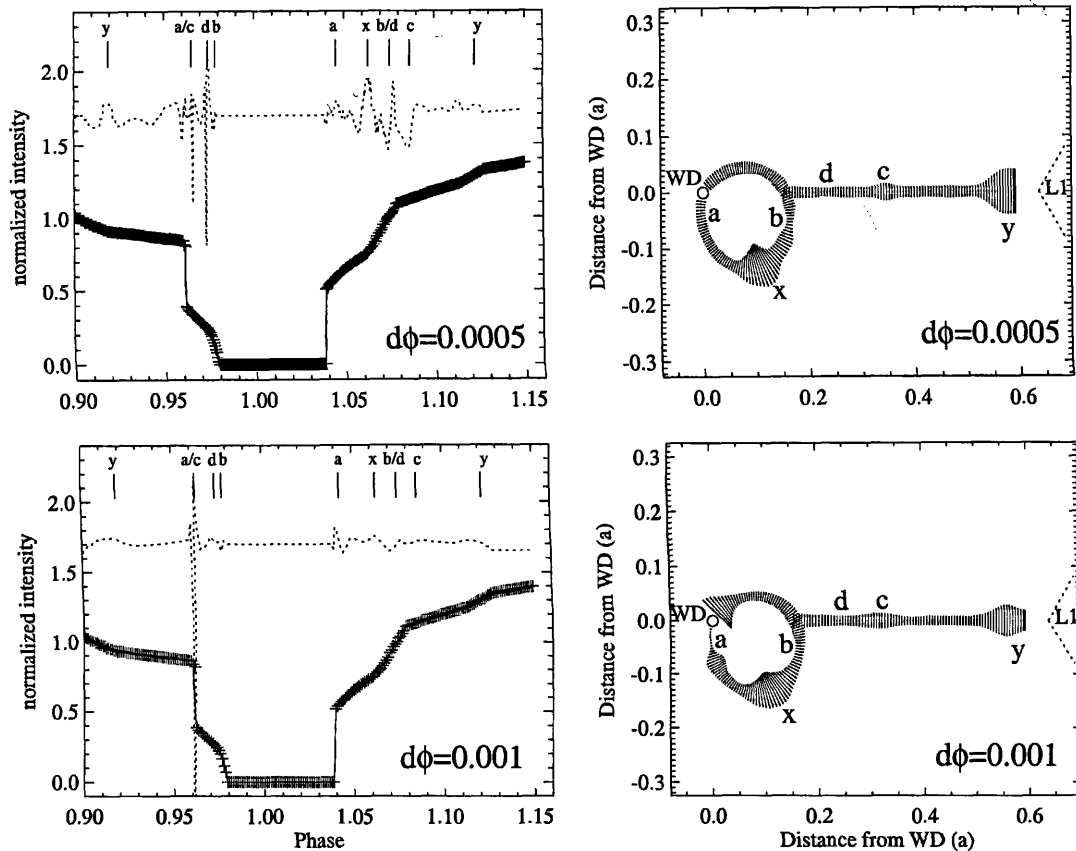
Figure 4.3: The effect of lowering the phase resolution of the light curve is shown for phase resolutions dϕ of 0.0005 (top) and 0.001 (bottom). As the phase resolution is decreased, the number and amplitude of the artefacts in the stream brightness distribution increases. The residuals are plotted on a scale of -30 to 30 (displaced vertically by +15 for clarity) for the dϕ = 0.0005 case, and -300 to 300 (displaced by +150) for the dϕ = 0.001 case. The regions of the stream labelled 'a', 'b', 'c', 'd', 'x' and 'y' are discussed in the text; the lines above the light curves indicate the approximate phases at which the stream points around 'a', 'b', 'c', 'd', 'x' and 'y' are eclipsed or come into view.

Reduced phase resolution

For a fixed number of emission points along the stream, the artefact number and amplitude is increased when the phase resolution is decreased. Fig. 4.3 contrasts the results for the two-pole stream example in section 4.2.1 at reduced phase resolutions $d\phi$ of 0.0005 and 0.001 ($d\phi = 0.0005$ corresponds to $\sim 4\,s$ and $d\phi = 0.001$ to $\sim 8\,s$ in a binary with $P_{orb} = 2\,h$). These results should be compared to the results in Fig. 4.2 where the light curve has $d\phi = 0.0001$. No noise is added to the light curves, and the data have a signal-to-noise of 1000. The fit to the data with $d\phi = 0.0005$ has $\chi^2/N = 6$, while the fit in the $d\phi = 0.001$ case is much worse, with $\chi^2/N = 85$. The model with $d\phi = 0.0005$ has located the bright regions of the input stream and has retrieved their amplitudes and shapes, but there is an excess of brightness around $0.33a$ (labelled 'c' in the top right-hand panel of Fig. 4.3) and a deficit on the lower half of the magnetic trajectory just below the junction between the ballistic and the magnetic trajectories (labelled 'b' on the top right-hand panel of Fig 4.3). With $d\phi = 0.001$ the artefact problem is worse: the model has located the two bright regions, but their shapes are distorted and their amplitudes are reduced. In addition, there is an excess of brightness on the ballistic stream near $0.33a$ (labelled 'c' on the bottom right-hand panel of Fig. 4.3), and the region near the white dwarf is badly misrepresented.

The artefacts in the brightness distributions, the distortion of the shapes of the bright regions on the stream, and the larger of the residuals in the fits can be explained by examining how well the model is able to resolve certain critical parts of the stream. These critical parts lie just below the orbital plane near the lower pole (labelled 'a' on the right-hand panels of Fig. 4.3), and just below the junction between the ballistic and the magnetic trajectories (labelled 'b'). The group of points at 'a' lies parallel to the limb of the secondary during eclipse ingress at phase $\phi \sim 0.965$, and the group of points at 'b' is parallel to the limb of the secondary during eclipse egress at $\phi \sim 1.075$. At these phases, several adjacent points at 'a' or

'b' are eclipsed or come into view in a single phase bin. As a result, the model is not able to assign brightnesses unambiguously to these points. Errors are propagated into the points on the ballistic stream that are eclipsed or that come into view in the same phase bin (in order to preserve the χ^2 of the model at that phase). For example, at $\phi \sim 0.965$ as the points at 'a' are eclipsed, the points along the ballistic trajectory at $\sim 0.32a$ (labelled 'c' on the right-hand panels of Fig. 4.3) are also being eclipsed. The points on the ballistic stream that come into view when the points at 'b' egress, are at $\sim 0.23a$ (labelled 'd' in Fig. 4.3). The brightnesses of emission points at 'c' and 'd' are thus not well-determined, and this accounts for the artefacts on the model streams at these positions (an excess of brightness at 'c' and diminished flux at 'd'). The largest residuals in the fit occur where the points 'a','b','c' and 'd' ingress and come into view: these phases are indicated by the relevant letters above the light curves in Fig. 4.3.

The artefacts on the low resolution $d\phi = 0.001$ model are particularly severe around the white dwarf, and the largest residuals occur in the light curve between $0.961 \lesssim \phi \lesssim 0.964$. This phase interval comprises just four phase bins during which 16 adjacent points just below the lower pole are eclipsed, the upper pole is eclipsed, and five points just above the upper pole are eclipsed. This large number of poorly-resolved points around the white dwarf leads to the spurious structure in the stream brightness distribution in this region, and hence to the poor fit to the light curve in the interval $0.961 \lesssim \phi \lesssim 0.964$.

The artefacts in the model stream are created as the algorithm attempts to preserve the χ^2 at a particular phase, but these artefacts result in a decrease of the *entropy* of the model light curve. This is because the knots of excess or diminished flux in the artefacts reduce the local smoothness of the stream brightness. Because the algorithm maximizes the entropy of the brightness distribution (by minimizing $-S$, see equation 4.1) as well as minimizing the χ^2 of the fit, the decrease in entropy caused by the artefacts must be compensated for by an increase in entropy elsewhere on the stream. This occurs at the bright region on the field line below the orbital

plane (labelled 'x' on the model streams). In the input stream (shown in the top panel of Fig. 4.2) this feature extends over 19 emission points and has a sharply peaked shape. In the low-resolution models, the feature is spread over a larger number of emission points, and is increasingly distorted (flattened) as the phase resolution is decreased. Large residuals in the model fits occur where this bright region is eclipsed and comes into view: these phases are labelled 'x' in Fig. 4.3 (the ingress of 'x' is not labelled due to lack of space: it occurs between the ingress of features 'd' and 'b'). The algorithm also smoothes and spreads out the feature near the L1 point in order to increase the entropy of the model stream: the ingress and egress of this feature are labelled 'y' in Fig. 4.3.

To check whether this explanation for the origin of the artefacts is correct, a fit was performed to a low phase resolution ($d\phi = 0.001$) eclipse profile generated using a stream where the emission points have a uniform brightness. The artefacts should disappear in this case, despite the low phase resolution. This is because the algorithm should not be able to compensate for the decrease in entropy (caused by artefacts) by smoothing other regions of the stream, since the stream brightness distribution is already the smoothest possible. Indeed, the algorithm does not produce artefacts on the model stream (see Fig. 4.4).

Lowering the phase resolution of the light curve thus has two main consequences: the mis-representation of the stream brightness at ambiguous points along the stream, and the smoothing of local extrema in the stream brightness distribution to compensate for the resulting decrease in entropy. Comparing the results of the $d\phi = 0.0005$ and $d\phi = 0.001$ models, it can be seen that that the quality and reliability of the model decreases dramatically if $d\phi \gtrsim 0.001$ for this number of emission points along the stream (see also section 4.2.2).

When applying the model to real data, it is possible to distinguish between artefacts and real brightenings along the stream. Once a model stream trajectory is found that produces acceptable fits to the original data, the ambiguous points in that stream can be identified. An analysis similar to the one above can then
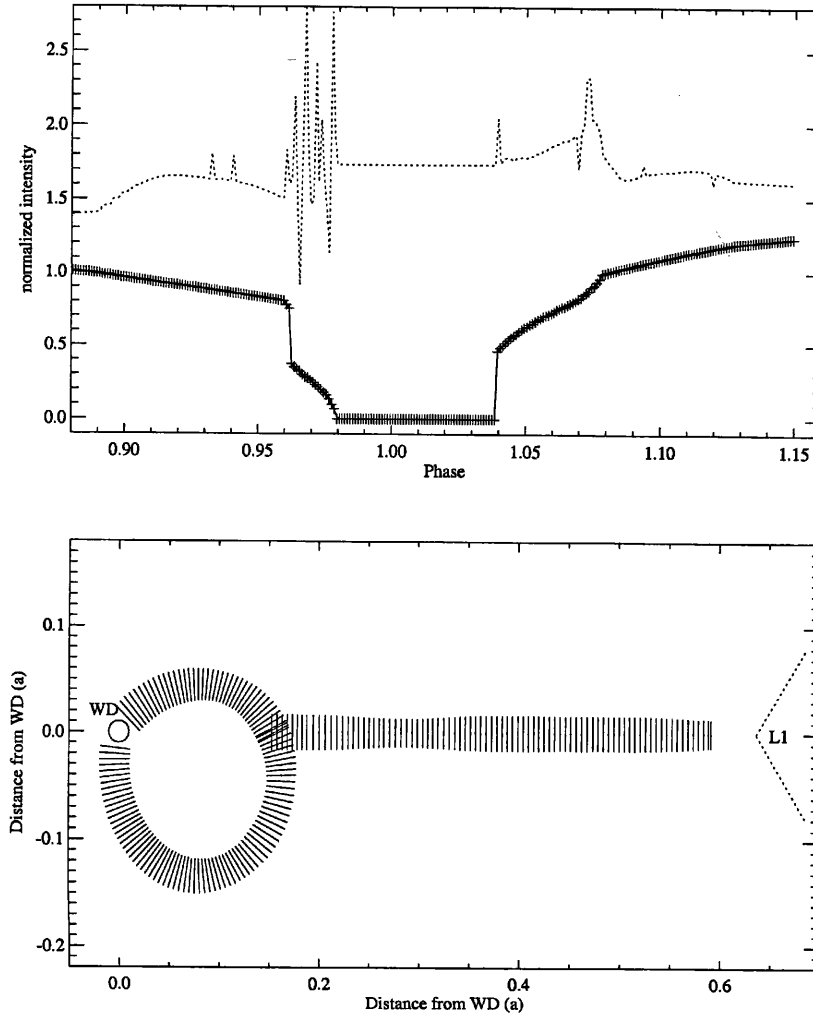
Figure 4.4: The lack of artefacts in the stream image derived from an eclipse profile generated at low phase resolution (top panel) but using a stream with a uniform brightness distribution. A low phase resolution tends to cause artefacts in the solution found by the algorithm. However, since this stream brightness distribution is already the smoothest possible, the algorithm cannot compensate for the decrease in entropy (caused by artefacts) by smoothing the stream. The resulting stream image (bottom panel) is thus free of artefacts.

be performed to identify the points on the stream that are likely to have poorly-determined brightnesses, and thus the regions of the stream that are likely to show artefacts.

The precise location of the ambiguous points on the stream depends on the system geometry i.e. the values of M_1, q, i, β, ζ and R_μ . For the stream trajectory assumed in section 4.2.1, the one-pole stream has no points that lie parallel to the limb of the secondary during ingress or egress. This explains why the artefact level in the one-pole case is much lower than in the two-pole example in section 4.2.1, even though the two light curves have the same phase resolution and neither have added noise.

Noisy data at high phase resolution

A noisy light curve is constructed by multiplying the normalized intensities of the synthetic light curve by a constant to convert them to 'counts' and then adding a background 'sky' value to each point. The sky contribution is assumed to be a constant fraction of the mean intensity of the light curve. The level of noise added to each point depends on its location in the eclipse profile. One of the dominant sources of noise in a polar light curve is the flickering from the accretion region; the phase intervals most affected by flickering are thus before the accretion region ingress and after its egress. The accretion stream ingress and the points during totality are not affected (since the accretion region is obscured during these phases) and therefore have a much lower noise level. For this reason, lower noise levels are assigned to the phases where the accretion region is obscured than when it is in view. The noise level for phases where the accretion region is in view is calculated using

$$\text{noise}_i = GRND \times \sqrt{\text{model}_i + \text{sky}} \qquad (4.4)$$

where $GRND$ is a random number taken from a Gaussian distribution with zero mean and unit variance; the noise level for the phases where the accretion region
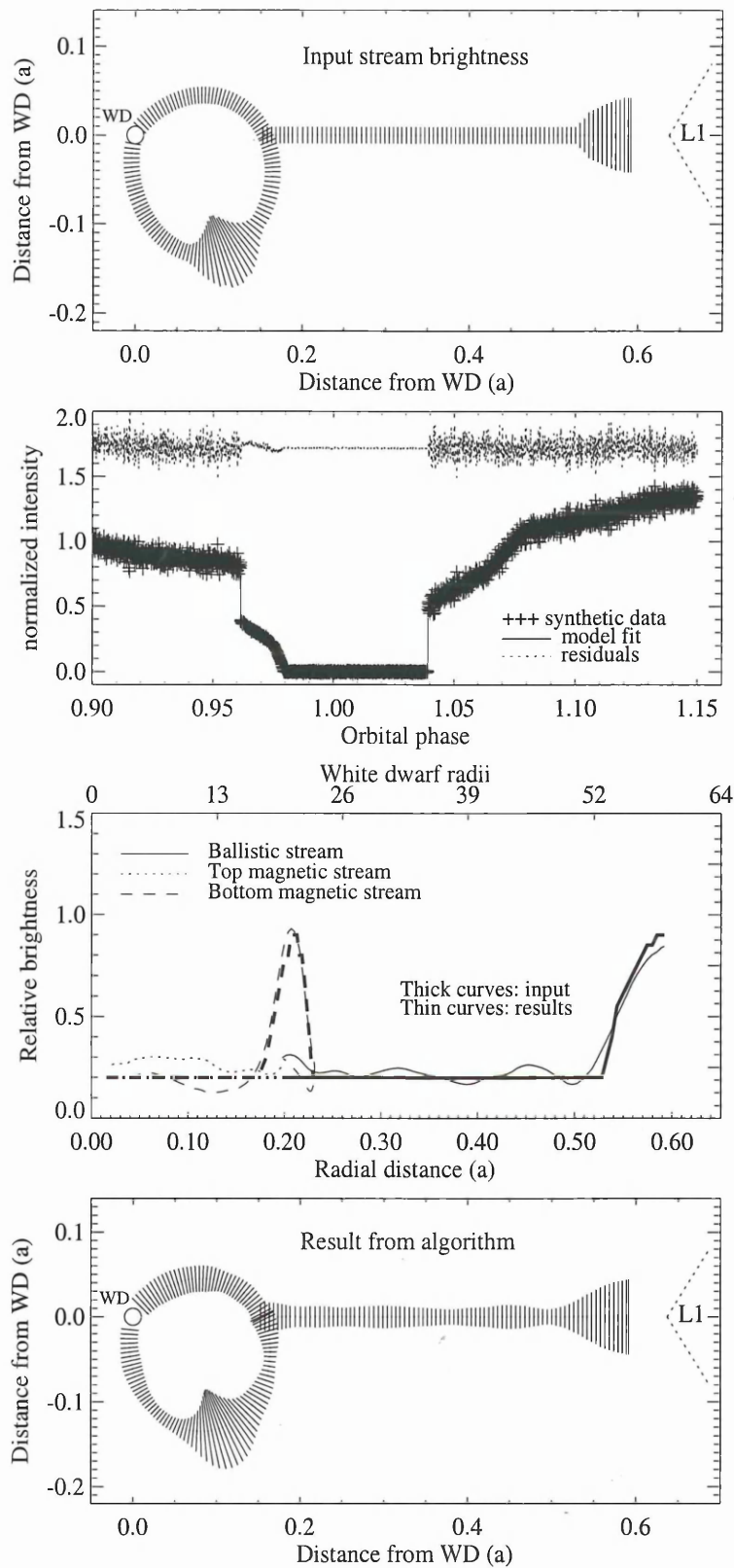
Figure 4.5: As for Fig. 4.2 but for a light curve with added noise (see text for details). The signal-to-noise ratio out of eclipse is approximately 20, and the phase resolution is $d\phi = 0.0001$. The residuals for the fit (second panel, dotted line) are plotted on a scale of -15 to 15 and are shifted vertically by $+11$ for clarity.

is obscured are assumed to be one quarter this quantity. Once the appropriate noise level is added to each model point, the light curve is re-normalized so that the pre-eclipse level is 1.0 as before.

Fig. 4.5 shows the results derived from a light curve with a phase resolution of $d\phi = 0.0001$ and with added noise such that the 'sky' background is equal to the mean intensity. The resulting signal-to-noise is ~ 20 out of eclipse and about 8 midway through the stream ingress. The fit to the input light curve has $\chi^2/N = 0.7$. There are some discrepancies between the input and the model streams. The model reproduces accurately the amplitude of the bright region below the orbital plane, but underestimates the brightness at L1; the two peaks differ in brightness by ~ 10 per cent while in the input stream they have the same relative brightness. The bright region near the L1 point is ~ 20 per cent wider than in the input stream. The number of artefacts has increased and their amplitude is at the ~ 10 per cent level. However, there are no artefacts in the model with amplitudes comparable to those of the bright peaks in the input stream. In general, the model has located accurately the bright regions on the stream, and has reproduced their shapes well.

Noisy data at reduced phase resolution

Fig. 4.6 shows the stream brightness distribution predicted for a light curve with $d\phi = 0.0007$ (about 5 s in a binary with $P_{orb} = 2$ h) and with added noise. The signal-to-noise ratio out of eclipse is ~ 20 and mid-way through the stream ingress is about 8. Despite the noise and the reduced phase resolution, the model fit to the light curve is good, with $\chi^2/N = 0.9$. The model stream brightness distribution in the fourth panel of Fig. 4.6 shows that the algorithm has located accurately the main features of the input stream, although their shapes and amplitudes are not exact. The shape of the bright region near L1 in the model has its peak brightness at $0.56a$ instead of at $0.58a$. The relative amplitudes of the two main features differ by 40 per cent, whereas they are the same in the input stream. The artefact level is 15 per cent, only slightly higher than in the noisy, high resolution case (section 4.2.2,
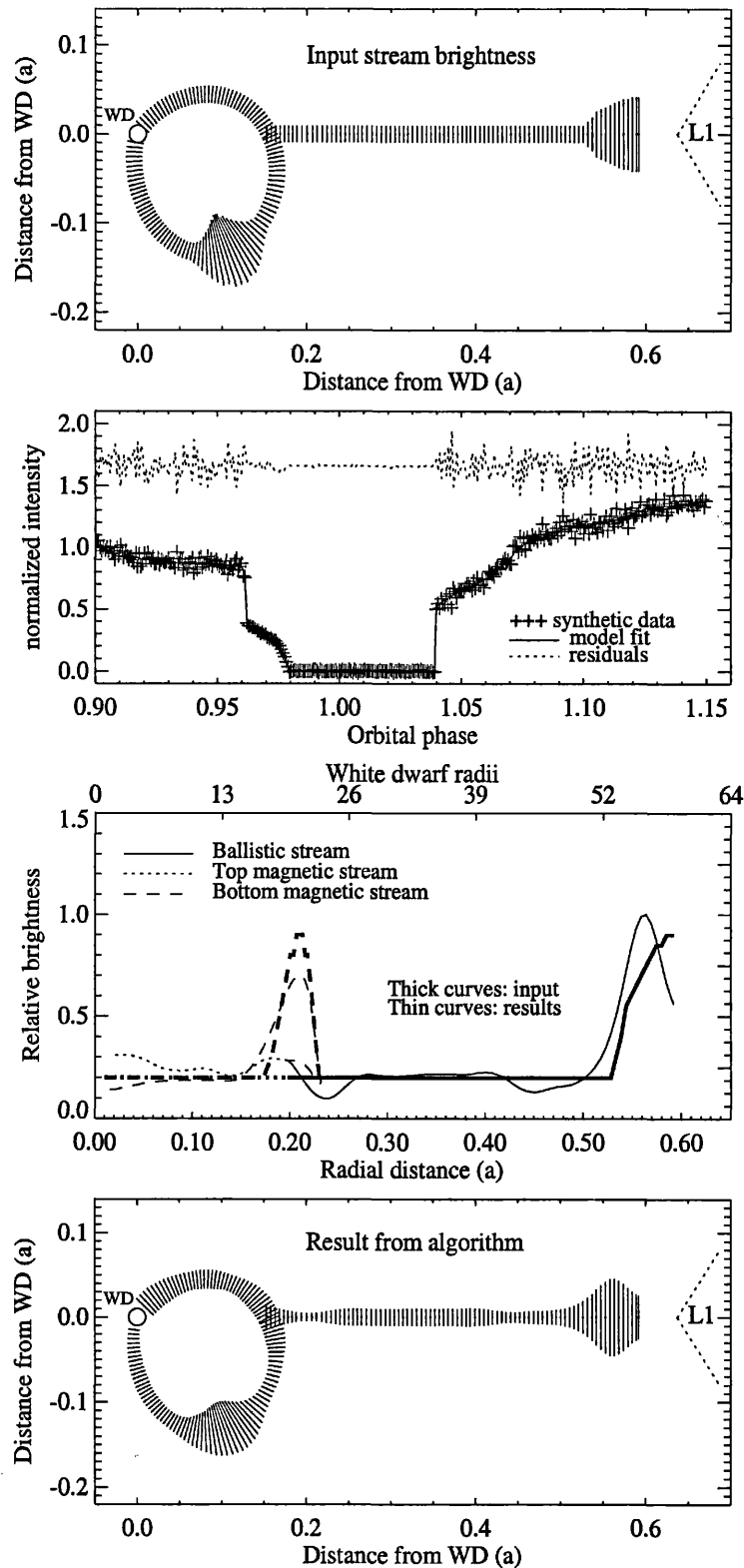
Figure 4.6: As for Fig. 4.2 but for a light curve with added noise and reduced phase resolution (see text for details). The signal-to-noise ratio out of eclipse is approximately 20, and the phase resolution is $d\phi = 0.0007$. The residuals in the second panel (dotted line) are plotted on a scale of -10 to 10 and have been shifted vertically by $+6$ for clarity.

Fig. 4.5). The algorithm has not added any spurious structure with amplitudes comparable to those of the bright regions in the input stream.

4.2.3 The stability of the solution

As mentioned in section 4.1.2, it is not possible to define a formal convergence criterion for the algorithm, since the GA does not improve the solutions at each stage by using gradient information. The stability of the solutions found by the algorithm can, however, be demonstrated by performing a number fits to a given eclipse profile, each starting from a different random population. The results of this exercise are shown in Fig. 4.7 for 50 fits to a noise-free eclipse profile and Fig. 4.8 for 50 fits to noisy data with a low phase resolution ($d\phi = 0.001$). In both cases, the algorithm finds essentially the same solution, irrespective of the initial parameter values. This is generally not the case with more traditional steepest descent-based optimization methods.

4.2.4 Ambiguity of the model geometry

When applying the method to real data, one may not know *a priori* whether to fit an eclipse profile with a model stream accreting onto one or onto two poles. I therefore investigated whether, on the basis of the quality of the fit alone, it is possible to determine which of the two accretion geometries is the better approximation for a given eclipse profile. To do this, a synthetic light curve constructed from a two-pole stream was fitted using a model stream accreting only at one pole; and conversely, a profile obtained from a one-pole geometry was fitted with a two-pole model.

Fig. 4.9 shows the results of applying a two-pole model to the single-pole light curve of section 4.2.1 (shown in the top panel of Fig. 4.1). The model should produce a two-pole model stream with no brightness on the field line below the orbital plane. The resulting two-pole model fit (top left panel of Fig. 4.9) has $\chi^2/N = 7.5$. The model stream (top right panel of Fig. 4.9) has placed the bulk of the brightness on
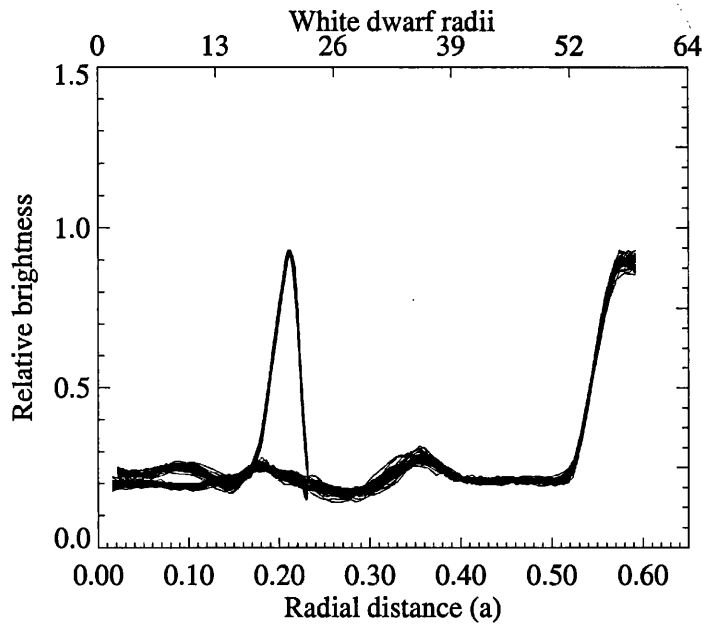
Figure 4.7: The stability of the solutions found by the optimizing algorithm for noiseless data; the solutions shown are for the two-pole geometry. The plot shows brightness versus radial distance from the white dwarf for 50 solutions of the stream brightness distribution where each solution was generated using a different random initial population. This demonstrates that the algorithm finds the same minimum of equation 4.1, irrespective of the starting values for the solution parameters.
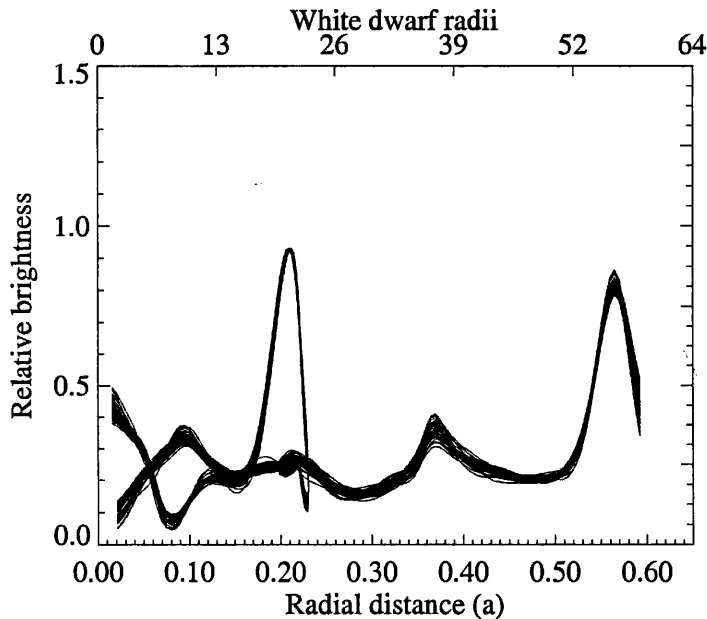
Figure 4.8: As Fig. 4.7, but for a noisy synthetic data set with $d\phi = 0.001$.

the magnetic trajectory above the orbital plane (as expected), but there is some lower-level emission on the field line below the orbital plane, particularly in the region marked 'a' on Fig. 4.9.

The feature at 'a' is eclipsed during the interval $0.970 \lesssim \phi \lesssim 0.975$ and comes into view again during $1.056 \lesssim \phi \lesssim 1.063$. During its ingress, the other points on the stream that are also being eclipsed are those on the upper field line just before R_μ (labelled 'b' on Fig. 4.9), and those on the ballistic stream around $0.32a$ (labelled 'c'). During the egress of the feature 'a', the only other points that are coming into view are the points on the upper magnetic trajectory at 'b' — the same points that are eclipsed with 'a' during $0.970 \lesssim \phi \lesssim 0.975$. There is a brightness deficit on the model stream at 'b', and also on the ballistic stream near 'c'. The reason for this is that the model cannot distinguish between the emission points at 'a' and the points at 'b', because they are eclipsed *and* come into view during the same phase intervals. The algorithm reassigns some of the brightness at 'b' (and to a lesser extent some of the brightness at 'c') to the region below the orbital plane at 'a' in order to preserve the χ^2 during these phases. This accounts for the deficit of

brightness around 'b' and 'c'. The artefact produced at 'a' decreases the entropy of the solution, since the stream is now less locally smooth. To compensate for this, the algorithm increases the entropy of the solution by smoothing out the bright region at the junction between the ballistic and the magnetic trajectories.

The points at 'a' are the only ones on the lower magnetic trajectory which are eclipsed *and* come into view during the same phase interval as one other region on the rest of the stream (in this case, the points at 'b'). These points can be identified in any model with a two-pole geometry, and any brightness assigned to the model stream in this region will be known to be uncertain.

The lower half of Fig. 4.9 shows the results obtained by applying a one-pole model to a two-pole light curve. A poor fit to the light curve is expected, since the light curve contains more information than the model being used to fit it. The fit is shown in the bottom left-hand panel of Fig 4.9 and is exceptionally poor, with $\chi^2/N = 3130$. This is two orders of magnitude worse than any of the fits obtained previously using light curves with reduced phase resolution or added noise. The poor fit, in particular the large systematic errors in the fit around $\phi=0.978$, 1.04 and 1.07, might prompt us to try the alternative two-pole model.

In principle therefore, on the basis of the model results alone, it is possible to determine whether to use a model with a two-pole or a one-pole geometry. However, in the examples discussed above, the correct values of M_1, q, i, β, ζ and R_μ have been known in advance. In practice the situation may be more complicated: there may be a combination of parameters that produce very poor fits even though the correct geometry is being used. In cases like this, other sources of information (e.g. polarization light curves) can be used to substantiate the choice of the model geometry.
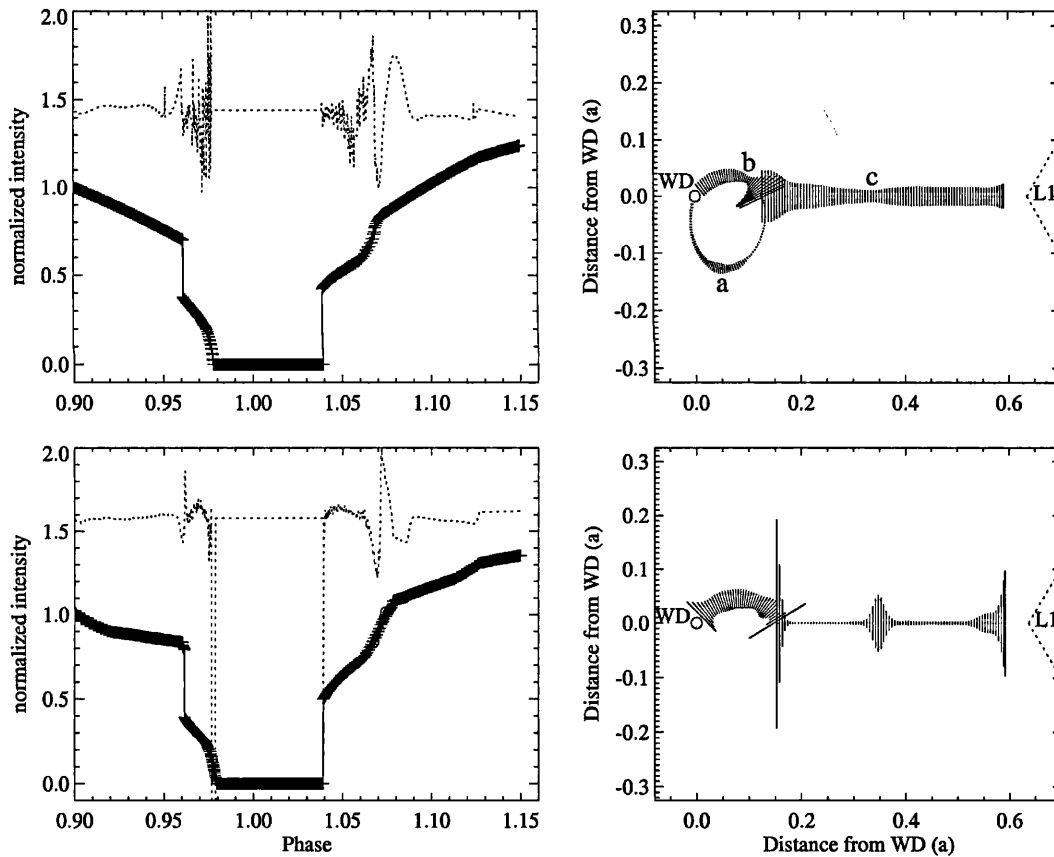
Figure 4.9: Top panel: fitting a synthetic light curve constructed from a stream accreting onto one pole, with a two-pole model stream. The model fit is on the left; the residuals of the fit are plotted on a scale of -30 to 30 and are displaced vertically by $+14$. The resulting stream brightness distribution is on the right. The regions of the stream labelled 'a', 'b' and 'c' are discussed in the text. Bottom panel: as for the top panel, but for a two-pole synthetic light curve fitted by a one-pole model. The residuals of the fit are plotted on a scale of -500 to 500 and are displaced by $+300$.

4.2.5   The choice of lambda

Fig. 4.10 shows the effect of using different values of λ in solutions computed using the noisy synthetic data in section 4.2.2 (the input stream is shown in the top panel of Fig. 4.5). These models illustrate the trade-off between minimizing χ^2 and maximizing the entropy by adjusting the value of λ. The stream image in the top panel of Fig 4.10 has $\lambda = 1.0 \times 10^6$, about an order of magnitude larger than necessary. With a large λ, the fitness function is dominated by the entropy term, and the algorithm attempts to increase the entropy (by minimizing $-S$) at the expense of χ^2. The input features of the stream are not reproduced accurately because they are local maxima in the stream image brightness distribution: the entropy in these parts of the stream is comparatively low and the algorithm smoothes preferentially these parts of the stream. The solution has $\chi^2/N = 1.2$. The stream image computed using $\lambda = 1.0 \times 10^5$ is shown in the middle panel: this value of λ is appropriate for these data (this is the solution presented in Fig. 4.5). The solution has $\chi^2/N = 0.7$, much better than the solution obtained using the large value of λ. The solution with too small a value of λ (bottom panel of Fig.4.10) has $\lambda = 1.0 \times 10^4$, about an order of magnitude smaller than required. The solution thus follows the original data (including the noise in the data) very closely, and has $\chi^2/N = 0.5$. The features of the input stream are discernible, but there are many artefacts in the stream distribution: these are the result of the model fitting the noise in the data as well as the original structure in the stream.

4.3   Discussion and conclusions

4.3.1   Information obtainable from the stream images

The stream imaging method in its current form is applicable to systems where the component of the eclipse due to the accretion stream can be distinguished from that due to the accretion region, and where the accretion stream contributes significantly
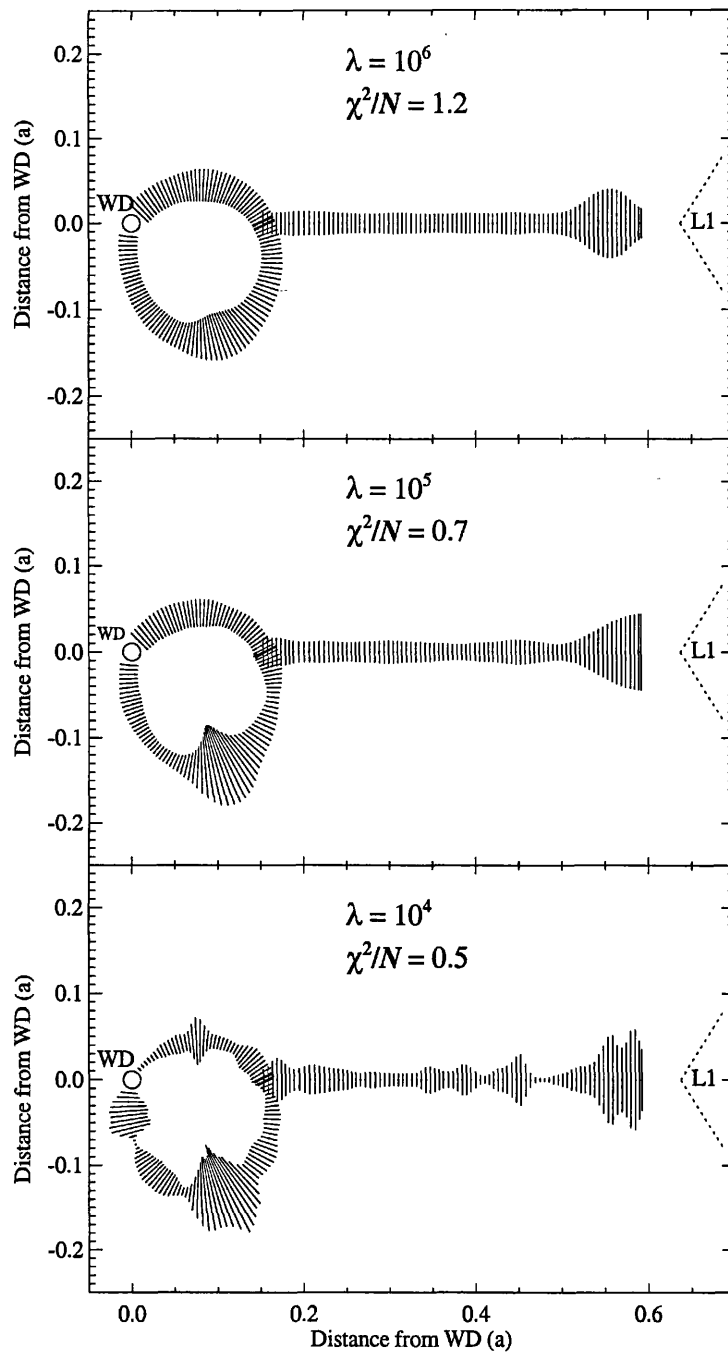
Figure 4.10: The effect of the Lagrange multiplier λ in solutions computed using the noisy synthetic data shown in Fig. 4.5. The top panel shows the stream image computed using a value of λ an order of magnitude too large: the entropy is maximized at the expense of χ^2. The lower panel shows a solution with λ an order of magnitude too small: the algorithm fits the noise in the data at the expense of the smoothness of the solution. The middle panel shows the solution calculated using an appropriate value of λ.

to the overall flux. The method performs well in the presence of noise, but requires a high phase resolution to reduce the artefact level in the model streams. If the data have a lower phase resolution it is necessary to reduce the number of emission points on the model stream accordingly.

The method is able to reconstruct features such as a brightening of the stream towards the L1 point (which may be expected if the secondary is strongly irradiated by the primary in a high accretion state), a bright region where the stream becomes threaded onto the field lines (as suggested by e.g. Lamb 1985 and Hameury et al. 1986) and can identify regions of enhanced emission at specific locations within the magnetosphere of the white dwarf. The stream brightness distributions can therefore be used to to extract information on such structures from real data, and thus provide observational constraints for the properties of the accretion stream. For example, once R_μ has been obtained from the model, an estimate of the mass transfer rate through the stream can be obtained by using equation 1.10.

Given the complexities of the accretion stream–magnetosphere interaction, it is unlikely that the accretion stream would follow precisely the trajectory used in these models. Although the models are unable to place constraints on the three-dimensional size of the threading region, they *can* show, for example, whether there is a bright region where threading is expected to occur. This would allow constraints to be placed on the extent of this region along the direction of the pre-set trajectory.

A dipole magnetic field has been assumed for the white dwarf. In some systems, the inclusion of higher order multipoles may be important to specify the stream trajectory (especially near the white dwarf). Higher order multipoles could easily be included in the model if warranted by the data.

Chapter 5

HU Aquarii — high accretion state

I now apply the stream imaging technique developed in the previous chapter to *UBVR* high speed photometry of the eclipsing polar HU Aquarii. The stream images are used to deduce the distribution of luminous matter between the secondary star and the white dwarf and to examine the changes in the stream over time and in different wavelengths. The stream images are also used to deduce the wavelength dependence of the emission from different sections of the stream and hence to examine the temperature structure of the stream.

A shortened version of this chapter has been submitted to *Monthly Notices of the Royal Astronomical Society* (Harrop-Allin et al. 1998b).

5.1 Observations

HU Aqr was observed during August 1993 when the system was in a high accretion state ($V \sim 15.1$). The data were acquired at a time resolution of 0.2 s (August 17 1993) or 0.1 s (August 18 and 20 1993) using the Stiening high-speed photometer mounted on the 2.1 m reflector at McDonald Observatory, Texas. The Stiening photometer is a four channel instrument enabling the simultaneous acquisition of
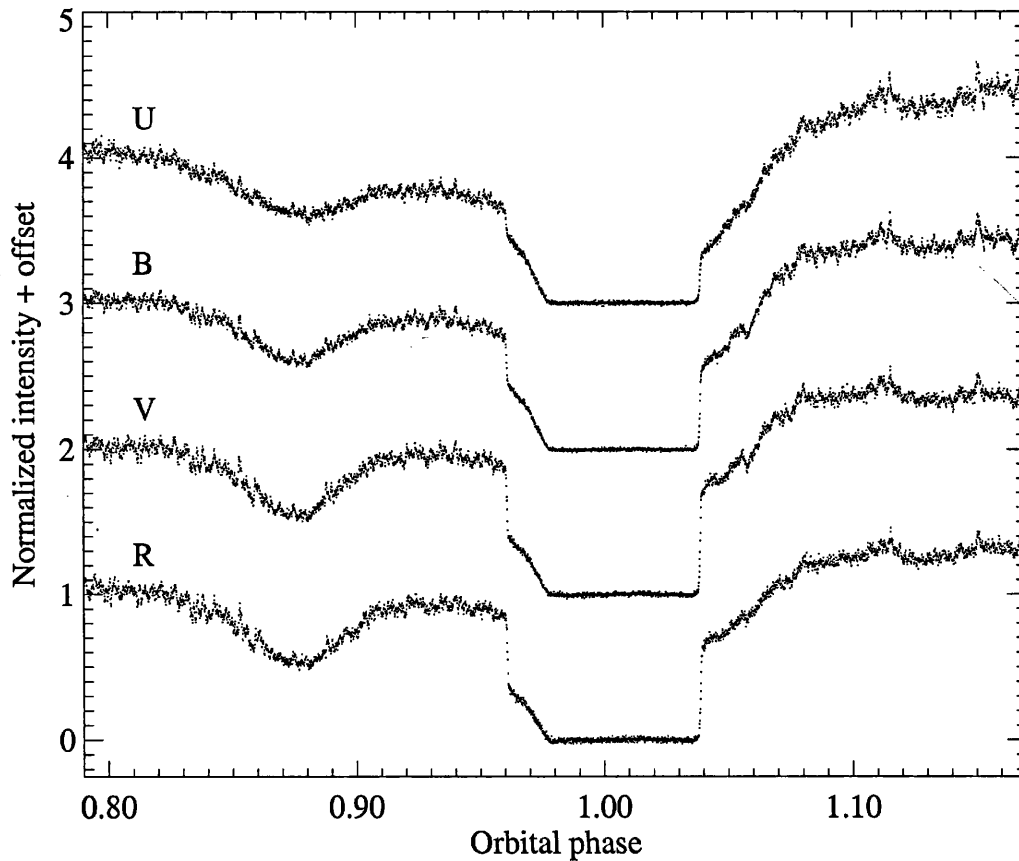
Figure 5.1: Phase-folded light curves of HU Aqr in a high accretion state for the period 17–20 August 1993. The orbital phase range shown includes the pre-eclipse absorption dip and the eclipse by the secondary star of the accretion region on the white dwarf and the accretion stream. The ordinate is in units of normalized intensity and the V, B and U light curves have been offset by 1.0, 2.0 and 3.0 for clarity.

high-speed photometry in four bands similar to the standard U, B, V and R band-passes (the incoming light is split using dichroics, and as a result the bandpasses are not standard because the wavelength ranges of adjacent filters do not overlap). A fifth photomultiplier mounted on an offset guider is used to monitor a comparison star. A log of observations is shown in Table 5.1. The cycle numbers quoted are with respect to the ephemeris in Schwope et al. (1997).

The data were reduced by subtracting the sky background, which was measured approximately every hour. Atmospheric extinction was corrected using extinction

Table 5.1: Log of observations: HU Aquarii high-speed photometry

Date	HJD start	Cycle number	Resolution (seconds)	Mean out-of-eclipse magnitude			
				U	B	V	R
17/08/1993	2449216.66614	3688	0.2	14.9	15.0	15.1	15.0
18/08/1993	2449217.63900	3699–3701	0.1	14.8	14.9	15.0	15.0
20/08/1993	2449219.63511	3722–3724	0.1	14.9	15.0	15.1	15.0

coefficients calculated for each the four bands from observations of ten standard stars. The data were binned to a phase resolution of dϕ=0.0001 (approximately 0.72 s) to reduce the noise due to flickering in the out-of-eclipse phases. The high state data contain seven eclipses of which five were considered suitable for application of the modelling technique (the remaining two were spoilt by non-photometric conditions and/or poor guiding). The data were calibrated using the standard star observations. The mean out-of-eclipse magnitudes in each waveband for the three nights are listed in Table 5.1; these were converted into spectral irradiance using the values quoted in Allen (1973) to enable comparisons between eclipses obtained on different nights and between features in different bandpasses.

5.2 Results

5.2.1 The eclipse profiles

Fig. 5.1 shows the mean light curves in each of the four bands in the (orbital) phase range ϕ =0.79–1.16. The eclipse by the secondary star occurs between phases $\sim$ 0.96 and $\sim$ 1.14, and a pronounced pre-eclipse dip is visible from $\phi \sim$ 0.83 to $\phi \sim$ 0.92. The eclipse profiles are asymmetric in all four bands, unlike those in low accretion states where the profile is asymmetric in U and R and more symmetric in B and

V (Hakala et al. 1993). The eclipse ingress comprises a rapid drop (lasting $\sim$ 5s in U, $\sim$ 8s in B and R, and $\sim$ 7s in V) followed by a more gradual fading to the mid-eclipse level (lasting $\sim$ 130s in U, $\sim$ 124s in B and V and 129s in R). Totality lasts for $\sim$ 445s in U and R, and $\sim$ 451s in B and V. The components of the eclipse egress are similar: a rapid rise in brightness lasting a few seconds, followed by a more gradual rise to the out-of-eclipse brightness level. The components of the eclipse profile have been identified by Hakala et al. (1993), Glenn et al. (1994) and Schwope et al. (1997): the steep ingress/egress is due to the cyclotron emitting accretion region where the stream impacts on the surface of the white dwarf, while the gradual ingress and egress components are due to the accretion stream. There is no obvious signature of the white dwarf photosphere in the eclipse profile (see later for a discussion). The accretion region is the source of the flickering (occurring on time scales of $\sim$ 10 − −30s) in the light curve: once the accretion region has been eclipsed (at $\phi \approx 0.962$), the stream ingress is free from flickering noise. The flickering variations of the accretion region probably indicate a non-homogeneous accretion flow incorporating denser blobs of material.

The eclipse width $\Delta\phi$ (measured here as the phase duration of the eclipse of the accretion region) is remarkably stable, not just throughout the duration of the high state data, but also between the high and low accretion state data. The mean value in the high state is $\Delta\phi = 0.0779 \pm 0.0002$ and is consistent with that in the low state: $\Delta\phi = 0.078 \pm 0.001$ (measured from data in Hakala et al. 1993; see also chapter 7). These measurements are also consistent with that of Schwope et al. (1997) who report an eclipse width of 584.6s (corresponding to $\Delta\phi = 0.0779$) from observations taken contemporaneously with the high state data.

The shape of the stream ingress component shows slight variations from cycle to cycle. If these changes are due to a varying distribution of emission along the accretion stream, the corresponding stream images should show accompanying changes (see section 5.3.2). The *duration* of the stream ingress, on the other hand, is constant in a given waveband. This is in contrast to the dramatic variability observed

Table 5.2: Mean spectral irradiances of the stream and the accretion region ('spot') components during high state eclipse ingress (the uncertainties quoted are 1-sigma errors), and the ratio of the fluxes of the stream to the spot flux. For comparison, the ratio of the stream flux to the spot flux in the low accretion state is listed; these values are taken from Hakala et al. (1993).

	spot $(10^{-15}\,\mathrm{erg\,cm^{-2}\,s^{-1}\,A^{-1}})$	stream $(10^{-15}\,\mathrm{erg\,cm^{-2}\,s^{-1}\,A^{-1}})$	high state ratio (stream/spot)	low state ratio (stream/spot)
U	0.6 ± 0.2	2.00 ± 0.02	~ 3.3	~ 0.67
B	2.0 ± 0.4	2.5 ± 0.2	~ 1.3	~ 0.19
V	1.6 ± 0.2	1.2 ± 0.1	~ 0.75	~ 0.03
R	0.8 ± 0.1	0.52 ± 0.08	~ 0.65	~ 0.45

by Glenn et al. (1994) where the accretion stream ingress duration increased by approximately one minute between two successive eclipses (see Fig. 2.8).

The relative brightnesses of the stream and accretion region components are functions of wavelength and of the accretion state of the system. The calibration of the high state data allows a direct comparison between the brightness of the stream and the accretion region in the four bands; the measurements of the brightnesses of the stream and spot components during the eclipse ingress are listed in Table 5.2. Table 5.2 also lists the ratio between the stream and the spot component fluxes in the four wavebands in both the high and the low state (see also chapter 7, section 7.1.1). In the high state, both the stream and the accretion region are brightest in B, while the accretion region is faintest in U and R, and the stream is faintest in R. The brightness of the accretion region in the four bands is roughly that expected for cyclotron emission in a magnetic field of $\sim 37\,\mathrm{MG}$ (as calculated for HU Aqr by Schwope et al. 1993 and Glenn et al. 1994), since the cyclotron intensity is expected to peak in the 4-6th harmonics (Wickramasinghe & Meggitt 1985).

In the high state the stream's contribution to the total emission in each of the

four bands is comparable to, and in U and B exceeds, the emission from the accretion region. In the low state, the stream is comparable in U to the accretion region. The fact that the stream contributes significantly to the system emission was stressed by Hakala et al. (1993) and Hakala (1995). HU Aqr is not the only system with a bright accretion stream in the optical. The unfiltered high state eclipse profile of UZ For in Bailey (1995) has a stream component that contributes approximately 55 per cent of the pre-eclipse brightness. The eclipse profiles of V2301 Oph presented in Barwig et al. (1994) also show bright stream components: the contributions to the out-of-eclipse level are ~ 53 per cent in U, B and V, and ~ 57 per cent in R. The possible origins of the bright emission from the accretion stream are discussed in section 8.3.

An interesting feature appears in the eclipse of cycle 3688 just after the accretion column egress (indicated on Fig. 5.2 by a bracket at the top of the plot): this is a sharp decrease in brightness between $\phi \approx 1.043$ and $\phi \approx 1.056$ during the stream egress component. The feature has a depth that matches closely an associated feature that occurs just before the accretion region ingress, between phases $\phi \approx 0.942$ and $\phi \approx 0.960$ (also indicated on Fig. 5.2 by a bracket). The depth of both these features varies from band to band in a consistent way. The dips are largest in B, and increasingly smaller in V, U and R. Interestingly, a similar feature has also been seen by Schwope et al. (1998; their figure 6) in contemporaneous data. Their data were obtained a day earlier (August 16 1993) than the cycle 3688 eclipse profile. In Schwope et al. (1998) the feature occurs between $\phi = 1.039$ and $\phi = 1.041$, slightly earlier in phase than in these observations, and is also deepest in B (Schwope et al. 1998 do not display the phases immediately preceding eclipse, so it is not known whether there is a dip corresponding to the pre-eclipse feature in their data). A possible origin for these features is discussed in section 5.4.2.

A persistent characteristic of the eclipse profiles is the change in gradient that occurs during the stream ingress component at $\phi \approx 0.970$ in all four wavebands. It is possible that this feature is the eclipse of a bright component of the system
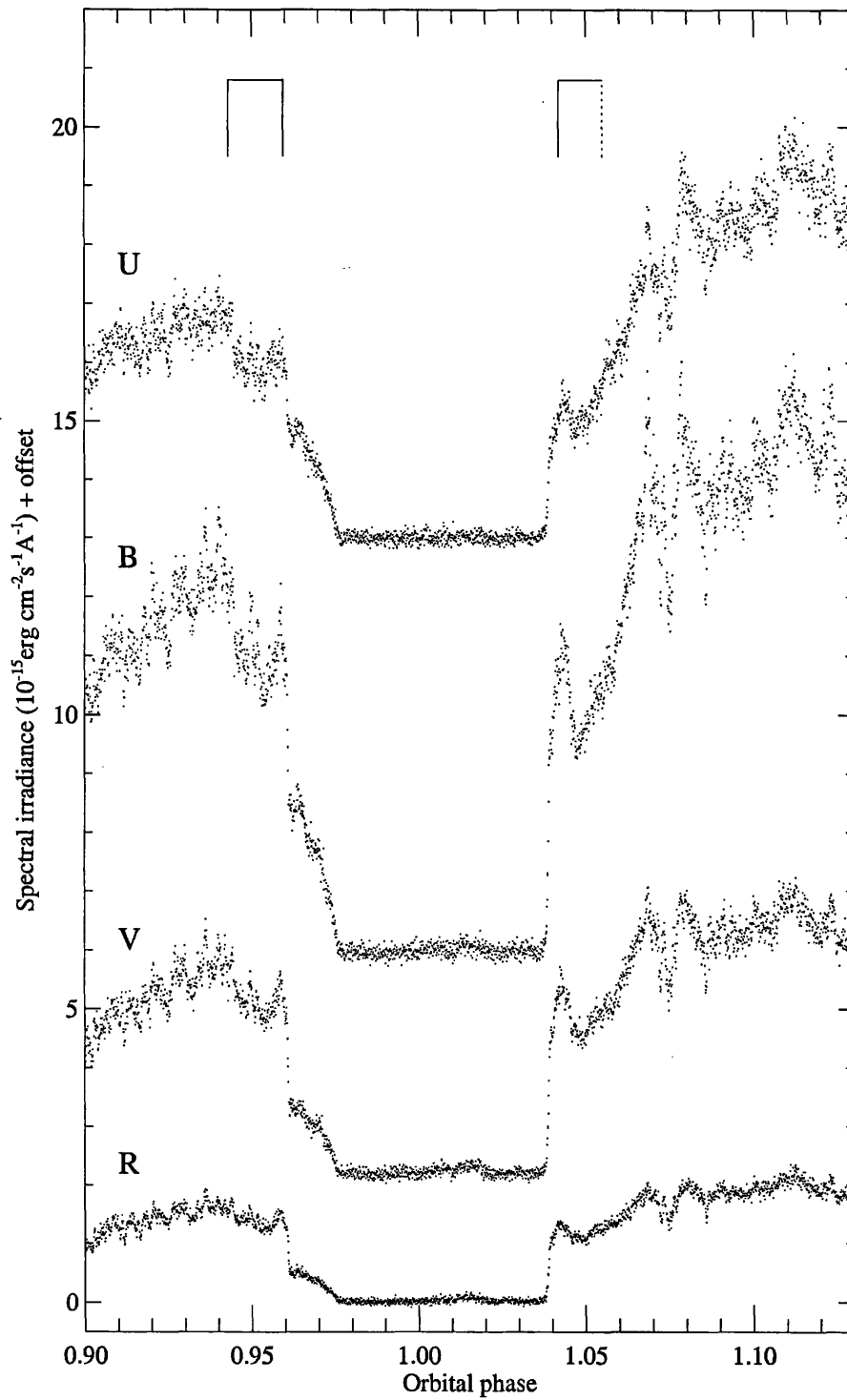
Figure 5.2: The eclipse profiles of cycle 3688, showing the suspected absorption features before and after eclipse. For clarity, the V, B and U data are offset by 2.2, 6.0 and $13.0 \times 10^{-15}\,\mathrm{erg\,cm^{-2}\,s^{-1}\,\mathring{A}^{-1}}$ respectively.

other than the accretion stream and the accretion region. An obvious candidate is the white dwarf photosphere, since its ingress and egress will straddle the accretion spot ingress and egress respectively (see, for example, the low state eclipses of UZ For: Bailey & Cropper 1991). The duration of the component between the accretion region ingress and before the gradient change is approximately 55 s. If this represents the lower limit to the duration of a white dwarf photosphere eclipse, a lower limit to the radius and thus an upper limit to the mass of the white dwarf can be deduced, given the inclination and the mass ratio of the system. For this calculation a mass ratio q of 0.25 was used, and i is taken to be 85° (these estimates for q and i are taken from Hakala et al. 1993, Glenn et al. 1994, Schwope et al. 1997 and section 5.3.2). The implied mass of the white dwarf for an eclipse duration of 55 s is less than $0.2 M_\odot$. This is unlikely, since estimates of the primary mass in HU Aqr by other authors are around $0.9 M_\odot$, and certainly more than $0.6 M_\odot$ (Hakala et al. 1993; Glenn et al. 1994). In addition, the mean primary mass of the sample of polars discussed in Cropper, Ramsay & Wu (1998) is $\sim 0.94 M_\odot$. The change in gradient during the stream ingress is therefore not due to the white dwarf but is instead caused by the non-uniform distribution of emission along the stream. This issue is explored in section 5.3.2.

Since the white dwarf photosphere *must* be present at some level in the eclipse profile, the data were examined to see whether such a component is evident. If the white dwarf photosphere does contribute significantly to the system brightness, any component due to the photosphere in the eclipse must be dealt with appropriately by the stream imaging model. First, the duration of the eclipse produced by the photosphere of the white dwarf in HU Aqr was calculated using the fact that the radius of a $0.9 M_\odot$ white dwarf is approximately $0.62 R_\odot$ (using equation 1.6). Using $q = 0.25$, $i = 85°$ and an orbital period of 2.083 h, the duration of the eclipse of the photosphere is found to be 25.4 s. This component, if present, will occur on either side of the accretion region ingress and egress. Around the spot ingress it is difficult to separate the photospheric component from that of the stream. At

eclipse egress, however, there is a good opportunity to isolate the photospheric component, because part of the photosphere should come into view at the end of eclipse totality and before the spot egress. Close inspection of the eclipse profiles around these phases ($1.038 \lesssim \phi \lesssim 1.039$) reveals that the longest possible duration for a photospheric component between totality and the rapid rise due to the egress of the accretion region is $\lesssim 6\,\mathrm{s}$ in U, and shorter in the other wavebands: $\lesssim 4\,\mathrm{s}$ in B and $\lesssim 3\,\mathrm{s}$ in V and R.

The relative duration of the photospheric component occurring before the spot egress to that afterwards depends on the position of the accretion region on the white dwarf. The position of the spot is given by the magnetic colatitude β of the dipole field, and its longitude ζ. The stream imaging models imply $\beta = 25°$ for HU Aqr in the high state (see section 5.3.2); this is in agreement with the value of β (also 25°) found by Schwope et al. (1997). The models do not constrain the value of ζ well (see later); a nominal $\zeta = 10°$ is used. Schwope et al. (1997) have $\zeta = 40°$. With $\zeta = 10°$, the length of the photosphere component before the spot egress is $\sim 12\,\mathrm{s}$: this is much longer than the 7 s observed in U. If $\zeta = 40°$, the predicted length of the component is even longer: 15 s. To produce a component of 6 s, ζ would have to be $-60°$, i.e. the accretion region would have to *trail* the line of centres between the two stars by a significant amount. No previous study of HU Aqr has found the accretion spot to lag the line of centres. It can thus be concluded that there is no significant photospheric component in the eclipse profiles, and that a white dwarf photospheric component may safely be omitted from the models.

5.2.2   The pre-eclipse dip

HU Aqr shows a conspicuous pre-eclipse dip in all four bandpasses (see Fig. 5.1). Using Gaussian fits, the dip centre is seen to change noticeably over the course of the run, moving to increasingly earlier phases as the run progresses. In cycle 3688, the dip centre occurs at $\phi \approx 0.883$ while in cycle 3724 the dip centre has moved to
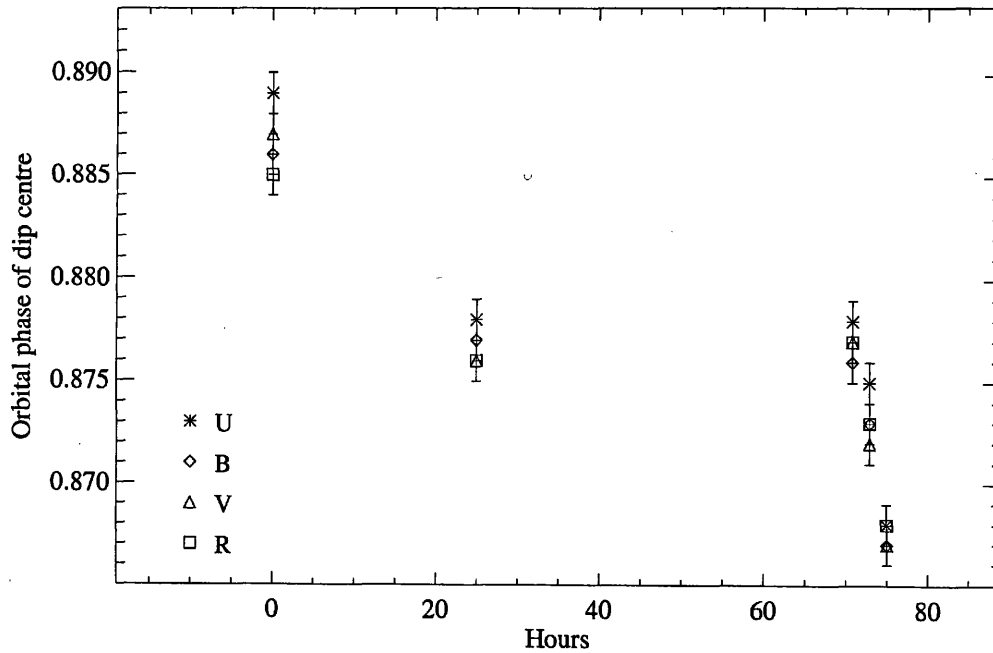
Figure 5.3: The variation in phase of the centre of the pre-eclipse dip at $\phi \sim 0.88$ with time and with wavelength. The horizontal axis shows time since mid-eclipse of cycle 3688. The dip occurs at increasingly earlier phases as the run progresses, and in each cycle occurs latest in U.

$\phi \approx 0.867$, a difference of approximately two minutes. Fig. 5.3 shows this trend (the uncertainties on the dip centre measurements represent the 99 per cent confidence level derived using the method of Lampton, Margon & Bowyer 1976). This change in phase corresponds to a change in azimuth of the absorbing material from $42°$ to $48°$ from the line of centres. Schwope et al. (1997) find the centre of the absorption dip at $\phi = 0.882 \pm 0.003$ measured from phase-folded B-band data from the period 16–18 August 1993, immediately preceding these observations. There appears to be no time-dependent variation of the 1-sigma width of the dip within the data. The dip width is consistently largest in U, and then similar in the other wavebands.

5.3   Indirect imaging of the accretion stream

5.3.1   Details of the model

Before the imaging procedure can be applied an assumption has to be made concerning the accretion geometry of the stream. The stream trajectory is pre-set for each model calculation and consists of a ballistic trajectory from the L1 point (Lubow & Shu 1975), followed by a magnetically-channeled trajectory which follows a dipole field line out of the orbital plane. It must be specified whether the the stream accretes onto one or onto both footpoints of the field line. In the case of HU Aqr, there is evidence for both one and two-pole accretion in the high state. On the one hand, the overall shape of the high state light curve is consistent with cyclotron beaming from a single pole (Schwope et al. 1995); also, Schwope et al. (1998) claim that HU Aqr has not shown signs of a second active pole. On the other hand, optical circular polarimetry (Hakala, unpublished data) obtained in June 1993 shows large negative (~ -7 per cent) and smaller positive (~ 3 per cent) excursions during the orbital period, implying accretion onto (at least) two regions of the white dwarf with opposite polarity. Although these polarization observations were not made simultaneously with the current data, the overall shape of the intensity light curve in June 1993 is very similar to the shape of the high state light curves from August of the same year (and is also similar to the high state light curves of Schwope et al. 1995 and Schwope et al. 1997). It could be argued, however, that the excursions of opposite sign in the circular polarization could be the result of viewing a tall accretion column from below. I have therefore performed model fits to the eclipse profiles using both one- and two-footpoint geometries.

To create images of the stream there are a number of parameters that are fixed for each model calculation (see section 4.1.4 for full details). These are physical parameters such as the primary mass M_1, the radius R_μ at which the accretion stream couples onto the magnetic field, the brightness of the accreting pole(s) and the mass ratio q of the system; and geometric parameters such as the binary inclination i, the

magnetic colatitude β of the dipole field, and its longitude ζ. Fortunately, estimates of these parameters are available from previous studies. Glenn et al. (1994) estimate $i = 85° \pm 5°$ based on optical polarimetry obtained in the low state, while Schwope et al. (1993) find $i = 85° \pm 1°$. From the eclipse geometry, Glenn et al. (1994) derive a primary mass of approximately $0.9\,M_\odot$. This is in agreement with Hakala et al. (1993): their figure 8 implies a white dwarf mass of $M_1 \sim 1\,M_\odot$ and a mass ratio $0.2 < q < 0.4$ for $80° < i < 85°$. Schwope et al. (1997) deduce $q = 0.25$ from a model of the narrow component of the optical emission lines. The structures in Doppler tomograms of the main optical emission lines are consistent with a stream with $\beta = 25°$, $\zeta = 40°$ and $q = 0.25$, while the coupling radius (with respect to the line emission) is in the range $0.20a \lesssim R_\mu \lesssim 0.29a$ (measured from figure 14 in Schwope et al. 1997), where a is the orbital separation of the two stars. The fractional brightness of the accretion region is estimated from the steep components in the eclipse profiles.

Uncertainties are assigned to the data according to the structures in the eclipse profile at various phases. At phases earlier than 0.891 and later than 1.128 the model stream is fully visible. During these phases, there is no information in the shape of the profile to establish the relative brightnesses of the emission points along the stream. Large uncertainties are thus assigned to the light curve during these phases. At $\phi = 0.891$, points along the free-fall part of the stream near the L1 point begin to be eclipsed. The accretion region is eclipsed during $0.960 \lesssim \phi \lesssim 0.962$, and the light curve is free from flickering noise from here until eclipse totality. During the stream ingress, the small uncertainties from the phase binning of the original data are used (i.e. the standard deviation of points in each 0.0001 phase bin). During $1.038 \lesssim \phi \lesssim 1.040$ the accretion region emerges, whereafter the stream emerges, becoming fully visible by $\phi \approx 1.128$. Large errors are assigned to the narrow phase intervals where the accretion region is eclipsed. This is because the steep changes in the eclipse profile are not instantaneous, whereas the model assumes that the accretion regions are point sources and that their eclipses are instantaneous. A

very slight misalignment between the model curve and a data point on the steep component of a real eclipse profile would result in a large contribution to χ^2. Large uncertainties are used in these phase ranges to prevent the χ^2 from being dominated by the steep components where there is no useful information about the distribution of emission along the stream. During the phases where the stream elements are being eclipsed or uncovered, but where there is still flickering noise, uncertainties must be assigned that are sufficiently large to prevent the model from fitting the flickering, but small enough so that underlying shape of the light curve is preserved. To do this, a running average over 50 points ($\Delta\phi = 0.005$) is calculated, and the mean of the residuals between the original brightnesses and the running average is used as an estimate of the uncertainty at each point. In cycle 3688, large errors are used during the dip features shown in Fig. 5.2. Since different stream points are being eclipsed during $0.942 \lesssim \phi \lesssim 0.960$ from those being uncovered during $1.043 \lesssim \phi \lesssim 1.056$, these structures cannot be accounted for by structures on the model stream, and do not therefore lie within the assumptions of the model.

5.3.2   The stream brightness distributions

Two-footpoint geometry

The results of the stream imaging procedure are shown in Fig. 5.4 to 5.8, using model streams that accrete onto both footpoints of a dipole field line. All the models are constructed using $q = 0.252$, $i = 85°$ and $\zeta = 10°$. The values of R_μ and β found for the five cycles fall into a fairly narrow range: $0.21\,a \leq R_\mu \leq 0.23\,a$ and $22° \leq \beta \leq 27°$. The quality of the fits can be assessed by examining the value of χ^2/N (where N is the number of data points in the eclipse profile), which is a measure of the reduced χ^2 of the fit. In all cases, $\chi^2/N \sim 1$.

The quality of the model fits is influenced more by some parameters than others. As a result, some parameter estimates are more secure within the framework of the model. The width of the accretion region eclipse and the phase duration of totality
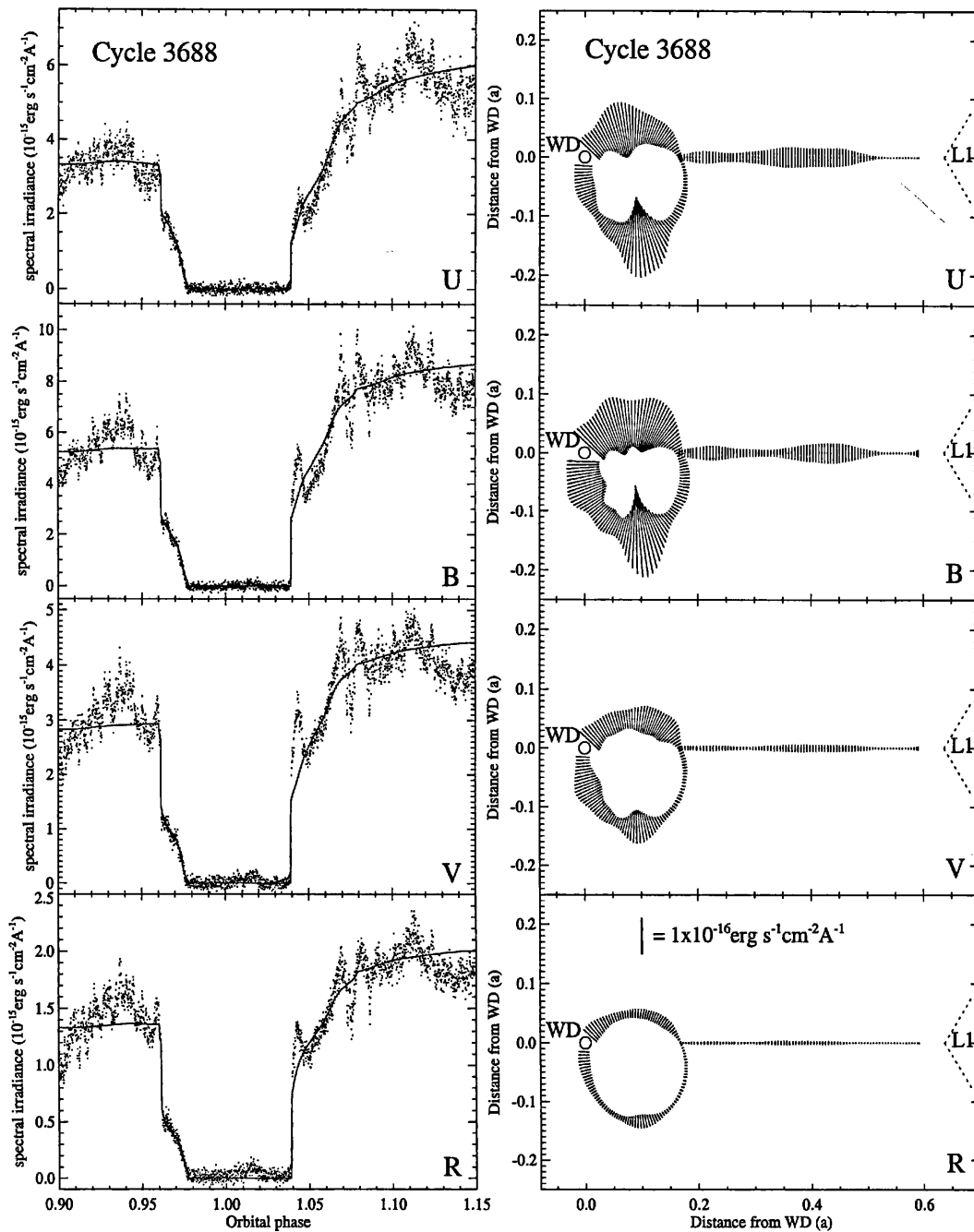
Figure 5.4: Model eclipse profiles and the corresponding images of the accretion stream for cycle 3688, using a stream that accretes onto both footpoints of a dipole field line. The stream images are shown projected onto the plane perpendicular to the orbital plane and passing through the centre of both stars (the $x - z$ plane). The brightness of each emission point is shown as a line through the point, perpendicular to the stream; the length of each line indicates the brightness of the point. The white dwarf is shown to scale as a circle (labelled 'WD'), and the secondary is shown (not to scale) to mark the position of the L1 point (labelled 'L1').
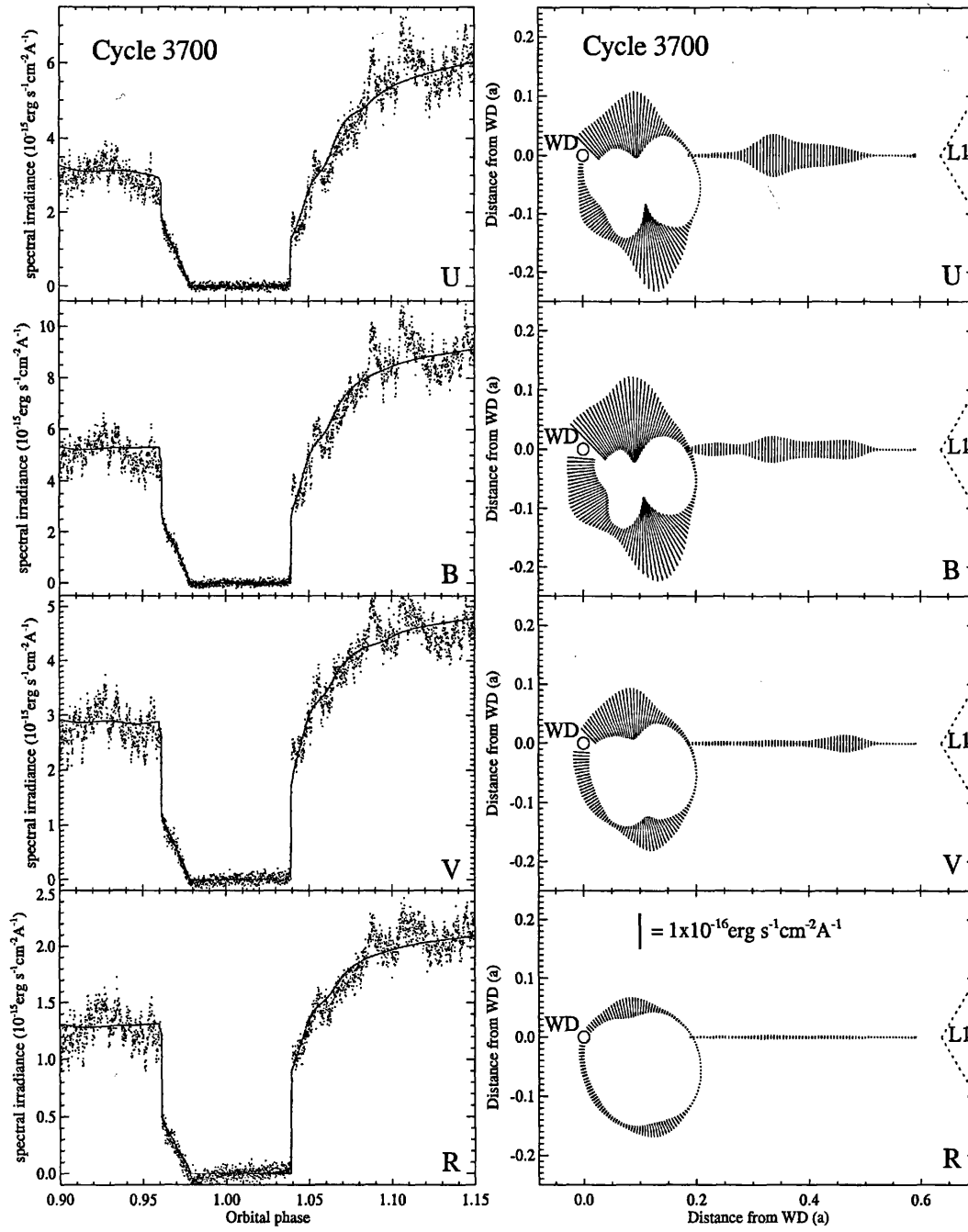
Figure 5.5: As Fig. 5.4 but for cycle 3700.
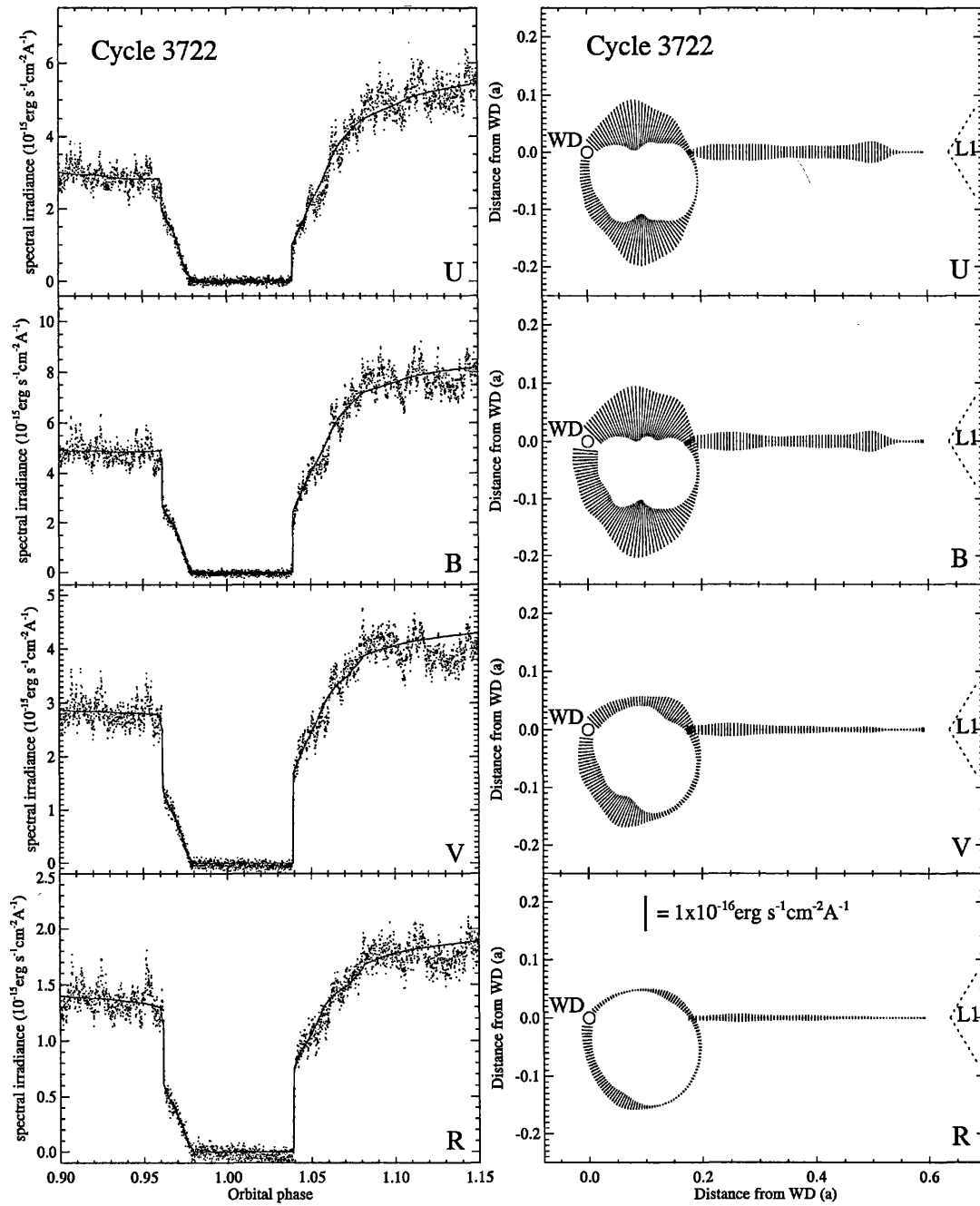
Figure 5.6: As Fig. 5.4 but for cycle 3722.
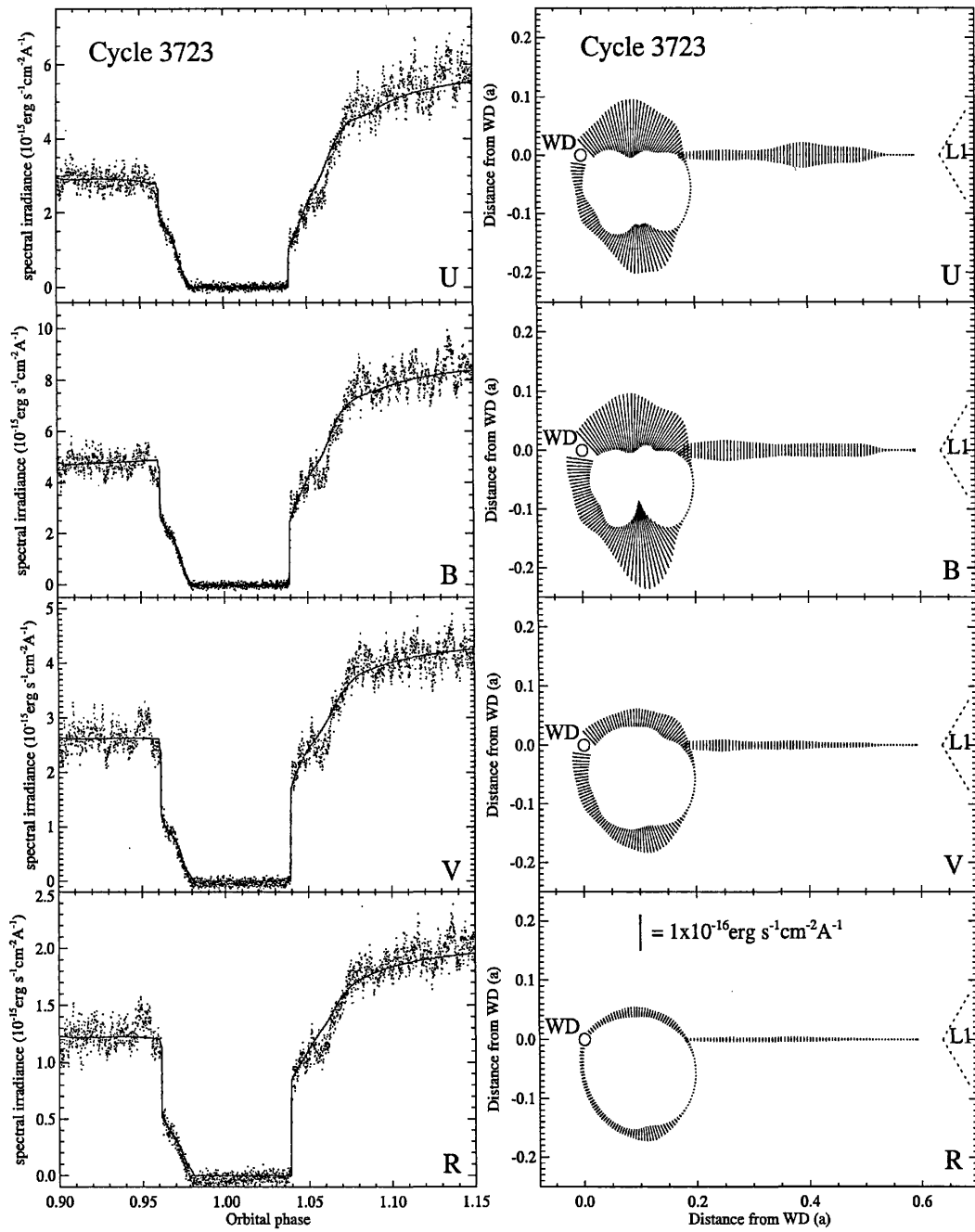
Figure 5.7: As Fig. 5.4 but for cycle 3723.
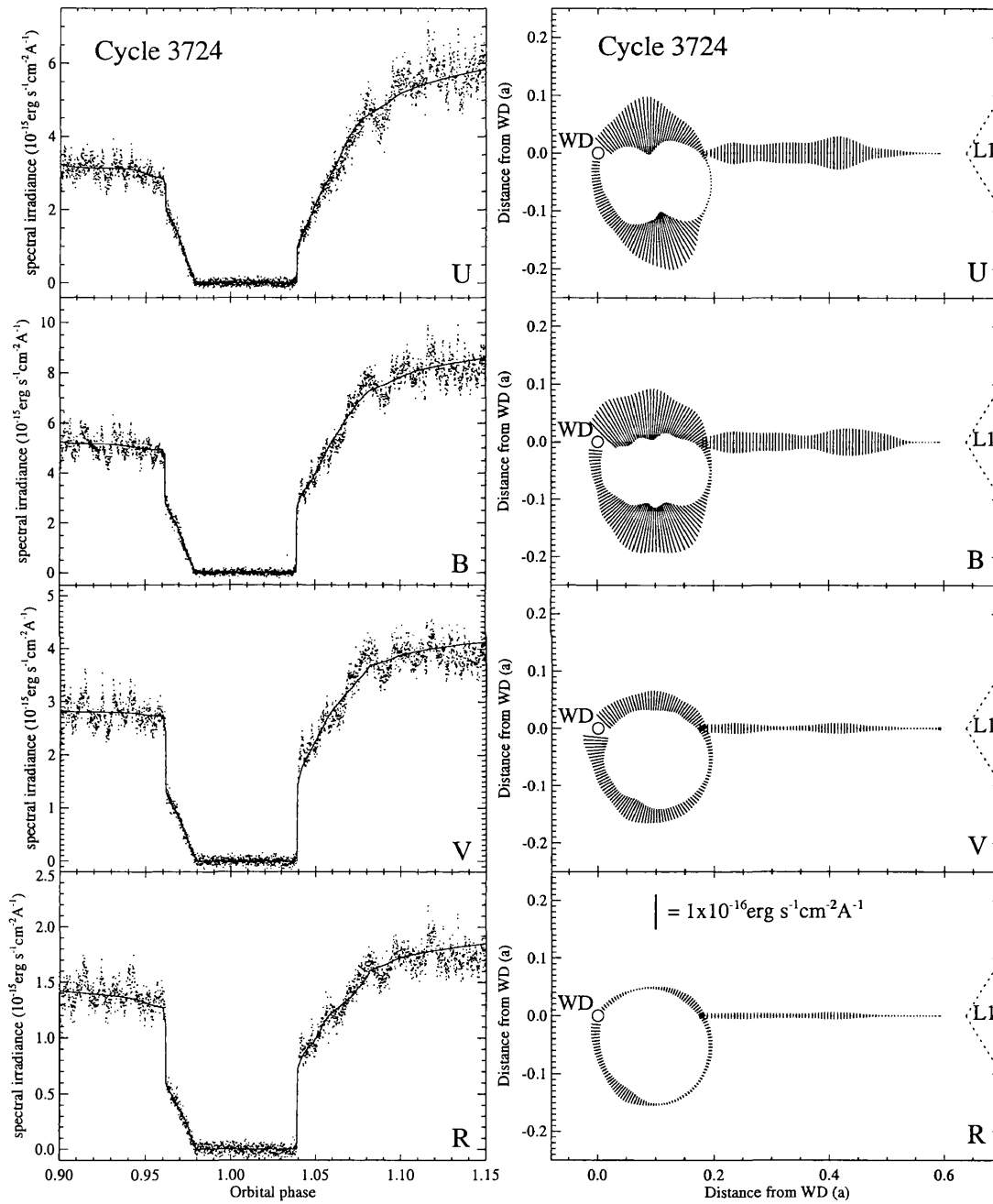
Figure 5.8: As Fig. 5.4 but for cycle 3724.
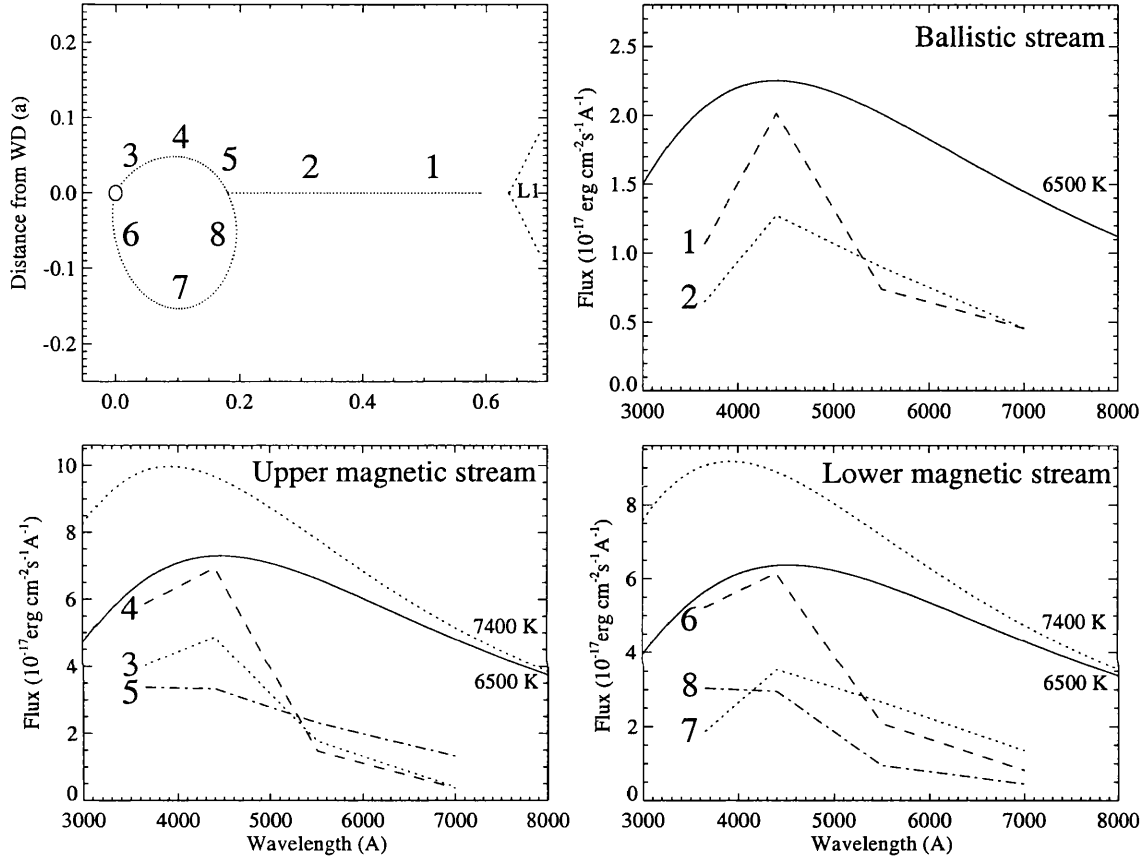
Figure 5.9: The wavelength dependence of the stream brightness distributions for cycle 3723, using the two-footpoint geometry (similar results are found for the other four cycles). The stream is divided into eight sections (top left panel) and the average flux per stream emission point in each section is plotted in the four wavebands for each of the eight sections of the stream. In most stream sections, the peak flux occurs in B. However, in sections 5 and 8, immediately adjacent to the coupling radius on the magnetically-channeled portion of the stream, the fluxes in U and B are comparable. Blackbody curves for temperatures of $6500\,\mathrm{K}$ and $7400\,\mathrm{K}$ are shown for illustration.

are very sensitive to small changes in q and i: acceptable fits to the eclipse profiles from all five cycles were obtained using $q = 0.252$ and $i = 85°$. The precise phase at which the model reaches totality is governed by β and R_μ and to a lesser extent by ζ. It was not necessary to adjust ζ for each model fit, and a constant $10°$ was used throughout; values in the range $0°–30°$ produce similar fits. Unlike ζ, small changes in the values of β and R_μ have a noticeable effect on the phase at which the model reaches totality. Since totality occurs within the narrow range $0.9755 < \phi < 0.9765$ in all observed cycles, β and R_μ are well-determined within the model. The range of values found for R_μ imply an angle between the magnetic part of the stream and the line of centres in the range $39–41°$. There appear to be no systematic trends in the variations of either R_μ or β over the course of the observations.

The geometric parameters of the model describe a magnetic field geometry and an orbital inclination such that the lower accreting pole (i.e. the pole on the opposite side of the orbital plane as the observer) is occulted by the white dwarf throughout the phases of interest. As a result, the only way in which the brightness chosen for the lower pole itself influences the stream model is due to the enforced continuity (by the regularisation term in the optimizing function, equation 4.1) with the stream emission points in its immediate neighbourhood. The steep components in the eclipse profiles and in the model fits are produced by the upper pole only. For these reasons, the value used for the fractional lower pole brightness, 0.10, is not constrained by the model. There are no obvious trends with time in the upper pole brightnesses in a given waveband.

There are several common features in the stream brightness distributions in the four wavebands and the five cycles spanned by the observations (Fig. 5.4 to Fig. 5.8). The emission is clearly not uniform along the stream, nor is it a simple function of the radial distance from the white dwarf. Rather, there are regions of the stream with localised brightness enhancements, particularly within the magnetosphere. In all model streams there is very little emission on the lower half of the magnetic part of the stream close to R_μ. There is, however, a very bright region on this half of the

stream closer to the white dwarf. This is a persistent feature in the two-footpoint stream models in all cycles. Interestingly, there is no obvious brightening of the stream as it approaches either the threading region or the white dwarf.

To investigate the wavelength dependence of the stream images, the stream is divided into eight sections and the average flux per stream emission point in each section is examined in turn. The ballistic stream is divided into two sections (of equal length), while the magnetic stream above and below the orbital plane is divided into three sections each (see Fig. 5.9). In all stream sections apart from the two sections on the magnetic field line immediately adjacent to R_μ, and all cycles, the stream flux (in $\mathrm{erg\,cm^{-2}\,s^{-1}\,\AA^{-1}}$) is highest in B and successively lower in U, V and R. In four of the five cycles, the stream flux is comparable in U and B in the two sections of the stream adjacent to R_μ (labelled '5' and '8' in Fig. 5.9). A possible explanation for this is outlined in section 8.3.

One-footpoint geometry

Fig. 5.10 to Fig. 5.14 show the model fits and stream images for the five cycles, using a stream that accretes onto the footpoint of the field line above the orbital plane only. The values for χ^2/N for the one-footpoint model eclipses are ~ 1.3, slightly higher than for the two-footpoint models. As for the models with two-pole geometry, the best fits for all five cycles are obtained using $q = 0.252$ and $i = 85°$. The magnetic colatitude β is not as well-determined as for the models using two-footpoint geometry: changes of up to $5°$ from the nominal $30°$ value (used for all fits) result in changes in χ^2/N of less than 0.1. The value of ζ used for all five cycles was $10°$, although (as before) fits of similar quality are obtained with ζ in the range $0°$–$30°$. There are no obvious trends in the fractional brightness of the accretion region with time in a given waveband. The R_μ values, on the other hand, decrease steadily as the run progresses: the fit for cycle 3688 requires $R_\mu = 0.20$ and the fit for cycle 3724 has $R_\mu = 0.17$. This corresponds to an increase in the angle between the magnetic part of the stream and the line of centres from $42°$ to $47°$.
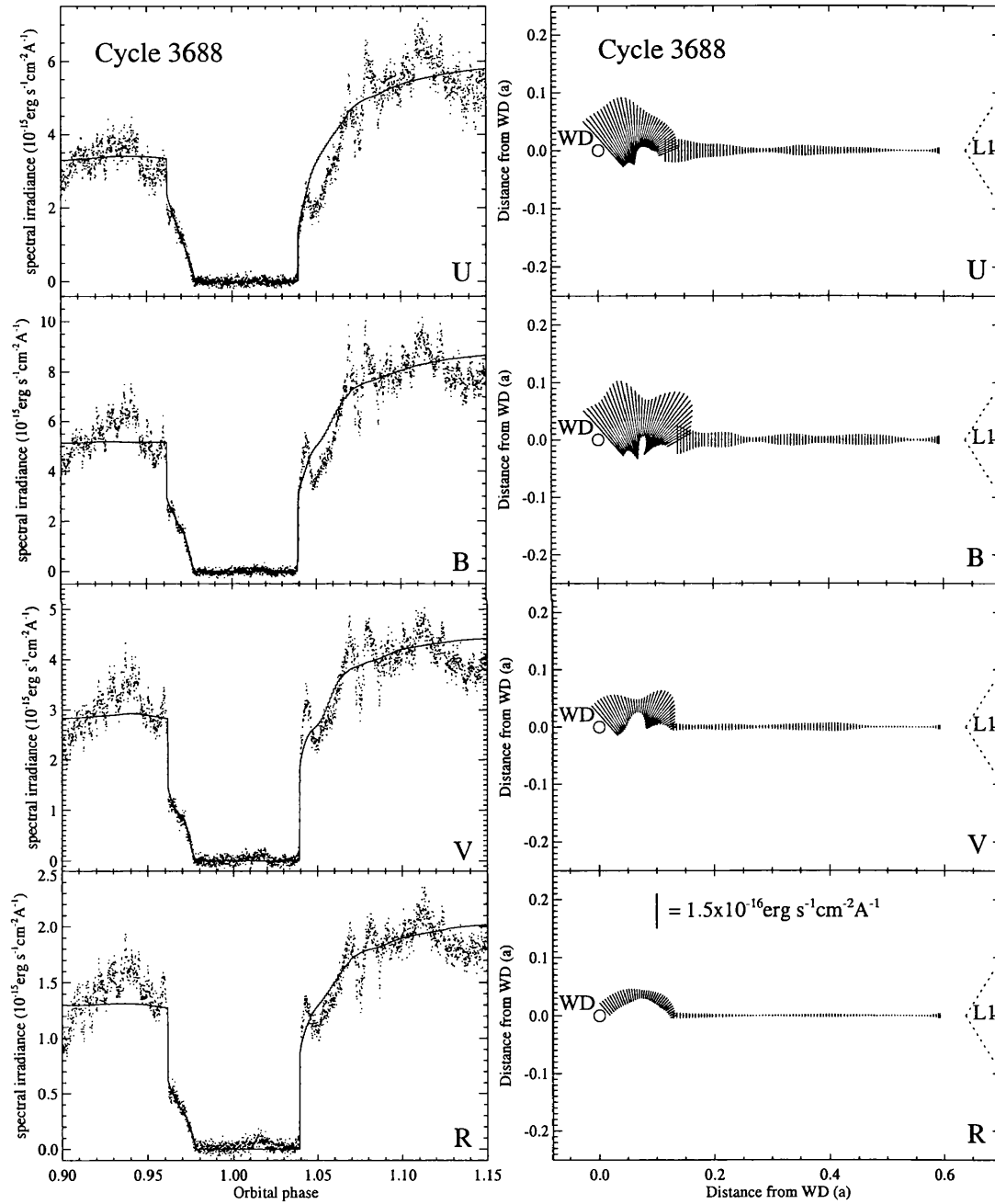
Figure 5.10: As for Fig. 5.4, but for a model stream that accretes onto only the footpoint of the field line above the orbital plane (on the same side of the orbital plane as the observer).
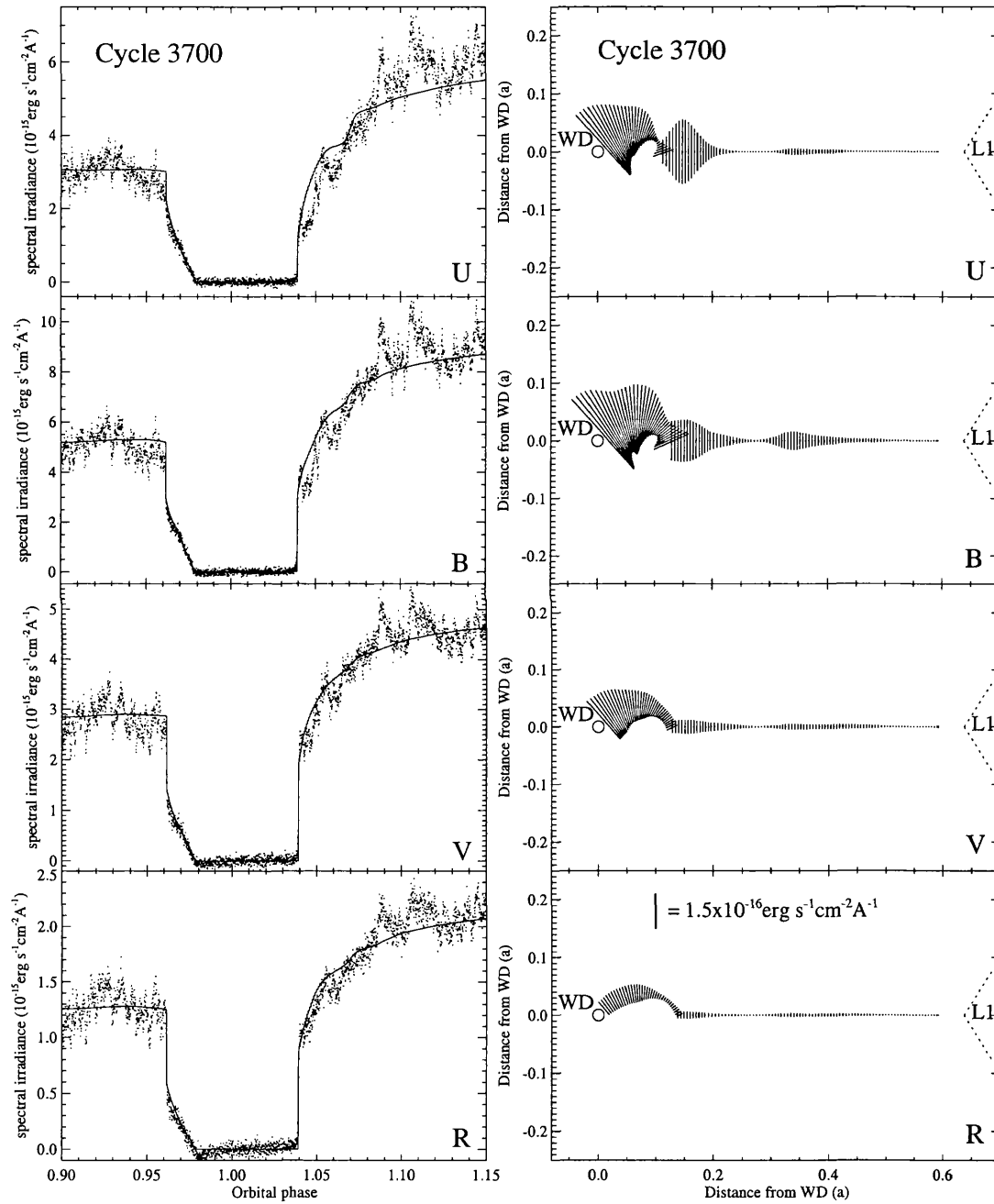
Figure 5.11: As for Fig. 5.10, but for cycle 3700.
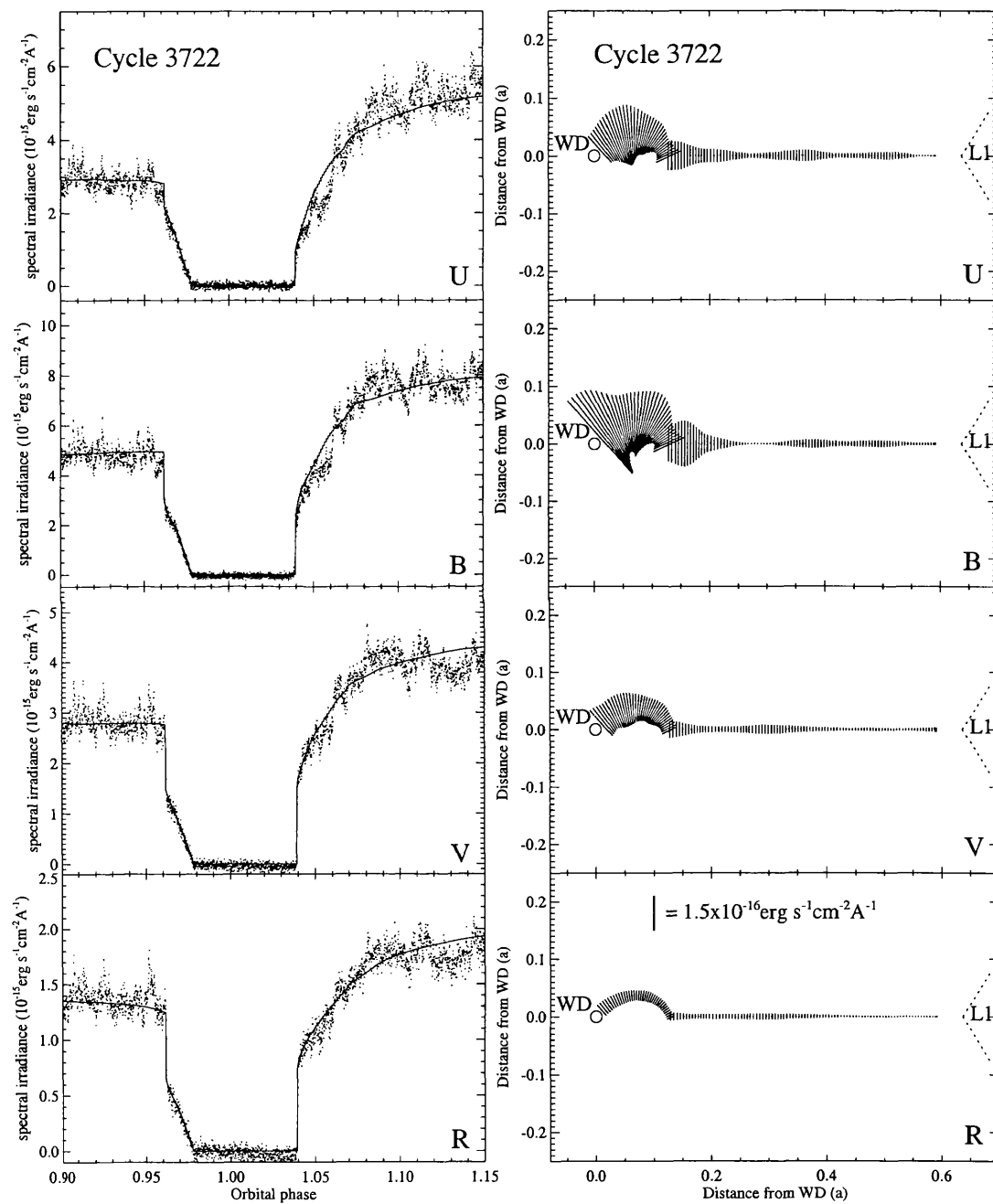
Figure 5.12: As for Fig. 5.10, but for cycle 3722.
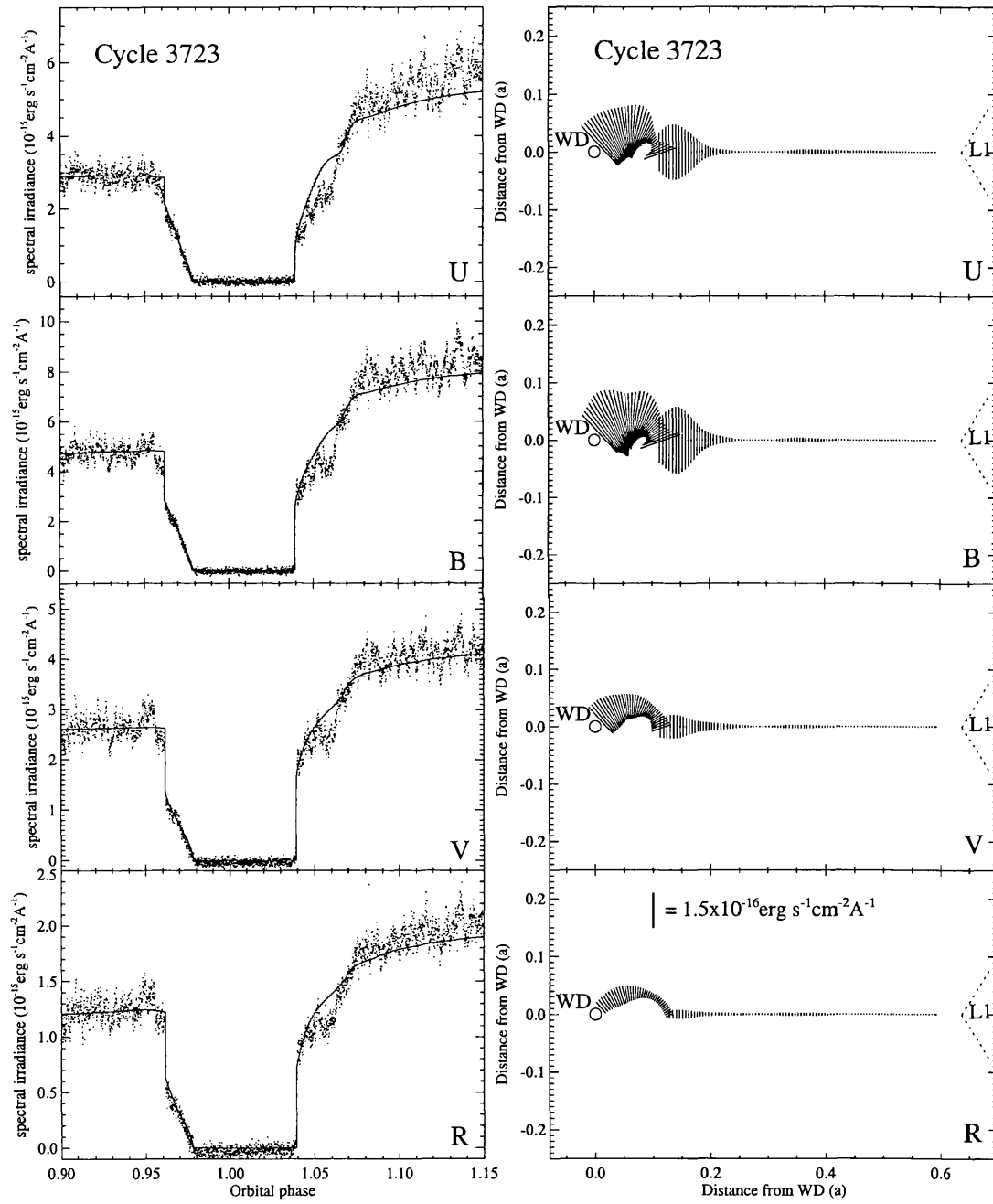
Figure 5.13: As for Fig. 5.10, but for cycle 3723.
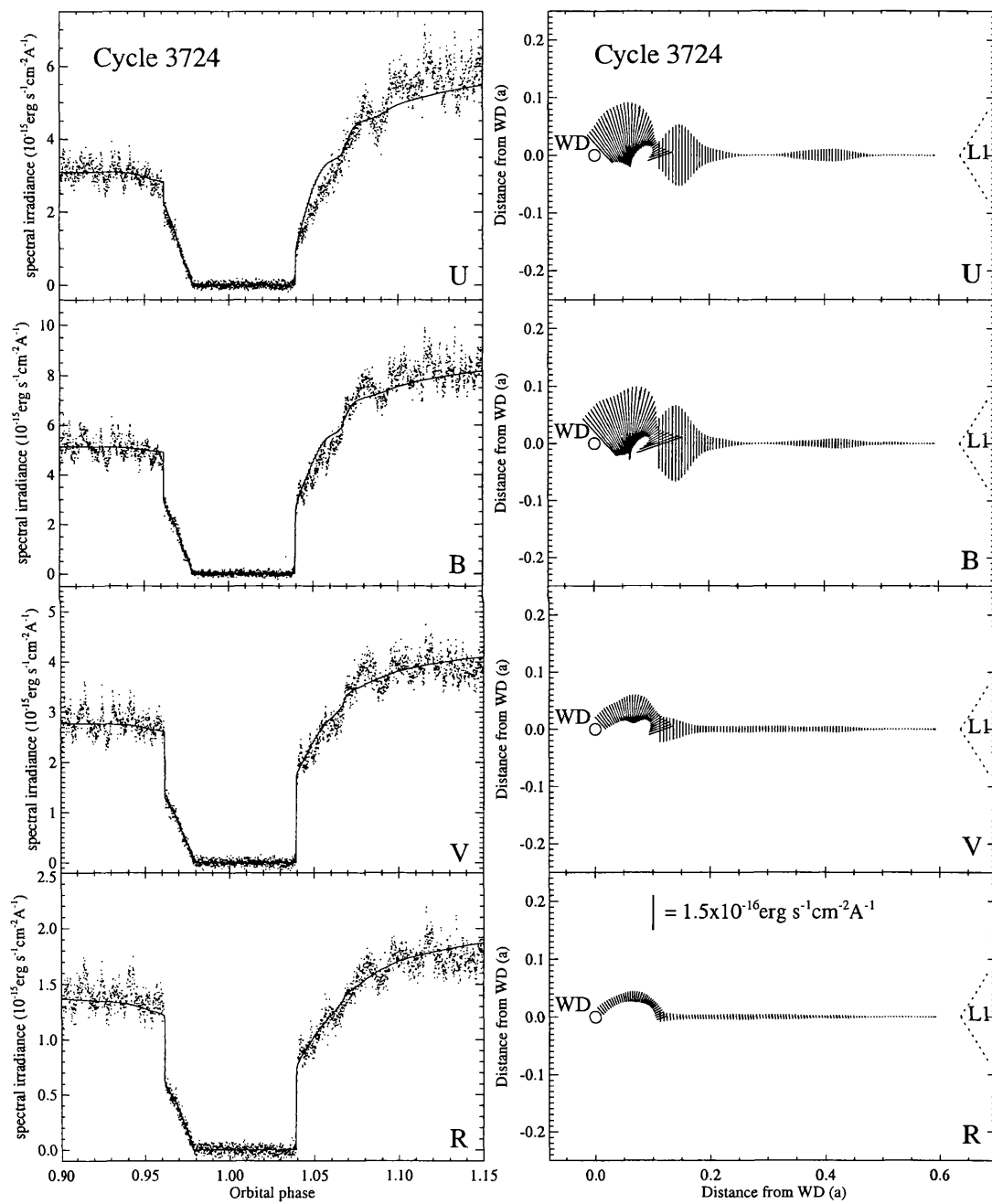
Figure 5.14: As for Fig. 5.10, but for cycle 3724.

The stream images for the one-footpoint geometry are quite different from the two-footpoint geometry results. There is very little emission from the ballistic stream in all cycles. The stream brightens as it approaches R_μ in all four wavebands. As the stream leaves the orbital plane it fades, and brightens once again as it approaches the accretion region. The brightest part of the stream is not always closest to the white dwarf, but occurs in U and B in cycles 3688, 3723 and 3724 about 0.08 a from the white dwarf.

The wavelength dependence of the stream brightnesses were examined as before by dividing the stream into sections. For this geometry, both the ballistic stream and the magnetic part of the stream were divided into two sections. In all cycles and in all four sections of the stream the flux is highest in B, and is successively lower in U and V and lowest in R.

The values of χ^2/N for the fits produced by the one-footpoint geometry are larger than those for the two-pole geometry fits, although it could be argued that this is simply because there are more parameters in the two-footpoint model. It is not straightforward to establish which of the two geometries produce a better fit: the application of an F-test to distinguish between the two models on statistical grounds is problematical because the quantity that is minimized is not χ^2, but χ^2 plus a maximum entropy regularization term (as described in section 4.1.1).

5.4 Discussion

5.4.1 Consistency checks

It needs to be established whether the physical and geometric parameters obtained from the model fits are realistic, and whether they agree with the results from previous studies of HU Aqr. The values of q and i that produce the correct eclipse widths and durations are in agreement with Schwope et al (1993), Hakala et al. (1993), Glenn et al. (1994) and Schwope et al. (1997). The values of β for the two-footpoint
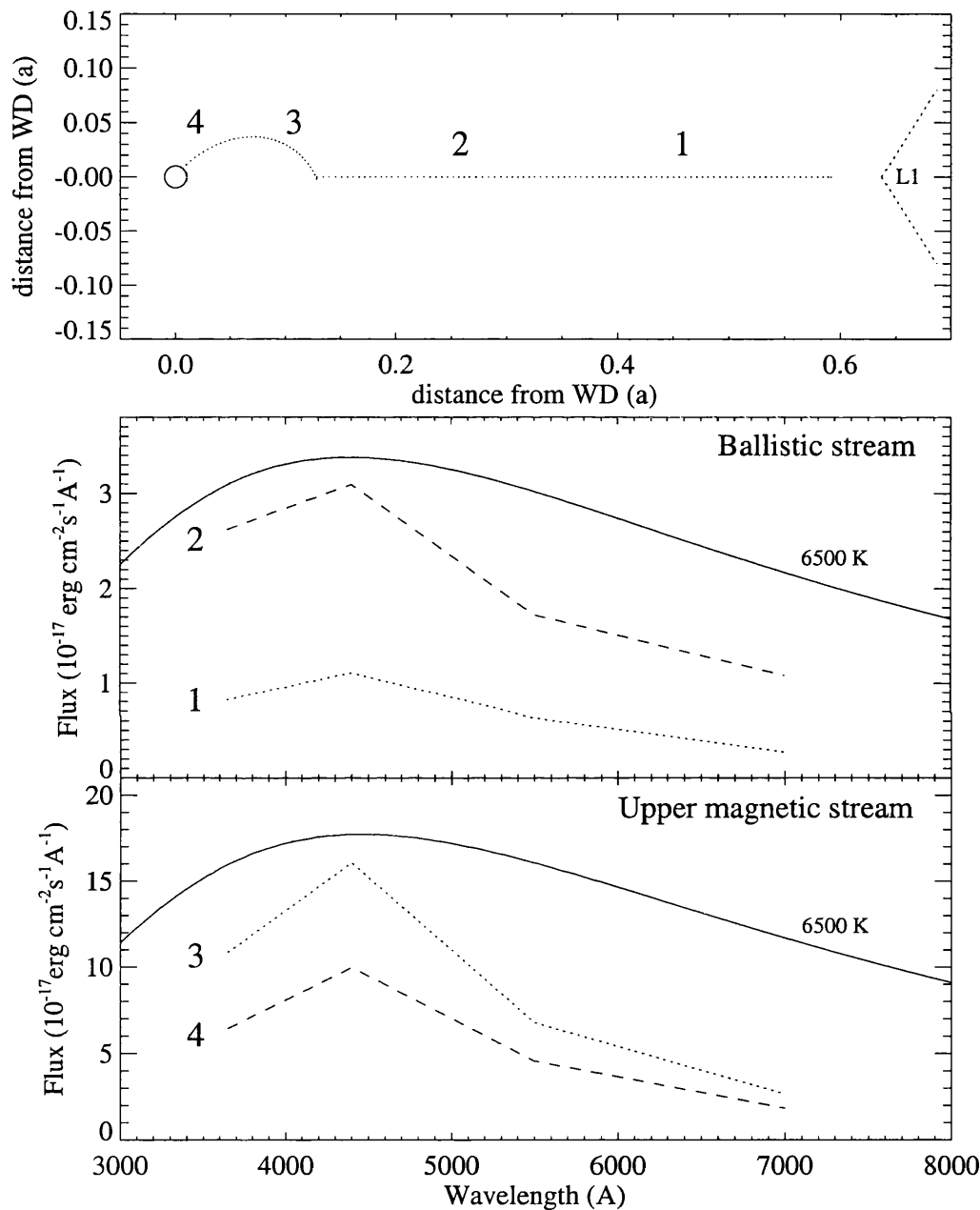
Figure 5.15: The wavelength dependence of the stream brightness distributions for cycle 3722, using the one-footpoint geometry (similar results are found for the other four cycles). The stream is divided into four sections (top panel) and the average flux per stream emission point in each section is plotted in the four wavebands for each of the four sections of the stream. In all stream sections, the peak flux occurs in B. A blackbody curve for a temperature of 6500 K is shown for illustration.

geometry ($22°$–$27°$) are consistent with the position of the accretion region ($\sim 27°$) obtained by Schwope et al. (1998) from models of the HST-FOS 1200–2500 Å light curve in August and September 1996. However, the values of β for both high state model geometries differ significantly from the value of $40°$ used by Sirk & Howell (1998) for their models of a EUVE lightcurve obtained in September 1996. The shape of the optical light curve at this epoch (figure 5 in Schwope et al. 1998) suggests that the system was in a low state at the time, so discrepancies are not unlikely. All previous studies do, however, indicate consistently that the main accreting pole is on the same side of the orbital plane as the observer, as is the case with the current models.

The derived values of R_μ are in the range 0.17–0.23 a; this corresponds to a distance from the white dwarf of $(1.0$–$1.3) \times 10^{10}$ cm, or 17–21 white dwarf radii. For comparison, Liebert & Stockman (1985) predict that the stream is diverted from the orbital plane at a radius of $(1.5$–$2.0) \times 10^{10}$ cm. Schwope et al. (1997) deduce a threading radius for HU Aqr in the range 0.20 a–0.29 a. This is in good agreement with the values of ~ 0.22 for the two-pole geometry models, and only slightly larger than the range of values used in the one-pole models. These results for R_μ are comparable to those found for other polars: QQ Vul has $R_\mu \sim 2.4 \times 10^{10}$ cm and ST LMi has $R_\mu \sim 1.9 \times 10^{10}$ cm (Mukai 1988), while Ferrario, Wickramasinghe & Tuohy (1989) find $R_\mu \sim 25$ white dwarf radii for V834 Cen and UZ For. The derived values of R_μ are therefore typical of the radius at which the bulk of the accretion stream becomes threaded to the white dwarf's magnetic field in polars.

5.4.2 The features in the cycle 3688 eclipse

At first glance, the features in the cycle 3688 light curve described in section 5.2.1 and shown in Fig. 5.2 appear to be large-amplitude flaring or flickering events, presumably originating in the accretion column. The occurrence of the post-eclipse feature at a very similar (but not identical) orbital phase in another eclipse of HU

Aqr (Schwope et al. 1998) suggests that these features may not be random flickering. Moreover, the similarity of the depths of the features at $\phi \sim 0.95$ and $\phi \sim 1.05$ may imply that the two features are connected, perhaps caused by absorption of the flux from the accretion region by intervening material on the same side of the orbital plane as the observer.

It is clear that emission from the accretion region is subject to absorption in high accretion states: this can be seen from the high state light curves, which have prominent pre-eclipse absorption dips (these are not present in low state light curves). Further evidence for absorbing material is seen in *ROSAT* HRI and *EUVE* light curves of HU Aqr (Schwope et al. 1998). During the phase interval between the pre-eclipse absorption dip (during which the X-ray flux drops to zero) and the eclipse itself, the flux is diminished to about a third of the post-eclipse flux. This suggests the presence of a 'curtain' of absorbing material above the orbital plane, perhaps comprised of finely-divided material that threads along the length of the ballistic trajectory (see section 2.6). This curtain could be responsible for the features around ~ 0.95 and ~ 1.05 in the cycle 3688 light curve. If this is the case, the curtain cannot be of uniform density, as it would then not be able to produce the narrow (in phase) features seen in cycle 3688.

5.4.3   The absorption dip and the movement of the stream

Absorption dips in polar light curves originate where the magnetically-channeled portion of the accretion stream occults the emission region on the white dwarf (see section 2.4 and Fig. 2.3). The dip in HU Aqr at $\phi \sim 0.88$ is almost certainly caused by absorption in the magnetically-channeled stream. First, HU Aqr has the necessary accretion geometry to produce such a dip: the condition $\beta < i$ (see e.g. Watson 1995) is satisfied since HU Aqr has $\beta \approx 26°$ and $i \approx 85°$ (Glenn et al. 1994; Schwope et al. 1997, this work). Secondly, the depth of the dip in a given wave-band is similar to the depth of the steep component during eclipse ingress,

suggesting that the dip is caused by the occultation of the accretion region emission. The evidence is strengthened by the fact that the strong optical emission lines in HU Aqr, which are thought to originate in the accretion stream (e.g. Lubow & Shu 1985), are not occulted during the absorption dip (Schwope et al. 1997).

The observed variation of the phase of the centre of the absorption dip (Fig. 5.3) has implications for the accretion flow: the absorbing material in the accretion stream moves from an azimuth of 42° to 48° from the line of centres (as measured from the white dwarf) on a time scale of a few days. This is evidence for the variable nature of the interaction between the stream and the magnetic field of the white dwarf.

Given that the absorbing material is located in the magnetically-confined part of the stream, the range of angles predicted by the pre-eclipse dip should correspond to the range of angles between the magnetically-entrained part of the stream trajectory and the line of centres as predicted by the stream models. The range predicted by the two-footpoint models is 39–41°, quite distinct from the range predicted by the dips; in addition, there is no obvious trend to larger angles with time. The one-footpoint models, on the other hand, show a remarkable agreement in both the trend of decreasing R_μ and the range of predicted angles (42°–47°).

It is tempting to try to link changes in R_μ (and the azimuth of the magnetically channeled part of the stream) to changes in the mass transfer rate in the stream, and thus to the overall brightness of the system. However, the mean out-of-eclipse magnitudes over the run are constant to within the measurement uncertainties (about 0.1 mag), so there are no obvious changes in the overall brightness of the system. A similar effect was observed by Schwope et al. (1998) in *ROSAT* HRI data of HU Aqr, where the azimuth of the magnetically-confined part of the stream moves by $\sim 17°$ without an obvious change in the HRI count rate.

5.4.4 Comparison with Doppler tomograms

The Doppler tomograms of HU Aqr in Schwope et al. (1997) were calculated using optical spectra obtained almost simultaneously with the high-speed photometry. This provides an opportunity to make a comparison between the tomograms and the images of the stream, with the caveat that the tomograms are images of line emission in velocity space, whereas the stream images show the total emission in spatial coordinates.

The tomograms are images in the (v_x, v_y) plane, where v_x is the velocity along the line of centres in the direction of the centre of the secondary star, and v_y is the velocity in the orbital plane, perpendicular to v_x; the positive v_y direction is in the direction of the orbital motion of the secondary. Fig. 5.16 is the Doppler map of the He II $\lambda 4686\,\text{Å}$ emission line components that originate in the accretion stream, taken from Schwope et al. (1997). The most prominent feature in the tomogram is the bright 'cometary' tail extending from $(v_x, v_y) \approx (-100, -200)\,\text{km s}^{-1}$ to $(v_x, v_y) \approx (-1000, -200)\,\text{km s}^{-1}$. Schwope et al. (1997) identify this feature as emission from the ballistic stream. Emission from the magnetically-channeled flow appears as the fainter region at $(v_x, v_y) \approx (-400, -300)\,\text{km s}^{-1}$.

A comparison between the stream images and the tomogram shows that *line emission is not the dominant emission mechanism in the stream*. While it may be difficult to relate the apparent flux in the tomogram to the emitted line flux, it is clear from Fig. 5.16 that the integrated flux in the tomogram in the velocity space appropriate to the ballistic stream exceeds that from the magnetically-channeled stream. Looking at the B-band images in Figs. 5.4 to 5.14, the reverse is the case: the emission from the magnetically-channeled part of the stream dominates the emission from the ballistic stream. The line flux is thus a small fraction of the total optical emission from the stream.

The large ratio of stream continuum emission to stream line emission (in the optical) can also be seen in optical spectra. The ratio of line to continuum emission in the
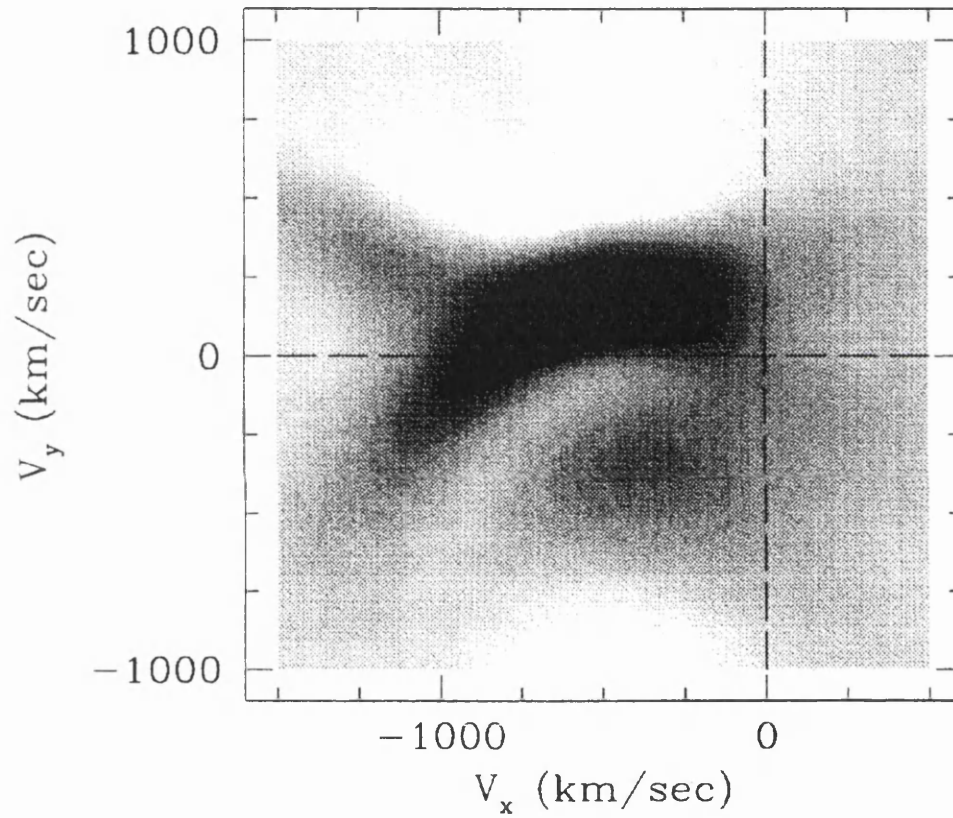
Figure 5.16: The Doppler map from Schwope et al. (1997) showing the HeII $\lambda4686$ Å emission line components that originate in the accretion stream. The features in the lower left-hand quadrant originate in the magnetically-channeled flow.

high state can be estimated using the mean spectrum in Schwope et al. (1997) (the mean out-of-eclipse magnitudes from table 5.1 are used to estimate the continuum level, as the spectrum presented in Schwope et al. (1997) is continuum-subtracted). The ratio of continuum emission to line emission is ~ 8 in the B-band. The fraction of the continuum due to the *stream* (as opposed to cyclotron emission from nearer the white dwarf) can then be estimated using the figures in Table 5.2: approximately 56 per cent of the pre-eclipse light level is due to the stream. This implies that the stream continuum flux exceeds the line emission flux by a factor of ~ 4.3 in the high state. The corresponding measurement in the low state, using the spectrum in Hakala et al. (1993), shows that even in reduced accretion states the continuum flux from the stream exceeds the line flux by a factor of ~ 2.5 in B.

5.4.5 The mass transfer rate

If it is assumed that R_μ is the radius at which the ram pressure of the stream is balanced by the magnetic pressure of the white dwarf field, the values of R_μ can be used to estimate the mass transfer rate in the stream via equation 1.10. For HU Aqr, $M_1 \approx 0.9\,M_\odot$, $\mu_{34} \approx 0.8$ and $B \approx 37\,\mathrm{MG}$. The width of the pre-eclipse absorption dip is used to estimate the radius of the stream (as in e.g. Watson et al. 1995). Since the inclination is high,

$$\sigma \approx \pi\, d\, \Delta\phi / \sin i \qquad (5.1)$$

where d is the distance from the white dwarf to the absorbing material in the stream. The absorption dips have $\Delta\phi \approx 0.080$. I make the assumption that the absorption occurs at a distance of R_μ, since i is near 90°. Equation 5.1 then implies $\sigma_9 \approx 3.0$. This is comparable to values of the stream radius from Lubow & Shu (1975) where $\sigma_9 \sim 1$. Using equation 1.10 with $\sigma_9 = 3.0$ and $0.17\,a \lesssim R_\mu \lesssim 0.23\,a$, the mass transfer rate is $(8 - 76) \times 10^{16}\,\mathrm{g\,s^{-1}}$.

This result is quite sensitive to the value of σ_9, since $\dot{M} \propto \sigma^2$. For example, if

$\sigma_9 = 1$, the implied mass transfer rate is reduced to $(1 - 5) \times 10^{16} \, \mathrm{g\,s^{-1}}$. Heerlein et al. (1999) find a value of $\sim 5 \times 10^{16} \, \mathrm{g\,s^{-1}}$ from their magnetic stripping model of the accretion flow in HU Aqr (see section 2.10), which is comparable to the values deduced for $\sigma_9 = 1$. By comparison, the mass transfer rate expected if the orbital evolution is driven only by gravitational radiation is $\sim 7 \times 10^{15} \, \mathrm{g\,s^{-1}}$ (using equation 1.2).

Chapter 6

Improvements to the model

In chapter 4, where the the stream imaging method is developed, and in chapter 5, where the method is applied to high accretion state data of HU Aqr, several simplifying assumptions are made in order to make progress. The stream is assumed to make an instantaneous transition between a ballistic and a magnetic trajectory, and the accretion region on the white dwarf is assumed to be a point source. In addition, it is assumed that the underlying orbital variation during the eclipse (due to cyclotron beaming) can be modelled using a step function, such that the cyclotron levels before and after $\phi = 1.0$ are *constant*, with the level after $\phi = 1.0$ being higher than the level before (as is indicated by the sizes of the steep components in the eclipse). The first two of these issues — the stream configuration, and the accretion region geometry — can be addressed only by substantial revision of the model. For instance, the stream trajectory could be modified to include a drag term so that the transition from the free-fall to the magnetic trajectory is not instantaneous (as used by, for example, Schwope et al. 1997). The stream could also thread onto several adjacent field lines (as in, for example, Mukai 1988; Achilleos, Wickramasinghe & Wu 1992) to produce an extended accretion region on the white dwarf. It is not yet clear that the inclusion of a drag term provides a better representation of the true stream trajectory. Such modifications of the model are beyond the scope of this thesis, but these are certainly issues to explore in any future development of

the imaging technique.

The third issue — the assumption of constant cyclotron brightness — is important to address here (and this is feasible without a substantial recasting of the model). If the underlying variation in cyclotron emission affects the shape of the stream components in the eclipse, the stream image deduced by the technique will not be an accurate representation of the stream brightness alone. Once an attempt is made to subtract the underlying variation, it is possible that the results will be quite sensitive to the precise way in which the cyclotron emission is determined and how it is subtracted. The aim of this chapter is to explore how the stream images change when these variations are taken into account.

6.1 Subtracting the orbital trend

The orbital trend is due to cyclotron beaming from the accretion region(s). Fig. 6.1 (upper panel) shows the *B*-band light curve of HU Aqr at cycle 3723 (according to the ephemeris of Schwope et al. 1997) from phase 0.2 to 1.8. The eclipse occurs near a local minimum of the orbital trend, and it is thus not possible to use (for example) a straightforward spline fit to the data on either side of the eclipse to approximate the trend during the eclipse[1]. Since the orbital variations are due largely to cyclotron beaming, they occur at the orbital frequency and the harmonics of the orbital frequency. It might be possible to construct a cyclotron intensity light curve using polarization data, and to use this to correct the total intensity for the variations due to cyclotron beaming. However, there are no simultaneous polarization measurements for the high state data. In the absence of polarization information, therefore, I have approximated the orbital trend using a harmonic series

---

[1]In the case of the low accretion state data, the eclipse does not occur at a local minimum in the orbital trend. In the neighbourhood of the eclipse, the trend is thus easily approximated using a spline fit — see chapter 7.
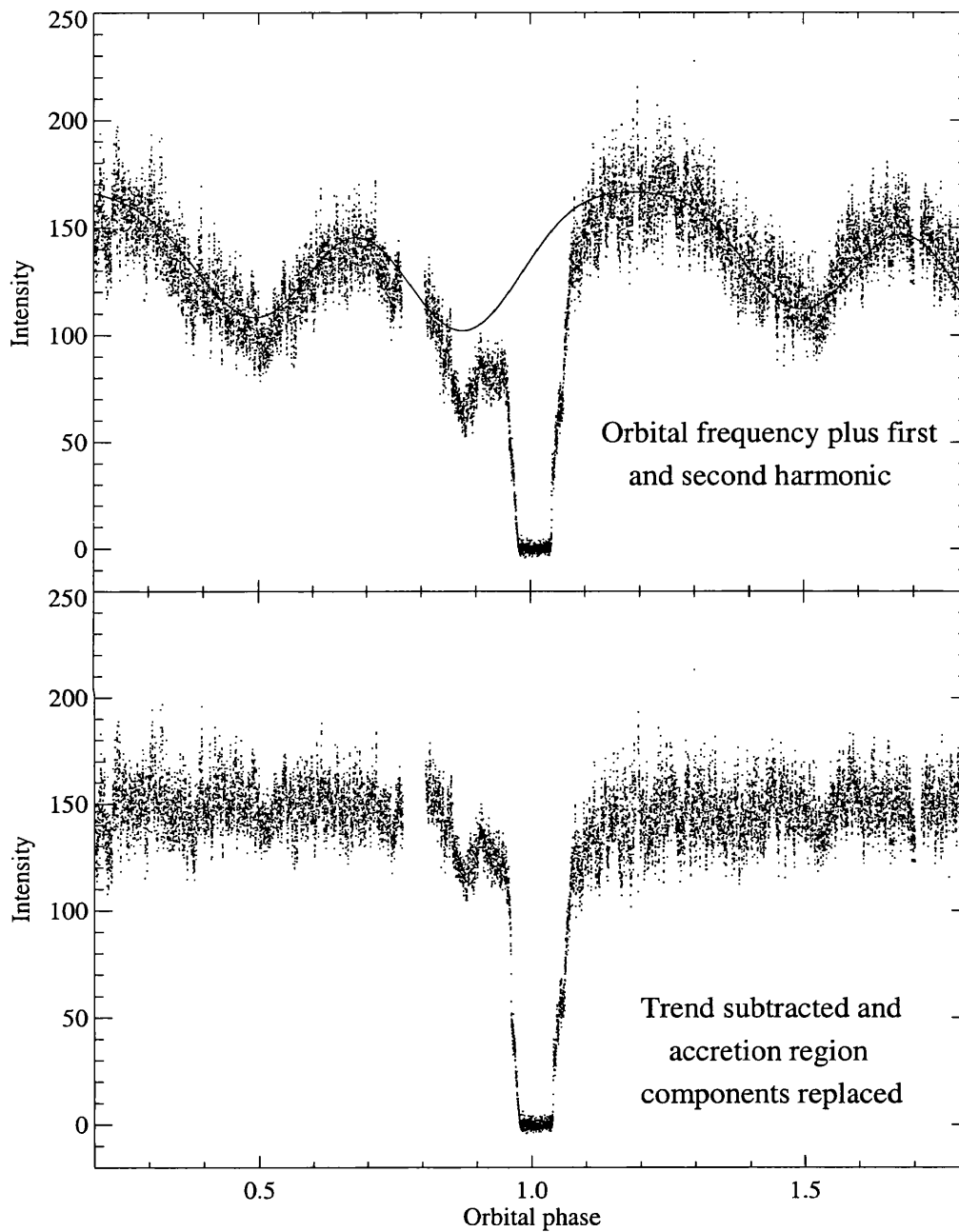
Figure 6.1: Subtracting the orbital trend in the high accretion state data of HU Aqr. The upper panel shows the U-band light curve surrounding the eclipse of cycle 3723; superimposed is the curve that is used to approximate the orbital trend. The lower panel shows the results of the subtraction procedure (see text for details).

$$F = \sum_{k=1}^{n} A_k \cos(k\,\Omega t + \phi_k) \tag{6.1}$$

where Ω is the orbital frequency. The frequencies, amplitudes A_k and phases ϕ_k are found using a simultaneous non-linear least-squares fit to the light curve, excluding the pre-eclipse absorption dip at $0.88 \lesssim \phi \lesssim 0.93$, and the eclipse at $0.94 \lesssim \phi \lesssim 1.2$. The curve obtained is then shifted to match (as closely as possible) the heights of the steep components of the light curve at $\phi \approx 0.961$ and $\phi \approx 1.039$, and the scaled curve is subtracted from the light curve at phases where the pole is visible, i.e. before the accretion column ingress and after column egress. To reconstruct the light curve (so that it can be modelled using the stream imaging technique), the accretion region components are added back to the light curve[2]. This procedure is performed for the light curve in each filter of cycle 3723 (this cycle was chosen because of the large baseline available on either side of the eclipse to establish the underlying trend during the eclipse).

There are two criteria the calculated curve must satisfy in order to be a good approximation to the cyclotron variation. First, the calculated curve should match the orbital variation outside the eclipse and the absorption dip as closely as possible. The other constraint is provided by the heights of the steep cyclotron components at $\phi \approx 0.961$ and $\phi \approx 1.039$. The steep components indicate *exactly* the cyclotron flux at these two phases. The calculated curve, which is an approximation to the cyclotron intensity light curve throughout the orbit, should match the heights of both steep components as closely as possible. To chose an appropriate value for n, therefore, the above procedure was applied to each waveband in turn for $n = 1$ to $n = 5$. The value of χ^2 was calculated for each fit for $\phi < 0.88$ and $\phi > 1.04$, and the

---

[2]The exact heights of the accretion region components that are added back to the light curve do not affect the stream brightness distribution deduced by the algorithm. This is because the algorithm does not use information from the accretion region components to deduce the distribution of brightness along the stream

value of the curve at $\phi \approx 0.961$ and $\phi \approx 1.039$ were compared to the heights of the steep components. Although lower values of χ^2 are obtained for higher values of n, the inclusion of additional harmonics causes an increasingly large mismatch between the relative heights of the steep components and the values of the calculated curve at $\phi \approx 0.961$ and $\phi \approx 1.039$. It was found that $n = 3$ provided a sufficiently low χ^2 outside the eclipse and an adequate match between the values of the curve at $\phi \approx 0.961$ and $\phi \approx 1.039$, and the heights of the steep cyclotron components in the eclipse.

Fig. 6.1 shows the results of applying this procedure to the B-band light curve using $n = 3$. The upper panel shows that this curve is a good approximation to the orbital trend, and the lower panel shows the results of the subtraction procedure. Although there are small residual dips at $\phi = 0.5$ and $\phi = 1.5$, the orbital trend is removed adequately with $n = 3$.

6.2   Comparison with previous results

The corrected light curves (obtained using $n = 3$ for the orbital trend) were used to construct stream images using the two-footpoint geometry; the light curves, model profiles and the stream images were then calibrated as before (see section 5.3). Fig. 6.2 compares the new model eclipse profiles to the original results. Good fits were obtained using same values of β, ζ and R_μ as before; the only parameters that required adjusting were the values for the pole brightnesses. This is because the orbital trend curve that is subtracted from the data does not always match exactly the heights of the steep components in the eclipse profile.

The values of χ^2/N for the new fits are comparable to those for the original data: these values are shown in Fig. 6.2 for each model profile. The corresponding stream images are shown in Fig. 6.3. It is clear that the subtraction of the orbital trend *does* affect the appearance of the stream images. The details of the distribution of brightness along the stream is altered; in particular, the bright regions along the
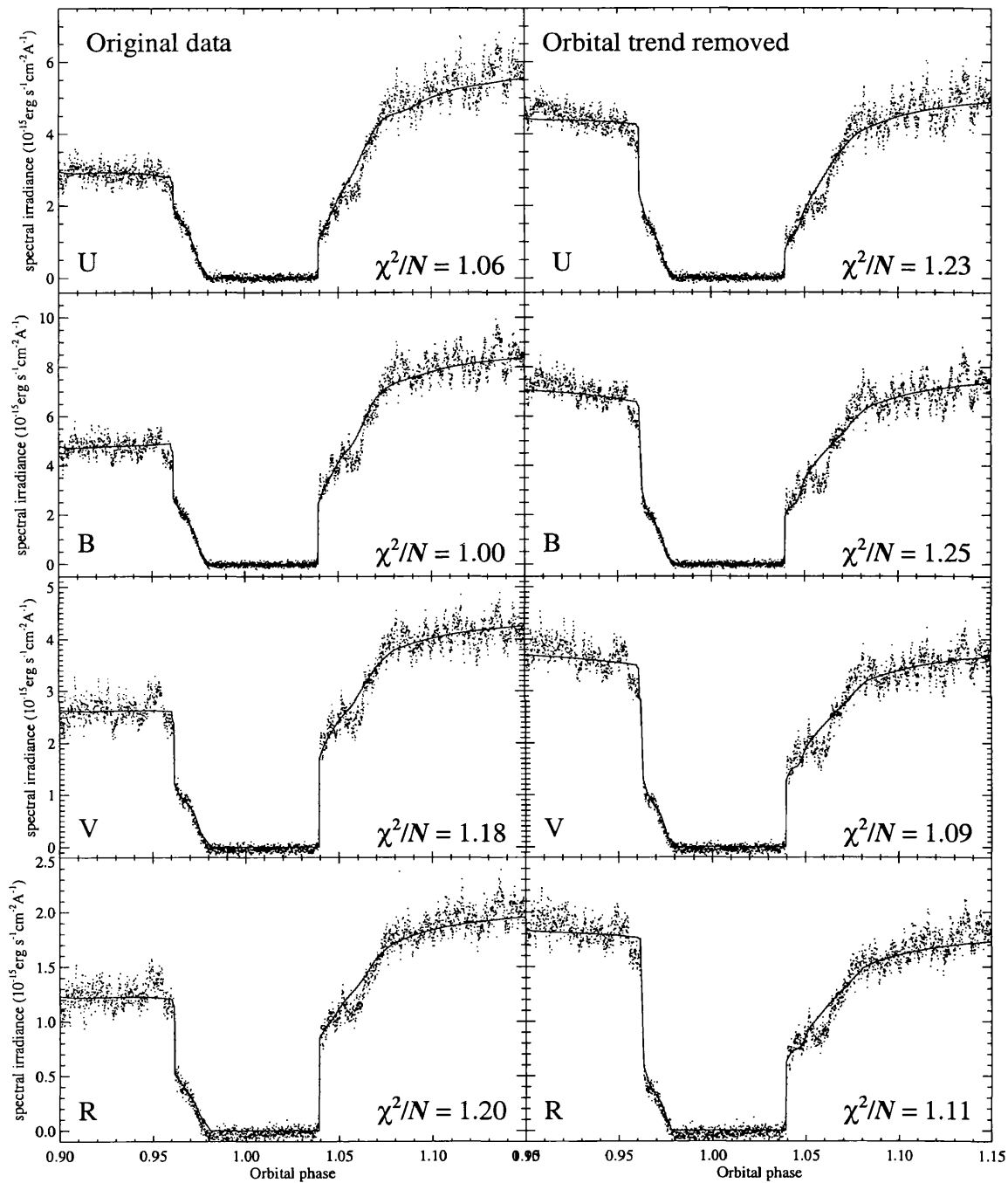
Figure 6.2: A comparison between the model fits obtained using the data for cycle 3723 in its original form and those obtained when the underlying orbital trend is subtracted prior to the application of the model. The parameters β, ζ and R_μ are unchanged. The values of χ^2/N for the original and the new fits are comparable.
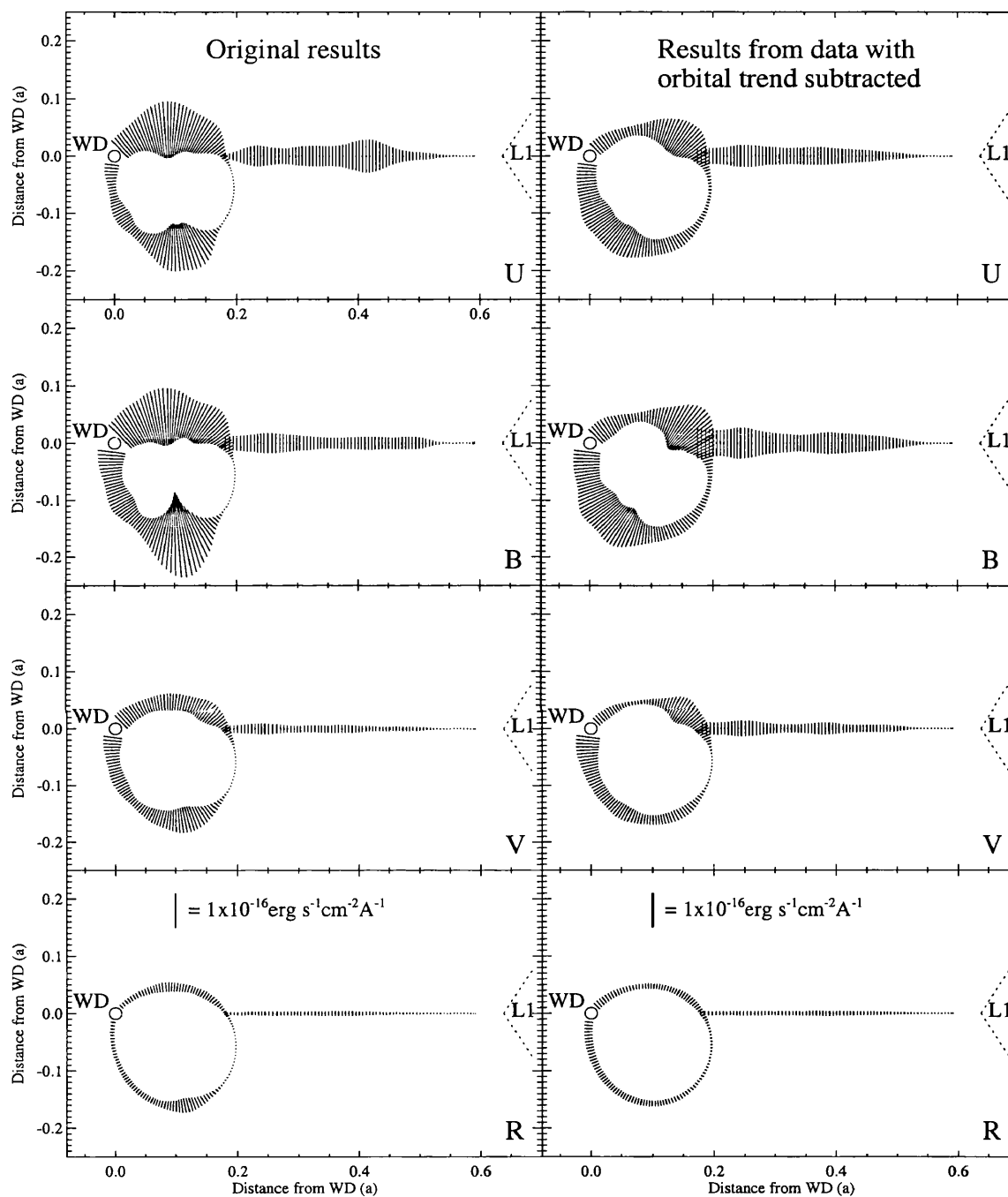
Figure 6.3: A comparison between the stream images obtained for the two-footpoint model geometry using cycle 3723 in its original form, and those obtained when the orbital trend has been subtracted from the data.
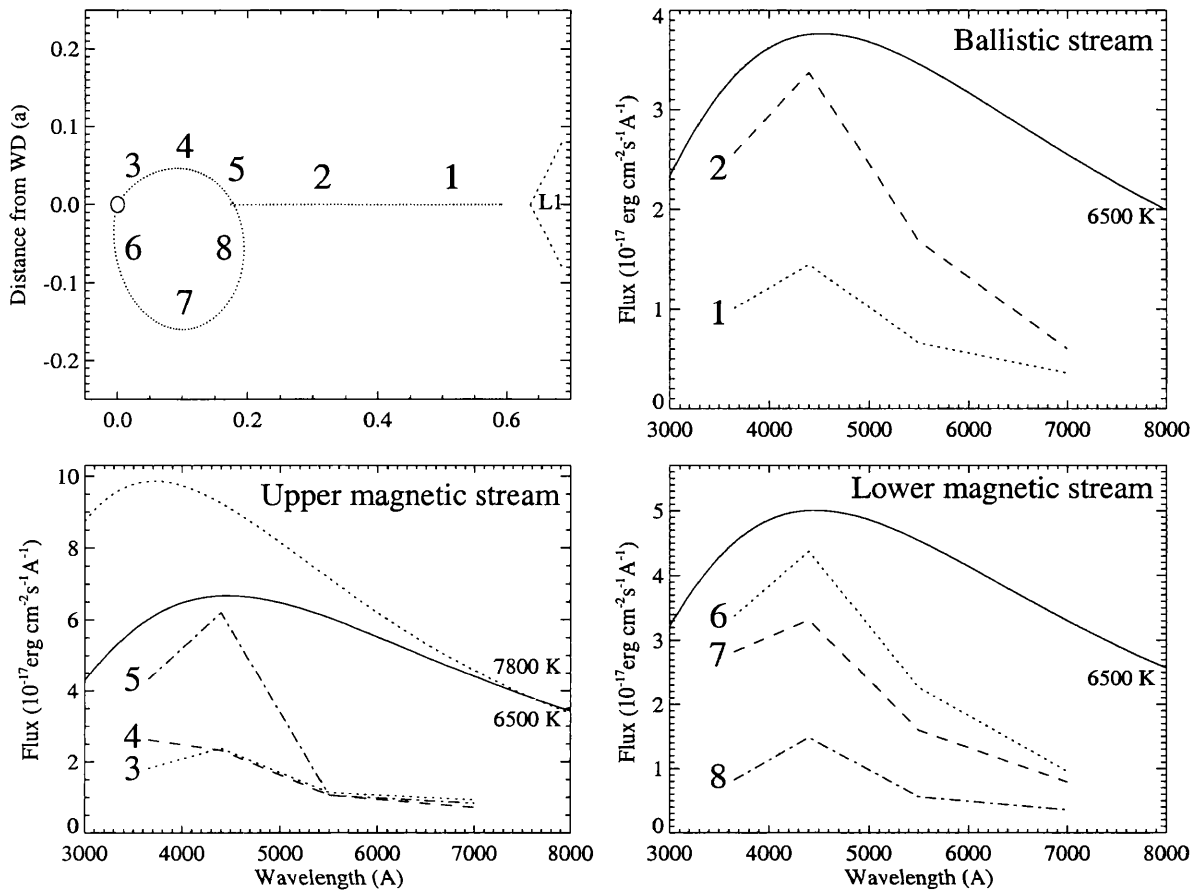
Figure 6.4: The wavelength dependence of the stream brightness distributions for cycle 3723 after subtraction of the orbital trend (compare this with Fig. 5.9). As before, the peak flux occurs in B in most stream sections. The exception in this case is section 4, where U exceeds B. Blackbody curves for temperatures of 6500 K and 7800 K are shown for illustration.

magnetically-entrained parts are in different locations. Also, there is a more obvious tendency for the stream to brighten as it approaches R_μ. However, there are also general similarities to the previous results. There are still localized bright regions within the magnetosphere (instead of a brightness distribution that is a function of radial distance from the white dwarf) and there is still very little flux on the lower half of the magnetic part of the stream immediately below the junction at R_μ. Also, the brightest region of the stream is not closest to the white dwarf, as was the case in the original results.

The wavelength dependence of the fluxes in different sections of the stream was examined as before (see section 5.3.2); these results are shown in Fig. 6.4. As was the case in chapter 5, most stream sections show a flux distribution that peaks in B, and is successively fainter in U, V and R. The exception in this case is section 4 (as opposed to sections 5 and 8 in the previous results) where the U flux slightly exceeds the flux in B.

6.3 Conclusions

Although many of the main results from chapter 5 remain unaltered, the details of the stream images *are* changed if the underlying orbital variation is subtracted prior to the application of the imaging technique. The details of the distribution of flux along the stream are altered, in that the localized bright regions occur in different places on the stream. The higher temperatures of the stream adjacent to the threading region suggested by the previous results (section 8.3) must be regarded as less secure, since the flux peaks in U in a different stream section when the orbital trend is subtracted.

Results that are unaltered by the orbital trend subtraction include the values of β, ζ and R_μ, the appearance of localized bright regions within the magnetosphere (instead of a distribution that is a function of the radial distance from the white dwarf), and the wavelength dependence of most sections of the stream, where the stream flux peaks in B.

Chapter 7

HU Aquarii: low accretion state

This chapter is an investigation of HU Aquarii in a low accretion state, based on simultaneous high speed optical photometry and polarimetry. I apply the stream imaging method described in chapter 4 to the high speed photometry to construct images of the accretion stream. I then use the polarization curves to construct images of the accretion region on the white dwarf using another genetic algorithm-based optimization method: Stokes Imaging (Potter et al. 1998). This method has the advantage of being more objective than previous polarization modelling methods, in that it does not assume *a priori* the shape of the cyclotron-emitting regions on the white dwarf in order to construct model polarization and intensity light curves.

The two imaging methods should produce compatible results if the assumptions for both methods are valid. This is because the accretion region lies at the footpoints of the field lines in the threading region. In principle, the structure and location of the threading region can be deduced from the shape of the accretion region on the white dwarf. The results may be difficult to interpret if the magnetic field in the threading region is distorted substantially by the incoming plasma, or if the field is dominated by higher order multipoles near to the white dwarf surface. Although the two imaging methods are not completely consistent (the stream imaging technique assumes that the accretion region is not extended, for example), they may be expected to give broadly compatible results. The two methods have sev-

eral assumptions and parameters in common: both methods assume that the white dwarf's magnetic field is an inclined dipole, and both methods derive values for the dipole offset β and its azimuth ζ. The simultaneous photometry and polarimetry thus provides an opportunity to use both Stokes Imaging and the stream imaging technique to connect the properties of the accretion flow to the shape and location of the accretion region on the white dwarf.

7.1 The observations

Simultaneous polarization and intensity observations of HU Aqr were made on October 12, 13 and 14, 1996, using the UCT Polarimeter (Cropper 1985a,b) on the 1.9 m telescope at the Sutherland site of the South African Astronomical Observatory. The polarimeter was used in its simultaneous linear and circular polarimetry and photometry mode. A white light bandpass (3200–9200 Å) defined by the RCA 31034A GaAs photomultiplier was used for all time-series observations. The integration time was 10 s for the high speed photometry and 60 s for the polarimetry.

The intensity of the polarized light is modulated as a function of the rotation angle of the rotating waveplates in the polarimeter. In the case of contra-rotating $\lambda/4$ and $\lambda/2$ waveplates (required for the simultaneous linear and circular polarimetry mode), the circularly polarized component is modulated at six times the rotation rate and the linear component is modulated equally at the fourth and the eighth harmonic. The polarization of a particular measurement is obtained by fitting fourth, sixth and eighth harmonics of the rotation rate to the rotation angle of the waveplates by least squares. The Stokes parameters are then calculated from the amplitudes and phases of the harmonics.

Sky measurements were made every ~ 35 min to correct for the background polarization. In order to maximize the signal-to-noise ratio of the sky measurements, for each angle of the waveplates (100 in all) the sky measurements were fitted by polynomials in time, and the sky polarization for each on-source measurement was

calculated by evaluating the 100 polynomials at the time of the star observation, and subtracting the sky value from the intensity measurement of the source at each rotation angle. A second order correction was then applied to the sky-corrected measurements by making use of the fact that the night sky has a negligible circular polarization.

V-band measurements of HU Aqr were obtained for calibration purposes on October 13 and 14. These were compared to the V magnitudes of star "C" of Schwope, Thomas & Beuermann (1993) (shown in their figure 1). The mean out-of-eclipse V magnitude of HU Aqr is found to be $V \approx 16.3$ (compare this to the mean out-of-eclipse magnitudes in the high state, where $V \approx 15.0$ — see table 5.1). HU Aqr was less than half as bright in October 1996 as it was in October 1992, when the star is described as being in an "intermediate" state (Schwope et al. 1995). It is thus reasonable to say that the October 1996 observations were made in a *low* accretion state (the exact distinction between a "high" and a "low" state is, of course, not precise).

The data were phase-folded using the ephemeris of Schwope et al. (1997) and the polarimetry was binned to a phase resolution of $d\phi = 0.02$ for the Stokes Imaging procedure. The original resolution of $10\,$s ($d\phi \approx 0.0013$) of the high speed photometry was retained for the stream imaging technique.

7.1.1   The light curve

The folded light curve is shown in the top panel of Fig. 7.1. There are pronounced differences between the high and the low state light curve (for comparison see e.g. the upper panel of Fig. 6.1). The high state light curve has a double-peaked shape with two maxima per orbit, while the low state light curve has only one peak per orbit. As a result, the eclipse in the high state occurs near a local minimum of the orbital trend, while the low state eclipse occurs between the orbital maximum (at $\phi \approx 0.80$) and the following local minimum at $\phi \approx 1.45$. There is no obvious pre-eclipse absorption
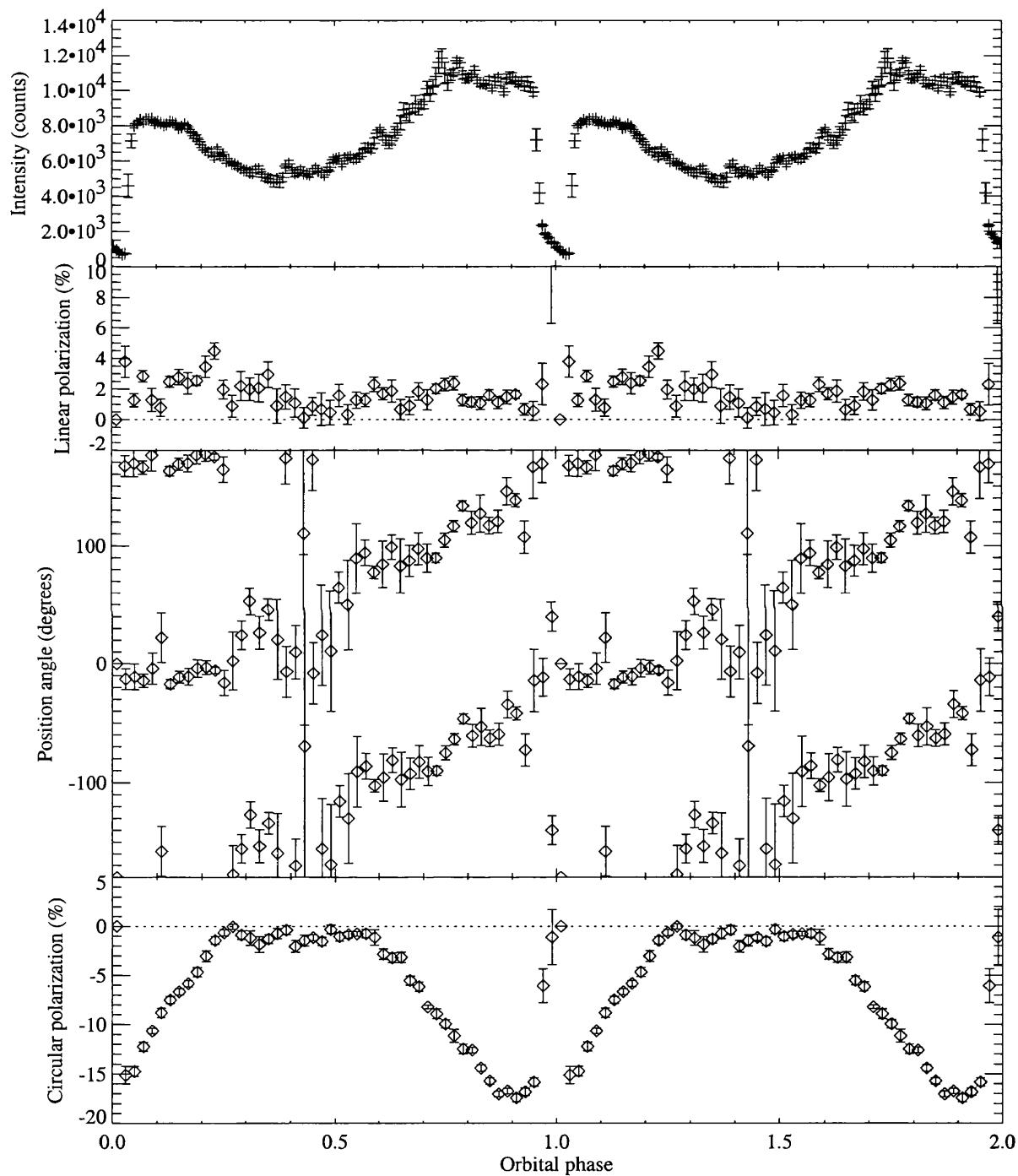
Figure 7.1: Phase-binned, folded white light photometry and polarization data of HU Aqr for 12, 13 and 14 October 1996.

dip in the low state optical light curve.

The low state eclipse profiles are similar to those in the high state in that they show a multi-component structure. The ingress and egress of the accretion region on the white dwarf occur at $\phi \approx 0.963$ and $\phi \approx 1.037$ respectively, and the ingress of the accretion stream occurs in the interval $0.96 \lesssim \phi \lesssim 1.00$. The ratio of the stream brightness to the accretion region brightness is 0.19, much smaller than in the high accretion state (see table 5.2). The duration of the stream ingress is more than twice as long as in the high state: ~ 290–410 s as opposed to ~ 125 s. There is no obvious stream egress component after the accretion region egress, although there is an interval after the eclipse ($1.05 \lesssim \phi \lesssim 1.16$) where the light curve is flat. This could represent the egress of the stream, added to the overall orbital trend; this possibility is investigated in section 7.2.1.

Four complete eclipses were observed during the three nights of observation (two successive eclipses were acquired on 13 October), corresponding to cycles 16964, 16975, 16976 and 16986 according to the ephemeris of Schwope et al. (1997) — these will be referred to as cycles 1, 2, 3 and 4 for brevity. They are shown in their original 10 s resolution in Fig. 7.2. Unlike the high state data, the duration of the accretion stream ingress in the low state data is highly variable from cycle to cycle. No two eclipses have the same stream ingress duration: the component changes from ~ 410 s in cycle 1, to ~ 390 s, ~ 270 s and ~ 300 s in cycles 2, 3 and 4 respectively. Note the large change between the two *successive* cycles of 13 October (cycles 2 and 3).

7.1.2   Polarimetry

The circular and linear polarization curves, and the variation of the position angle of the linear polarization, are shown in the bottom three panels of Fig. 7.1. The circular polarization curve is roughly sinusoidal and is negative at all phases, reaching -17 per cent at $\phi \approx 0.9$. The circular polarization curve is similar that of Hakala et
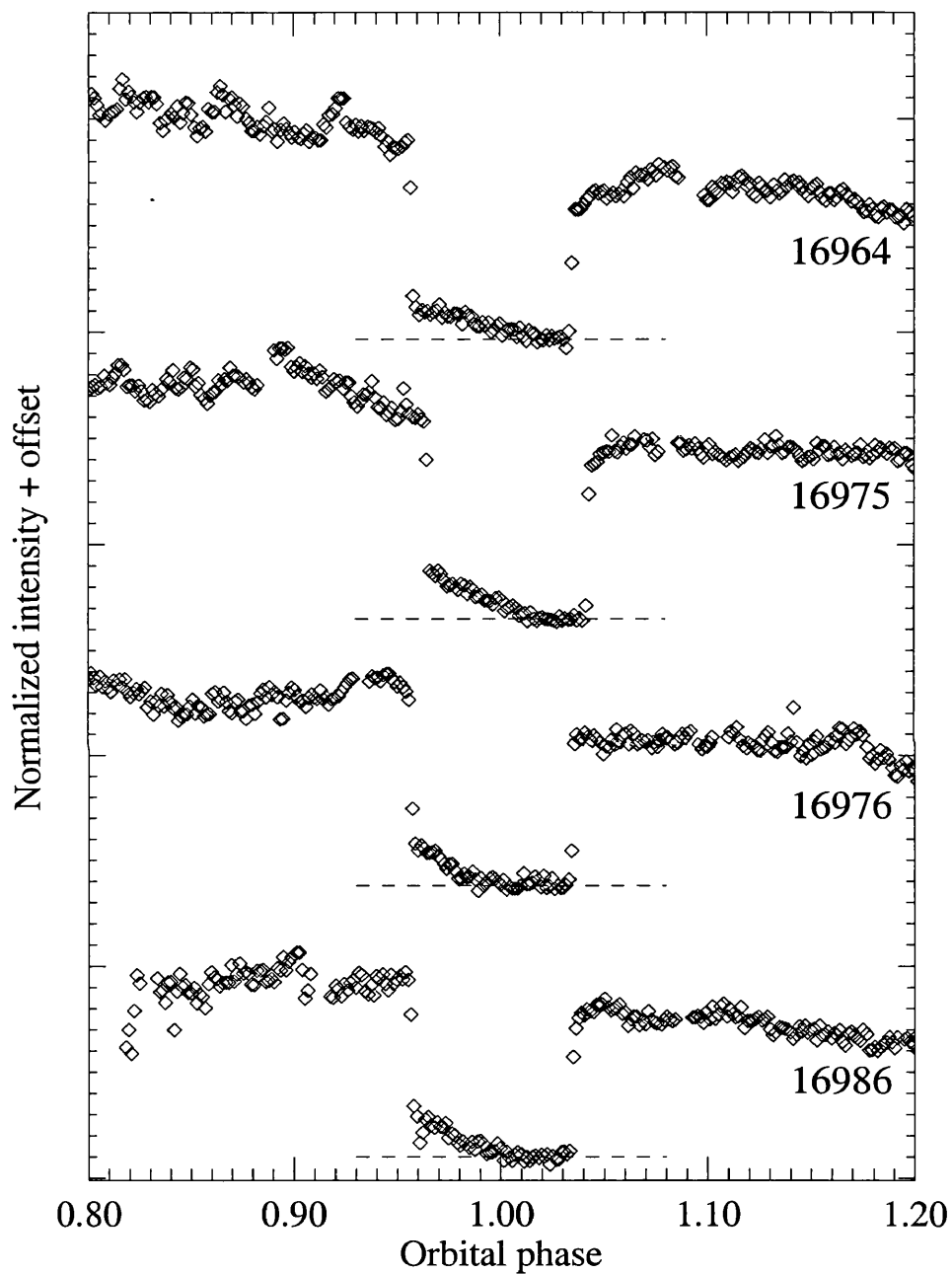
Figure 7.2: Eclipse profiles of HU Aqr in a low accretion state on 12, 13 and 14 October 1996. Each eclipse is labelled with the corresponding cycle number according to the ephemeris of Schwope et al. (1997). The eclipses of 12 and 13 October have been offset for clarity. The mid-eclipse intensity is shown as a dashed line for each eclipse.

al. (1993); in particular, the phasing and the shape of the curve are similar to those of the previous observations. The linear polarization is significant but low throughout the orbit: most measurements are below 5%. The high point in the linear polarization curve at $\phi \approx 0.24$ occurs approximately at the phase where the circular polarization curve reaches zero per cent polarization; this may indicate the phase at which the accretion region rotates behind the limb of the white dwarf. The high point at $\phi \approx 0.0$ is not reliable because the system is in mid-eclipse at this phase.

The circular polarization data suggest that the stream accretes onto only one pole, since the excursions in the curve are of only one sign. In this regard, HU Aqr in the low accretion state resembles ST LMi and VV Pup. It is interesting to note, however, that circular polarimetry of HU Aqr in the high state shows both positive and negative excursions (Hakala, unpublished data).

7.2   Indirect imaging of the accretion stream

7.2.1   Removal of the orbital trend

The results of the investigation in chapter 6 suggest that the orbital trend (due to cyclotron beaming) must be subtracted from the light curve before the application of the stream imaging technique. In fact, the stream imaging method cannot be applied successfully to the low state eclipse profiles until this procedure is performed, because there is no obvious stream egress in the light curve. The algorithm will allocate brightness to the model stream in order to reproduce the stream ingress component, but if the orbital trend is not subtracted, the model will not be able to reproduce the phases after eclipse. This is because there is no structure in the original light curve that represents the egress of an extended bright object.

Fortunately, it is much easier to remove the orbital trend from the low state data than was the case in the high state. The eclipse occurs between the maximum at

$\phi \sim 0.80$ and the following minimum at $\phi \sim 1.45$, and therefore the intensity at phases before and after the stream eclipse can be used to establish the orbital trend during the eclipse. This is done by smoothing the intensity values with $\phi \lesssim 0.90$ and $\phi \gtrsim 1.15$ using a running mean over 20 points (this range excludes the phases where the stream is being eclipsed or is coming into view), and then interpolating between the two intervals of smoothed data using a cubic spline. The spline curve is then subtracted from the original light curve (excluding the range $0.956 \lesssim \phi \lesssim 1.036$, where the cyclotron region is not visible). This procedure is illustrated in Fig. 7.3.

7.2.2 Details of the model

As described in chapter 5, several decisions have to be made before the imaging procedure can be applied — these include choosing values for the fixed parameters (M_1, q, i, R_μ, β and ζ), choosing whether to use a one-footpoint or a two-footpoint geometry, and deciding whether to include projection factors in the model calculation to account for optical depth effects.

The simultaneous circular polarimetry indicates one-pole accretion, implying that the one-footpoint geometry is the correct choice. The two-footpoint geometry may be more appropriate, however, if luminous threaded material accumulates in the magnetosphere on field lines whose footpoints lie near the second pole, without proceeding to the white dwarf surface. This stream plasma could contribute to the stream brightness without adding appreciably to the cyclotron flux. For the purposes of this investigation, however, I have opted for the more immediately obvious single footpoint model.

In the high state eclipse profiles, projection factors were included in the model because the stream in the high state is (at least partially) optically thick (see section 4.1.2): this can be seen by the presence of the pre-eclipse absorption dip. In the low state there is not as much direct evidence that optical depth effects are important: for instance, there is no pre-eclipse absorption dip in the optical light
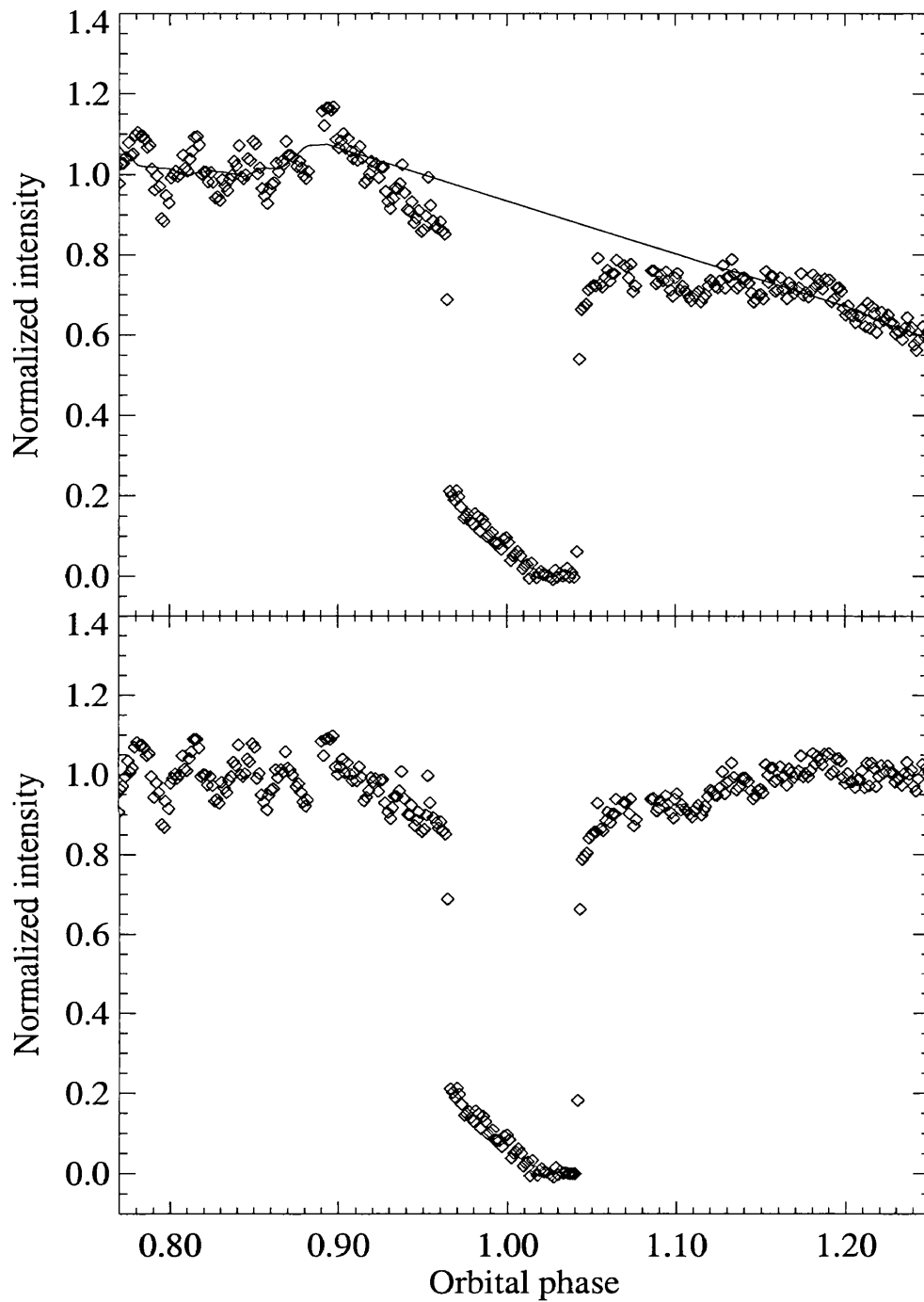
Figure 7.3: Subtracting the orbital trend in the low accretion state photometry of HU Aqr. The upper panel shows the light curve surrounding the eclipse (the eclipse shown is that of cycle 2); superimposed is the spline fit that is used to approximate the orbital trend during the eclipse. The lower panel shows the results of the subtraction procedure (see text for details).

curve. This implies that the parts of the stream that cut the line of sight are not significantly optically thick. However, this does not mean that the entire stream has negligible optical depth: projection effects may be necessary in other parts of the stream. I therefore decided to include projection effects in the stream.

Uncertainties were assigned to the light curves in the following way (this procedure is similar to that in section 5.3.1). Points with $\phi < 0.89$ or $\phi > 1.13$ were assigned large errors, since the accretion stream is fully visible for these phases, and thus no information is available from the eclipses. The narrow phase ranges during which the accretion region is eclipsed ($0.956 \lesssim \phi \lesssim 0.958$) and coming into view ($1.034 \lesssim \phi \lesssim 1.036$) were also assigned large errors, for the same reason as before (section 5.3.1): the model assumes that the accretion region is a dimensionless point, whereas in reality the accretion regions are extended and their eclipses are not instantaneous. The uncertainties used for the remainder of the eclipse profile were assumed to be equal to the Poisson uncertainties ($\sqrt{n}$, where n is the number of counts in a given integration).

The main difference between the high state and the low state eclipse profiles is the remarkably long stream ingress, which is more than twice as long in the low state than in the high state. This implies that the stream travels further away from the line of centres between the component stars and/or further out of the orbital plane before heading towards the white dwarf. The stream models can produce the long stream ingress in two ways. In the first configuration, the values chosen for ζ and R_μ are very large: $\zeta \sim 90°$ and $R_\mu \sim 0.50\,a$. These parameters produce a trajectory where the stream becomes coupled to a magnetic field line close to the secondary. The field line lifts the stream far out of the orbital plane. The long stream ingress component is thus produced by the ingress of the *magnetically-channeled* part of the stream (this configuration is referred to as the "ζ configuration" for brevity). In the second configuration, the ballistic stream is made to leave the L1 point at an angle greater than the usual $\sim 20°$ (Lubow & Shu 1975). By choosing $R_\mu \approx 0.30$, the stream has to travel far from the line of centres before being threaded. The

long stream ingress is then produced by the ingress of the *ballistic* stream (hereafter this configuration is referred to as the "L1 configuration"). The two models are illustrated in Fig. 7.4.

In the L1 configuration, the large angle between the the ballistic stream and the line of centres (approximately 32°) is achieved by increasing the velocities with which the stream leaves the L1 point from $320\,\mathrm{km\,s^{-1}}$ to $450\,\mathrm{km\,s^{-1}}$ in the y-direction (in the direction of the rotation of the secondary) and from $10\,\mathrm{km\,s^{-1}}$ to $100\,\mathrm{km\,s^{-1}}$ in the negative x-direction (along the line of centres towards the white dwarf). This is not justifiable on purely hydrodynamical grounds: Lubow & Shu (1975) calculate that the angle can be at most 28.37° (this occurs in the limit $q \longrightarrow \infty$ or $q \longrightarrow 0$).

An increase in the velocities of the stream at L1 might, however, be caused by the same mechanism that has been proposed to cause the low states in mCVs. Livio & Pringle (1994) invoke star spots on the secondary in the region of the L1 point to explain the low states of VY Scl stars. King & Cannizzo (1998) show that the low states of polars are also consistent with this model. A star spot could inhibit the flow of material through the L1 point by reducing the local scale height in the secondary's atmosphere. For the magnetic field to affect significantly the mass transfer rate, Livio & Pringle (1994) estimate that the magnetic pressure in the star spot would have to be comparable to the gas pressure there. The increased magnetic pressure in the star spot at the L1 point could modify the initial trajectory of the ballistic stream as it leaves the secondary. Although this justification for increasing the velocities of the ballistic stream is speculative, the behaviour of material in a star spot at the L1 point is not well understood, and it is therefore not unreasonable to propose that the increased magnetic pressure at the L1 point could increase the velocities through the L1 nozzle.
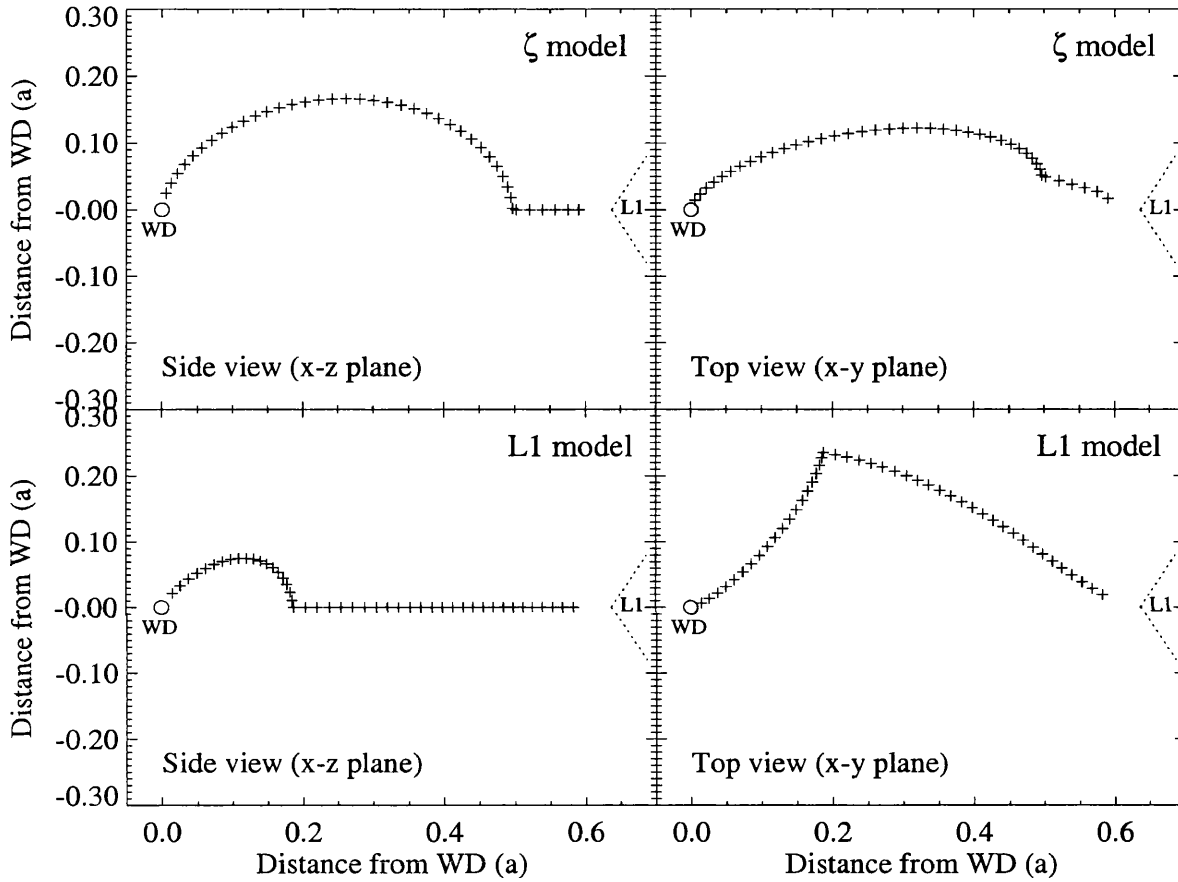
Figure 7.4: The two stream configurations used to model the low state eclipse profiles (the examples shown are those constructed to model the eclipse of cycle 4). The upper panels show the ζ configuration and the lower panels show the L1 configuration (see text for details). The streams are shown projected onto the x-z plane (side view) on the left, and projected onto the x-y plane (viewed from above the orbital plane) on the right.

7.2.3 Stream imaging results

ζ configuration

Fig. 7.5 shows the model fits and the corresponding stream images for the four low state eclipses using the ζ configuration. The dipole offset is $\beta = 25°$, and $R_\mu = 0.50$ in all four fits. The change between the long stream ingress components ($\sim 400\,\text{s}$) of cycles 1 and 2, and the much shorter stream ingresses of cycles 3 and 4 ($\sim 290\,\text{s}$) is achieved by decreasing the value of ζ from 90° for the first two eclipses, to 80° for the last two. The fits have $\chi^2/N \approx 3$.

All four cycles have streams which brighten towards the white dwarf; with the exception of cycle 1, the stream is brightest at the white dwarf. The stream image for cycle 1 has a localized bright region on the magnetically-channeled part of the stream; the other cycles have more slowly-varying brightness distributions along the field line. The first two cycles have bright ballistic streams; in cycle 1 the ballistic stream brightens as it approaches R_μ and in cycle 2 the ballistic stream fades as it approaches R_μ. The last two cycles have fainter ballistic streams, and almost all the stream emission occurs along the magnetically-channeled part of the stream.

The accretion spot (the footpoint of the field line) predicted by the model for cycles 1 and 2 is at a latitude of 12° and a longitude of 30°, where latitude is measured from the spin axis of the white dwarf towards the orbital plane and longitude is measured from the line of centres in the direction of the motion of the secondary star. The spot position for cycles 3 and 4 is slightly different: the latitude is 21° and the longitude is 30°.

L1 configuration

Fig. 7.6 shows the model fits and the corresponding stream images for the four low state eclipses using the L1 configuration. The stream images are shown as projections onto the $(x\text{–}y)$ plane (i.e. looking down onto the orbital plane) for clarity. The dipole offset is $\beta = 25°$ in all four fits. The duration of the stream ingress
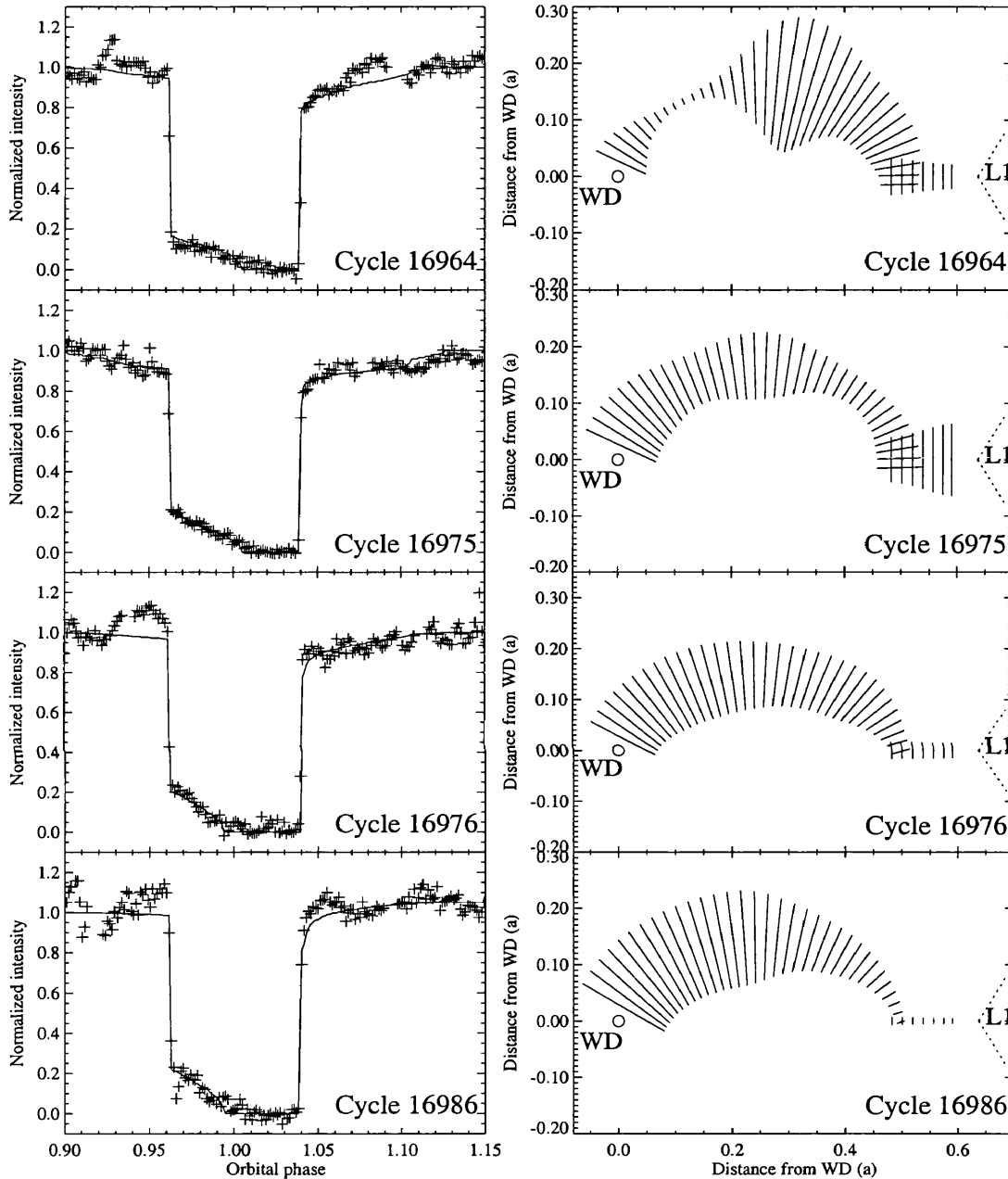
Figure 7.5: Model eclipse profiles and the corresponding stream images for the low state eclipses using the ζ configuration. The stream images are shown projected onto the $(x-z)$ plane. The brightness of each stream emission point is indicated as a line perpendicular to the stream; the length of the line represents the brightness of the point. The white dwarf is shown to scale as a circle (labelled 'WD'), and the secondary is shown (not to scale) to mark the position of the L1 point (labelled 'L1').

is controlled in these models by the value of R_μ: the longer the stream ingress, the smaller the value of R_μ required. The first two eclipses are modelled using $R_\mu = 0.28\,a$, while cycle 3 has $R_\mu = 0.34\,a$ and cycle 4 has $R_\mu = 0.30\,a$. The fits have $\chi^2/N \approx 3$.

The four images have a varied appearance: the ballistic stream brightens towards R_μ (cycles 3 and 4), fades towards R_μ (cycle 2) or stays roughly constant until R_μ (cycle 1), while the magnetically-channeled stream brightens towards the white dwarf (cycles 1, 2 and 4) or stays roughly the same (cycle 3). The cycle-to-cycle changes in the stream images are much larger in the low state than in the high state (this is the case for both the ζ and the L1 configurations).

The footpoint of the accreting field line in cycles 1 and 2 occurs at a latitude of 69° and a longitude of 30°, while in cycles 3 and 4 the footpoint is at 78° latitude and 33° longitude.

7.2.4 Which is the better model of the low state accretion stream?

As was the case with the two-footpoint vs. the one-footpoint geometry models for the high state data, it is difficult to distinguish between the two low state stream configurations on statistical grounds. However, the plausibility of the two models can be checked using other observations of HU Aqr in low accretion states. The main difference between the ζ and the L1 configurations is the angle between the magnetically-channeled part of stream and line of centres. This angle should coincide with the phase at which the absorption dip occurs (see chapter 5 section 5.4.3).

In the low state, although there is no absorption dip in the optical, there *is* an absorption dip in the soft X-rays. In a sequence of *ROSAT* PSPC and HRI light curves of HU Aqr obtained in 'reduced' accretion states from April 1994 to November 1996, Schwope et al. (1998) observe that the pre-eclipse absorption dip approaches the eclipse. During April 1994 and November 1995, the absorption dip
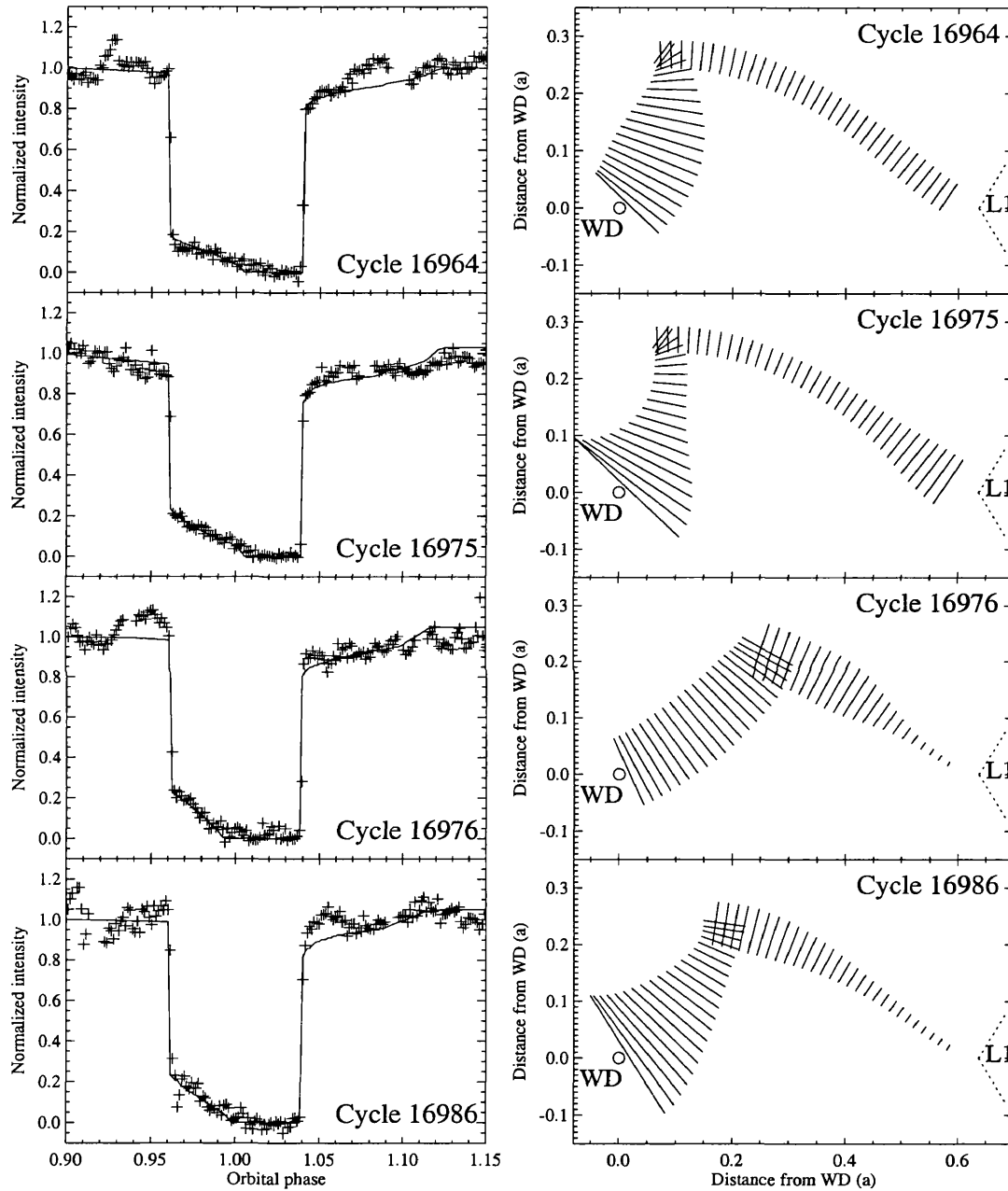
Figure 7.6: As Fig. 7.5 but for the L1 configuration. The stream images are shown projected onto the $(x–y)$ plane (looking down onto the orbital plane) for clarity.

and the eclipse appear as separate structures, while in April 1996 and November 1996 the structures are merged. The absorption dip (or the merged dip/eclipse feature) begins at $\phi \approx 0.885$ in April 1994 and at $\phi \approx 0.937$ in November 1996, implying an angle between the line of centres and the magnetically-channeled part of the stream in the range $23°–42°$. The range of angles in the stream images for the L1 configuration (see Fig. 7.6) is $41°–71°$. Since these two ranges barely overlap, it might be concluded that the L1 configuration is less plausible than the ζ configuration. This argument is not completely secure, however, because of the high degree of variability of the stream geometry observed in the low state. One could speculate that, given the wide range in angles observed in the soft X-ray light curves, much larger separations between the pre-eclipse dip and the eclipse are possible. Since the X-ray observational coverage is not complete, this possibility cannot be ruled out.

7.3 Stokes Imaging of the accretion region

Further clues regarding the nature of the accretion stream geometry can be found in the polarimetry obtained simultaneously with the high speed photometry. The polarimetry is modelled using the Stokes Imaging procedure (Potter et al. 1998) to deduce the structure and location of the accretion region on the white dwarf. The structures on the white dwarf are then compared to the results of the stream imaging technique in order to link the accretion flow between the two stars to the accretion structures on the primary.

7.3.1 Description of the method

The Stokes Imaging procedure produces images of the accretion region on the white dwarf by optimizing model fits to intensity and polarization light curves. The models are based on the cyclotron emission calculations of Wickramasinghe & Meggitt (1985), which are described in section 3.3.2.

The viewing angle to a cyclotron emission point on the white dwarf can be calculated using the formalism of Cropper (1989), which assumes that the white dwarf magnetic field is dipolar and is inclined with respect to the rotation axis by an angle β (this is the same formalism that is used to construct the magnetically-channeled part of the stream trajectories for the stream imaging technique). The cyclotron emission points are assumed to have no vertical height above the white dwarf surface. Given the viewing angle to the point, and values for the electron temperature T_e and the size parameter Λ, the Wickramasinghe & Meggitt cyclotron models can be interpolated to give the Stokes parameters (I, Q, U and V) emitted by the point for all cyclotron harmonics.

An extended emission region is constructed using several adjacent emission points. To calculate the model polarization and intensity, the Stokes parameters are calculated for each point in the region and summed to yield values for the intensity, percentage circular and linear polarization and the resulting position angle of the linear polarization. The corresponding light curves are then constructed by viewing the ensemble of points as a function of phase. Radiative transfer through the accretion region is not calculated; as a first order approximation to optical depth effects, a projection term (the cosine of the viewing angle) is included to simulate absorption effects within the extended accretion region (cyclotron emission is optically thick for the lower harmonics).

Another simplifying assumption used in the Stokes Imaging algorithm is the assumption that the accretion region has no vertical height above the white dwarf surface. This may be inaccurate because the height of the stand-off shock varies approximately inversely with the density of infalling material. In general, therefore, the rim of the shock (i.e. where the flow is less dense) is expected to rise to a considerable height above the white dwarf surface ($\gtrsim 0.1\,R_1$). This raised rim will cool by cyclotron radiation rather than bremsstrahlung (Liebert & Stockman 1985; Wickramasinghe & Meggitt 1985). Other limitations of the Stokes Imaging technique are discussed in Potter et al. (1998).
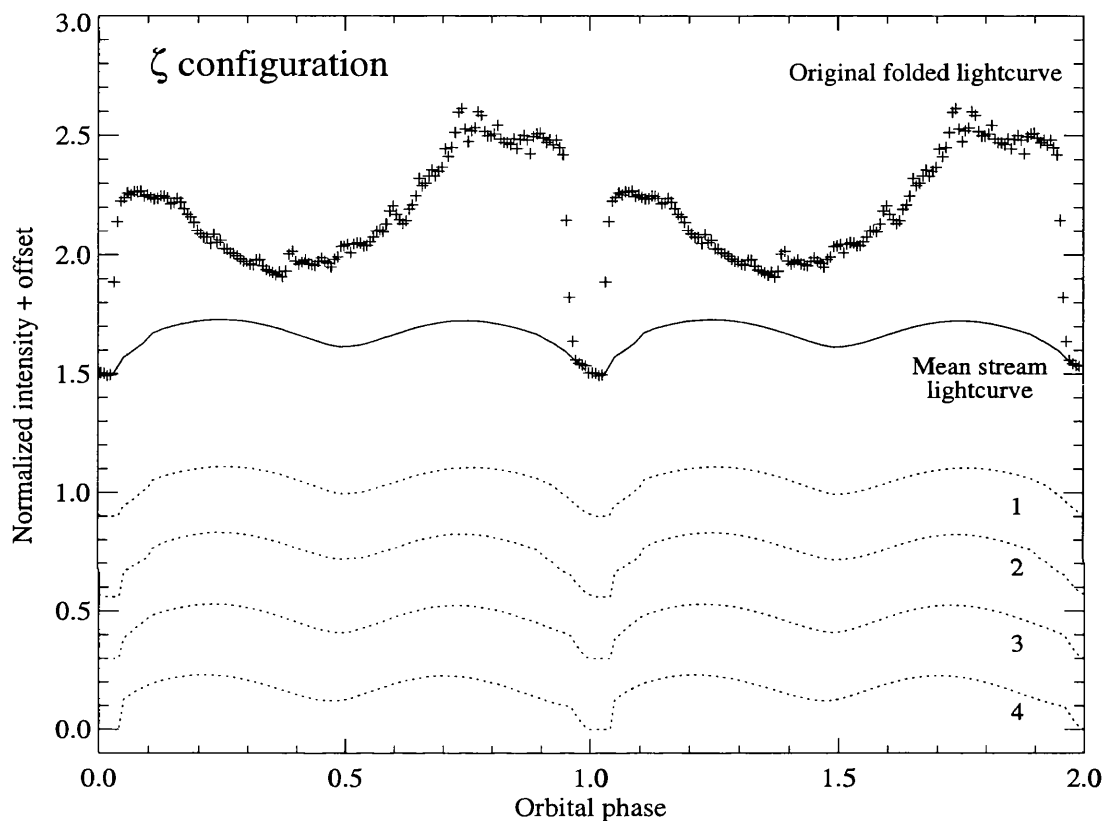
Figure 7.7: Constructing a mean stream light curve for the ζ configuration stream models. The stream light curves derived from the model streams for each eclipse profile are labelled with the corresponding cycle number. These individual light curves are averaged to obtain the mean stream light curve for the ζ configuration. This is shown superimposed on the original intensity light curve at the top of the figure.

Previously (see e.g. Cropper & Warner 1986, Ferrario & Wickramasinghe 1990, Potter et al. 1997, chapter 3), cyclotron intensity and polarization light curves have been modelled by assuming *a priori* the shape and location of the cyclotron region on the white dwarf. The parameters that describe the shape and location of the emission region are adjusted by trial and error until the fit to the polarization light curves is acceptable.

The Stokes Imaging technique performs this procedure in a more objective way by using a genetic algorithm. The surface of the white dwarf is divided into a grid of 1740 points, each representing an area of 6 square degrees in magnetic coordinates. Each emission point on the grid is assigned a value for Λ, and the Stokes parameters are calculated for the emission region for each phase to construct the intensity and polarization light curves as before. A random population of trial solutions is generated, each solution corresponding to a given accretion region on the white dwarf. The GA is then used to breed solutions based on their fitness. The fitness function used for Stokes Imaging has a similar form to equation 4.1, although a Tikhonov regularization term replaces the ME term. The solution from the GA is then refined using Powell's method, as is done in the stream imaging technique. For more details of the method, and tests using synthetic data, see Potter et al. (1998) and Potter (1998).

7.3.2 Removing the stream contribution from the light curve

The Stokes Imaging procedure assumes that the intensity is purely cyclotron in origin, and that the intensity variations are due only to cyclotron beaming of the accretion region emission. If there are other significant sources of optical emission, these should be removed from the intensity light curve before the Stokes Imaging procedure is applied.

The low state eclipse profiles indicate that the accretion stream is a significant contributor to the overall intensity. This contribution can be removed by using the
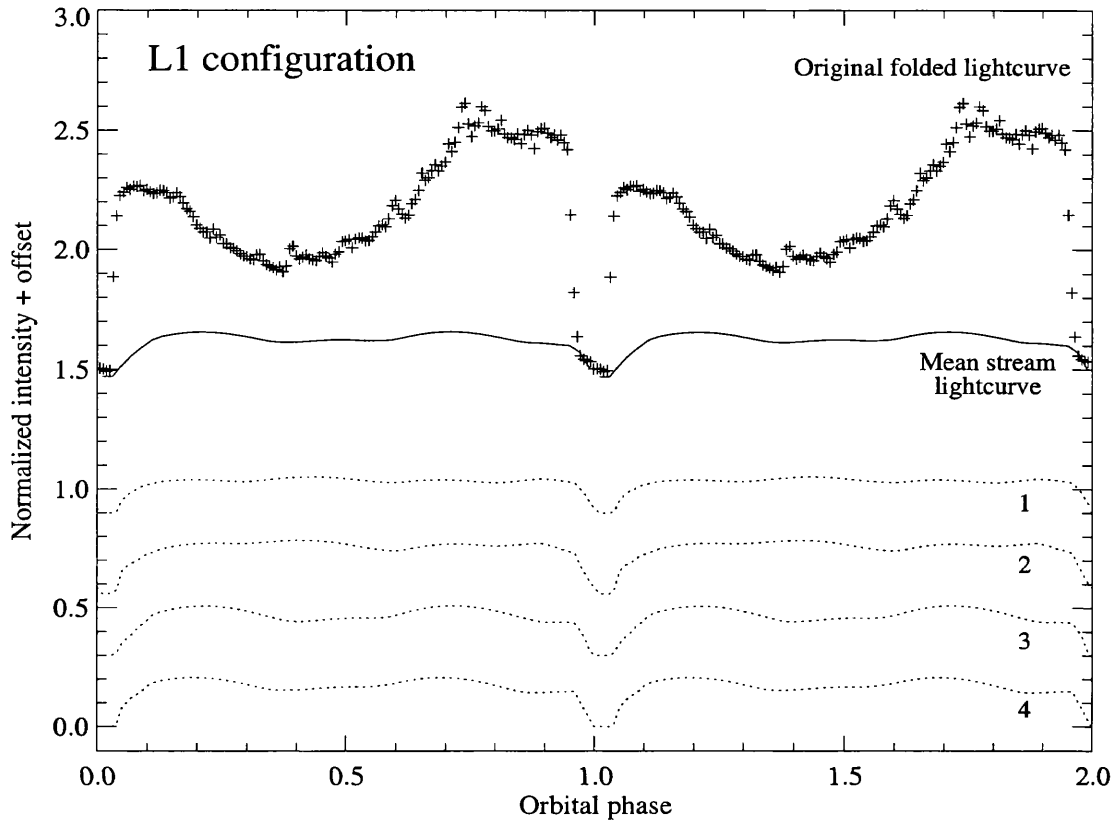
Figure 7.8: As for Fig. 7.7, but for the L1 configuration.

stream models constructed in section 7.2.3. Given a model stream, the corresponding stream light curve can be constructed by "observing" the model stream at all orbital phases. This stream light curve can then be subtracted from the original intensity light curve to yield a better approximation to a pure cyclotron intensity light curve.

The Stokes Imaging procedure is applied to the folded data because the signal-to-noise ratio of the individual intensity and polarization light curves is not sufficiently high to apply the technique to each in turn. It is therefore the folded light curve that must be corrected for the stream emission. A mean stream light curve must therefore be constructed from the individuals stream models for cycles 1–4. This is done by "observing" the model streams for each individual light curve for the whole orbit, and then calculating the mean light curve of the four individual ones.

This process is illustrated for each of the two stream configurations in Fig. 7.7 and Fig. 7.8.

The stream light curves obtained using the ζ configuration have larger amplitudes of variation than the stream light curves from the L1 configuration. This is because in the ζ configuration, the stream is more aligned with the line of centres, and is therefore seen almost edge-on at $\phi = 0.5$ — in projection, therefore, the stream is fainter at this phase (the stream is almost edge-on also at $\phi = 1.0$, when the eclipse by the secondary occurs). The L1 configuration stream is not as well-aligned with the line of centres, and the corresponding streams do not produce an orbital modulation with as large an amplitude because at least part of the stream is not closely aligned with the line of sight at any particular phase.

I subtracted the mean stream light curve for each of the two configurations from the folded intensity light curve to produce the intensity light curves for the Stokes Imaging process.

7.3.3 Stokes Imaging results

ζ configuration

The model fits to the polarization and intensity light curves are shown in Fig. 7.9. These fits were obtained using $i = 85°$ (e.g. Glenn et al. 1994 and chapter 5) and $B = 37\,\mathrm{MG}$ (e.g. Glenn et al. 1994; Schwope et al. 1997). The dipole field has $\beta = 14°$ and $\zeta = 72°$. The gross features of the data are predicted by the model, but some of the details are not well-reproduced. The model underestimates the intensity in the phase range $0.08 \lesssim \phi \lesssim 0.60$ and overestimates the magnitude of the circular polarization in the phase range $0.9 \lesssim \phi \lesssim 1.2$. The model also underestimates the linear polarization level in the range $0.15 \lesssim \phi \lesssim 0.40$.

The accretion region predicted by the model is shown in Fig. 7.10 as a grey-scale image. This figure is an equal-areas projection of the white dwarf in spin coordinates. The line of centres defines longitude zero on the primary; this line
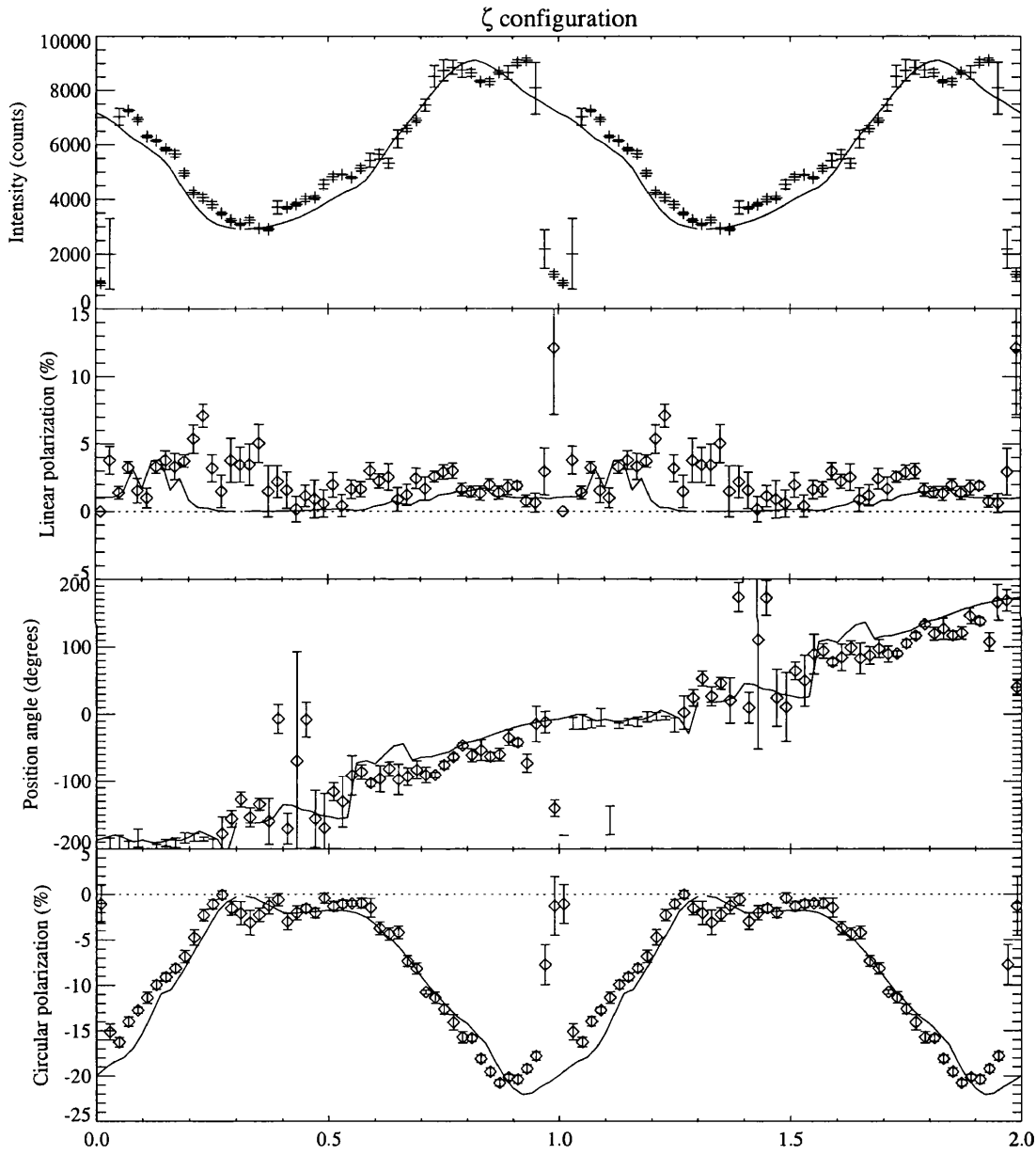
Figure 7.9: The Stokes Imaging model fits to the intensity and polarization light curves for the ζ configuration.

occurs at the centre of the diagram and longitude is measured from this line in the direction of motion of the secondary. Latitude is measured from 0° at the spin pole above the orbital plane (at the top of the diagram). The lines of latitude and longitude indicated are 30° apart. The position of the magnetic pole predicted by the Stokes Imaging method is shown as an asterisk. For comparison, the magnetic pole predicted by the stream imaging method is shown as a plus sign, and the average position of the footpoints of the field lines used in the stream imaging method is shown as a filled circle.

The Stokes Imaging algorithm has predicted a large, broken accretion region near the equator of the white dwarf (i.e. near the orbital plane) composed of two main regions, one extending from a latitude $\sim 50°$ to $\sim 90°$ and longitude $\sim 15°$ to $\sim 45°$, and the other extending from a latitude $\sim 60°$ to $\sim 90°$ and a longitude of $\sim 65°$ to $\sim 85°$. A third smaller and fainter region occurs at latitude $\sim 25°$ and longitude $\sim 100°$.

L1 configuration

The model fits for the L1 configuration are shown in Fig. 7.11. The dipole parameters for this fit are $\beta = 22°$ and $\zeta = 108°$. As for the ζ configuration model, the inclination and field strength were fixed at 85° and 37 MG respectively. The quality of these fits is better than those for the ζ configuration. The phase ranges where the model does not reproduce the data well are similar to the poorly-fit sections of the ζ configuration model. As before, the model underestimates the intensity in the range $0.08 \lesssim \phi \lesssim 1.6$ and overestimates the magnitude of the circular polarization in the range $0.9 \lesssim \phi \lesssim 1.3$. The percentage linear polarization is underestimated in the range $0.1 \lesssim \phi \lesssim 0.4$.

The image of the accretion region generated by the Stokes Imaging procedure is shown in Fig. 7.12. The magnetic pole is indicated by an asterisk in Fig. 7.12, near the third faint emission region. The magnetic pole predicted by the stream imaging method is shown as a plus sign, and the average position of the footpoints of the

Direction of motion of secondary
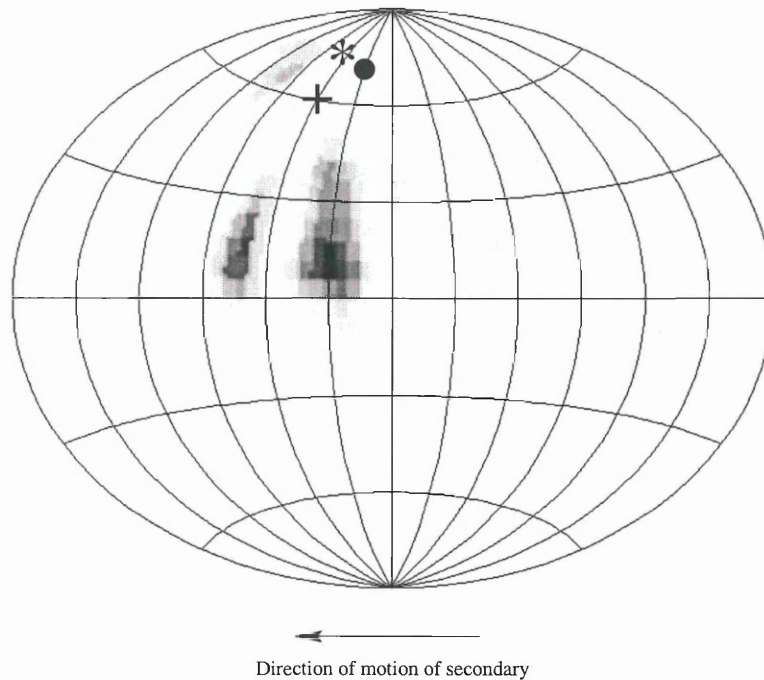
Figure 7.10: An equal-areas projection of the white dwarf surface in spin coordinates showing the results of the Stokes Imaging method for the ζ configuration. See text for details.

field lines used in the stream imaging method is indicated by a filled circle.

As in the ζ configuration, the accretion region is broken into three regions, with most of the emission concentrated in two of the three regions. One of the bright regions extends from a latitude of $\sim 35°$ to $\sim 95°$ and a longitude of $0°$ to $\sim 50°$, and the other is located between $60° - 90°$ in latitude and $55° - 90°$ in longitude. The third region is much fainter and (as before) occurs closer to the spin axis of the white dwarf and closer to the magnetic pole than the two brighter regions, at latitude $\sim 35°$ and longitude $\sim 95°$. The shapes and locations of the accretion regions for the L1 model are very similar to those for the ζ model.
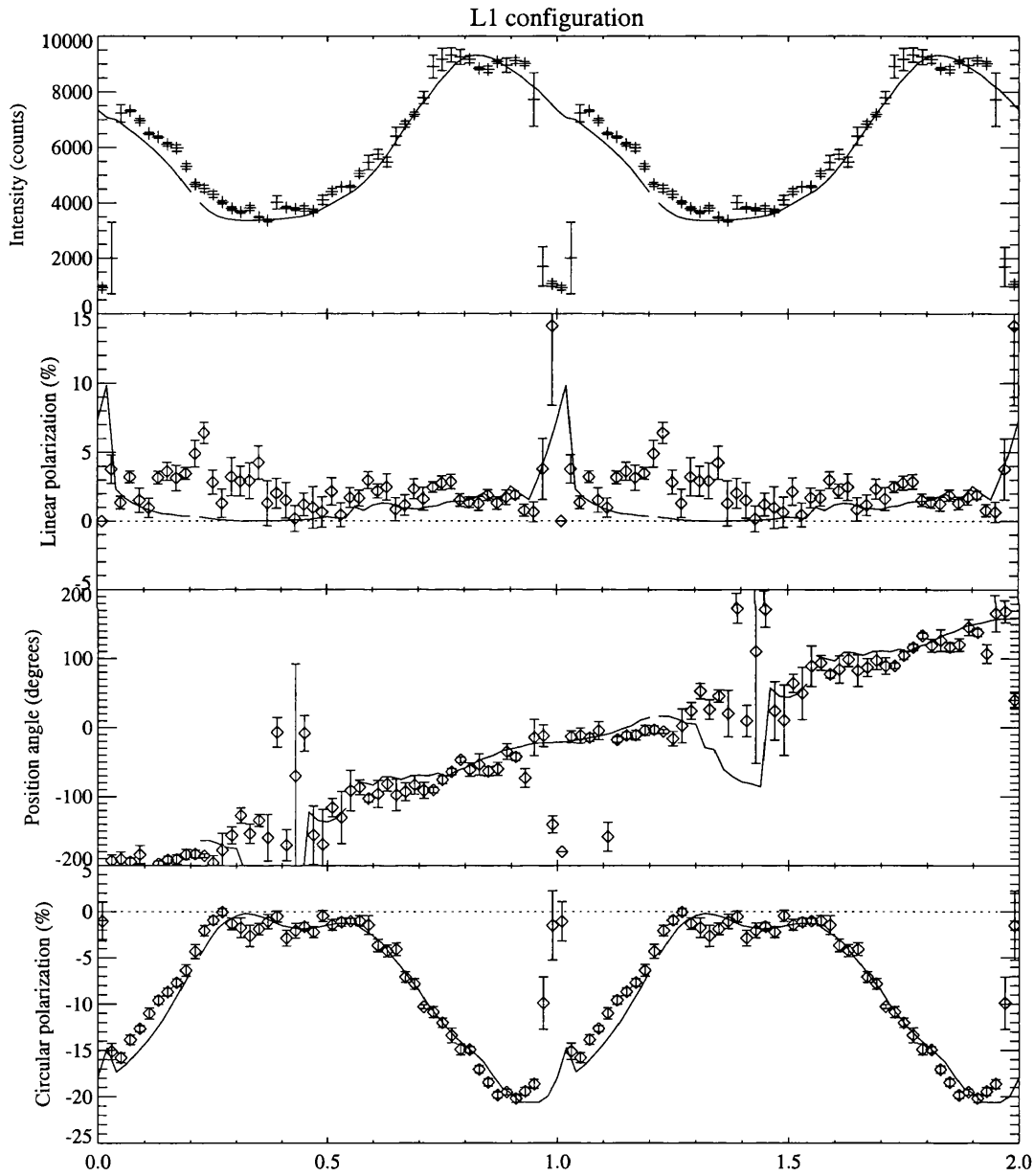
Figure 7.11: As for Fig. 7.9, but for the L1 configuration.

Direction of motion of secondary
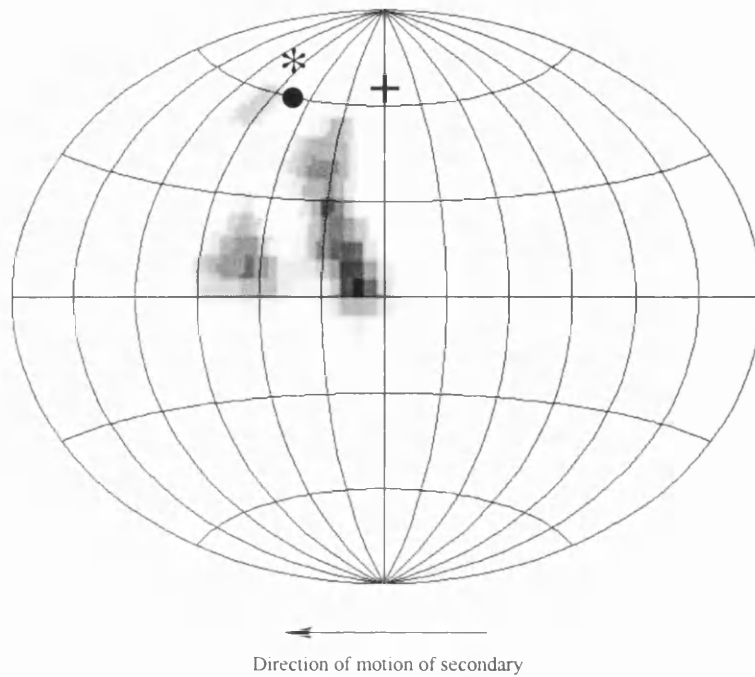
Figure 7.12: As Fig. 7.10, but for the L1 configuration.

7.4 Discussion

7.4.1 Photometry and stream imaging results

The fits to the low state eclipse profiles of HU Aqr are not as good as the fits to the high state data in chapter 5: the high state fits have $\chi^2/N \approx 1$ while the low state fits have $\chi^2/N \approx 3$. Also, the two models that are used to reproduce the extremely long ingress of the low state profiles are somewhat non-canonical. This suggests that the simple trajectory assumed for the stream is not as good an approximation in the low state as in the high state. One might expect that the low state stream would deviate more from the simple model, since the stream is less dense. The stream material is more likely to be threaded along the length of the ballistic stream, instead of the bulk of the stream threading near R_μ. The absence of a pre-eclipse absorption dip in the low state light curves also suggests that the accreting material is more spread out in the magnetosphere: there is no collimated portion of the stream on the same

side of the orbital plane as the observer that is sufficiently optically thick to produce an absorption dip (the alternative explanation for the absence of a dip, viz. that the stream is accreting onto the lower pole, is ruled out by the Stokes Imaging results).

The generally larger values of R_μ imply that the stream couples to the magnetic field further from the white dwarf than in the high state. In the ζ configuration, in particular, the values of R_μ are very large ($R_\mu = 0.50$). The mass transfer rate in the stream can be estimated by following the approach in section 5.4.5. Assuming $\sigma_9 = 3$ as in the high state (since there is no absorption dip in the low state to constrain this value), $M_1 = 0.9$, $B = 37\,MG$ and $q = 0.25$, the mass transfer rate is in the range $0.2 - 2.8 \times 10^{16}\,\mathrm{g\,s^{-1}}$. This is more than an order of magnitude below the values obtained for the high state (section 5.4.5). The main uncertainty in this calculation is the radius σ_9 of the stream, since $\dot{M} \propto \sigma^2$. It is likely that the flow does not remain collimated until R_μ, but threads along the length of the ballistic stream — if this is the case, the estimate of $\dot{M}$ using equation 1.10 will be unreliable, since the equation assumes that the stream has a circular cross-section.

7.4.2   Stokes Imaging results

The shapes and locations of the accretion regions (shown in Figs. 7.10 and 7.12) are similar for both configurations. This is expected, since the two emission distributions produce similar polarization and intensity light curves. The location of the dipole field is, however, noticeably different in the two models. The latitudes of the poles differ by 8°, but the longitudes differ by 36°. The only difference between the input data for the ζ and the L1 configurations is the intensity light curve: the polarization curves for both configurations are identical. The results of the Stokes Imaging process are thus sensitive to slight changes in the intensity light curve.

The shapes and locations of the emission regions on the white dwarf are a direct result of how and where the accretion flow threads onto the magnetic field. Material that is diverted from its ballistic trajectory soon after leaving the secondary will

accrete close to the magnetic pole, while material that threads closer to the white dwarf will accrete further from the pole. Looking at Figs 7.10 and 7.12, the faint region near the magnetic pole could be the accretion region of material that threads far from the white dwarf, while the bright regions nearer the equator might result from material that travels much closer to the white dwarf before being threaded. Since the regions further from the magnetic pole are much brighter than the region near the pole, this suggests that the bulk of the flow penetrates deeply into the magnetosphere before coupling to the field.

The locations of the emission regions are not, however, consistent with a rigid dipolar magnetic field and a straightforward accretion geometry. In the conventional scenario, material that is threaded soon after leaving the secondary should accrete near the line of centres between the two stars. More dense material, which takes longer to be penetrated by the field, will travel further along its ballistic trajectory and closer to the white dwarf before being threaded. This material would thus accrete further from the line of centres. The emission regions on the white dwarf that are closer to the line of centres should thus also be closer to the magnetic pole, while the emission regions far from the pole should be further from the line of centres. This is clearly not the case in in Figs 7.10 and 7.12, where the emission region closest to the magnetic pole is the furthest from the line of centres.

It is therefore likely that the accretion geometry in the low accretion state is quite complex. The magnetic field could be distorted so that the threading region is azimuthally extended — this would enable material to thread onto field lines with footpoints closer to the line of centres, even though the threading occurs close to the white dwarf. Another possiblility is that the assumption of a dipolar field close to the white dwarf is incorrect, and that the field is dominated by higher-order multipoles near the surface.

7.4.3   Comparison of results from the two imaging methods

Figs 7.10 and 7.12 show the locations of the magnetic poles and accretion spots as predicted by the stream imaging models. The magnetic poles for the two imaging methods are very close in the case of the ζ model, but are separated by $\sim 90°$ in longitude in the L1 model. In the L1 model, however, the accretion spot predicted by the stream imaging method is in closer agreement with the emission regions calculated using Stokes Imaging. Although there is not a very close correspondence between the results of the two imaging methods, the accretion regions and magnetic poles all lie within the region between $10°$ and $95°$ in latitude and $0°$ and $100°$ in longitude.

The discrepancies arise because the assumptions of one or both methods are not applicable. The limitations of the stream imaging method are discussed in chapters 4 and 6. A source of error in the Stokes Imaging algorithm that would lead to inaccuracies in the location of the accretion region is the assumption that the accretion region has no vertical height above the white dwarf surface. In reality, it is expected that the cyclotron emitting material is raised significantly above the surface of the white dwarf (see section 7.3.1).

A further consideration is that the field lines might be distorted by the accretion flow. If the assumption of a dipolar field is valid, it might be possible to deduce the way in which the field is distorted by comparing the positions of the accretion region predicted by the two imaging methods.

Chapter 8

Summary of main findings and further discussion

In this chapter I summarize the main results of chapters 3–7. The results are discussed in the light of chapters 1 and 2 (in particular, the questions in section 2.11) to see where progress has been made, and to identify areas where further investigation is required.

8.1 The blobby accretion flow in HU Aqr and the implications for threading

The eclipse profiles of HU Aqr show unambiguously that the source of the flickering in the light curve is the accretion region: the flickering disappears after the accretion column ingress, and reappears immediately after the column egress. The most straightforward interpretation is that the flickering is caused by the impact of inhomogeneities in the stream on the white dwarf. Although the high state does not show clear flare-like events (as seen in e.g. VV Pup: Cropper & Warner 1986), the time scale on which the flickering occurs can be used to obtain a rough estimate of the blob size in the flow. The flickering time scale is $\sim 30\,\mathrm{s}$. Following the argu-

ments outlined in section 2.4, and assuming that the blobs form at R_μ (which, from chapter 5, is approximately $0.2\,a$), the length of the blobs at R_μ in the high state is $\sim 9.3 \times 10^8$ cm.

It is not possible to estimate the blob size in the low state because the light curves have a much poorer time resolution. However, since there is less flickering activity in the low state, it is probable that the stream is less inhomogeneous than in the high state. There is no pre-eclipse absorption dip in the low state, and this is consistent with a stream where there are no dense blobs along the line of sight that would produce an absorption dip. Another eclipsing system that shows pronounced flickering in the high state and almost none in the low state is V895 Cen. This gives weight to the idea that the accretion flow in the high accretion state is more inhomogeneous than in reduced accretion states, i.e. that the mass transfer rate is an important factor in determining the composition of the stream (cf. question 2 in section 2.11).

As outlined in section 2.6, the blobs will not thread where their ram pressure is equal to the magnetic pressure of the white dwarf's field if their dynamical timescale is smaller than the time scale τ_{drag} on which the blob loses energy by exciting Alfvén waves (equation 2.3). Using the above estimate of the blob length, and $R_\mu = 0.20\,a$ (from chapter 5), $B = 37\,\mathrm{MG}$, $M_1 = 0.9$ and a temperature of $10^4\,\mathrm{K}$ at R_μ (Hameury, King & Lasota 1986), $\tau_{\mathrm{drag}} \sim 10^4\,\mathrm{s}$ while $\tau_{\mathrm{dyn}} \sim 10^2\,\mathrm{s}$. These quantities can be compared to the Kelvin-Helmholtz timescale, i.e. the time scale on which a blob is eroded (equation 2.1). For $\eta \lesssim 0.1$, the Kelvin-Helmholtz time scale is $\tau_{\mathrm{KH}} \gtrsim 2 \times 10^4$ s. This means that the velocity of the blobs perpendicular to the field is reduced on a similar time scale as the blobs are eroded, and that both these time scales are much longer than the dynamical time scale. It is thus likely that blobs in the high state accretion flow are capable of penetrating far into the magnetosphere before being threaded or eroded.

The available evidence suggests that the flow in the high state is highly inhomogeneous and threads close to the white dwarf, and in the low state the flow is

less inhomogeneous and threads further from the white dwarf. One might predict, therefore, that if the stream threads close to the white dwarf, the system will have a larger soft X-ray excess. Interestingly, this is precisely the opposite of the correlation noted by Ramsay et al. (1994), who found that the larger the soft X-ray excess, the *larger* the (spherical) Alfvén radius.

It is difficult to reconcile the Ramsay et al. (1994) correlation with our current understanding of the origin of the blobs in the flow. If the stream couples to the magnetic field far from the white dwarf, one would expect that any dense blobs in the stream would have a greater chance of being eroded by the time they reach the white dwarf. This means that the systems with *smaller* values of R_μ should have the *larger* soft X-ray excesses. A speculative solution to this paradox is as follows. If the blobs are formed near the L_1 point (as opposed to in the threading region) and the stream threads far from the white dwarf, the threading process will be less turbulent, since the stream has not accelerated significantly by the time the material is threaded. Conversely, if the stream threads near to the white dwarf, the kinetic energy of the stream material will be considerable when the stream reaches R_μ, and the dissipation of this energy at might destroy more of the blobs as the stream is threaded. For this scenario to work, however, one has to assume that the threading process preserves the blobs in the stream. In addition, the blobs must survive intact until they reach the white dwarf: this would be the case if the Kelvin-Helmholtz efficiency η (see equation 2.1) is very low (i.e. $\eta \ll 0.1$).

8.2   The high and low accretion states of HU Aqr

There is clearly a substantial change in the accretion flow of HU Aqr from the high to the low accretion state. One major difference is that the ratio of the stream brightness to the accretion column brightness is much smaller in the low than in the high state. This means that, as $\dot{M}$ decreases, the stream brightness drops more rapidly than the column brightness at optical wavelengths. Simplistically one would

think that the ratio would stay the same: a smaller $\dot{M}$ implies a lower stream density, which implies less shock heating in the stream and/or reduced absorption of high energy photons, but then a smaller $\dot{M}$ should also imply a reduced accretion flux. It is interesting that the brightness of the stream is more sensitive than the brightness of the accretion region to changes in the mass transfer rate.

There are two other systems that are similar to HU Aqr in this regard. These are V895 Cen (D. Buckley, private communication) and UZ For (Bailey & Cropper 1991; Bailey 1995). In its high accretion state, V895 Cen shows a prominent stream component in the eclipse profile, while in the low state the stream component vanishes and only the accretion column component remains (e.g. Stobie et al. 1996). In UZ For, the low state eclipse profile shows components due to a single accretion region and the white dwarf photosphere (Bailey & Cropper 1991). In the high state (Bailey 1995), a prominent stream component appears (and, interestingly, *two* accretion regions are now visible in the eclipse profile). The evidence from HU Aqr, V895 Cen and UZ For suggests, therefore, that the overall stream brightness is very sensitive to $\dot{M}$ (cf. question 5 in section 2.11).

There is considerable evidence to support the idea that the accretion flow in the low state is more complicated than the simple quasi-one dimensional models adopted in chapter 7: in addition to the evidence that the low state flow has a complicated geometry (described in section 7.4.1 and 7.4.2), the low state flow is much more variable than the high state flow on short time scales. In the stream imaging models, both the parameters for the model and the resulting stream images are highly variable from cycle to cycle (in both the L1 and the ζ configurations). The most dramatic change occurs on 13 October 1996, where the stream ingress component changes from 390 s to 270 s in two successive cycles. This change is modelled in the L1 configuration as an increase in R_μ from 0.28 a to 0.34 a, and in the ζ configuration as decrease in ζ from 90° to 80°. This behaviour is strongly reminiscent of the change observed by Glenn et al. (1994), illustrated in Fig. 2.8. Here too, the stream ingress lengthens by more than a minute between successive

eclipses. Interestingly, the observations of Glenn et al. (1994) were also made when the system was in a low state ($V \sim 16.5\,$mag); the overall shape of their light curve is very similar to that in the top panel of Fig. 7.1. By contrast, the parameters used to model the high state data (section 5.3.2) are very steady over the five days of observation, with only small drifts in R_μ. Dramatic variability such as that observed in the low state has not been seen in high accretion state observations to date.

The sequence of HRI light curves from Schwope et al. (1998), described in section 7.2.4, were all obtained in a 'reduced' accretion state. During the initial observations, the absorption dip and the eclipse appear as separate structures, while at later epochs the structures are merged. This is further evidence for a high degree of variability in the trajectory of the accretion flow during low accretion states.

This evidence is relevant to question 7 in section 2.11, viz. the causes of variability in the accretion flow. Changes in the flow trajectory can occur without a change in $\dot{M}$; also, the flow shows a much larger degree of variability in low accretion states. This, of course, raises another question: why is the high state accretion flow more stable than the low state flow?

The discussion in section 8.1 suggests that the high state flow is more inhomogeneous than the low state flow, and the above discussion implies that the trajectory of the low state flow is more variable than that in the high state. An interesting conclusion results: the more homogeneous flow has a more variable trajectory than the inhomogeneous flow. This is contrary to the expectation outlined in question 7 in section 2.11.

8.3 Cooling mechanisms for the accretion stream

One of the more remarkable features of the eclipse profiles of HU Aqr in both its high and low accretion states is that the fraction of the overall system brightness due to the accretion stream is comparable to the brightness of the accretion region on the white dwarf. I thus examine the emission mechanisms that could operate in the

stream, and discuss whether they are able to account for the observed stream flux and for the wavelength dependence of the stream brightness distributions observed in the models of the high state data. Cyclotron cooling, line emission, free-free emission and blackbody emission are examined as possible mechanisms to account for the bright accretion stream component. This discussion addresses question 3 in section 2.11.

The optical flux of polars is often dominated by polarized cyclotron radiation. The cyclotron flux will be greatest where the thermal velocities of the electrons are highest; the bulk of the cyclotron radiation will thus be emitted in the post-shock flow near the white dwarf surface. The height of the cyclotron-emitting region above the white dwarf surface has been estimated from models of optical intensity and polarization variations by Cropper (1986) and Cropper & Warner (1986) to be very much smaller than the radius R_1 of the white dwarf ($\sim 0.01\,R_1$ in VV Pup, and $< 0.005\,R_1$ in ST LMi). Brainerd (1989) proposes an alternative model where the optical and infrared cyclotron radiation is emitted from a hot plasma *above* the accretion shock, as opposed to an extended low-density region surrounding the X-ray emitting core of the accretion region (as is proposed for models of inhomogeneous accretion: see e.g. Wickramasinghe & Meggitt 1985). In this model, the cyclotron-emitting region is still relatively close to the white dwarf surface, and cannot account for the brightness of the accretion stream many white dwarf radii from the white dwarf surface. Evidence from simultaneous optical polarimetry and high-speed photometry of HU Aqr suggests that the stream emission has low polarization levels: when the accretion region is obscured during the eclipse ingress, the percentage circular polarization decreases sharply and remains low for the duration of the stream ingress, before the low signal-to-noise during totality precludes accurate polarization measurements. This suggests that the accretion stream emission has very low polarization levels, and is thus not likely to be of cyclotron origin.

Can the bright stream emisson be accounted for by line emission? The common perception is that the accretion stream contributes to the optical light chiefly in the

form of line emission (e.g. Schwope et al. 1998). As discussed in section 5.4.4, this is *not* the case for HU Aqr. In the high state, the ratio of the stream continuum flux to the line flux exceeds ~ 4, while even in the low state the stream continuum flux exceeds the line flux by a factor of ~ 2.5. Also, the brightest feature in the Doppler tomograms corresponds to emission from the ballistic part of the stream (see Fig. 5.16), whereas the stream images show that the total emission from the ballistic stream is far less than that from the magnetosphere.

The dominant cooling mechanism for the stream plasma is thus continuum emission (free-free or bound-free emission) with a low level of polarization. First, I investigate whether the observed stream continuum flux can be accounted for by free-free emission. To do this, estimates are required for the emitting volume V, the temperature T and the electron number density n_e of the stream plasma. Liebert & Stockman (1985) estimate a temperature of $\sim 10^4$ K in the magnetically-channeled part of the stream; line ratios indicate electron densities n_e in the range 10^{13} cm^{-3}–2×10^{14} cm^{-3}. The emitting volume V can be estimated from the stream models by assuming that the emitting volume is cylindrical in shape, with radius $\sigma_9 = 3.0$ (as calculated in section 5.4.5) and a length equal to the sum of the ballistic and the magnetic stream path lengths. This yields V in the range $(1.1–1.9)\times 10^{30}$ cm^3. The total free-free luminosity is given by

$$L_{\text{ff}} = 2.1 \times 10^{-26}\, n_e^2\, V \text{ erg cm}^{-3}\,\text{s}^{-1} \tag{8.1}$$

(Blumenthal & Tucker 1974) where the integration is performed over optical energies only, and the Gaunt factor for $E \sim kT$ is used. The resulting free-free flux is in the range 3×10^{-13}–2×10^{-10} erg cm^{-2} s^{-1} for a distance of 250 pc (Schwope et al. 1993).

These values have to be compared to the optical continuum flux due to the stream. The mean magnitudes in Table 5.1 were used to estimate the continuum emission of the system in each waveband, and the values in Table 5.2 were used to estimate the fraction of the continuum emission that originates in the stream. The

total continuum stream emission is approximately $8 \times 10^{-12}\,\mathrm{erg\,cm^{-2}\,s^{-1}}$, which falls into the range of values for L_{ff}. The distance of 250 pc is a lower limit; the system would have to be further than 490 pc for the smallest value of L_{ff} to yield a flux less than the observed amount.

There are several reasons, however, why free-free emission cannot be the only component of the continuum emission from the stream. Firstly, the stream material is optically thick both in the emission lines and in the continuum. The optical depth of the stream in the continuum can be seen in the shape of the pre-eclipse absorption dip: the accretion stream has an approximately Gaussian optical depth profile, where the core of the stream is significantly optically thick and the wings are less so. The emission lines in polar spectra have inverted line strengths relative to recombinational values, implying optically thick emission (Hakala et al. 1993; Schwope et al. 1997).

The fluxes of the stream as deduced from the stream models (section 5.3.2) do not have the correct wavelength dependence to match a free-free emission spectrum. Instead, the fluxes in the various sections of the stream are closer to blackbody spectra (see section 5.3.2 and Figs 5.9 and 5.15). They do not match a blackbody curve exactly, deviating in the U and R fluxes which fall significantly below a blackbody curve (i.e. the four-point 'spectrum' has too convex a shape to fit a blackbody curve); this is the case for both the two-footpoint and the one-footpoint geometry model results. Adding a free-free component to the model spectrum exacerbates the problem in that it tends to flatten out the curved shape of the model spectrum.

The stream fluxes in the various sections of the stream peak in B in most cycles and most stream sections (for both geometries); this is roughly consistent with a black-body of temperature 6500 K. This temperature is of the same order of magnitude as that used above for the magnetically-channeled part of the stream (10^4 K: Liebert & Stockman 1985). The exceptions occur in the results from the two-footpoint geometry models. In four out of the five cycles in the two-footpoint geometry models, the stream sections on the magnetic part of the stream immedi-

ately adjacent to R_μ have fluxes that are consistent with a slightly higher blackbody temperature of 7400 K. The observed fluxes have not been corrected for reddening, either intrinsic to the system or interstellar in origin. If the fluxes are reddened significantly, the U-band fluxes will suffer the most, and the temperature estimates will be systematically too low.

If the two-footpoint model is the more accurate representation of the stream, and it is assumed that the stream fluxes can be characterized roughly by a blackbody spectrum, the four-point spectra of the stream sections imply that the stream material that has just been threaded at $\sim R_\mu$ is slightly hotter than the fully-threaded plasma closer to the white dwarf and than the free-falling plasma before R_μ. This is consistent with the scenario described in section 2.6, where the stream plasma experiences shock heating as it interacts with the magnetic field near R_μ. This result is not very secure, however, since the one-footpoint model results do not imply elevated temperatures near R_μ. Also, when the orbital trend is subtracted prior to the application of the stream imaging technique (chapter 6), the region of the stream with U comparable to B is not adjacent to R_μ, but is closer to the white dwarf.

Since the stream is significantly optically thick in both the lines and the continuum, a detailed description of the cooling mechanisms that cause the stream to radiate at $T \sim 10^4$ K must include a full treatment of the radiative transfer through the stream.

8.4 The bright regions in the stream images

An important finding of the stream imaging technique (as applied to data of HU Aqr) is that, in most cases, there is no obvious brightening towards or at the join point between the ballistic and the magnetically-channeled parts of the stream (some exceptions to this are the stream images of the high state data for the one-footpoint configuration). This means that the total stream emission is *not* dominated by

emission from the interaction region (cf. question 4 in section 2.11). This cannot be deduced from Doppler tomography, because the velocities of the plasma in the threading region are not known — a unique transformation from velocity to spatial coordinates cannot therefore be made.

If the dominant heating mechanism in the stream were photoionization, the stream images might be expected to be brightest near the white dwarf. Also, if the interaction between the plasma and the magnetic field in the threading region were an important heating mechanism, one would expect the stream images to be bright in the region near R_μ. Instead of showing bright regions near R_μ or at the white dwarf, many of the stream images show localized bright regions on the 'top' or 'bottom' of the field line, i.e., where the threaded material is closest to the critical Roche surface of the primary. Threaded material is expected to slow down as it follows a field line and climbs out of the potential well of the primary: in the stream models of both Mukai (1988) and Heerlein et al. (1999), threaded material decelerates as it climbs out of the Roche potential (possible mechanisms whereby the threaded material is lifted out of the orbital plane are discussed by Li 1999). In principle, the material could be lifted out of the orbital plane but not have sufficient energy to go 'over the hill' in the Roche potential. This material could stagnate near the 'top' of the field line with zero velocity. The bright regions in the stream images could correspond to emission from stagnation regions out of the orbital plane. The bright regions of the stream thus do not correspond to regions where the local mass transfer rate is high, but rather regions where there is a large volume of (perhaps stationary) emitting material.

8.5 Improvements to the stream imaging method

The stream imaging method could be improved significantly by using a more realistic stream trajectory. Given our incomplete understanding of the stream behaviour, however, it is not straightforward to decide how best to modify the simple quasi-one

dimensional model. Possible modifications include a stream trajectory calculation incorporating a drag term to simulate the opposition of the flow perpendicular to the field (e.g. King 1993; Wynn & King 1995, section 2.10) as is used by Schwope et al. (1997) to model the location of the components in their Doppler tomograms of HU Aqr. Another possibility would be to use the stream geometry from the 'magnetic stripping' model of Heerlein et al. (1999) (see section 2.10).

In principle, the stream imaging technique could be modified so that a pre-set stream trajectory is not required. A three-dimensional grid could be set up between the two stars with an emission point at each node of the grid. The number of emission points in the model would be several orders of magnitude greater than in the current models, and the time taken to compute solutions would be substantially longer than in the quasi-one-dimensional case, since the time taken to evaluate the fitness function for each solution increases dramatically with the number of free parameters. Formally, the problem would not require additional constraints other than the ME regularization. In practice, however, because many points in the grid would be eclipsed at each phase step, the results might be more artefact-prone than those from the quasi-one-dimensional model. The results would be more difficult to interpret than those presented here.

In its present form, the effectiveness of the stream imaging technique would be improved by applying the method to spectrally-resolved (i.e. narrow band) eclipse light curves. This is the approach used by Rutten et al. (1994) to extend the ME eclipse mapping technique of Horne (1983, 1985) in order to reconstruct the spectra from isolated parts of the accretion disc of the nova-like variable UX UMa. Using spectrally-resolved data of eclipsing polars, a spectrum of the different sections of the stream could then be constructed as in Fig. 5.9 and 5.15, but with much better spectral resolution. Such observations of eclipsing polars are scheduled in early 1999 using the new generation of colour-sensitive optical Super-conducting Tunnel Junction detectors (for a description see e.g. Peacock et al. 1997).

Spectrally-resolved eclipse profiles would allow the continuum emission of the

stream to be separated from the line emission. The stream images constructed using the light curves of individual emission lines would then be directly comparable to Doppler tomograms. This would remove the current problems of interpretation that arise because the stream images show the total emission in a broad waveband while the Doppler tomograms are images of a single emission line.

8.6 The major findings of this study

In this final section, I summarize the major findings of this thesis. They are:

- The high $\dot{M}$ of V1309 Ori implies that the orbital evolution of polars above the period gap cannot be driven by gravitational radiation alone. Magnetic braking still plays a significant role despite the suppression of the wind from the secondary by the strong primary magnetic field.

- The stream is not the source of flickering; the accretion region is.

- The threading region of the accretion stream is not, in most cases, significantly hotter or brighter than the rest of the stream.

- The brightest parts of the stream are not necessarily those nearest the white dwarf, nor do they correspond to regions where there is a large local mass transfer rate. The bright regions of the stream correspond instead to regions where material accumulates in the flow, e.g. at the 'top' of field lines where threaded material decelerates as it is lifted out of the orbital plane towards the critical Roche surface.

- The behaviour of the accretion flow in HU Aqr in the low accretion state is far more variable on short time scales than the flow in the high state.

- The evidence suggests that the stream in HU Aqr may be capable of distorting the magnetic field of the white dwarf even in the low accretion state.

- The dominant cooling mechanism in the stream is not line emission. In high accretion states, the continuum flux from the stream may even exceed the cyclotron flux from the accretion region.

- Doppler tomograms and the stream images provide complementary pictures of the accretion stream of HU Aqr. While Doppler tomograms show that most of the *line* emission from the stream originates in the ballistic stream, the stream images indicate that most of the *total* (line and continuum) emission originates in the magnetically-channeled region.

- The brightness of the stream is strongly dependent on the accretion state of the system, and is more sensitive to changes in the mass transfer rate than is the brightness of the accretion region.

References

Achilleos N., Wickramasinghe D.T., Wu K., 1992, MNRAS, 256, 80

Allen C.W., 1976, Astrophysical Quantities (3rd ed). Athlone Press, London

Arons J., Lea S.M., 1976, ApJ, 207, 914

Arons J., Lea S.M., 1980, ApJ, 235, 1016

Bailey J., 1981, MNRAS, 197, 31

Bailey J., 1988, in Coyne G.V. et al., eds, Polarized radiation of circumstellar origin. Vatican Obs., Vatican, p. 105

Bailey J., 1995, in Buckley D.A.H., Warner B., eds, Cape Workshop on magnetic cataclysmic variables, ASP Conf. Ser. no. 85. ASP, California, p. 10

Bailey J., Cropper M., 1991, MNRAS, 253, 27

Bailey J., Ferrario L., Wickramasinghe D.T., 1991, MNRAS, 251, 37

Bailey J.A., Ferrario L., Wickramasinghe D.T., Buckley D.A.H., Hough J.H., 1995, MNRAS, 272, 579

Bailey J., Watts D.J., Sherrington M.R., Axon D.J., Giles A.B., Hanes D.A., Heathcote S.R., Hough J.H., Hughes S., Jameson R.F., McLean I., 1985, MNRAS, 215, 179

Baker J.G., Menzel D.H., 1938, ApJ, 88, 52

Barwig H., Ritter H., Bärnbantner O., 1994, A&A, 288, 204

Bath G.T., Evans W.D., Pringle J.E., 1974, MNRAS, 166, 113

Beasley D., Bull D.R., Martin R.R., 1993, Univ. Computing, 15, 58

Berg R.A., Duthie J.G., 1977, ApJ, 211, 859

Beuermann K., Burwitz V., 1995, in Buckley D.A.H., Warner B., eds, Cape Workshop on Magnetic Cataclysmic Variables, ASP Conf. Ser. no. 85. ASP, California, p. 99

Beuermann K., Thomas H.C., 1993, Adv. Space Res., 13, 115

Biermann P., Schmidt G.D., Liebert J., Stockman H.S., Tapia S., Kühr H., Strittmatter P.A., West S., Lamb D.Q., 1985, ApJ, 293, 303

Blandford R.D., Eichler D., 1987, Phys. Rep., 154, 1

Blumenthal G.R., Tucker W.H., 1974, in Giacconi R., Gursky H., eds, X-ray Astronomy. Reidel, Dordrecht, p. 99

Bonnet-Bidaud J.M., Mouchet M., 1987, A&A, 188, 89

Brainerd J.J., 1989, ApJ, 345, 978

Buckley D.A.H., Haberl F., Motch C., Pollard K., Schwarzenberg-Czerny A., Sekiguchi K., 1997, MNRAS, 287, 117

Buckley D.A.H., O'Donoghue D., Hassall B.J.M., Kellett B.J., Mason K.O., Sekiguchi K., Watson M.G., Wheatley P.J., Chen A., 1993, MNRAS, 262, 93

Buckley D.A.H., Sekiguchi K., Motch C., O'Donoghue D., Chen A.-L., Schwarzenberg-Czerny A., Pietsch W., Harrop-Allin M.K., 1995, MNRAS, 275, 1028

Buckley D.A.H., Shafter A.W., 1995, MNRAS, 275, L61

Buckley D.A.H., Twohy I.R., 1989, ApJ, 344, 376

Burwitz V., Reinsch K., Beuermann K., Thomas H.-C., 1996, A&A, 310, 25

Campbell C.G., 1989, MNRAS, 236, 475

Campbell C.G., 1997, Magnetohydrodynamics in binary stars, Kluwer, Dordrecht

Cannizzo J.K., 1993, in Wheeler J.C., ed., Accretion Discs in Compact Stellar Systems. World Sci. Publ. Co., Singapore, p. 6

Chanmugam G., 1992, Ann. Rev. Astron. Astrophys., 30, 143

Chanmugam G., Wagner R.L., 1977, ApJ, 213, L13

Charbonneau P., 1995, ApJSS, 101, 309

Clayton K.L., Osborne J.P., 1994, MNRAS, 268, 229

Cowley A.P., Crampton D., 1977, ApJ, 212, L121

Cowley A.P., Crampton D., Hutchings J.B., 1982, ApJ, 259, 730

Crawford J.A., Kraft R.P., 1956, ApJ, 123, 44

Cropper M., 1985a, MNRAS, 212, 719

Cropper M., 1985b, Ph.D. thesis, University of Cape Town

Cropper M., 1986, MNRAS, 222, 853

Cropper M., 1989, MNRAS, 236, 935

Cropper M., 1990, SSRv, 54, 195

Cropper M., Harrop-Allin M.K., Mason K.O., Mittaz J.P.D., Potter S., Ramsay G., 1998, MNRAS, 293, L57

Cropper M., Horne K., 1994, MNRAS, 267, 481

Cropper M., Mason K.O., Allington-Smith J.R., Branduardi-Raymont G., Charles P.A., Mittaz J.P.D., Mukai K., Murdin P.G., Smale A.P., 1989, MNRAS, 236, L29

Cropper M., Mukai K., Mason K.O., Smale A.P., Charles P.A., Mittaz J.P.D., Machin G., Hassall B.J.M., Callanan P.J., Naylor T., van Paradijs J., 1990, MNRAS, 245, 760

Cropper M., Ramsay G., Wu K., 1998, MNRAS, 293, 222

Cropper M., Warner B., 1986, MNRAS, 220, 633

Daly P.N., Beard S.M., 1994, Starlink User Note 27, Rutherford Appleton Laboratory

de Jager O., 1991, ApJ, 378, 286

de Kool M., 1992, A&A, 261, 188

Dhillon V.S., Marsh T.R., 1993, in Regev O., Shaviv G., eds, Cataclysmic variables and related physics. Inst. Phys. Publ., Bristol, p. 34

Dhillon V.S., Marsh T.R., Duck S.R., Rosen S.R., 1997, MNRAS, 285, 95

Diaz M.P., Steiner J.E., 1994, A&A, 283, 508

Downes R.A., Webbink R.F., Shara M.M., 1997, PASP, 109, 345

Drell S.D., Foley H.M., Ruderman M.A., 1965, J. Geophys. Res., 70, 3131

Elsner R.F., Lamb F.K., 1976, Nature, 262, 356

Faulkner J., 1971, ApJ, 170, L99

Ferrario L., Bailey J., Wickramasinghe D.T., 1993, MNRAS, 262, 285

Ferrario L., Bailey J., Wickramasinghe D.T., 1996, MNRAS, 282, 218

Ferrario L., Wickramasinghe D.T., 1990, ApJ, 357, 582

Ferrario L., Wickramasinghe D.T., Bailey J., Buckley D.A.H., 1995, MNRAS, 273, 17

Ferrario L., Wickramasinghe D.T., Tuohy I.R., 1989, ApJ, 341, 327

Frank J., King A.R., Lasota J.-P., 1988, A&A, 193, 113

Frank J., King A.R., Raine D., 1985, Accretion power in astrophysics (1st ed). Cambridge University Press, Cambridge

Frank J., King A.R., Raine D., 1992, Accretion power in astrophysics (2nd ed). Cambridge University Press, Cambridge

Frank J., Lasota J.P., Chanmugam G., 1995, ApJ, 453, 446

Garnavich P.M., Szkody P., Robb R.M., Zurek D.R., Hoard D.W., 1994, ApJ, 435, L141

Glenn J., Howell S.B., Schmidt G.D., Liebert J., Grauer A.D., Wagner R.M., 1994, ApJ, 424, 967

Greeley B.W., Blair W.P., Long K.S., Raymond J.C., 1999, ApJ, 513, 491

Haberl F., Motch C., 1995, A&A, 297, 37

Haberl F., Thorstensen J.R., Motch C., Schwarzenberg-Czerny A., Pakull M., Shambrook A., Pietsch W., 1994, A&A, 291, 171

Hakala P.J., 1995, A&A, 296, 164

Hakala P.J., Watson M.G., Vilhu O., Hassall B.J.M., Kellett B.J., Mason K.O., Piirola V., 1993, MNRAS, 263, 61

Hameury J.M., King A.R., 1988, MNRAS, 235, 433

Hameury J.-M., King A.R., Lasota J.-P., 1986, MNRAS, 218, 695

Hameury J.-M., King A.R., Lasota J.-P., Ritter H., 1987, ApJ, 316, 275

Harrop-Allin M.K., Cropper M., Hakala P.J., Hellier C., Ramseyer T., 1999b, MNRAS, submitted

Harrop-Allin M.K., Cropper M., Potter S.B., Dhillon V.S., Howell S.B., 1997, MN-RAS, 288, 1033

Harrop-Allin M.K., Hakala P.J., Cropper M., 1999a, MNRAS, 302, 362

Hearn D.R., Richardson J.A., Clark G.W., 1976, ApJ, 210, L23

Heerlein C., Horne K., Schwope A.D., 1999, MNRAS, 304, 145

Heise J., Brinkman A.C., Gronenschild E., Watson M., King A.R., Stella L., Kieboom K., 1985, A&A, 148, L14

Hellier C., 1993, MNRAS, 264, 132

Hellier C., Mason K.O., Cropper M., 1990, MNRAS, 242, 250

Hellier C., Mason K.O., Rosen S.R., Cordova F.A., 1987, MNRAS, 228, 463

Hellier C., Mukai K., Beardmore A.P., 1997, MNRAS, 292, 397

Hessman F.V., Hopp U., 1990, A&A, 228, 387

Hoard D.W., 1999, in Hellier C., Mukai K., eds, Proc. Annapolis Workshop on Magnetic Cataclysmic Variables, ASP, vol. 157, p. 201

Horne K., 1983, Ph.D. thesis, California Institute of Technology

Horne K., 1985, MNRAS, 213, 129

Horne K., 1999, in Hellier C., Mukai K., eds, Proc. Annapolis Workshop on Magnetic Cataclysmic Variables, ASP, vol. 157, p. 349

Howell S.B., Szkody P., Cannizzo J.K., 1995, ApJ, 439, 337

Iben I., Livio M., 1993, PASP, 105, 1373

Ishida M., Silber A., Bradt H.V., Remillard R.A., Makashima K., Ohashi T., 1991, ApJ, 367, 270

Jablonski F., Busko I.C., 1985, MNRAS, 214, 219

Joy A.H., 1954a, PASP, 66, 5

Joy A.H., 1954b, ApJ, 120, 377

Kaitchuck R.H., Schlegel E.M., Honeycutt R.K., Horne K., Marsh T.R., White J.C., Mansperger C.S., 1994, ApJS, 93, 519

Kaul C.L., Kaul R.K., Bhat C.L., 1993, A&A, 272, 501

Kim S.-W., Wheeler J.C., Mineshige S., 1992, ApJ, 384, 269

King A.R., 1985, MNRAS, 217, 23

King A.R., 1989, MNRAS, 241, 365

King A.R., 1993, MNRAS, 261, 144

King A.R., 1995, in Buckley D.A.H., Warner B., eds, Cape Workshop on magnetic cataclysmic variables, ASP Conf. Ser. no. 85. ASP, California, p. 21

King A.R., Cannizzo J.W., 1998, ApJ, 499, 348

King A.R., Lasota J.P., 1979, MNRAS, 188, 653

Kolb U., 1995 in Evans A., Wood J.H., eds, Cataclysmic variables and related objects. Kluwer, Dordrecht, p. 433

Kopal Z., 1959, Close Binary Systems. Chapman & Hall, London

Kraft R.P., 1962, ApJ, 135, 408

Kraft R.P., 1963, Adv. Astron. Astrophys., 2, 43

Kraft R.P., 1964, ApJ, 139, 457

Krzeminski W., Kraft R.P., 1964, ApJ, 140, 921

Krzeminski W., Serkowski K., 1977, ApJ, 216, L45

Kuijpers J., Pringle J.E., 1982, A&A, 114, L4

Kuiper G.P., 1941, ApJ, 93, 133

Lamb D.Q., 1985, in Lamb D.Q., Patterson J., eds, Cataclysmic variables and low-mass X-ray binaries. Reidl, Dordrecht, p. 179

Lamb D.Q., 1988, in Coyne G.V. et al., eds, Polarized radiation of circumstellar origin. Vatican Obs., Vatican, p. 151

Lamb D.Q., Masters A.R., 1979, ApJ, 234, L117

Lamb D.Q., Melia F., 1988, in Coyne G.V., et al., eds, Polarized Radiation of Circumstellar Origin, Vatican Obs., Vatican, p. 45

Lamb F.K., Aly J.-J., Cook M.C., Lamb D.Q., 1983, ApJ, 274, L71

Lampton M., Margon B., Bowyer S., 1976, ApJ, 208, 177

Lang K.R., 1974, Astrophysical Formulae, Springer-Verlag, Berlin

Li J., 1999, in Hellier C., Mukai K., eds, Proc. Annapolis Workshop on Magnetic Cataclysmic Variables, ASP, vol. 157, p. 235

Li J., Wickramasinghe D.T., 1998, MNRAS, 300, 718

Li J., Wu K., Wickramasinghe D.T., 1994a, MNRAS, 268, 61

Li J., Wu K., Wickramasinghe D.T., 1994b, MNRAS, 270, 769

Liebert J., Stockman H.S., 1985, in Lamb D.Q., Patterson J., eds, Proc. 7th North American Workshop on Cataclysmic Variables and Low Mass X-ray Binaries. Reidl, Dordrecht, p. 151

Linnell A.P., 1949, Sky & Tel., 8, 166

Linnell A.P., 1950, Harv. Circ. no. 455

Livio M., Pringle J.E., 1994, ApJ, 427, 956

Livio M., Soker N., 1988, ApJ, 329, 764

Lubow S.H., Shu F.H., 1975, ApJ, 198, 383

Lubow S.H., Shu F.H., 1976, ApJ, 207, L53

Marsh T.R., Horne K., 1988, MNRAS, 235, 269

Mason P.A.., Liebert J., Schmidt G.D., 1989, ApJ, 346, 941

Mason P.A., Ramsay G., Andronov I., Kolesnikov S., Shakhovskoy N., Pavlenko E., 1998, MNRAS, 295, 511

Mason K.O., Watson M.G., Ponman T.J., Charles P.A., Duck S.R., Hassall B.J.M., Howell S.B., Ishida M., Jones D.H.P., Mittaz J.P.D., 1992, MNRAS, 258, 749

Meggitt S.M.A., Wickramasinghe D.T., 1982, MNRAS, 198, 71

Michalsky J.J., Swedlund J.B., Stokes R.A., 1975, ApJ, 198, L101

Mountain C.M., Robertson D.J., Lee T.J., Wade R., 1990, in Crawford D.L., ed., Proc. SPIE 1235, Instrumentation in Astronomy VII, SPIE, Bellingham, p. 25

Mukai K., 1988, MNRAS, 232, 175

Mukai K., 1998, ApJ, 498, 394

Mukai K., Charles P.A., 1985, MNRAS, 212, 609

Nikulin N.S., Kuvshinov V.M., Severny A.B., 1971, ApJ, 170, L53

Norton A.J., McHardy I.M., Lehto H.J., Watson M.G., 1992, MNRAS, 258, 697

Osborne J.P., 1988, Mem. Ast. Soc. Italy, 59, 117

Osborne J.P., Mukai K., 1989, MNRAS, 238, 1233

Osborne J.P., Rosen S.R., Mason K.O., Beuermann K., 1985, SSRv, 40, 143

Ostriker J.P., 1976, in Eggleton P.P., Whelan J., eds, Structure and Evolution of Close Binary Systems. Reidl, Dordrecht, p. 206

Paczyński B., 1976, in Eggleton P.P., Whelan J., eds, Structure and Evolution of Close Binary Systems. Reidl, Dordrecht, p. 75

Paresce F., 1984, AJ, 89, 1022

Patterson J., 1979, ApJ, 234, 978

Patterson J., 1984, ApJS, 54, 443

Patterson J., 1994, PASP, 106, 209

Peacock T., Verhoeve P., Rando N., Perryman M.A.C., Taylor B.G., Jakobsen P., 1997, A&AS, 123, 581

Penning W.R., 1985, ApJ, 289, 300

Penning W.R., Schmidt G.D., Liebert J., 1986, ApJ, 301, 881

Piirola V., Hakala P., Coyne G.V., 1993, ApJ, 410, L107

Potter S.B., 1998, Ph.D. thesis, University of London

Potter S.B., Cropper M., Mason K.O., Hough J.H., Bailey J.A., 1997, MNRAS, 285, 82

Potter S.B., Hakala P.J., Cropper M., 1998, MNRAS, 297, 1261

Press W.H., Teukolsky S.A., Vetterling W.T., Flannery B.P., 1992, Numerical Recipes in FORTRAN. Cambridge Univ. Press, Cambridge

Priedhorsky W.C., 1977, ApJ, 212, L117

Ramsay G., Buckley D.A.H., Cropper M., Harrop-Allin M.K., 1999, MNRAS, 303, 96

Ramsay G., Cropper M., Wu K., Mason K., Hakala P., 1999b, MNRAS, submitted

Ramsay G., Cropper M., Wu K., Potter S., 1996, MNRAS, 282, 726

Ramsay G., Mason K.O., Cropper M., Watson M.G., Clayton K.L., 1994, MNRAS, 270, 692

Ramsay G., Wheatley P.J., 1998, MNRAS, 301, 95

Ramseyer T.F., 1994, ApJ, 425, 243

Rappaport S., Joss P.C., Verbunt F., 1983, ApJ, 275, 713

Regős E., Tout C.A., 1995, MNRAS, 273, 146

Reinsch K., Beuermann K., 1990, A&A, 240, 360

Reinsch K., Burwitz V., Beuermann K., Schwope A.D., Thomas H.-C., 1994, A&A, 291, 27

Ritter H., Kolb U., 1998, A&AS, 129, 83

Robinson E.L., Barker E.S., Cochran A.L., Cochran W.D., Nather R.E., 1981, ApJ., 251, 611

Rosen S.R., Mason K.O., Cordova F.A., 1987, MNRAS, 224, 987

Rosen S.R., Mittaz J., Buckley D.A.H., Layden A., McCain C., 1995, in Buckley D.A.H., Warner B., eds, Cape Workshop on magnetic cataclysmic variables, ASP Conf. Ser. no. 85. ASP, California, p. 279

Rutten R.G.M., Dhillon V.S., Horne K., Kuulkers E., 1994, A&A, 283, 441

Saar S.H., 1990, in Stenflo J.O., ed, The Solar Photosphere: Structure, Convection, and Magnetic Fields. Kluwer, Dordrecht, p. 427

Schmidt G.D., Liebert J., Stockman H.S., 1995, ApJ, 441, 414

Schmidt G.D., Stockman H.S., 1991, ApJ, 371, 749

Schmidt G.D., Stockman H.S., Grandi S.A., 1983, ApJ, 271, 735

Schmidt G.D., Szkody P., Smith P.S., Silber A., Tovmassian G., Hoard D.W., Gänsicke B.T., de Martino D., 1996, ApJ, 473, 483

Schneider D.P., Young P., 1980a, ApJ, 238, 946

Schneider D.P., Young P., 1980b, ApJ, 240, 871

Schwarz R., Greiner J., 1999, in Hellier C., Mukai K., eds, Proc. Annapolis Workshop on Magnetic Cataclysmic Variables, ASP, vol. 157, p. 139

Schwope A.D., Beuermann K., 1990, A&A, 238, 173

Schwope A.D., Beuermann K., Burwitz V., Mantel K.-H., Schwarz R., 1995, in Bianchini A., Della Valle M., Orio M., eds, Cataclysmic variables. Kluwer, Dordrecht, p. 389

Schwope A.D., Buckley D.A.H., O'Donoghue D., Hasinger G., Trümper J.; Voges

W., 1997b, A&A, 326, 195

Schwope A.D., Mantel K.H., Horne K., 1997, A&A, 319, 894

Schwope A.D., Schwarz R., Mantel K.-H., Horne K., Beuermann K., 1995b, in Buckley D.A.H., Warner B., eds, Cape Workshop on magnetic cataclysmic variables, ASP Conf. Ser. no. 85. ASP, California, p. 166

Schwope A.D., Thomas H.C., Beuermann K., 1993, A&A, 271, 25

Schwope A.D. et al., 1998, in Howell S., Kuulkers E., Woodward C., eds, ASP Conf. Ser. 137, Proceedings of the 13th North American Workshop on CVs. ASP, California, p. 44

Shafter A.W., Reinsch K., Beuermann K., Misselt K.A., Buckley D.A.H., Burwitz V., Schwope A.D., 1995, ApJ, 443, 319

Shortridge K., Meyerdierks H., Currie M., Clayton M., 1996, Starlink User Note 86.12, Rutherford Appleton Laboratory

Shu F.H., 1982, The Physical Universe. University Science Books, California

Šimić D., Barwig H., Bobinger A., Mantel K.H., Wolf S., 1998, A&A, 115

Sirk M.M., Howell S.B., 1998, ApJ, 506, 824

Spruit H.C., Ritter H., 1983, A&A, 124, 267

Stobie R.S., Okeke P.N., Buckley D.A.H., O'Donoghue D., 1996, MNRAS, 283, 127

Stockman H.S., 1988, in Coyne G.V. et al., eds, Polarized radiation of circumstellar origin. Vatican Obs., Vatican, p. 237

Stockman H.S., 1995, in Buckley D.A.H., Warner B., eds, Cape Workshop on magnetic cataclysmic variables, ASP Conf. Ser. no. 85. ASP, California, p. 153

Stockman H.S., Liebert J., Bond H.E., 1979, in van Horn H.M., Weidemann V., eds, White dwarfs and variable degenerate stars. University of Rochester Press, Rochester, New York, p. 334

Stockman H.S., Lubenow A.F., 1987, Ap&SS, 131, 607

Stockman H.S., Schmidt G.D., Angel J.R.P., Liebert J., Tapia S., Beaver E.A., 1977, ApJ, 217, 815

Stockman H.S., Schmidt G.D., Lamb D.Q., 1988, ApJ, 332, 282

Storey P.J., Hummer D.G., 1995, MNRAS, 272, 41

Swedlund J.B., Kemp J.C., Wolstencroft R.D., 1974, ApJ, 193, L11

Szkody P., Brownlee D.E., 1977, 212, L113

Tapia S., 1977a, ApJ, 212, L125

Tapia S., 1977b, IAUC no. 3054

Thomas H.-C., Beuermann K., Schwope A.D., Burwitz V., 1996, A&A, 313, 833

Thompson A.M., Cawthorne T.V., 1987, MNRAS, 224, 425

Väth H., 1997, A&A, 317, 476

Väth H., Chanmugam G., Frank J., 1996, 457, 407

Verbunt F., Zwaan C., 1981, A&A, 100, L7

Visvanathan N., Wickramasinghe D.T., 1979, Nature, 281, 47

Walker M.F., 1954a, PASP, 66, 71

Walker M.F., 1954b, PASP, 66, 230

Walter F.M., Wolk S.J., Adams N.R., 1995, ApJ, 440, 834

Warner B., 1995, Cataclysmic variable stars. Cambridge Univ. Press, Cambridge

Warner B., 1995b, Ap&SS, 225, 249

Warner B., 1997, Ap&SS, 241, 263

Watson M.G., 1995, in Buckley D.A.H., Warner B., eds, Cape workshop on magnetic cataclysmic variables, ASP Conf. Ser. no. 85. ASP, California, p. 179

Watson M.G., King A.R., Jones M.H., Motch C., 1989, MNRAS, 237, 299

Watson M.G., Rosen S.R., O'Donoghue D., Buckley D.A.H., Warner B., Hellier C., Ramseyer T., Done C., Madejski G., 1995, MNRAS, 273, 681

West S.C., Berriman G., Schmidt G.D., 1987, ApJ, 322, L35

Wheatley P., 1999, in Hellier C., Mukai K., eds, Proc. Annapolis Workshop on Magnetic Cataclysmic Variables, ASP, vol. 157, p. 47

Wickramasinghe D.T., Cropper M., Mason K.O., Garlick M., 1991, MNRAS, 250, 692

Wickramasinghe D.T., Ferrario L., Bailey J.A., Drissen L., Dopita M.A., Shara M., Hough J.H., 1993, MNRAS, 265, L29

Wickramasinghe D.T., Meggitt S.M.A., 1985, MNRAS, 214, 605

Wickramasinghe D.T., Tuohy I.R., Visvanathan N., 1987, ApJ, 318, 326

Wickramasinghe D.T., Wu K., 1994, MNRAS, 266, L1

Wickramasinghe D.T., Wu K., Ferrario L., 1991, MNRAS, 249, 460

Woelk U., Beuermann K., 1992, A&A, 256, 498

Woelk U., Beuermann K., 1993, A&A, 280, 169

Woelk U., Beuermann K., 1996, A&A, 306, 232

Wu K., Wickramasinghe D.T., 1993, MNRAS, 260, 141

Wynn G.A., King A.R., 1995, MNRAS, 275, 9

Wynn G.A., King A.R., Horne K., 1997, MNRAS, 286, 436

Young P., Schneider D.P., 1979, ApJ, 230, 502

ACKNOWLEDGEMENTS

To Darragh O'Donoghue for the use of his period analysis software Eagle, which was used in chapter 6.

To all the other people I've met at the lab: Cynthia, Jon, Kerry, Rex, Encarni, Dave, Phil and Stefan. Thanks for the lunch-time walks! Thanks especially to Mat and Gav for putting up with my constant stressed state.

To Mark Garlick, for being the first person to tell me about CVs, and the first to explain to me what 'double glazing' is.

To Lorna, for helping me maintain a sensible perspective on life, and reminding me that there is more to life than sitting behind a computer for eight hours a day.

To my parents, for all their support and encouragement throughout my academic career. I'm sure they are now extremely relieved that their younger daughter is going to go out and get a proper job!

... and finally to Chris, for being an unfailing source of love and encouragement, and for repeatedly reassuring me that recalcitrant computer programs do not constitute sufficient grounds for major existential crises.